Durham E-Theses

Study of extensive air showers at sea level using a flash tube chamber

Pavaresh, A.

How to cite:

Use policy

STUDY OF EXTENSIVE AIR SHOWERS

AT SEA LEVEL USING A FLASH

TUBE CHAMBER

by

A. PARVARESH, B.Sc.

A thesis submitted to the

University of Durham

for the Degree of Doctor of Philosophy

April, 1975.

CONTENTS

ABSTRACT

The density spectrum of extensive air shower particles was measured using a proportional counter. It was found that the slope of the integral spectrum changes from -1.5 to -2.0 at about 1,000 m^{-2}. Using this spectrum the primary energy spectrum of cosmic rays was derived.

In measuring the density spectrum of extensive air showers, the selection system consists of three large liquid scintillators placed horizontally on the roof of a large volume flash tube chamber. In each trigger the passage of the penetrating component through the chamber were photographed. The density spectrum of the penetrating component of extensive air showers was measured and the results compared with the expected spectrum folding the derived number spectrum, measuring the density spectrum of extensive air showers, into the lateral distribution of muons.

The energy spectra of charged and neutral hadrons in extensive air showers of median shower size of $2.7.10^5$ particles have been measured. The results have been related to the energy spectra of hadrons in shower range of 2.10^4 to 4.10^5 particles.

A search for charged $e/3$ particles (quarks) close to the core of extensive air showers, of median size of $2.7.10^5$ particles, has been carried out. In 5,420 hrs running time no quark candidate has been observed. The upper limit on the quark flux being $5.5.10^{-11}$ $cm^{-2}s^{-1}st^{-1}$ at 90% confidence level.

PREFACE

This thesis describes the work performed by the author in the Physics Department of the University of Durham while he was a research student under the supervision of Dr. F. Ashton.

A proportional counter in conjunction with a large volume flash tube chamber has been used to study the different components of extensive air showers selected by the predetermined local electron densities.

The day-to-day running of the proportional counter and the analysis and interpretation of the data has been the author's sole responsibility. The author has shared with his colleagues the collection of data obtained by flash tube chamber, and has been responsible for the calculations and data interpretation described in the thesis.

The preliminary results, described in this thesis, on the density spectra of electron, muons and a quark search have been reported by Ashton et al. (1973b,c,d).

CHAPTER 1

INTRODUCTION

1.1 General

Among 20 cloud chamber photographs containing tracks
of cosmic ray particles, Skobel'tsyn (1929) observed three
photographs with two particles and one photograph with three
particles. This showed the ability of cosmic ray particles
in producing groups of simultaneous particles. The existence
of this kind of phenomena, called extensive air showers (EAS),
encompassing areas amounting to a thousand square metres and
more was disclosed by Auger (1938) and independently by
Kolhörster et al., (1938).

The discovery of EAS coincided with the theory of electron-
photon cascades proposed by Bhabha (1937) and thus led Euler
(1940) in suggesting that EAS as being electron-photon cascades
produced in the atmosphere by means of high energy electrons.

Schein et al. (1941) observed hard particles in cosmic
rays and found that only a few per cent of these particles
associated with EAS and that the intensity of hard particles
in cosmic rays increases as the height of observation increases.
These observations led Schein et al., to conclude that primary
cosmic rays are protons and that soft component were second-
aries originated by the primary protons, probably through the
production of mesons that subsequently decay into electrons
(Carlson, 1941).

In 1947, Lattes, Occhialini and Powell exposed nuclear
emulsion plates to cosmic radiation at mountain altitudes,
which led to the discovery of pion . The pion was later

associated with the Yukawa particle, the theoretical particle proposed by Yukawa to explain the binding force of nucleons. In the same year Rochester and Butler (1947) discovered 'strange' particles.

The discovery of mesons in cosmic radiation and other experimental observations led Zatsepin (1949) and Hayakawa (1949) to formulate the nature of EAS. According to their views: EAS are generated by primary nucleons. These nucleons interact in the atmosphere producing, soft, penetrating and nuclear-active components of EAS. All this taken as a whole transformed cosmic ray particles into a branch of nuclear physics, and the study of EAS turned out into a method to investigate the properties of high energy nuclear interactions.

The energy region of EAS which one can study high energy physics is still far beyond the energy available in accelerators, i.e. far beyond the order of 10^{12} eV (ISR energy region).

1.2 Density spectra of electrons and muons

By flying balloons with nuclear emulsion payloads to great heights, and more recently using satellites, it has been possible to study the primary cosmic radiation directly up to energies of $\simeq 10^{12}$ eV/nucleon. Information at higher energies than $\simeq 10^{12}$ eV/nucleon is not possible by means of direct measurements. Thus above this energy indirect measurements have been used. This includes the study of EAS for energies of $\gtrsim 10^{14}$ eV.

The density spectrum of EAS determines the size spectrum which in turn could be related to the primary energy spectrum.

An experiment has been carried out to measure the density spectrum of EAS. This is described in chapter 3.

Another parameter of the EAS which could be related to the primary spectrum is the number spectrum of muons. Using the flash tube chamber, as a visual detector, the density spectrum of muons of $\gtrsim$ 0.2 GeV has been measured which is described in chapter 4.

Measuring the angular distribution of the muons observed in the chamber and measuring the barometric coefficient of EAS the attenuation length of the shower particles have been deduced. The results have been explained in chapter 5.

1.3 Energy spectra of hadrons

Measuring the burst width spectra of the hadrons observed in the flash tube chamber below the lead and iron absorbers, in showers of median size of $2.7.10^5$ particles, the energy spectra of hadrons in showers have been determined.

Chapter 6 describes the results obtained, and in chapter 7 the nuclear physical aspects of the results have been considered.

1.4 Search for quarks

Above $\simeq 10^{12}$ eV cosmic rays are the only accessible high energy beam; they are, therefore, still contributing to the field of high-energy physics, in particular to search for theoretically predicted particles such as quarks, intermediate bosons, monopoles and tachyons.

A search for quarks close to the core of EAS of the median size of $2.7.10^5$ particles has been conducted using

the flash tube chamber.   This is described in chapter 8.

A type of event showing the production of single backward moving secondary has been observed in the flash tube chamber.   This is investigated in chapter 9 and a possible explanation of their production has been proposed.

CHAPTER 2

REVIEW OF MEASUREMENTS ON EAS

2.1 Introduction

When a high energy cosmic ray particle, say of energy
$\gtrsim 10^{14}$eV, arriving at the top of the atmosphere collides
with a nucleon of an air nucleus, a large number of second-
aries are produced - pions, nucleons, antinucleons, kaons
and other strong interacting particles. Charged mesons,
surviving nucleons and other produced strong interacting
particles suffer further collisions and generate more
secondaries. The neutral pions decay immediately into
two gamma rays which initiate electromagnetic cascades in
the atmosphere. As their energy becomes less the decay
probability of charged pions and kaons becomes comparable
to their interaction probability and muons are formed by
$\pi \to \mu + \nu$ and $K \to \mu + \nu$. These processes give rise to
the penetrating component of air showers. This process
of hadronic and electromagnetic cascade generation continues
deep down in the atmosphere and results in a large number of
secondary particles which spread laterally to considerable
distances from the shower axis. The reasons for this are
as follows:

i)   the finite transverse momentum of the produced strongly
interacting particles.

ii)   the angular divergence of gamma rays and muons formed
in decay processes.

iii)   the deflection of charged particles due to the earth's magnetic field.

iv)   the multiple scattering of charged particles in traversing the atmosphere.   The resulting phenomenon is called an extensive air shower (EAS).

The hadronic and electromagnetic cascades reach their maximum at different depths in the earth's atmosphere depending on their primary energy and the details of the collision processes.

Since the majority of the electrons are relativistic and have velocities greater than the velocity of light in the atmosphere, they give rise to Cerenkov radiation, a significant proportion of which is in the visible part of the electromagnetic spectrum.   The electrons also give rise to coherent emission of radio waves in the frequency range of 1 MHz to several hundreds of MHz.   The energy radiated in the form of radio waves is however 10^{-4} times less than the energy radiated by Cerenkov radiation.

At the observation level, whether at mountain altitudes or at sea level most of the air shower particles arrive in the form of thin discs a few meters in thickness.

Thus the following components are available for experimental observations, (i) the soft component, (ii) the penetrating (muon)component, (iii) the hadronic component, (iv) Cerenkov light and (v) radio waves.

It is hoped that by studying different components of EAS (both laterally and longtitudinally) and the relationship between them, one can derive primary energy spectrum beyond $\sim 10^{14}$eV, primary mass composition and directional distri-

bution of primaries, as well as the characteristics of high energy nuclear interactions.

2.2 The lateral distribution of electrons

The investigation of the lateral distribution of charged particles has made it possible to obtain a considerable amount of information about the pattern of the formation and development of EAS, as well as the lateral distribution of shower particles, which makes it possible to determine the total number of particles at the level of observation. This is the most important parameter in the analysis of the experimental data on EAS, since knowing the longtitudinal development of shower it is possible to estimate the energy of the primary particle producing the shower.

The lateral distribution function of charged particles has been derived theoretically by Nishimura and Kamata (1952, 1958) for pure electromagnetic cascades considering the multiple scattering of electrons due to the Coulomb field of the medium. A simplified version of the formula has been suggested by Greisen (1956) and is called Nishimura – Kamata – Greisen (NKG) formula given by

$$f(\frac{r}{r_1})= C(S) \; (\frac{r}{r_1})^{S-2} \; (\frac{r}{r_1}+1)^{S-4.5} \qquad \text{where } r_1$$

is called the Moliere or scattering unit and defines the lateral distance through which an electron with critical energy, E_c, is scattered in traversing one radiation length (the value of r_1 is 79 m at sea level and about 120 m at mountain altitude), r is the perpendicular distance from the shower core, s is the cascade age parameter and indicates the

development stage of the shower and C(S) is a normalisation factor such that

$$\int_0^\infty 2 \pi f(x) \, x \, dx = 1 \quad \text{where} \quad x = \frac{r}{r_1}$$

Values of C(S) are as follows (Greisen, 1956)

S	0.6	0.8	1.0	1.2	1.4	1.6	1.8
C(S)	0.22	0.31	0.40	0.44	0.43	0.36	0.25

Thus assuming the lateral distribution function is independent of shower size the electron density at distance r, $\rho(N,r)$, from the core in a shower of size N is simply

$$\rho(N,r) = \frac{N}{r_1^2} \, f\left(\frac{r}{r_1}\right)$$

Greisen (1960) has put forward the following emperical expression for the lateral electron density, based on experimental results which cover a range of shower sizes varying from 2.10^3 to 2.10^9 particles, atmospheric depths varying from 537 g cm^{-2} to 1,800 g cm^{-2}, and at core distances running from 5 cm to 1,500 m, namely

$$\rho(N,r) = \frac{0.4N}{r_1^2} \left(\frac{r_1}{r}\right)^{0.75} \left(\frac{r_1}{r_1+r}\right)^{3.25} \left(1 + \frac{r}{11.4 \, r_1}\right)$$

Without the last factor on the right - hand side of the above expression the equation is the same as the NKG formula with age parameter S = 1.25. A simple calculation shows that in a shower of 2,000 particles, at sea level, there is only one particle within 10 cm of the core, only 17 within a metre and only one particle per 120 m^2 at 100 m far from the core using the above mentioned equation.

Therefore the measurements on the lateral structure

function near and far from the core needs more precision and some discrepancies between different experimenters are expected.

The measurements of Sydney group at sea level (Hillas, 1970a) give a much flatter distribution function compared with the emperical formula of Greisen. The flatness is due to the observation of a large proportion of multi core showers for showers induced by primaries of energy $\gtrsim 10^{15}$ eV. The function is expressed by

$$\rho(N,r) = 2.12 \cdot 10^{-3} \frac{N}{r+1} \exp(-\frac{r}{75}) \quad \text{where r is in meters.}$$

The Kiel group (Hillas, 1970a) measurements on the particle densities (with neon tube hodoscopes) near shower axes at sea level are represented by

$$\rho(N,r) = 1.08 \cdot 10^{-2} \frac{N}{(r+1.1)^{1.5}} \exp(-\frac{r}{120}) \quad \text{where r is in meters.}$$

The analytic expressions mentioned above for the lateral structure of electrons due to Greisen, Kiel group and Sydney group are shown in figure 2.1. All three functions are normalised to unity.

As figure 2.1 shows that there is good agreement between the measured lateral density distribution of electrons between different experimenters in the region of $r \simeq 10 - 300$ m from the shower axis.

The observed discrepency between measurements at both large and small core distances is partly due to the experimental errors in core location.

It is interesting to note that while most of the measurements of the lateral electron density distribution indicate
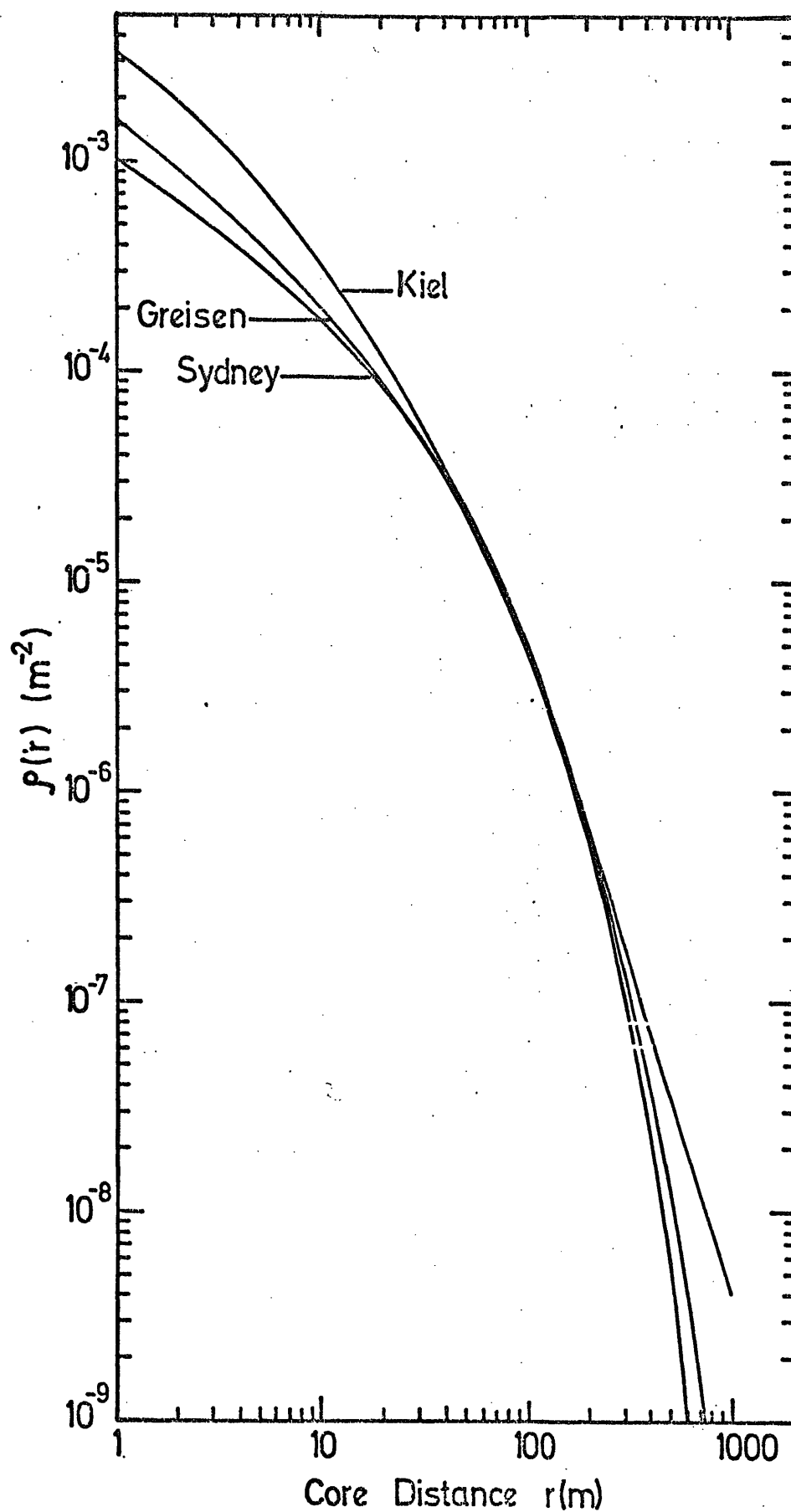
Figure 2.1   Lateral structure function of EAS particles. The curves are due to emperical formula given by Greisen (1960) and observations of Kiel group and Sydney group Hillas (1970a). The ordinate gives electron density for a shower size of N = 1.

that the function is independent of shower size (Greisen, 1960), there is some evidence which suggests that not only does the function depend on shower size, but for higher sizes the average age parameter increases as shower size increases as shown in figure 2.2 (Miyake et al. 1973, Vernov et al. 1970). This is surprising because as the shower size increases one would expect the showers to be younger since there would be higher energy nucleons feeding into the electromagnetic components. As figure 2.2 shows the increase in average value of age parameter $\bar{S}$ (the age parameter fluctuates, see Vernov et al, 1968) starts from the showers of sizes $\gtrsim 2.10^7$ (equivalent to $\simeq 4.10^{16}$ eV primary) at 730 g cm^{-2} atmospheric depth as measured by Miyake et al., and of size $\gtrsim 2.10^6$ at sea level (equivalent $\simeq 2.10^{16}$ eV primary) as reported by Vernov et al, (to convert shower size to primary energy a factor of 2 GeV per particle at mountain altitude and 10 GeV per particle at sea level is assumed). To account for this behavier, Miyake et al., suggest a change in the characteristics of nuclear interaction above $\simeq 10^{17}$ eV.

The increase in age parameter for large shower sizes has been explained by Linsley (1973) to be due to the fact that the age parameter measured at large distances should be larger than average, and that measured at small distances, smaller than average. Now since large showers typically have been measured far from the core, the measured age parameter shows an increase.
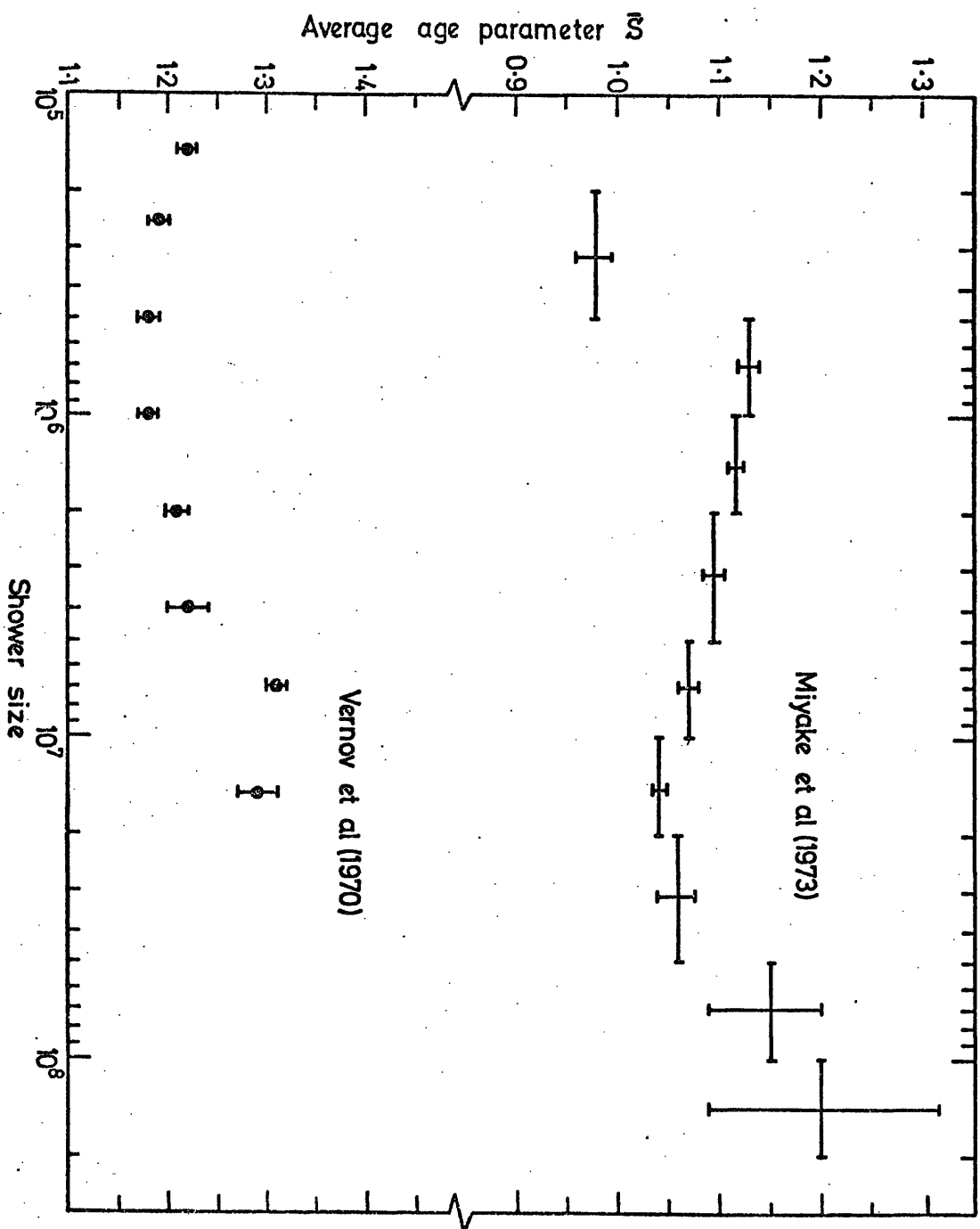
Figure 2.2   The dependence of average age parameter as a function of
shower size measured by Vernov et al. (1970) at sea level
and by Miyake et al. (1973) at 2770 m. elevation.

2.3   The muon component

2.3.1   General remarks

Tranverse momentum acquired by mesons during their generation plays a decisive role in the deflection of the muons from the shower axis (Vavilov et al., 1957). Thus the study of the lateral distribution function of muons gives information about the transverse momentum of mesons. On the other hand it should be noted that the lateral and energy properties of muons associated with air showers as a whole are connected with the characteristics of nuclear interactions at high energy, and with pecularities in the development of the nuclear cascade avalanche with depth. They depend only indirectly on the characteristic of the collision of the primary particle which has given rise to the EAS with the nucleus of the air atom. The characteristics of the nuclear interaction at $E \lesssim 10^{12}$ eV have been investigated in much more direct measurements. The interesting feature of the measurements of the lateral distribution function of muons at high energy and at large distances from the core, is that it is expected that they have originated high up in the atmosphere in the first few collisions. Thus it is possible to get some information about the primary mass composition (Orford and Turver, 1970).

Linsley and Scarsi (1962) have pointed out the correlation between primary mass composition and the total number of muons in a shower of size N.

In general, measurements of the muon number spectrum at

sea level enables one to calculate a rather more accurate primary spectrum. This result follows from the long shower attenuation length of the muons in the atmosphere compared to electrons.

2.3.2   The lateral distribution of muons

The experimental data of Clark et al. (1958) with E $\geq$ 1.2 GeV in the range of N = 2.10^5 - 2.10^8 is given by Greisen (1960) namely

$$\rho_\mu(N,r) = 18 \ (\frac{N}{10^6})^{0.75} \ r^{-0.75} \ (1+\frac{r}{320})^{-2.5}$$

where $\rho_\mu(N,r)$ is the density of muons m^{-2} falling at core distance r metres in a shower of size N.

The data of the Cornell group (Bennett et al., 1962) with energy threshold of E GeV in the size range of N = 10^3 - 10^7 particles show about 20% reduction in absolute rate compared to the results of Clark et al., and is represented by

$$\rho_\mu\left(N,r,> E\right) = 14.4 \ (\frac{N}{10^6})^{0.75} r^{-0.75}(1+\frac{r}{320})(\frac{51}{E+50})(\frac{3}{E+2})^{0.14 \ r^{0.37}}$$

where $\rho_\mu(N,r,> E)$ is the density of muons m^{-2}, r is in meter and E is in GeV.

Subsequent measurements on the lateral density of muons at the low energy region (up to about 20 GeV) show a general agreement with the above equation for r $\geq$ 20 m, as shown in figure 2.3. The lateral distribution function given by Greisen, as it is plotted in figure 2.3, is steeper than the other measurements. This could be explained as a result of
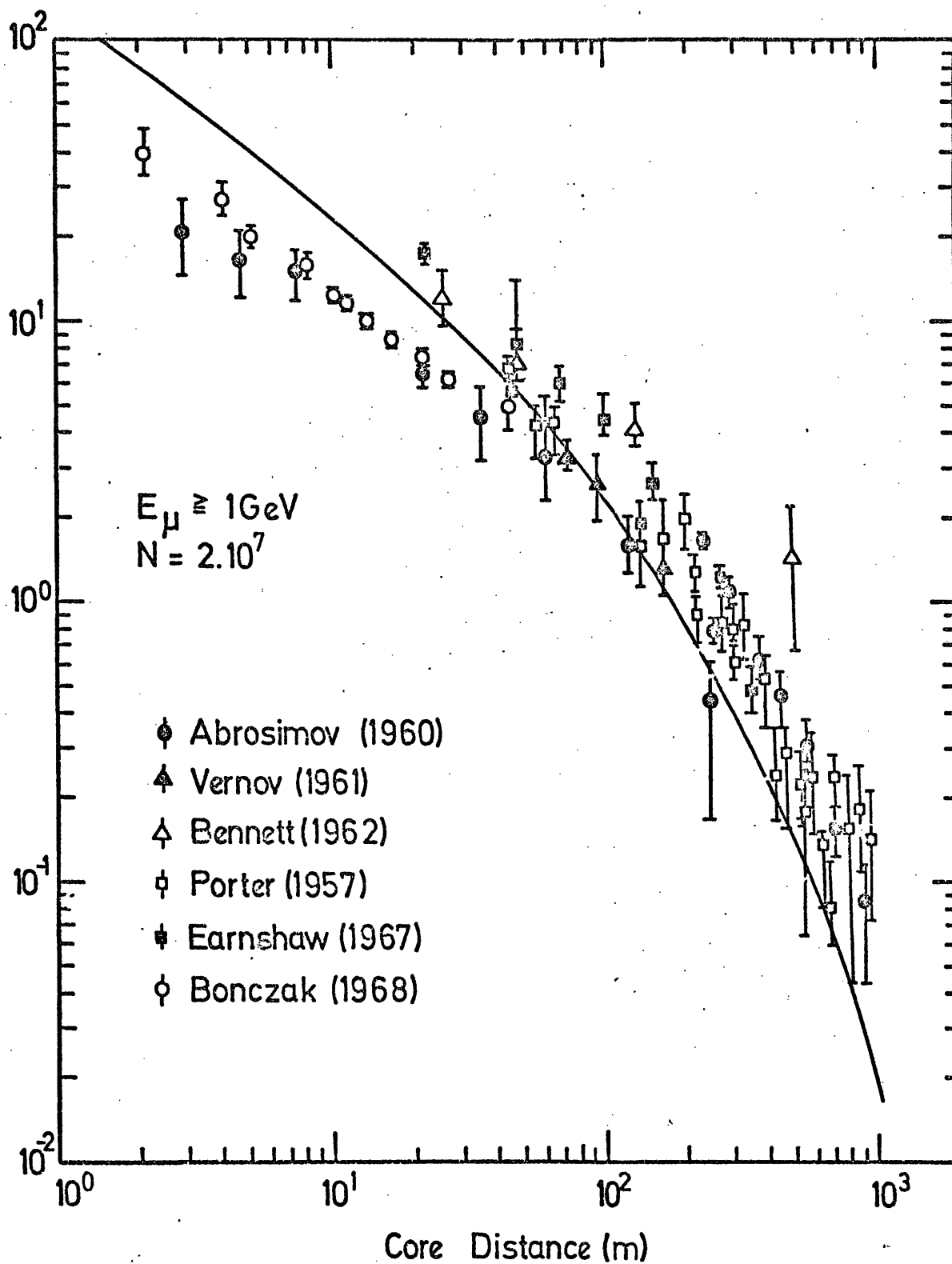
Figure 2.3   The muon lateral distribution for 1 GeV energy
threshold.   All data are normalised to a shower
size N = 2.10[7] particles.   The continuous curve
was calculated according to Greisen's formula.
(After Wdowczyk, 1973).

the inaccuracy in core location, as well as the effect
of normalisation which has been introduced by Wdowczyk
(1973) to bring all the measured results into harmony,
i.e., normalised to $N = 2 \cdot 10^7$.

Murthy et al. (1968b), however, have compared the
predicted lateral distribution of muons ($E_\mu > 1$ GeV) in a
shower of size $3 \cdot 10^7$, assuming different models for core
distances $r = 1 - 1,000$ m with Greisen's fit to the experi-
mental data. They find that all models predict a steeper
lateral distribution function than experimental measurements.

2.3.3   Total number of muons

Integrating the lateral muon density over all core
distances gives the total number of muons, N_μ, of energy
threshold E GeV in a shower size N. Table 2.1 shows a
representative number of experimental results.

Using the relationship between $N_\mu (> E$ GeV) and N_e
at the level of observation Suga et al. (1963) and Gawin et
al. (1963) adopted a method based on the expectation that a
gamma ray induced shower will be characterised by practically
no muons or at best very few muons compared to hadron induced
showers, since the cross section for photo-meson production
is very low.

Kamata et al. (1968) carried out an experiment at
an atmospheric depth of 530 g cm^{-2}. The minimum size of
showers recorded for which the angular information has
also been available was equal to 10^4. The muon component

Reference	Relationship between N_μ and N	Range of shower size
Greisen (1960)	N_μ (> 1 GeV)$= 95000 \times (\frac{N}{10^6})^{0.75}$	$N = 2.10^5\text{-}2.10^8$
Vernov et al. (1968)	N_μ (> 10 GeV) $= (4.9 \pm 0.7)10^3 \times (\frac{N}{10^5})^{0.78 \pm 0.025}$	$N \simeq 10^5\text{-}10^8$
Barrett et al. (1952)	$\frac{N_\mu \ (> 56 \text{ GeV})}{N^{0.58 \pm 0.05}}$	-
Earnshaw et al. (1968)	N_μ (> 100 GeV)$= 10^4$	$N = 2.10^7$
Chatterjee et al. (1965)	N_μ (> 220 GeV) $= 50 \times (\frac{N}{10^6})^{0.47 \pm 0.1}$	$N = 10^5\text{-}10^6$
Greisen (1960)	N_μ (> 560 GeV) $= 75 \times (\frac{N}{10^6})^{0.7}$	$N \gg 10^3$

Table 2.1   This shows the relationship between the observed number of muons N_μ at a particular energy threshold associated with EAS of sizes N.   The related range of shower sizes are given.

was detected by plastic scintillators under 320 g cm^{-2} of concrete and lead absorber. The results of Kamata et al. showed that

(i)   there is a distinct class of mu poor showers in the range of $N = 3.10^4 - 3.10^6$ with ratio of 5.10^{-4} of all showers in the size range and there is no evidence for their existence for $N > 5.10^6$.

(ii)   there is no marked anisotropy for this size range which can be attributed to point gamma ray sources.

The results of Catz et al. (1970, 1971) at sea level using neon hodoscopes showed that in the energy range $10^{15} - 10^{16}$ eV the relative number of showers which were mu - poor showers was 3.10-3 of all showers. They found that the zenith angle distribution of mu - poor showers is considerably different from normal showers. The median angle of mu - poor shower is $\sim 37^{\circ}$ compared to 22° for proton induced showers and $\sim 24^{\circ}$ of all showers. This ruled out the possibility that mu - poor showers are due to the fluctuations in the collision characteristics of hadrons responsible for normal showers. However Catz et al. claimed that the muon content of the mu - poor showers in their experiment is considerably higer than what is expected on the basis of the expected photonuclear cross section at these energies.

2.4   The hadron component

2.4.1   General remarks

It is known that nuclear cascade plays a basic role in the development of EAS in the atmosphere.   Thus a knowledge of the properties of hadronic component gives information about the characteristics of high energy interactions and therefore determines the primary spectrum by studying them at different depths.

A sensitive parameter to the assumed model of high energy interaction is the total number and energy spectrum of hadrons of energy E in a shower initiated by a fixed primary energy (Grieder, 1973a).   Thus it is of great interest to measure these parameters in EAS.   This can be achieved in principle by measuring the lateral distribution of hadrons in showers of fixed N_e.

2.4.2   The lateral distribution of hadrons

The lateral distribution function of hadrons has been measured for different hadron energies and different ranges of slower size and at different altitudes.

The overall experimental observation show an exponential function in the form of $\exp(- \frac{r}{r_o})$.   A parameterised expression is given by Kameda et al. (1965) in the form of

$$ n(E,r,N)dE \, dr = 0.35 \; N^{0.35} \; E^{-1.2} \, \exp \, (- \frac{r}{r_o})dE \, dr $$

where $r_o = 2.4 \; N^{0.32} \; E^{-0.25}$

In this formula $n(E,r,N)$ represents the density of hadrons m^{-2} with energy between E and E + dE (in units of 100 GeV)

that fall at core distances r m to r + dr m in a shower of N particles (in units of 10^5 particles). The experiment was carried out at sea level for showers of size $4.10^4 - 4.10^6$ particles and hadrons of energy in the range of 100 -1,000 GeV.

The experimental results of Kameda et al. together with a number of different measurements carried out at different atmospheric depths for hadrons with different energy thresholds in different shower size ranges as defined in table 2.2 are shown in figure 2.4.

Table 2.2   The available information about the experimental observations of the lateral density of hadrons plotted in figure 2.4.

Reference	Energy threshold of hadrons (GeV)	Range of shower size (N)	Altitude of observation (g cm^{-2})
Kameda et al. (1965)	300	$4.10^4 - 4.10^6$	1030
Chatterjee et al. (1968)	200	$1.8.10^5 - 3.2.10^5$	800
Tanaka (1961)	100	$\geq 10^4$	1030
Van Staa et al. (1973)	200	$10^{5.1} - 10^{6.5}$	730

The value of r_0 (the reciprocal of the slope of the lateral distribution of hadrons) as reported by Kameda et al. and Chatterjee et al. increases with shower size.

According to Chatterjee et al. a model in which the p_t (transverse momentum of hadrons) distribution and inelasticity
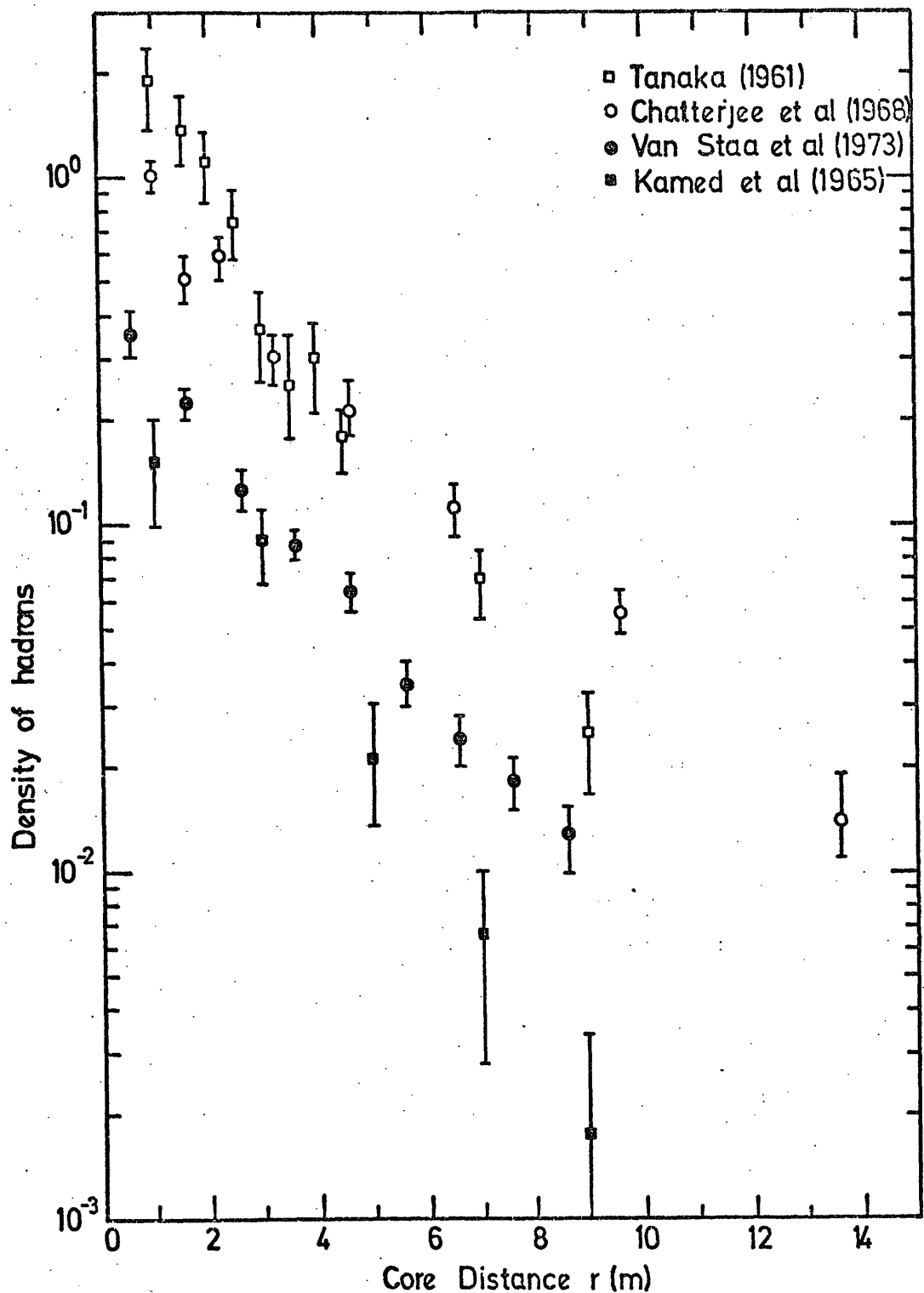
Figure 2.4 The hadron lateral distribution for different energy threshold and different shower sizes observed at different altitudes. The available information is summarised in table 2.2. The ordinate is in units of particles m^{-2} for the observation of Chatterjee et al and Van Staa et al and it is arbitary unit for the data of Tanaka and Kemeda et al.

are invariant (Murthy et al. 1968c) could not explain the
observed lateral distribution function, nor can it be
explained by any conceivable change in primary composition
with energy since such models$_\wedge$ predict a slight steepness in
the$_\wedge$ slope of$_\wedge$ lateral distribution of hadrons with increase
in shower size. A model with the following changes in
interaction characteristics above 10^5 GeV was more satisfactory
to fit the data of Chatterjee et al. (i) increase in elast-
icity, (ii) increase in average transverse momentum of
charged created particles, (iii) a faster increase in
multiplicity of charged particles.

Van Staa et al. found that the value of r_o is virtually
independent of shower size. However, they found that the
mean distance of hadrons from the shower axis is larger ($\bar{r} = 2r_o$)
than the value obtained from the Monte Carlo calculation
performed by Bradt and Rappaport (1967) by a factor of $\simeq \frac{4}{3}$.
Since the calculation of Bradt and Rappaport is based on a mean
transverse momentum of $\bar{p}_t = 0.35$ GeV/c, the value of $\bar{p}_t$ obtained
by Van Staa et al. is $\bar{p}_t = 0.5$ GeV/c assuming $\bar{r}$ is proportional
to $\bar{p}_t$.

It is interesting to note that there is some evidence
based on the observation on multicore showers, which suggests
a much higher value of $\bar{p}_t$. Miyake et al. (1970) suggest an
average transverse momentum of 6 GeV/c at an energy of 3.10^{12}ev.
Samorski et al. (1971) who find very few multicore events
are of the opinion that $\bar{p}_t$ at air shower energies is not
different from what has been reported at lower energies.

2.4.3 Flux and energy spectrum of hadrons

Chatterjee at al. (1968) have summarised the results of a number of experimental observations obtained on the flux and energy spectrum of hadrons. This is shown in table 2.3.

As the table indicates the integral energy spectrum of hadrons of $E > 100$ GeV follows a power law with slope of $\simeq -1$ and is approximately proportional to shower size.

The slope of integral energy spectrum is in close agreement with model calculations by the Monte Carlo method performed by Bradt and Rappaport (1967) and Thielheim and Beirsdorf (1969) based on an $E^{1/4}$ law for multiplicity. These authors found a value of -1.2 for the exponent of the integral energy spectrum of hadrons in the range of $E = 100 - 2,000$ GeV.

An attempt has been made by Grieder (1973a) to compare the experimental results of Tanahashi (1965) at sea level with different assumed models for high energy interactions. He finds that the model called SFB^* (single fire ball model) when the probability of excitation of the projectile to an isobaric state is unity gives satisfactory results. The SFB^* model, however, follows a multiplicity in the form of $<n_s> \propto S^{1/2}$ (Grieder, 1970 private communication) where S is the square of the available energy in centre of mass system (CMS) for the creation of secondary particles.

Tanaka (1961) gives the following expression for the total number of hadrons with energy threshold of E_N GeV in a shower of size N.

Reference	Number of hadrons of energy ≥ 100 GeV		Slope of integral energy spectrum	Exponent of size variation	Altitude of observation (g cm-2)	Detector
	shower size (10^5)	shower size (10^6)				
Tanaka et al.(1961) Fukui et al.(1960)	50	625	1.0±0.1	1.1 ±0.1	1000	Transition chamber
Kameda et al.(1965)	7.2	72	0.75±0.1	1.0 ±0.1	1000	Cloud chamber
Tanahashi (1965)	9	110	1.0	1.1	1000	pb glass Cerenkov underground scintillators.
Nikolski (1963)	10	100	1.0 ±0.1	1.0	All altitudes	Different detectors
Hasegawa et al. (1965)	10	80	0.9 ±0.1	0.8 ±0.1	530	Lead shielded scintillators
Chatterjee et al. (1968)	105	630	1.1±0.05	0.78±0.05	800	Total absorption spectrometer(TAS)

Table 2.3   Rate of hadrons in EAS of 100 GeV energy threshold and the slopes of the integral energy spectrum of hadrons and its dependence on shower size obtained at different elevations.

$$n\ (> E_N,\ N)\ =\ \frac{5.10^{12}}{E_N}\ (\frac{N}{10^5})^{1.1}$$

Thus for showers of sizes 10^3, 10^4, 10^5 respectively there is only one hadron with energy threshold of 3.10^{10}eV, 4.10^{11}eV and 5.10^{12}eV. Tanaka then argues that though it is not yet assured that there is always one and only one such high energy particle in each shower, those hadrons of more than E_N could be tentatively assumed to be surviving primary particles. Therefore Tanake suggests that primary particles still hold on the average more than 0.3 - 0.5% of their initial energies at sea level. Assuming the collision mean free path to be equal to 100 g cm^{-2} thus the geometric mean of inelasticity is approximately 0.4 - 0.5.

2.5   The measured electron number spectrum

The standard procedure to derive the primary energy spectrum for $E_p \gtrsim 10^{14}$eV is to measure the number spectrum and relate it to primary energy spectrum assuming a model for the development of showers through the atmosphere.

Since the majority of secondary charged particles of EAS are electrons (about 90%) and the primary energy spectrum can not be derived with an accuracy better than 10%, an estimate of electron number spectrum at the level of observation could be related to the primary energy spectrum with reliable accuracy.

To construct the number spectrum one can use both direct data on the frequency of occurrence of showers at a particular number of particles with a given location of the shower axis, and indirect measurements of the "density spectrum". In the latter case a knowledge of the lateral structure function of

electrons and its dependecne on shower size is essential.

Over the years very many measurements of the electron size spectrum (direct method) have been made with a variety of detectors and with varying degrees of precision. The available data on the integral size spectrum both at sea level and at mountain altitudes is summarised by Hillas (1970b) and is plotted as integral rate x $N^{1.5}$ as a function of shower size (N) in figure 2.5.

Inspection of figure 2.5 indicates the following features.

(i) There appears to be a transition from a region of virtually constant slope to another of greater exponent at about $N \simeq 5.10^5$ at sea level and $N \simeq 2.10^6$ at mountain altitudes.

(ii) The transition region is rather short, i.e., there is a sharp change of slope.
The experimental results shown in figure 2.5, at sea level, parametârises as follows:

$$R (\geq N) = 52 \ N^{-1.5} \ m^{-2} \ s^{-1} \ st^{-1} \ \text{for} \ N \leq 5.10^5$$

$$R (\geq N) = 36,920 \ N^{-2.0} \ m^{-2} \ s^{-1} \ st^{-1} \ \text{for} \ 5.10^5 \leq N \leq 3.10^7$$

$$R (\geq N) = 6.76 \ N^{-2.0} \ m^{-2} \ s^{-1} \ st^{-1} \ \text{for} \ N > 3.10^7$$

where $R(\geq N)$ is the integral rate of showers containing more than N particles at sea level.

The slope of integral number spectrum for $N \gtrsim 3.10^7$ has not yet been clearly determined. It is shown recently by Khristiansen et al.(1974) that the slope of the integral number spectrum for $N > 10^7$ is about 2.4 - 2.5. The tendency of the flattening in the slope for $N > 10^7$ is also suggested by Khiristiansen et al. considering the muon number spectrum as it is shown in figure 2.6. According to figure 2.6 the integral
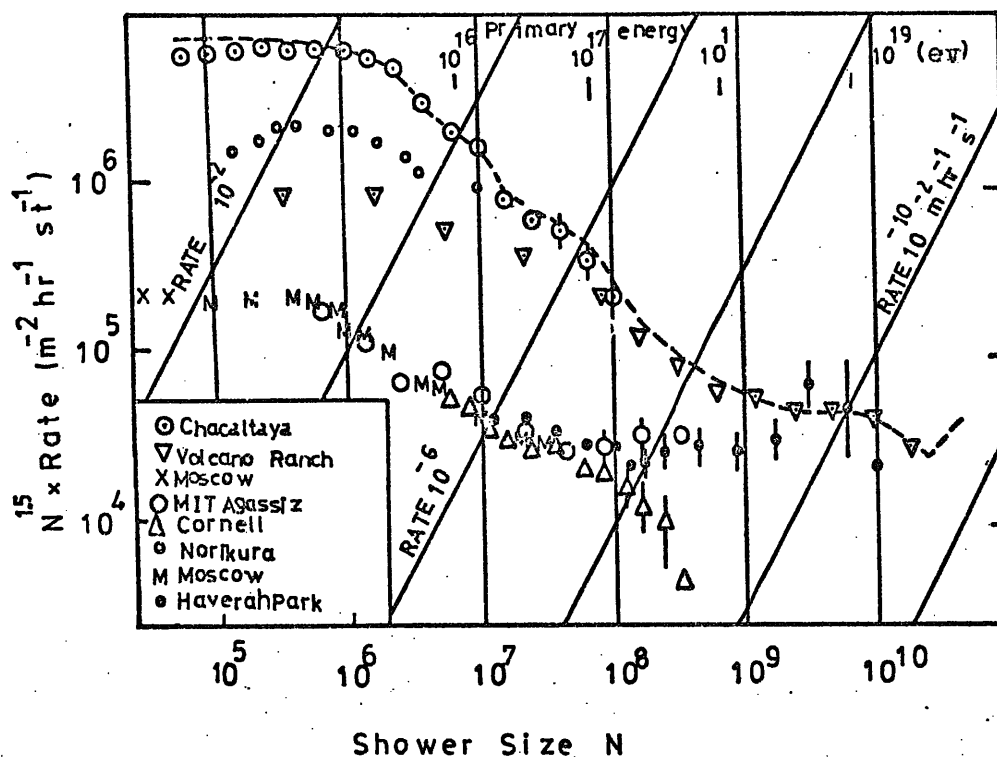
Figure 2.5   The rate of showers of more than
             N particles (plotted as R X $N^{1.5}$)
             observed at various altitudes and
             the derived energy spectrum.
             Data: Haverah Park: Hollows et al.
             (1968) and Andrew et al. (1970);
             Volcano Ranch: Linsley (1964);
             Moscow: Vernov and Khristiansen
             (1968), Mishnev and Nikolskii
             (1960); Chacaltaya: Bradt et al.
             (1965); Cornell: Delvaille et al.
             (1960); MIT: Clark et al. (1960);
             Norikura: Katsumata (1964).
             (After Hillas 1970b).
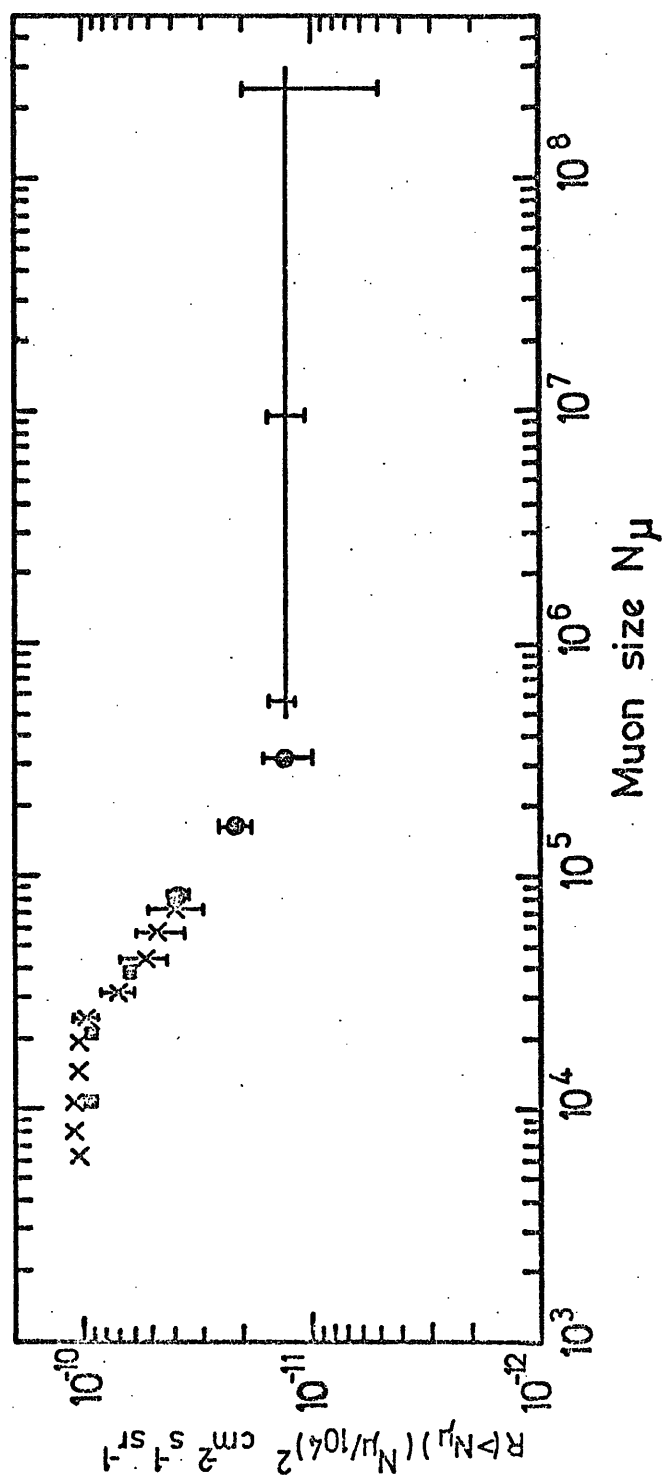
Figure 2.6   The rate $R(> N_\mu)$ of muons associated with showers (plotted as $R(N_\mu/10^4)^2$) with energy exceeding 5 GeV.

(After Khristiansen et al.,1974).

muon number spectrum at sea level (E $\geq$ 5 GeV) is represented by

$$R(\geq N_\mu , \geq 5 \text{ GeV}) = 1.05 \cdot 10^{-2} \quad N^{-2.0} \text{ for } 7.10^3 \lesssim N_\mu \lesssim 2.5.10^4$$

$$R(\geq N_\mu , \geq 5 \text{ GeV}) = 31.5 \quad N^{-2.8} \text{ for } 2.5.10^4 \lesssim N_\mu \lesssim 4.10^5$$

$$R(\geq N_\mu , \geq 5 \text{ GeV}) = 1.3 \cdot 10^{-3} \quad N^{-2.0} \text{ for } 4.10^5 \lesssim N_\mu \lesssim 3.10^8$$

where $R(\geq N_\mu , \geq 5 \text{ GeV})$ is the integral muon number spectrum of energy ≥ 5 GeV in units of $cm^{-2}s^{-1}st^{-1}$.

Converting muon number $,N_\mu,$ to electron number, N_e, using the relation between them as given by Greisen (1960) indicates that there is a tendency in the flattening of the slope of the number spectrum for $N_e \gtrsim 10^7$ to about - 1.5. However the data of Cornell group, as indicated in figure 2.5, shows that the slope of integral number spectrum at sea level for $N_e \gtrsim 10^7$ remains constant at about - 2.

The experimental data on the number spectrum, however, suggests a change in the slope around 5.10^5 at sea level and 2.10^6 at mountain altitudes which could be attributed to a change in the primary energy spectrum around $10^{15} - 10^{16}$ eV.

2.6   Relation between the electron number spectrum and electron density spectrum.

The integral density spectrum $H(>\Delta)$ is defined as the frequency with which the charged particle density at a fixed point in space exceeds the value Δ .   As mentioned earlier

one can derive the number spectrum, indirectly by measuring density spectrum.

The density spectrum has been measured quite often and is found that it follows a power law in the form of $H(>\Delta) = K\Delta^{-\beta}$

Let us assume that all showers have the same lateral distribution function, thus

$$\Delta(r) = \frac{N}{r_1^2} f\left(\frac{r}{r_1}\right)$$ where $\Delta(r)$ is the density of particles

in a shower of size N at core distance r, r_1 is the Moliere unit and $f\left(\frac{r}{r_1}\right)$ is the lateral distribution function of electrons.

Now assuming the integral number spectrum is expressed by $R(>N) = C N^{-\gamma}$ one may calculate the density spectrum by

$$H(>\Delta) = \int_0^\infty 2\pi r \, dr \, R(>N)$$

$$= 2\pi C \, r_1^{-2\gamma} \Delta^{-\gamma} \int_0^\infty \left[f\left(\frac{r}{r_1}\right)\right]^\gamma dr$$

Thus the exponents of the number spectrum and density spectrum are exactly the same assuming the following conditions:

(i)   The slope of the number spectrum is independent of shower size.

(ii) The lateral distribution of electrons is independent of shower size.

Therefore a measurement of the density spectrum gives indirectly the number spectrum and consequently the primary energy spectrum assuming the relation between the lateral structure function of electrons and shower size is known.

2.7 Primary energy spectrum

The primary energy spectrum has been obtained by two distinct procedures, (a) the direct method and (b) the indirect method.

2.7.1 Direct method

The direct measurements have been carried out using ionization calorimeters in satellites (Grigorov et al., 1971) and also using an ionization spectrometer flown at balloon altitudes (Ryan et al., 1972). The measurements have been extended to about 10^{12} eV per nucleus. One of the advantages in measuring the primary spectrum by the direct method is that it is possible to obtain the primary energy spectrum per nucleon, i.e., to distinguish between different elements and thus to obtain the primary mass composition.

The results of Ryan et al. indicate that the slope of differential energy spectrum of protons in the range of 50 to $\geq$1,000 GeV is - 2.75 $\pm$ 0.03 and for helium nuclei is - 2.77 $\pm$ 0.05. They find that the ratio of proton to helium primaries is 26 $\pm$ 3 at 40 GeV/nucleon and is constant within errors up to 400 GeV/nucleon.

Grigorov et al. found that the slope of proton spectrum steepens at 10^{12} eV and suggest heavy primaries predominate for $E_p > 10^{12}$ eV.

Webber (1973) has summarised the measured differential primary spectra in the range of $\simeq 10^9 - 10^{12}$ eV obtained by The Max Plank Institute group and The Goddard group (both of these experiments use the total energy Calorimeters). The result is shown in figure 2.7.
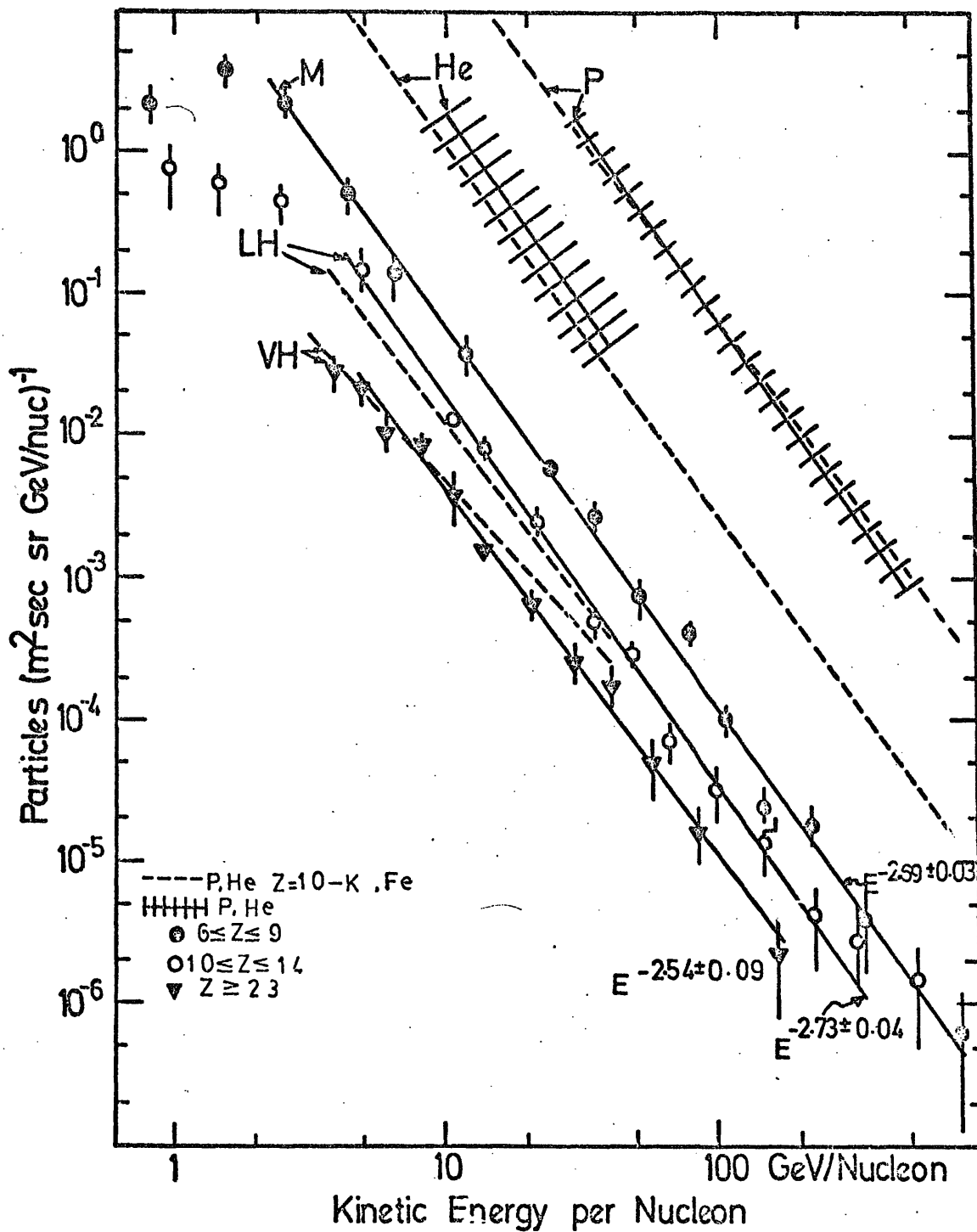
Figure 2.7   Differential energy spectra of various groups of
nuclei obtained by The Max Plank Institute group
and The Goddard group.   Both of these experiments
use total energy calorimeters. (After Webber, 1973).

The different Z ranges in the primary spectra given by Webber are VH, M, LH corresponding to $Z \geq 23$, $6 \leq Z \leq 9$ and $10 \leq Z \leq 14$ respectively. Using the primary composition (Wolfendale, 1973) the primary energy spectrum per nucleon of each group has been converted to the energy spectrum per nucleus and the results are shown in figure 2.8 (the proton and helium spectrum have also converted to integral spectra per nucleus). The broken spectra for proton and helium and the solid spectra for M, LH and VH group were taken from figure 2.7 to derive the integral energy spectra per nucleus shown in figure 2.8 and is plotted as $R(>E_p) E_p$ as a function of energy (E_p) per nucleus. The spectrum called A in figure 2.8 is the addition of all primaries.

2.7.2 Indirect method

Since the primary spectrum falls off very rapidly, indirect measurements above about $3 \cdot 10^{12}$ eV take over.

The procedure up to about 10^{14} eV is to measure the energy spectrum of muons and hadrons at different levels of observation in the atmosphere and assume a model for nucleonic development of primaries to derive the primary spectrum. Brooke et al. (1964) have derived the primary spectrum over the range of $10^{10} - 3 \cdot 10^{13}$ eV /nucleon from the measured sea level spectrum of protons and muons. Together with geomagnetic data on the primary spectrum they have expressed their results by

$R(>E) = 0.87 \begin{smallmatrix} +0.5 \\ -0.3 \end{smallmatrix} E^{-1.58}$ cm^{-2}s^{-1}st^{-1} where $R(>E)$ is the integral energy spectrum with $E \geq E$ GeV.

The derivation of the primary spectrum beyond $E_p \gtrsim 10^{14}$ eV has been carried out by measuring different components of EAS

Figure 2.8   Integral energy spectrum of primary cosmic rays in the range 10^{10}-10^{20} eV. LH, M, VH, He and P are calculated integrating the differential spectra of various components given by Webber (1973), as mentioned in the text, and A is obtained summing the spectra of these components. The experimental data are from Kempa et al. (1974). G is from Greisen (1965). S is the Sydney experiment (Bell et al., 1974), H is the Haverah Park experiment (Edge et al.,1973) and Y is the Yakutsk experiment (Krasilnikov, 1973).
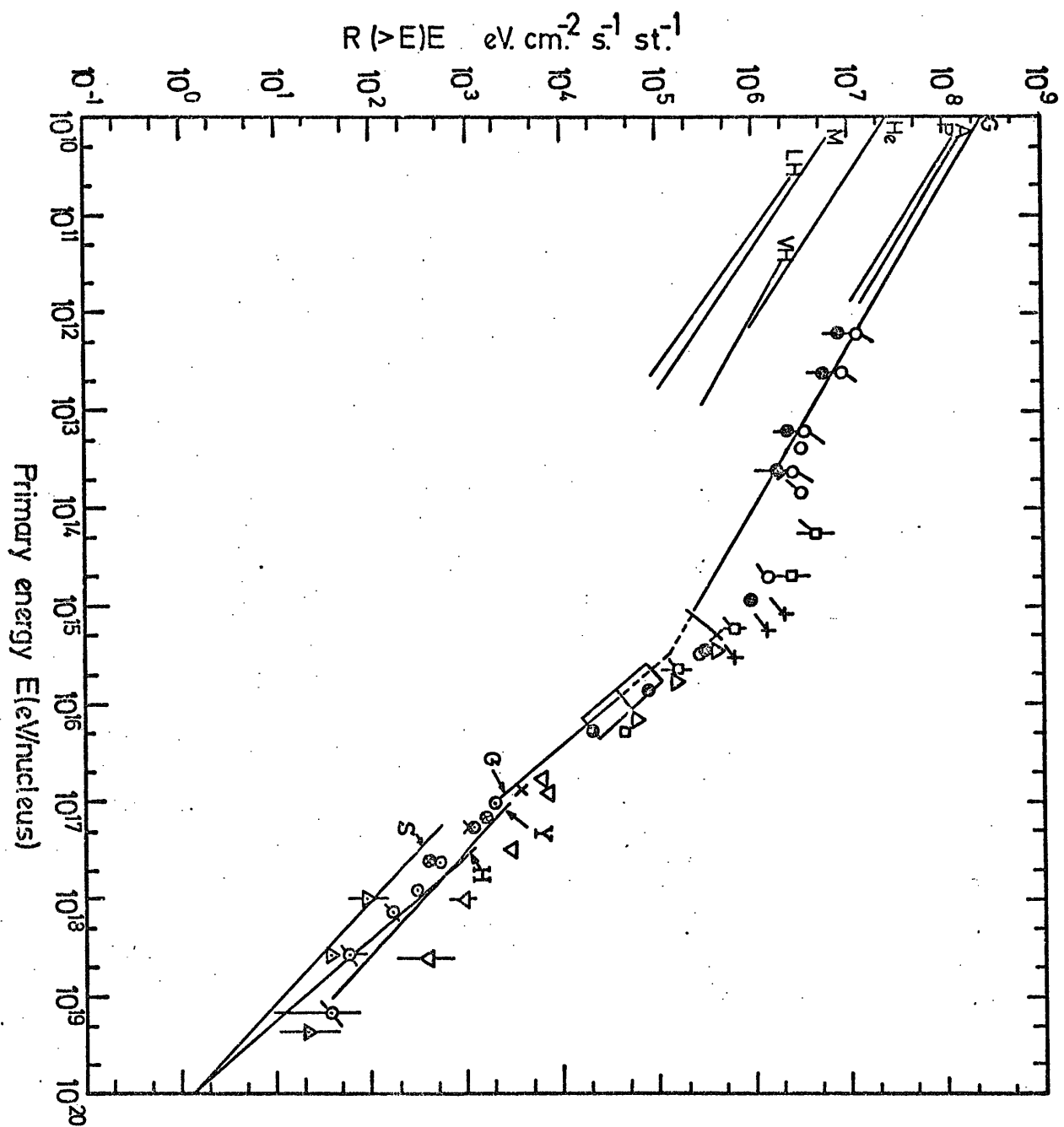
particles as follows.

Measurements of EAS are made largely on the electron component at sea level and mountain altitudes to derive the primary spectrum. Although there are some indications that the maximum accuracy occurs when the experimental location is near the level of maximum development (Bradt and Rappaport, 1967) the primary spectrum derived from the measured sea level spectrum gives close agreement with measurements carried out at mountain altitudes, where showers initiated by primaries in the range of $E = 10^{14} - 10^{17}$ eV are at their maximum development. For example, the primary spectrum obtained by Saxena (1973), measuring the size spectrum at 920 g cm^{-2}, expressed by

$$R(\geq E) = (3.74 \pm 0.20)\, 10^{-10} \left(\frac{E}{10^{15}}\right)^{-2.16 \pm 0.10} \text{cm}^{-2}\, \text{s}^{-1}\, \text{st}^{-1} \quad \text{for} \quad 5.10^{14} \leq E \leq 2.10^{16} \text{ eV}$$

is in reasonable agreement with the results of Clark et al. (1963) measuring the size spectrum at 530 g cm^{-2} and 630 g cm^{-2}. Clark et al. express their results for the integral primary spectrum as

$$R(\geq E) = (2.0 \pm 0.4)\, 10^{-14} \left(\frac{E}{10^{17}}\right)^{-2.2 \pm 0.15} \text{cm}^{-2}\, \text{s}^{-1}\, \text{st}^{-1} \quad \text{for} \quad 6.10^{14} < E < 4.10^{17} \text{ eV}$$

Studies of the muon component at sea level, in general give rather more accurate primary spectrum measurements due to the long shower attenuation of the muons in the atmosphere and consequently smaller sensitivity to zenith angle (and other factors). The energy spectrum of primary cosmic rays has been derived measuring the muon number spectrum by the Sydney group for energies of $\gtrsim 10^{17}$ eV (Bell et al., 1974).

Another method has been used by the Haverah Park group to derive the primary spectrum. This group have related the measured response of EAS particles at about 600 m distance from the core in deep water Cerenkov detectors (mixture of

electrons and muons) at sea level to the primary energy.
This quantity has been shown by Hillas (1970b) to be a useful
parameter to relate to primary energy and has less sensitivity
to primary mass composition and the assumed model for high
energy interactions.

Although there is close agreement between different
experiments up to about 10^{17} eV in deriving the primary spectrum
the situation is not very clear beyond 10^{17} eV.

. Greisen (1965) has summarised the available data on the
primary spectrum and given the following expression for the
integral energy spectrum of primary cosmic rays.

$$R(>E) = 10^{-4} \left(\frac{10^{14}}{E}\right)^{1.6} m^{-2}s^{-1}st^{-1} \quad \text{for} \quad 10^{10} < E < 10^{15} eV$$

$$R(>E) = 210^{-10} \left(\frac{10^{17}}{E}\right)^{2.2} m^{-2}s^{-1}st^{-1} \quad \text{for} \quad 10^{16} < E < 10^{18.5} eV$$

$$R(>E) = 41C^{-16} \left(\frac{10^{20}}{E}\right)^{1.6} m^{-2}s^{-1}st^{-1} \quad \text{for} \quad E > 10^{18.5} eV.$$

Subsequent derivations on the primary energy spectrum
for $E \geq 10^{17}$ eV by means of more reliable models for high
energy interactions and other parameters, indicate that the
slope of integral spectrum beyond 10^{17} eV continues to be
around -2. Different groups dealing with the primary spectrum,
for $E \gtrsim 10^{17}$ eV, give the following expressions:

$$R(>E) = (4.5 \pm 0.5)10^{-10} \left(\frac{E}{10^{17}}\right)^{-2.17 \pm 0.03} m^{-2} s^{-1} st^{-1} \quad \text{for} \quad 310 < E < 10^{19} eV,$$

due to Edge et al. (1973), measuring the response of deep
water Cerenkov detectors at 600 m from the core at sea level;

$$R(>E) = (3.5 \pm 0.5)10^{-12} \left(\frac{E}{10^{16}}\right)^{-1.93 \pm 0.07} m^{-2} s^{-1} st^{-1} \quad \text{for} \quad 10^{17} < E < 10^{19} eV,$$

obtained by Krasilnikov (1973) from measurements of the

Cerenkov light flux density at the core distance 400 m and measuring the number spectrum of electrons in the range of $10^{17} - 10^{18}$ eV and $10^{18} - 10^{19}$ eV respectively; and finally,

$$R(>E) = 10^{-12.03 \pm 0.01} \left(\frac{E}{10^{18}}\right)^{-1.96 \pm 0.02} m^{-2} s^{-1} st^{-1} \text{ for } 10^{17.5} < E < 10^{20.25} \text{ eV}$$

representing the primary spectrum of Bell et al. (1974) obtained from measuring the muon number spectrum at sea level. In all the above expressions $R(>E)$ is the measured integral primary spectrum and E is expressed in eV.

The integral spectrum given by Greisen for $E < 10^{17}$ eV and the measured spectra obtained by the Sydney group, Haverah Park group and Yakutsk group for $E > 10^{17}$ are shown in figure 2.8 in the form of integral rate x E in units of (eV $cm^{-2}s^{-1}st^{-1}$) and are specified by letters G, S, H and Y respectively.

The data from a variety of experiments have been re-examined by Kempa et al. (1974) for $E > 10^{12}$ eV. The experimental points shown in figure 2.8 are from Kempa et al.

2.8 Conclusion

Some of the experimental results on EAS reviewed in this chapter suggest that on average showers develop faster than expected, a fact that appears to indicate that the multiplicity in extremely high energy interactions increases even faster than given by an $E^{1/4}$ law (Kane ko et al.,1971). This is very important since various theoretical models require a logarithmic increase (Feynman, 1969). According to the scaling model (the logarithmic increase in multiplicity against primary energy is called the scaling model) the mean transverse momentum of secondary produced particles is almost independent of primary energy while EAS data shows a slow increase in the mean transverse momentum as the primary energy increases.

CHAPTER 3

MEASUREMENTS OF THE DENSITY SPECTRUM

OF EAS AT SEA LEVEL

3.1   Introduction

Measurements of the sea level density spectrum gives
information about the sea level size spectrum assuming the
lateral distribution of particles about the shower axis and
its size dependence are known.   Using available knowledge
about the physics of high energy particle interactions and
available experimental data on shower development the relation-
ship between sea level size and primary energy can be estab-
lished.   In this way the measured sea level density spectrum
can be used to make an accurate estimate of the primary cosmic
ray spectrum for energies $> 10^{13}$ eV where direct measurements
using balloons and satellites have not yet been carried out.
The spectrum has been measured quite often with a variety of
detectors and although all measurements are consistent with
each other up to densities of about $\Delta = 1,000$ m^{-2}, there are
some discrepancies for higher density regions.

These were the main motivations to measure the density
spectrum.   The experiment was performed using a proportional
counter.   Before describing the present experiment a number
of previous works of density spectrum of EAS, carried out at
sea level and mountain altitudes, using different types of
detectors will be explained in the next section.

3.2 Previous measurements of the electron density spectrum

3.2.1 R.J. Norman (1956)

The integral density spectrum of EAS in the range of $\Delta = 20 - 1,000 \text{ m}^{-2}$ has been measured by Norman with a proportional counter. The experimental arrangement comprised three proportional counters of the control grid type (Norman, 1955) each 0.05 m^2 in area, arranged in a horizontal plane at the three corners of a 5 metre equilateral triangle at 60 m elevation above sea level. A three fold coincidence was used as a method of EAS selection. The pulse height distribution of observed densities recorded by a single counter were photographed on an oscilloscope and converted to a density spectrum, assuming the most probable pulse height of single muons observed in a calibration run is equivalent to one particle. Norman expressed his results by

$$R(>\Delta) = 540 \quad \Delta^{-1.39 \pm 0.04} \text{ hr}^{-1} \text{ for } 20 < \Delta < 500 \text{ m}^{-2}$$

with evidence of an increase of the slope to -2.2 at $\Delta = 1,000 \text{ m}^2$.

Consequently he predicted a number spectrum in the form of

$$R(>N) = 2.3.10^{-4} \left(\frac{N}{10^6}\right)^{-1.4 \pm 0.1} \text{ hr}^{-1} \text{ m}^{-2} \quad N < 10^6$$

with evidence of a rapid increase in the exponent above $N = 10^6$.

To derive a number spectrum mentioned above, Norman assumed an age dependence on shower size given by

$S = 1.4 - 0.1 \log \frac{N}{200}$ where S is the age parameter and

N is the shower size.

However the integral primary energy spectrum derived by Norman, from the measured integral density spectrum at sea level, follows as

$$R(> E) = 0.32 \left(\frac{E}{10^{14}} \right)^{-1.5} m^{-2} \, hr^{-1} \, st^{1}$$ where E is in eV,

for $10^{13} < E < 10^{15}$ eV, above which the exponent increases rapidly reaching about -3 at E = 10^{17} eV.

3.2.2   J.R. Prescott (1956)

Cylindrical ionisation chambers 57.6 cm long and 8.8 cm in diameter filled to 39 atmosphere with nitrogen were employed by Prescott to measure the density spectrum of EAS.   The apparatus was made up of two ionization chambers at 3m and 5m from the master group.   The master group consisted of three G - M tubes in coincidences located immediately above one of the chambers to identify EAS.

The experimental data for coincidence bursts greater than a given size in both chambers at a separation of 5m obtained in 725.8 hr running time indicated that there is 7% probability that a single line of slope -1.45 fits all the observed data in the range of Δ = 400 - 4,500 m^{-2}.   Prescott, however, measured the distribution of burst sizes in a single ionisation chamber 5m apart from the master group.   In 627.9 hr running time 115 bursts were observed.   At density of $\Delta \lesssim$ 1,000 m^{-2} the slope of spectrum was found to be the same as it was obtained previously, though its absolute rate was greater by a factor of two compared to the former one.   The probability that the experimental results obtained, analysing the results of a single ionisation chamber, fit a single line in the whole range of measured densities with slope of - 1.45 was found to be 4%.   The observation based on the second method showed that the slope of integral density spectrum is - 1.54 $\pm$ 0.14 in region of Δ = 500 - 1,000 m^{-2} for integral density spectrum

at sea level.

3.2.3   R.J. Reid et al.(1961, 1962)

The differential density spectrum of EAS was measured
by Reid et al.using a counter controlled cloud chamber.   The
experiment was carried out at three different stations, Jamaica,
Ireland and Sydney.   At each station two cloud chambers were
employed with their axes at right angles to each other, but
only the number of tracks through one of the chambers counted
and related to the density spectrum.   The illuminated areas
of the chambers at Jamaica, Dublin and Sydney were 540 cm^2,
360 cm^2 amd 0.11 m^2 respectively.   A considerable number of
triggering criteria were used to trigger the cloud chambers.

Though they found some discrepancy in the observed slope
of the density spectrum due to the difference in triggering
criteria, the overall results corrected for Poissonian fluct-
uations of the number of particles crossing the chambers, and
also corrected for the triggering probability of the chamber
system showed that the slope of differential density spectrum
is -2.5 in the region of Δ = 50 - 500 m^{-2} and - 3.9 $\pm$ 0.5 for
$\Delta \gtrsim$ 1,100 m^{-2}.

Further observations were made at the Jamaica station
(Reid et al.,1962) and it was concluded that the slope of
density spectrum in differential form is - 2.6 $\pm$ 0.3 for
densities in the range of Δ = 200 - 1,000 m^{-2} and - 4.0 $\pm$ 0.5
for Δ = 1,000 -5,000 m^{-2} with a chi - square probability,
P = 0.72.

3.2.4   J. Gemesy et al.(1964)

Gemesy et al. employed a cloud chamber to investigate the density spectrum of EAS. A coincidence pulse of four G - M counters (of an area of 320 cm^2 each) placed at the corners of a (10 x 9) m^2 rectangle enclosing the chamber. The chamber was a multiplate one, where only the volume above the upper plate in the chamber was scanned when counting the number of tracks shown on the photographs. The illuminated area of the uppermost plate of the chamber was 150 cm^2. The observation was carried out at 410 m elevation.

A total of 3,274 coincidences were recorded in the region of Δ = 70 - 13,000 m^{-2}. They found that there is no significant change in the slope of density spectrum and their results are summarised in table 3.1.

Table 3.1   The exponents of integral density spectrum obtained by Gemesy et al.

Range of density (m^{-2})	70 - 200	300 - 700	800 - 13000	70 - 13000
Exponent of integral density spectrum	-1.49 ± 0.08	-1.83 ± 0.12	-1.63 ± 0.13	-1.57 ± 0.03

3.2.5   J.B.T. McCaughan et al.(1965a)

The differential density spectrum was measured at sea level by means of a controlled cloud chamber. The chamber was 30 cm in diameter and illuminated to a depth of 17 cm. EAS were selected by the coincidence of three G - M trays

(each of area 64.4 cm^2) located at the apices of a triangle (2.4 x 2.4 x 1.2 metre) just above the chamber.

The experimental results showed that the differential density spectrum could be represented by two power laws of exponents - 2.491 ± 0.036 and - 3.42 ± 0.32 respectively, joining at Δ = 560 ± 180 m^{-2} (McCaughan et al., 1965b).

3.2.6   Measured density spectrum at mountain altitudes

The density spectrum of EAS has been measured using proportional counters and cloud chambers at mountain elevations.

The experimental results of the measured integral density spectrum obtained by McCaughan et al.(1965b), Swinson and Prescott (1965 - 1968) showed that the slope of spectrum is about - 1.4 for lower densities and increases continuously.

The transition region, i.e. the region where before it the slope of spectrum is fairly constant (about - 1.4) depends on the altitude of observation.

Swinson and Prescott (1965) have shown that at all altitudes the spectra are essentially the same shape and that, apart from absolute rates, the spectra can be superimposed by a density scale - change in the approximate proportions, 1 : 7.5 : 22 for sea level, 2,285 m and 3,260 m respectively (densities are expressed in units of particles m^{-2}). This was done in the first instance by a trial and error fit of the sea level spectrum to those at the higher altitudes, in which the density spectrum was displaced in steps until the ordinates of the two curves bore the same ratio to each other at six points. They applied a similar technique to the cloud chamber data of McCaughan et al.(1965b) and found a ratio of about seven between sea level and 2,285 m, in good agreement with the proportional

counter data. Swinson and Prescott (1968) also investigated
the density spectrum at 1,575 m elevation using proportional
counters. They however showed that the transition region
increases as altitude of observation increases and found a
ratio of 1 : 5 : 7.5 : 22 for sea level, 1,575 m, 2,285m and
3,260 m elevation respectively. These values were obtained
using proportional counters for the density spectrum measure-
ments. If densities are expressed per square lateral scatter-
ing unit, the above proportions become 1 : 7 : 13.5 : 47 for
sea level, 1,575 m, 2,285 m and 3,260 m respectively as shown in
figure 3.1.

3.2.7 <u>Discussion of the previous measured density spectrum</u>

The integral density spectra (explained in this section)
measured at sea level and mountain altitudes are shown in
figures 3.2 and 3.3 respectively.

Greisen (1960) gives the following expression for the
integral density spectrum based on summarised experimental
results.

$$R(>\Delta) = R_o \Delta^{-(a + 0.5b \log \Delta)} \quad \text{for} \quad 1 < \Delta < 10^4 \ m^{-2}$$

where $R_O = 0.15 \ s^{-1}$, $a = 1.3$ and $b \simeq 0.11$ at sea level and

$R_O = 1.6 \ s^{-1}$, $a = 1.25$ and $b \simeq 0.13$ at 3,260 m (705 g cm^{-2}).

The absolute intensities of the measured integral density
spectra have not been reported in all experiments, thus for
ease of comparison each measured density spectrum, shown in
figure 3.2, has been normalised so that the rate at $\Delta = \Delta_o$
be identical to the rate given by Greisen at sea level (Δ_o is
the minimum density measured in each experiment). Gemesy et
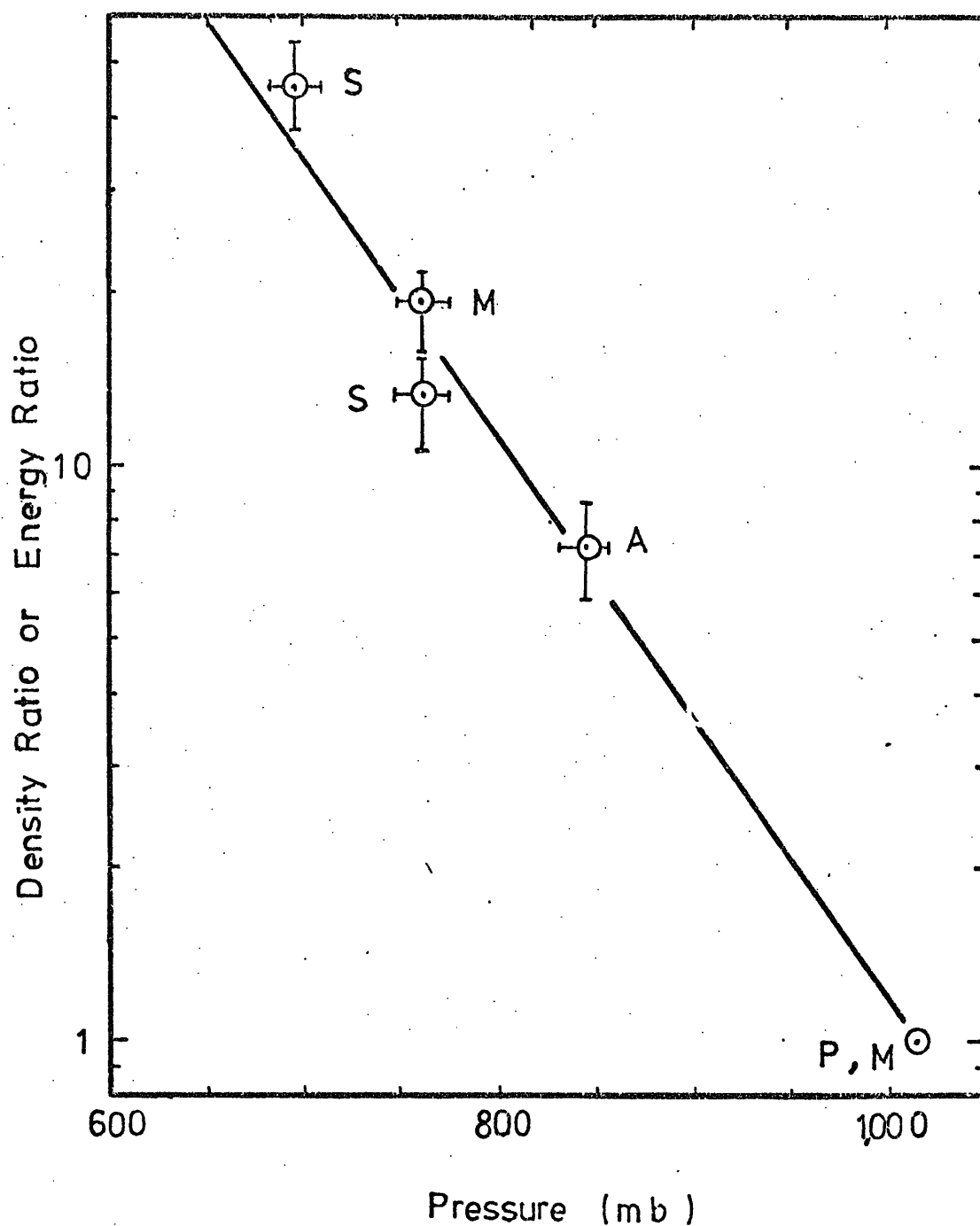
Figure 3.1 Relative values of density observed at
different altitudes. P is from Prescott
(1956), S is from Swinson and Prescott
(1965), M is from McCaughan et al. (1965b)
and A is from Swinson and Prescott (1968).
The straight line shows the relative energy
retained by a Proton as a function of alti-
tude.

The plot contains the following axes and legend:

Y-axis: $R(>\triangle)$ hr^{-1} with values 10^1, 10^0, 10^{-1}, 10^{-2}, 10^{-3}, 10^{-4}

X-axis: Density $\triangle(m^{-2})$ with values 10^1, 10^2, 10^3, 10^4

Legend:
- NORMAN (1956)
- PRESCOTT (1956)
- ▽ MCCAUGHAN et al (1965 b)
- ▲ GEMESY et al (1964)
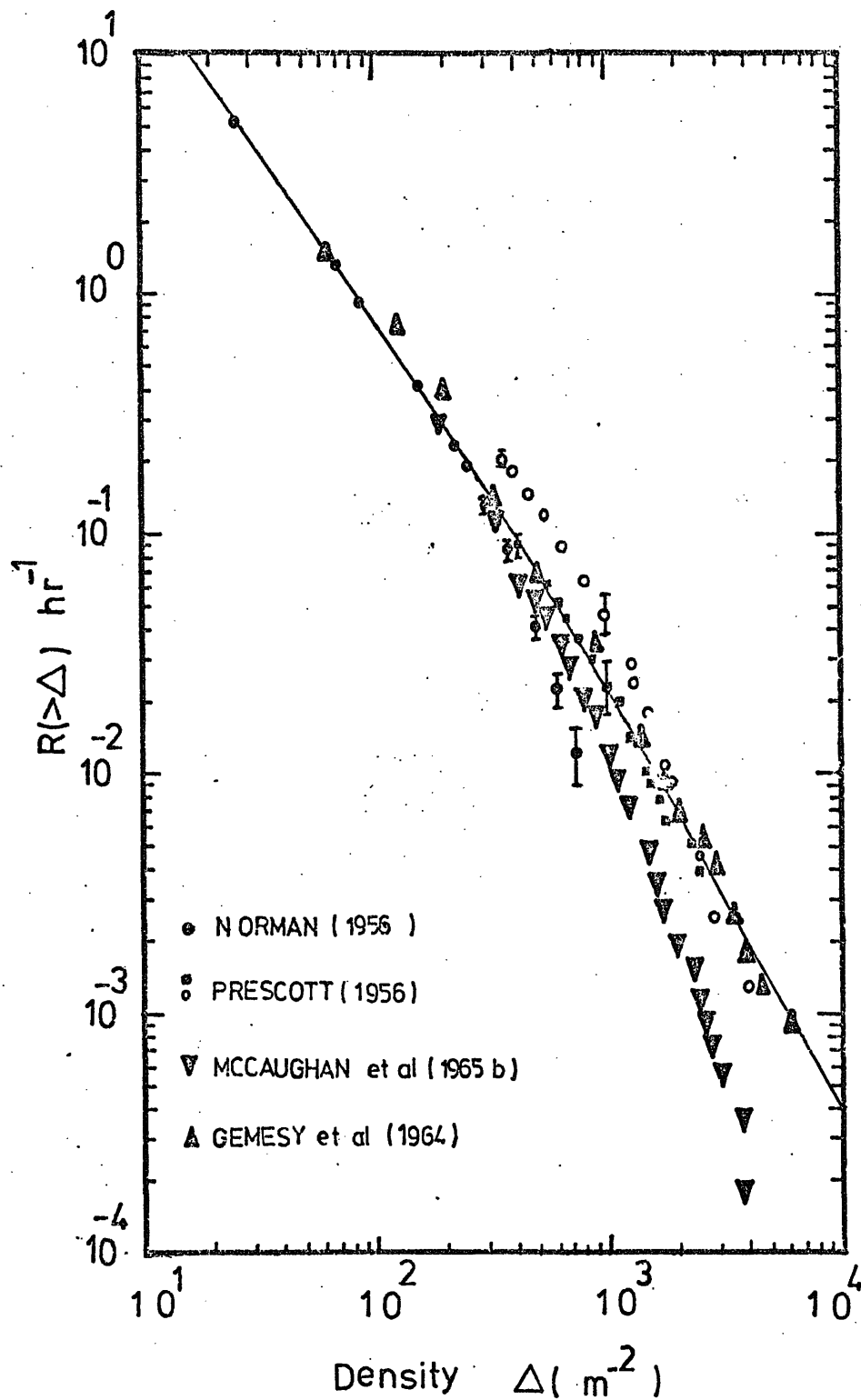
Figure 3.2   Integral density spectra of EAS measured
at sea level.   The solid curve is due to
Greisen (1960).   The experimental observ-
ations are normalised to the solid line
such that all spectra give the same rate
as obtained by Greisen at their minimum
observed densities.

Elevation
(m.)

⊙ 3,260

× 2,285   Swinson and Prescott (1965)

⊕ 1,575   Swinson and Prescott (1968)

○ 2,285   Mccaughan et al (1965b)

Density Δ (m^{-2})

R $(>\Delta)$ (hr^{-1})
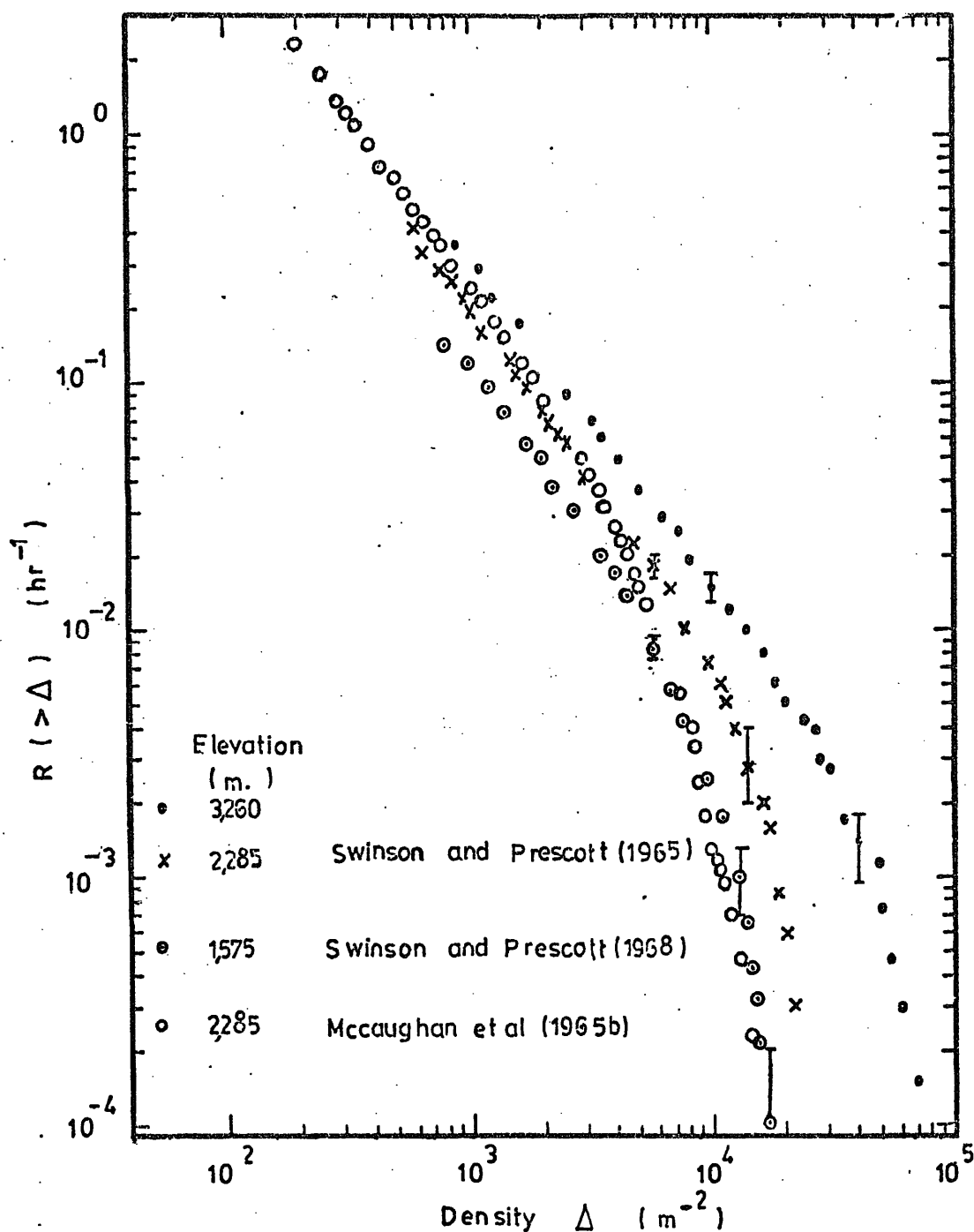
Figure 3.3   Integral density spectra observed at
Mountain altitudes, with proportional
Gunter (Swinson and Prescott) and
Cloud Chamber (McCaughan et al.).
All data are normalised to the rate
given by Greisen (1960) at 705 g cm^2,
assuming a 140 g cm^{-2} absorption length
at their minimum observed densities.

al.(1964) have reported their measured spectrum in the form
of $R(>N)$ as a function of N where N is the number of tracks
observed in their cloud chamber. To convert the number of
tracks, N, to densities in units of m^{-2}, it is assumed that
$\Delta = \frac{N}{S} \, m^{-2}$ where S is the area of their chamber, i.e.
$S = 0.015 \, m^2$. It is obvious that the absolute rate of the
density spectrum is a function of the level of observation.
Absolute rates are assumed to be correct at 705 g cm^{-2}
atmospheric depth as given by Greisen; for the other altitudes
they were derived from the normalised data assuming a 140 g cm^{-2}
absorption length for the rate at lower densities, as found in
earlier experiments. The available information about the
running time or the total number of observed events greater
than the minimum measured electron density are summarised in
table 3.2.

Inspection of figures 3.2 and 3.3 indicate the following
features (i) On average it is likely that the slope of density
spectrum does not remain constant throughout the measured density
ranges (1 - 6,000 m^{-2}).

(ii) The transition region of the spectrum is rather short
at sea level but the change in the slope occurs gradually at
mountain altitudes.

(iii) The transition region occurs at lower densities using
cloud chambers than proportional counters or ionisation
chambers.

(iv) The transition region has a strong dependence to the
level of observation as it is shown in figure 3.1.

Reference	Running time (hr)	Total number of observed events		Altitude of observation.
		Frequency	Minimum density (m^{-2})	
Prescott (1956)	627.9 (Curve B in fig.2)	115	400	Sea level
	725.8 (Curve A in fig.2)	70	500	
Gemesy et al. (1964)	-	3,300	70	410 m
McCaughan et al. (1965b)(at Sydney station)	-	2,087	200	Sea level
McCaughan et al. (1965b)	6,979	20,000	200	2,285 m
Swinson & Prescott (1965)	3,150	-	-	2,285 m
	7,000	-	-	3,260 m
Swinson & Prescott (1968)	3,012	1,500	800	1,575 m

Table 3.2   Available information about running time and the total number of observed events obtained by various experimenters (mentioned in section 2) and the altitude of observation.

The importance of the measured density spectrum is
clear considering the features mentioned above.   In general
the change in the slope of spectrum has been interpreted due
to (a) a change in the characteristic of nuclear interaction
or (b) as a result of a cut-off in the primary energy per nucleon
spectrum.

As mentioned earlier Swinson and Prescott found that the
various spectra (measured at different altitudes) have the
same shape and could be superimposed, apart from observed rates,
by a change in the density - scale, for example by a factor
of 13.5 from 2285 m elevation to sea level, and that these
proportions, as shown in figure 3.1, matched the rate at which
a nucleon would on average lose energy, its energy E after
depth x m.f.p. being, for an elasticity β in collisions,

$$E = E_0 \, \beta^x$$

Swinson and Prescott calculated the fractional energy, f,
retained by primary, i.e. $f = \dfrac{E}{E_0}$, as a function of atmos-
pheric depth X g cm^{-2} assuming an elasticity 0.45 and an
interaction length of 75 g cm^{-2}.   The solid line in figure
3.1 shows their calculated ratio $f = \dfrac{E}{E_0}$.

Swinson and Prescott thus suggest that the density spectrum
reflects the energy per nucleon spectrum at some higher level
in the atmosphere and then the observed cut-off in the measured
density spectrum indicates a cut-off in the primary proton
spectrum, originally proposed by Peters (1952), Norman (1956)
and suggested by Bray et al.(1964) to interpret the observation
on the core structure of showers at sea level, made with the
Sydney air shower array.

3.3 Introduction to the present experiment

A proportional counter of rectangular cross section was employed in present experiment to measure the density spectrum of EAS. The counter is made up of aluminium walls with external dimensions of $(15 \times 15 \times 101)$ cm^3. The central wire of the counter is made of tungsten 7.610^{-3} cm in diameter stretched along the central axis of the counter. The wall is 6 mm thick. The counter is filled with 90% argon and 10% methane (to prevent photo production) to atmospheric pressure. The central wire (anode) of the counter is shorter than the length of the counter by 4.5 cm at each end. To minimise the irregularities of the electric field at its ends each end is enclosed by a glass cylinder. A scale diagram of the counter and the electronic circuit diagram used as a head unit are shown in figures 3.4b and 3.4a respectively.

To measure the density spectrum of EAS it is essential to calibrate the counter and to be sure that the counter works in the proportional region. What is measured in the proportional counter is ionisation loss and before describing the main experiment a knowledge of the properties of the counter are necessary. This is done by measuring the response and gas gain of the counter due to the passage of incoherent cosmic ray particles and the results are explained in the following section.

3.4 Calibration of the proportional counter

3.4.1 Most probable energy loss

The parameter which is measurable by the proportional
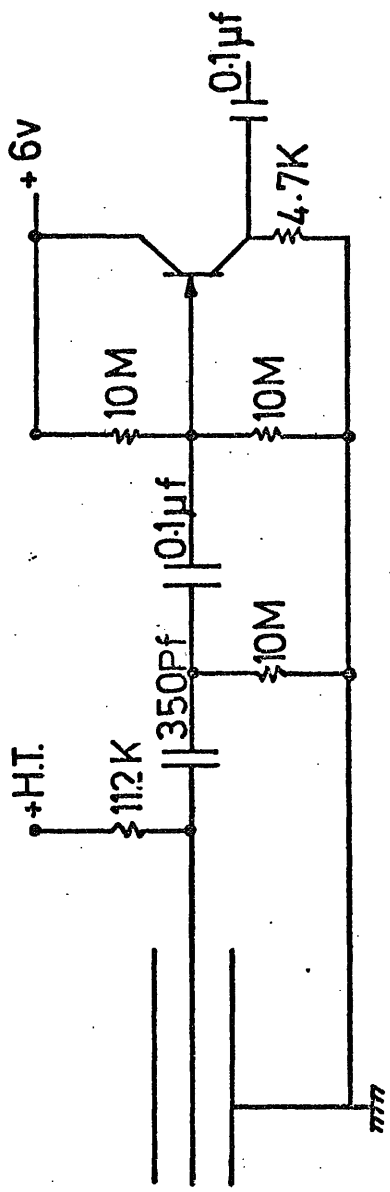
Figure 3.4a   The proportional counter head unit.
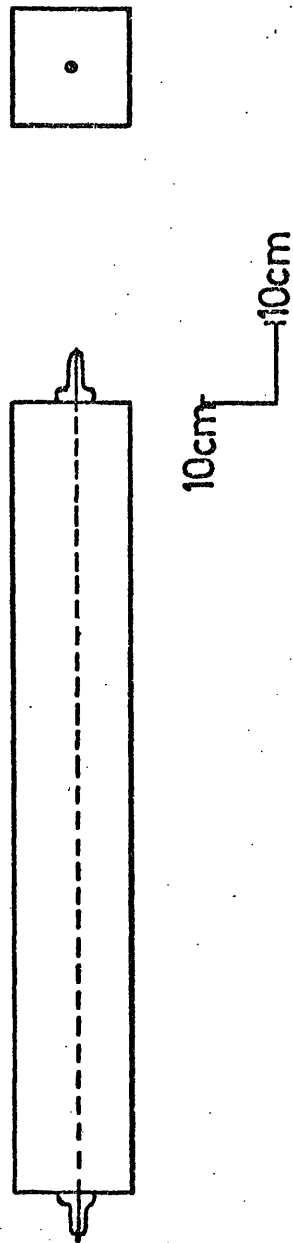
Figure 3.4b   Scale diagram of the proportional counter.

counter is the energy loss of ionising particles in traversing
the counter. In a thin absorber like the proportional counter,
employed in the present experiment, what is measured is the
most probable energy loss which is due to the more frequent
low energy transfer collisions of charged particles. The
most probable energy loss has been derived by Symon (1948) and
his results are summarised by Rossi (1952), namely,

$$E_p = \frac{2c\, m_e\, c^2\, x}{\beta^2} \left(Ln\, \frac{4c\, m_e^{\,2}\, c^4\, x}{(1-\beta^2)\, I^2(z)} - \beta^2 + J \right)$$

where $c = 0.15\, \dfrac{Z}{A}\, cm^2\, g^{-1}$, x is the thickness of matter

$(g\, cm^{-2})$, β is the velocity of particle relative to the velocity
of light, $I(z)$ is the ionisation potential of the medium and
J is given by Rossi in graphical form and takes its asymptotic
value of 0.37 for the present case.

The above formula is calculated for a track length of
13.8 cm (internal thickness of the counter) of the gas of the
counter as a function of Lorentz factor and the result is shown
in figure 3.5.

3.4.2   The density effect

This effect was pointed out by Swan (1938) and causes a
reduction in most probable energy loss and is more predominant
in dense materials. It has been investigated by Fermi (1940)
and Sternheimer (1952, 1956) theoretically. The analytic
expression for the density effect due to Fermi and Sternheimer
are given by Rossi (1952) and Hayakawa (1969) respectively by

$$\Delta(\beta) = \frac{2c\, m_e\, c^2}{\beta^2}\quad Ln\varepsilon \quad for \quad \beta < \varepsilon^{-1/2}$$
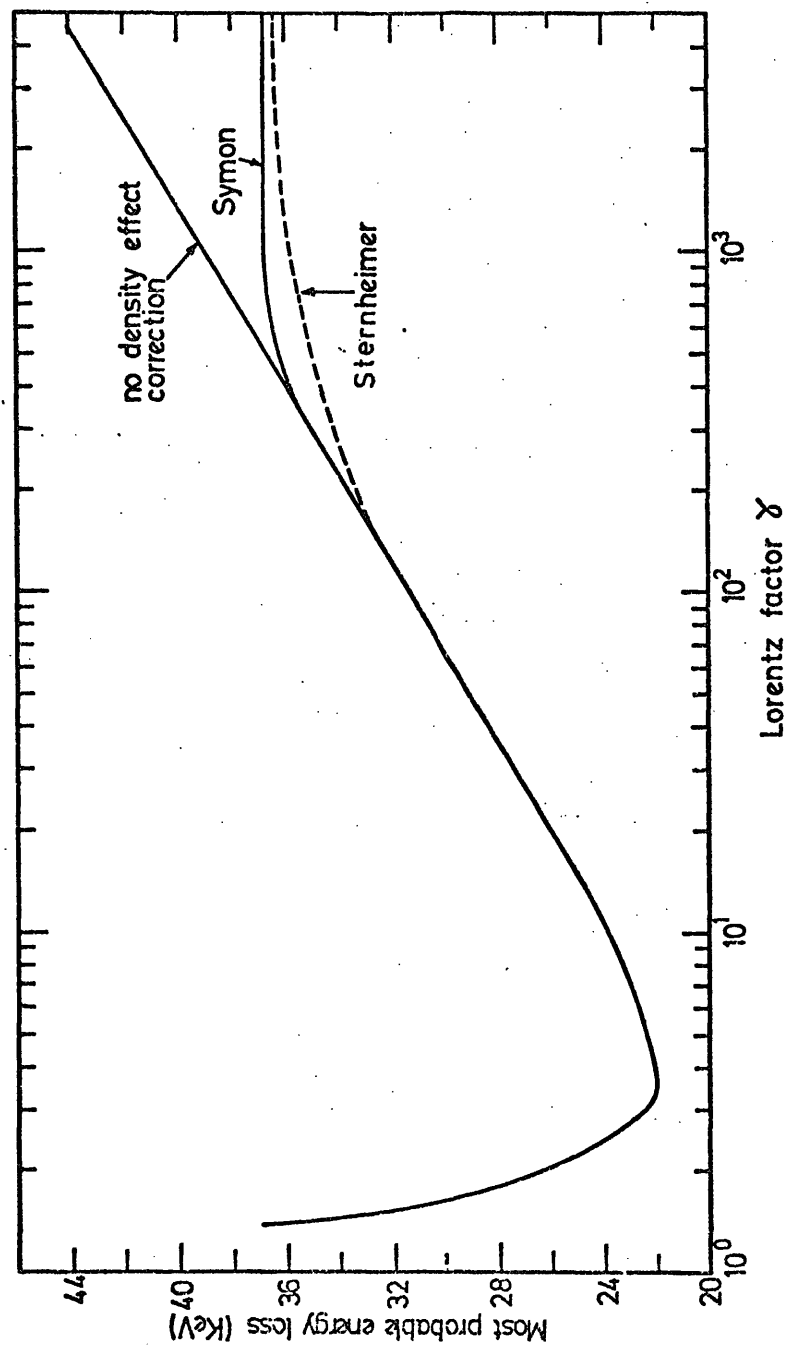
Figure 3.5   The most probable ionisation loss as a function of the lorentz
factor, γ, for 13.8 cm of proportional counter gas.   The Symon
and Sternheimer curves, take the density effect into account.

$$\Delta(\beta) = \frac{2C \, m_e C^2}{\beta^2} \left(\text{Ln} \frac{\varepsilon - 1}{1 - \beta^2} + \frac{1 - \varepsilon \beta^2}{\varepsilon - 1} \right) \quad \text{for} \quad \beta > \varepsilon^{-1/2}$$

where ε is the dielectric constant of the medium relative to vacuum and the other terms have their usual meanings. For the present case $\varepsilon - 1 = 1.2 \times 10^{-5}$.

The above expressions were due to Fermi. Sternheimer gives the following expressions

$$\Delta(\beta) = 4.606 \, y + c + a \, (y_1 - y)^b \quad \text{for} \quad y_o < y < y_1$$

$$\Delta(\beta) = 4.606 \, y + c \quad \text{for} \quad y > y_1$$

where $y = \log \frac{P}{mc}$, P being the momentum of the primary particle and m its mass. The values a, b, c, y_1 and y_o are tabulated by Hayakawa for argon and methane.

The corrected value of the most probable energy loss, after subtracting the density effect due to Fermi and Sternheimer, for the proportional counter as a function of the Lorentz factor of primary particle is shown in figure 3.5. According to figure 3.5 the ratio of minimum ionisation to plateau ionisation is $\simeq 60\%$. Ramana Murthy (1968) measured most probable energy loss in a proportional counter and found a ratio of $(45 \pm 5)\%$ at $\frac{P}{mc} = 2,000$ which is lower than the predicted ratio. This ratio has been investigated for neon flash tubes and will be described in Appendix A.

3.4.3 Statistical fluctuations in the energy loss by collision

Since the collisions which are responsible for energy loss are independent the amount of energy lost for particles of a given kind and incident energy are not the same. This will

cause a fluctuation in the most probable energy loss and has been investigated theoretically by Symon (1948). Rossi (1952) has plotted Symon's results for thin absorbers. The distribution obtained is shown in figure 3.6a.

Blunck and Leisegang (1950) and Blunck and Westfald (1951) have modified the Laundau theory, including the binding energy of electrons. Their results are shown in figure 3.6b for different values of b^2, where b^2 is defined by following expression

$$b^2 = \frac{20\,\bar{\Delta}\,z^{4/3}}{\left(0.3\,\frac{zx}{A}\,\left(\frac{me\,c^2}{\beta^2}\right)^2\right)^2}$$ where $\bar{\Delta}$ is the average

energy loss in traversing x g cm^{-2} of matter and the other terms have their usual meanings.

For $b^2 \ll 3$ the distribution is identical to the one predicted by Landau.

3.4.4   Pulse height distribution of single particle

To investigate the density spectrum of EAS one needs to measure the response of the detector when a single particle passes through it. Incoherent cosmic ray particles were selected by the coincidence between two trays of G.M. tubes, placed above and below the counter for this purpose. Each tray consits of three tubes placed beside each other in a horizontal plane. The proportional counter is positioned between two trays. The distance between the central wire of the counter and the anodes of the top tray is 25 cm and from the anodes of the bottom tray is 19 cm . The whole apparatus is mounted on an aluminium frame. The G.M. tubes are cylindrical (made of glass) with external and internal diameters of 3.6 cm and 3.26 cm respectively. The anode of each tube is
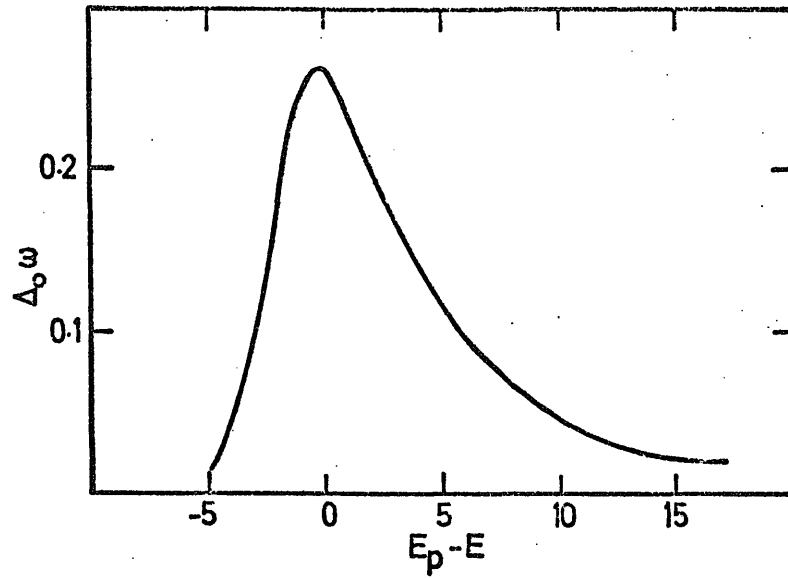
Figure 3.6a   The Landau distribution in energy loss calculated using the theory of Symon for the proportional counter used.
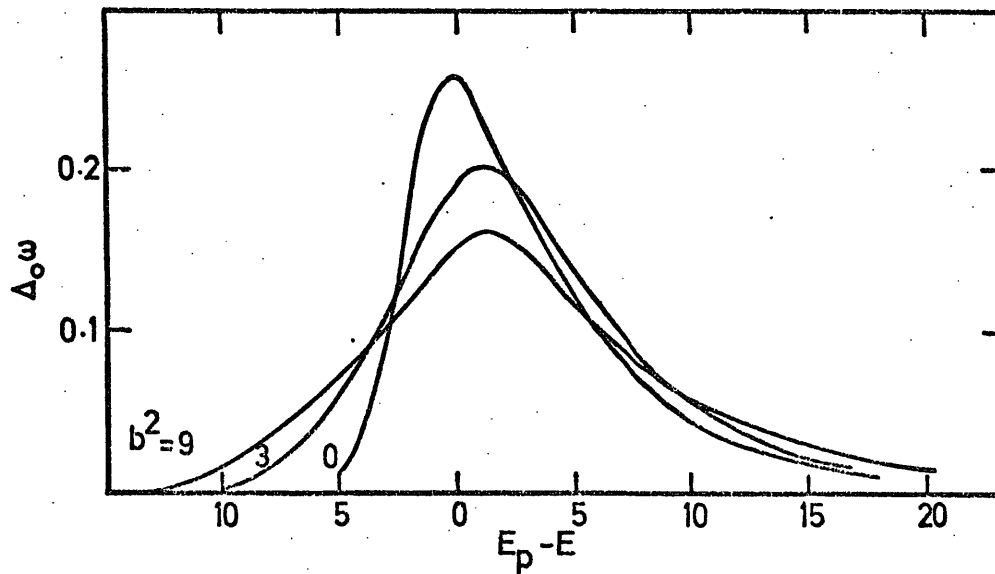
Figure 3.6b   The Blunck and Westphal distributions in energy loss for various b^2, normalised to compare with Landau distribution. The $b^2 = 0$ curve is identical to the Landau.

26 cm long. A coincidence from both trays shows that a particle has traversed the proportional counter as shown in figure 3.7a. The coincidence rate is a function of the atmospheric pressure and was, on average, $\simeq$ 10 min^{-1} for a pressure of 76 cm Hg. The pulse height distribution of single particles was measured by an oscilloscope triggered externally from the coincidence pulse of the G - M trays at different values of the voltages V_o, applied to the proportional counter. An example is shown in figure 3.7b for V_o = 2.40 KV. The dashed distribution is the expected one from Laundau theory. The probability of the expected and the measured distributions being identical is 0.57, using a Chi - square test.

3.4.5 The effects of other processes on the pulse height distribution.

The main effects which could broaden the measured pulse height spectrum are as follows:

(i) Knock-on electrons from the wall of the counter could broden the spectrum. Since the minimum energy of a knock-on electron produced in the middle of the wall is 1.8 Mev, calculated using the range - energy relationship given by Wilson (1951) for aluminium, the total probability of knock-on production, in the wall of the counter by muons (which is the main component in cosmic rays at sea level) is 3.4%. This value is calculated from the Rutherford formula (Rossi,1952).

(ii) Taking the geometric interaction mean free path of a proton in aluminium, L_g = 87 g cm^{-2}, and thickness of the wall, x, the number of particles, N, that will interact for N_o incident particles is given by
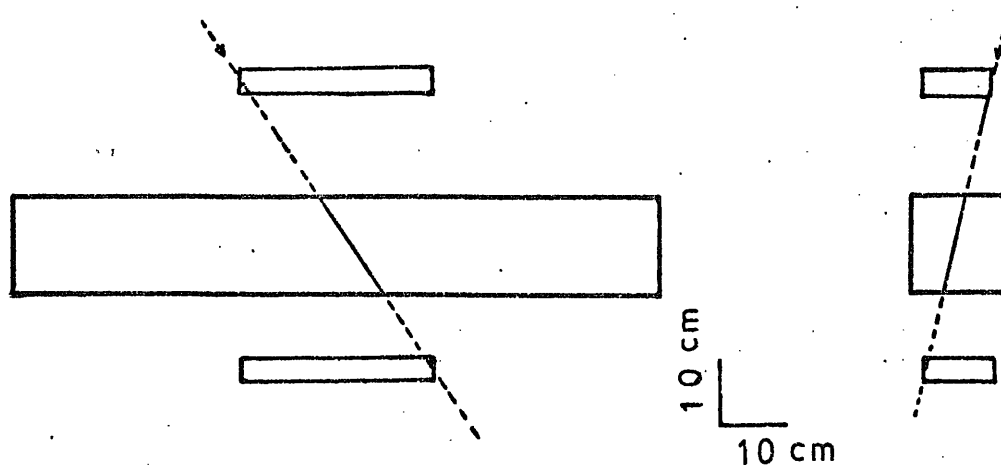
Figure 3.7a   The G-M counter calibration arrangement.
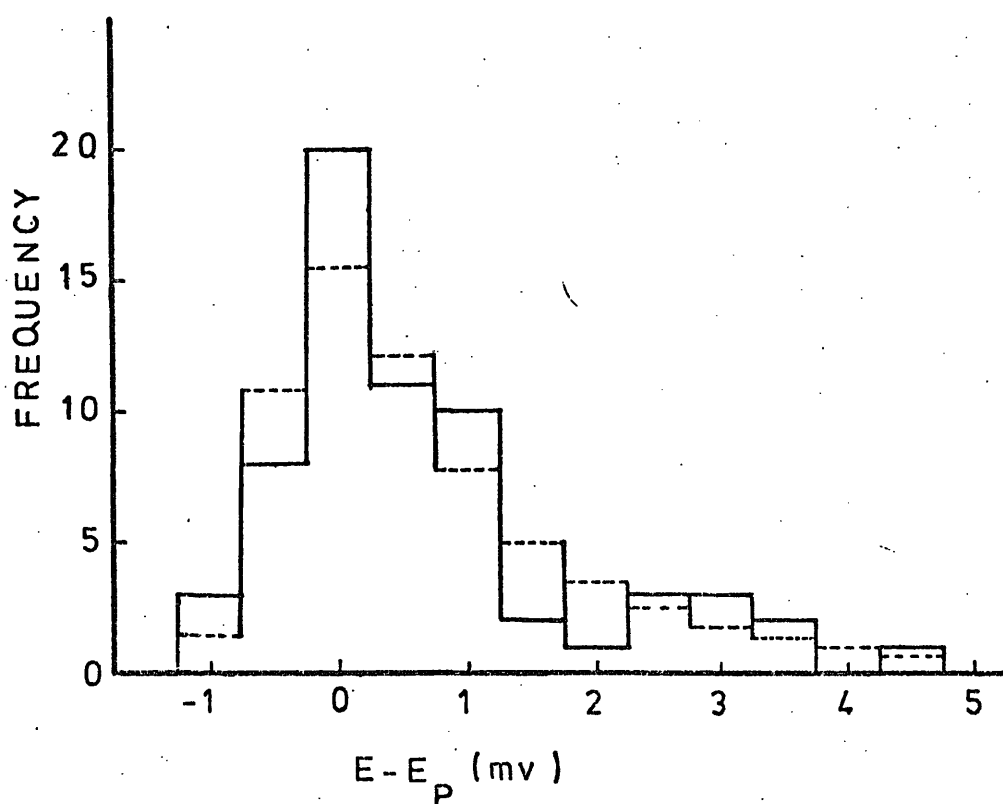
Figure 3.7b   The expected single particle distribution
                according to Landau (dotted distribution)
                compared with the measured single particle
                distribution (solid distribution) from the
                proportional counter at Vo = 2.40 KV.

$$N = N_0 \left(\exp \left(\frac{-x}{L_g} \right) - 1 \right)$$

Substituting the values for x and L_g, one obtains a value of 1.85% for the interaction probability.

(iii)   The effect of the uncertainty in the track length distribution in the gas of the counter is investigated in the following way:

The area of the G - M trays are divided into 16 small areas and for each small area of the top tray all possible tracks which meet the coincidence requirements have been considered.   The distribution in track length is found to be very narrow since the counter is of rectangular shape. Thus the imposed width in the pulse height spectrum due to the uncertainty in track length is negligible.   Therefore the measured pulse height spectra for different values of high voltages, V_0, applied to the proportional counter represents the single particle spectrum.   The mean pulse height of each spectrum is assumed to represent the equivalent energy loss of one particle having traversed the gas of the counter at the corresponding high voltage, V_0.   The results are shown in figure 3.8.   This graph shows that the counter operates in the proportional region.

3.4.6   Gas gain of the proportional counter

Let us assume the capacitance of the counter plus the head unit system is C_0. Suppose the amount of charge collected by the central wire of the counter when traversed by a charged particle is Q.   Then $Q = CV_0$ where V_0 is the output pulse height from the counter.
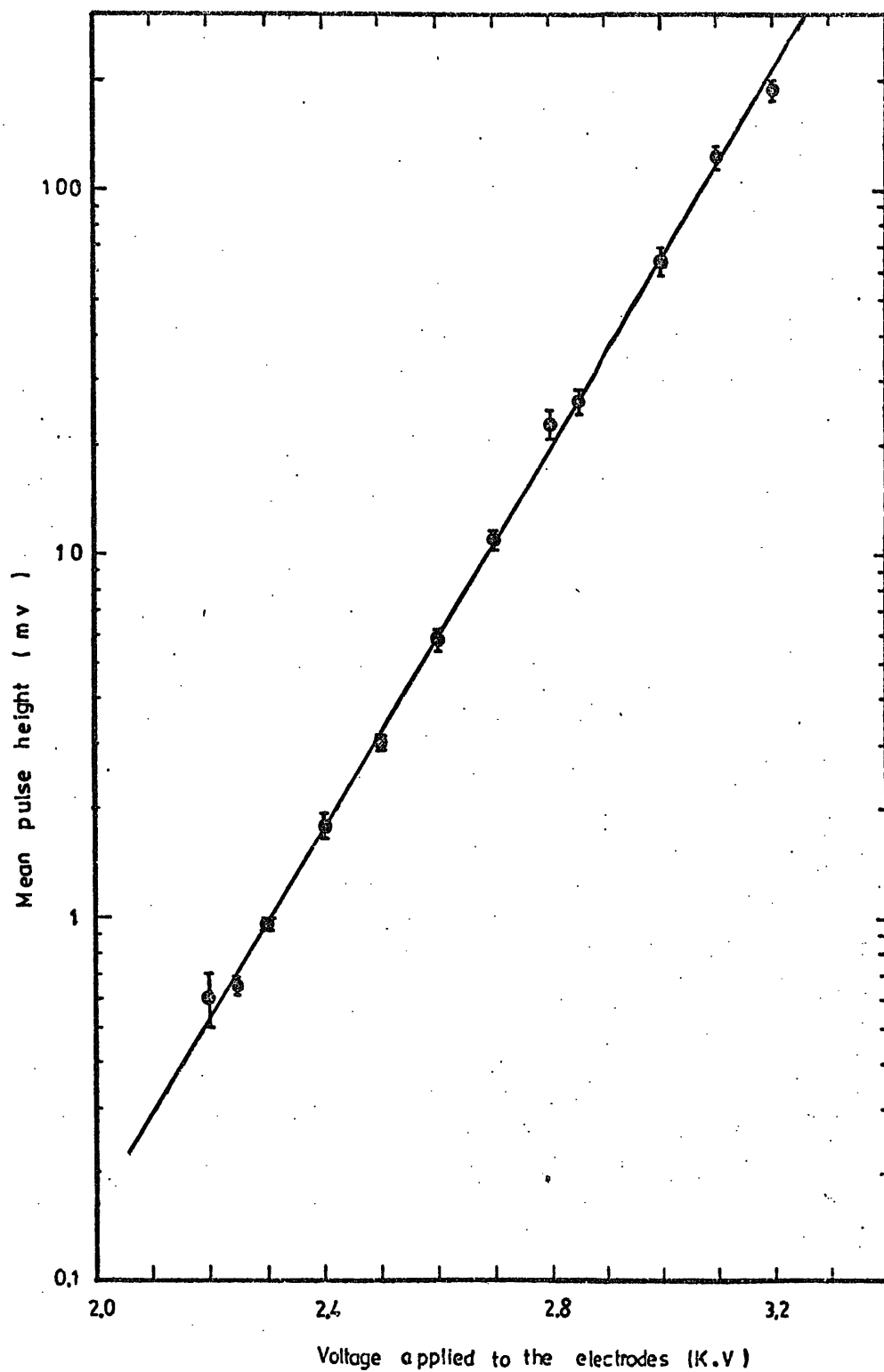
Figure 3.8   The variation of the mean pulse height, with operating voltage for the proportional counter.

Suppose one includes in the head unit circuit an additional capacitance, C, in parallel with C_o. The output pulse height will decrease to a value v where $V = \dfrac{Q}{C + C_o}$.

Therefore a plot of C against $\dfrac{1}{v}$ is expected to be a straight line with an intercept on the ordinate equal to C_o.

For a fixed value of applied voltage, V_o, to the counter the distribution in pulse height from the counter was obtained using the same procedure as described in the single particle calibration. The mean of each distribution, for different values of C, was taken as the corresponding value of v. The experimental results are shown in figure 3.9. From figure 3.9 one obtains $C_o = (54.3 \pm 8)$ Pf.

The median Lorentz factor for a single particle to meet the triggering requirements is 29.5, as will be described in section 3.6. The energy required to release one ion pair in the gas of the counter is 26.9 eV, Rossi (1952). This value refers to an electron of 17.4 KeV in argon (which is 90% of the gas in the proportional counter) and is assumed to be the same for the single particle in calibration run. Thus the number of ion pairs produced when a single particle traverses through the gas of the counter is 1,017.5. This is derived assuming 27.5 KeV energy loss (most probable energy loss) for a charged particle traversing the counter with $\gamma = 29.5$, as obtained from figure 3.5. Therefore the mean gas gain of the counter, M, is given by

$M = (333.5 \pm 49.1)\, v$ where v is the mean pulse height measured in mV. A plot of the gas gain, M, as a function of voltage, V_o, is shown in figure 3.10.
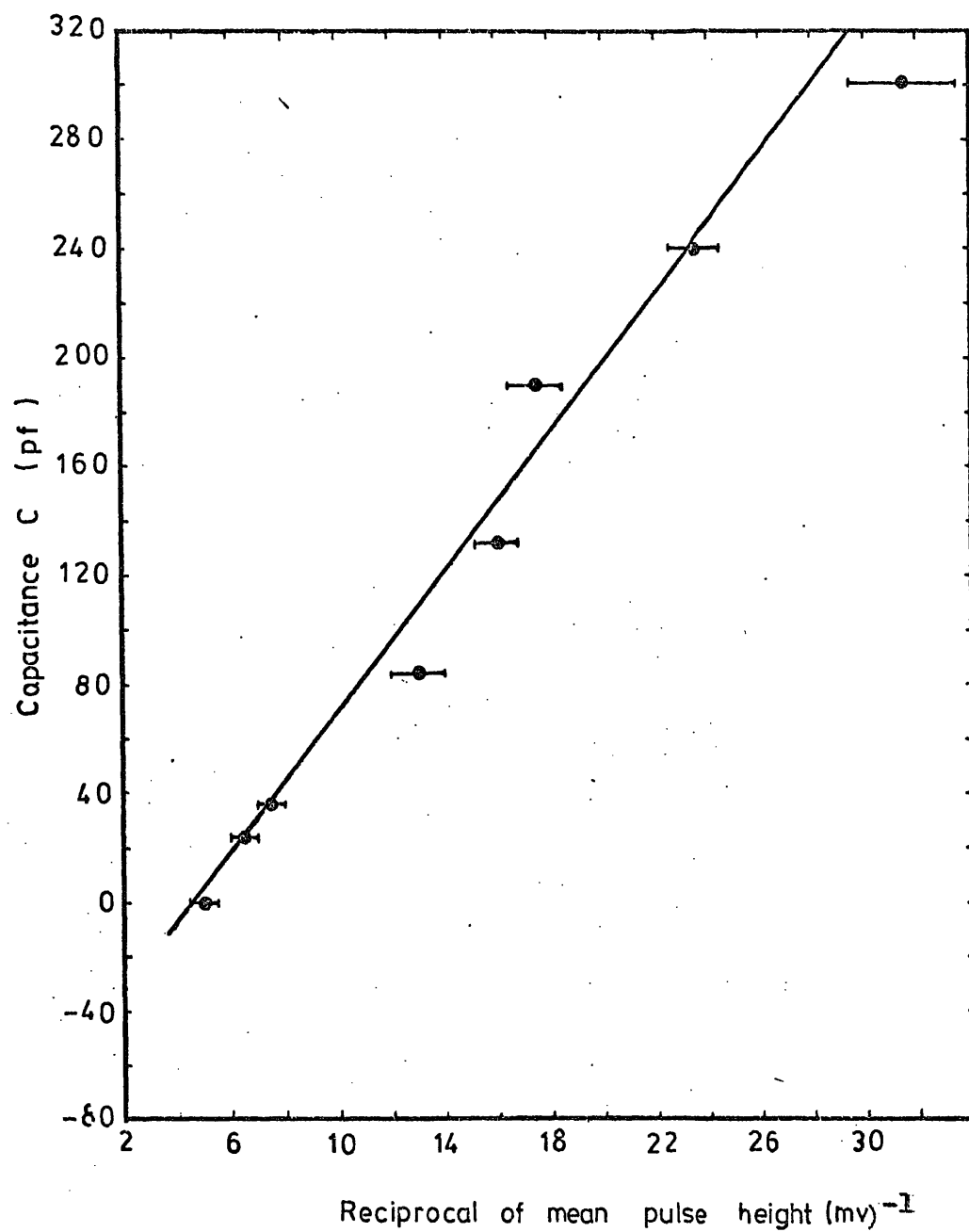
Figure 3.9   Reciprocal of the mean pulse height
$(mV)^{-1}$, obtained for values of the
capacitance C, inserted in the circuit
for $V_O = 2.80$ KV.
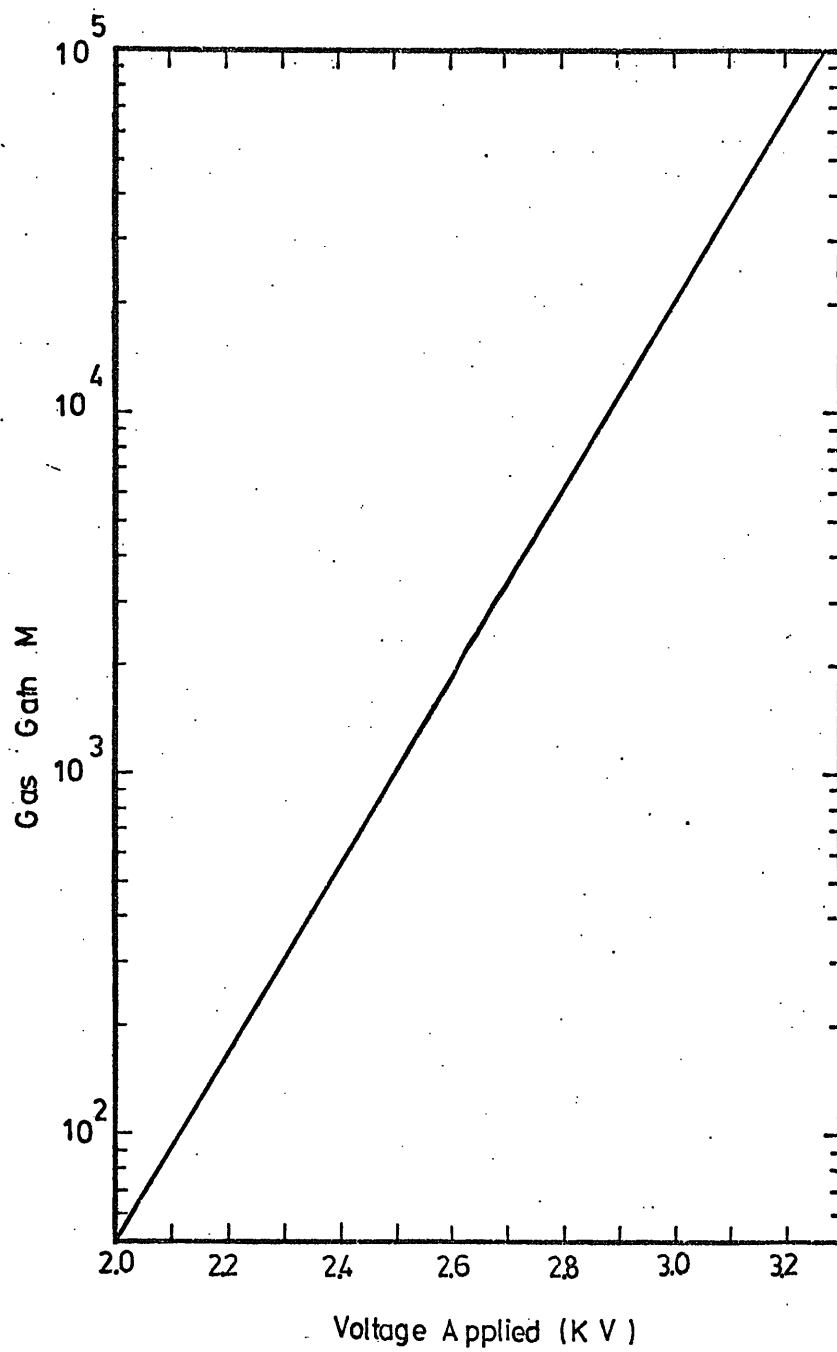
Figure 3.10   The gas gain – voltage charac-
teristic for the proportional
counter.

3.5   Experimental arrangement

3.5.1   General

For measurements of the density spectrum of EAS one
needs a system consisting of several detectors spread a few
metres apart to identify the arrival of an EAS.   The system
is called a master trigger.   In the present experiment the
master trigger is made of three large area liquid scintillators
placed horizontally beside each other on the roof of a large
volume flash tube chamber.   The proportional counter is
located on the top of the middle scintillator, M, under a
light roof (4 g cm^{-2} in thickness).   The counter is mounted
on an aluminium frame.   The distance between the top layer
of the liquid scintillator and the anode of the counter is
57.5 cm.

When the electron density, Δ , measured by the liquid
scintillators exceeds a minimum value, the output pulse from
the counter is photographed on an oscilloscope.   The
oscilloscope camera is triggered by the coincidence pulse from
the liquid scintillators through a cycling system.   The
experiment was carried out in three runs called E, F and G
corresponding to minimum EAS local electron densities of
40 m^{-2}, 160 m^{-2} and 511 m^{-2} respectively.   One scintillation
particle is defined as the mean of the measured pulse height
spectrum obtained in a single particle calibration using the
same procedure as described for the calibration of the prop-
ortional counter.   In run E the pulse length and in runs
F and G the pulse height spectrum of EAS particles was measured.
The electronic circuit diagram used in run E, converting pulse

height to pulse length, is shown in figure 3.13a.   Plate 3.1

shows an example of pulses obtained in run E and run F.

For each EAS trigger not only was the proportional

counter pulse height recorded but also the tracks of particles

in the flash tube chamber situated below the proportional counter

were photographed .   The flash tube chamber is described in

the next section.

3.5.2   The neon flash tube chamber

A scale diagram of the flash tube chamber is shown in

figure 3.11.   The chamber uses 10,748 flash tubes.   These

are cylindrical and made of soda glass filled with a gas

mixture of 98% neon gas and 2% of helium gas to a pressure of

60 cm of mercury.   Each tube is 2 m long with mean external

diameter of 1.78 cm and internal diameter of 1.58 cm.   Each

tube is covered with polythene sleeving to inhibit light

passing to neighbouring tubes.   The chamber contains 124 layers

of flash tubes, alternate layers having 84 or 85 tubes placed

horizontally.

Above every second layer of tubes are aluminium electrodes,

0.122 cm in thickness, 3.3 cm apart.   In the sections F2 and

F3 (figure 3.11) the area of the electrodes is 2.95 m^2, while

in F1 and F4 the electrodes are shorter in depth by 30 cm,

and cover an area of 2.48 m^2.

Between F1a and F1b there is 15 cm of steel which allows

one to study the cascade showers produced in the steel, and to

identify the parent particles in F1a as being charged or

neutral.

Directly below the iron, and also below F4a, there are

PLATE 3.1

An example of a pulse obtained in
the F series, from the proportional
counter. $\Delta_e = 3,125 \ m^{-2}$

An example of a pulse obtained in
the E series, from the proportional
counter. $\Delta_e = 175 \ m^{-2}$

N   M   S

SIDE

F1a (8 layers)
IRON
A.
F1b (6 layers)
F2 (52 layers)
F3 (44 layers)
F4a (6 layers)
B.
F4b (8 layers)

FRONT

LEAD

CONCRETE

Scale:- 0 ___ 50 cms.
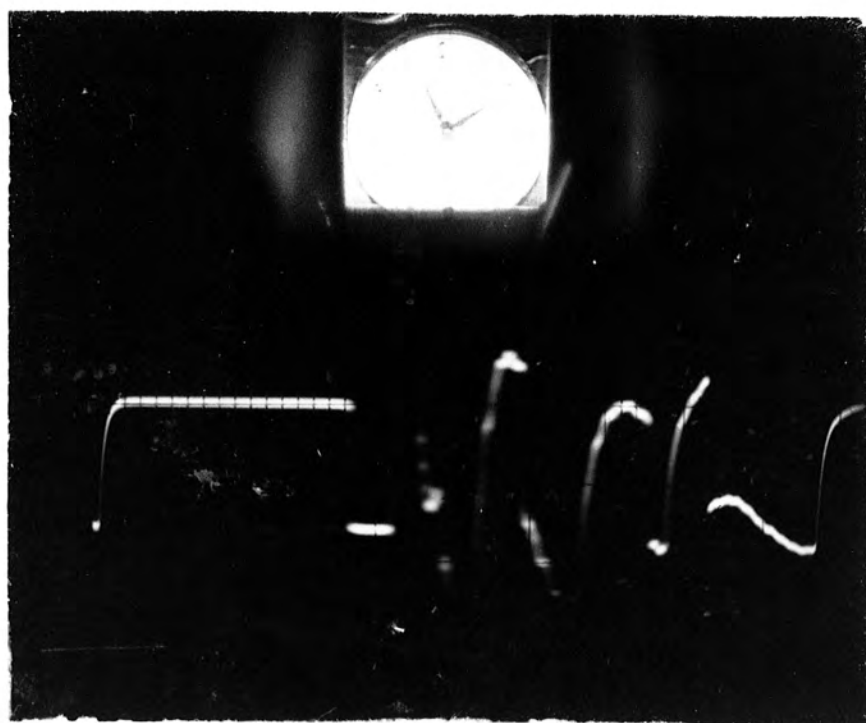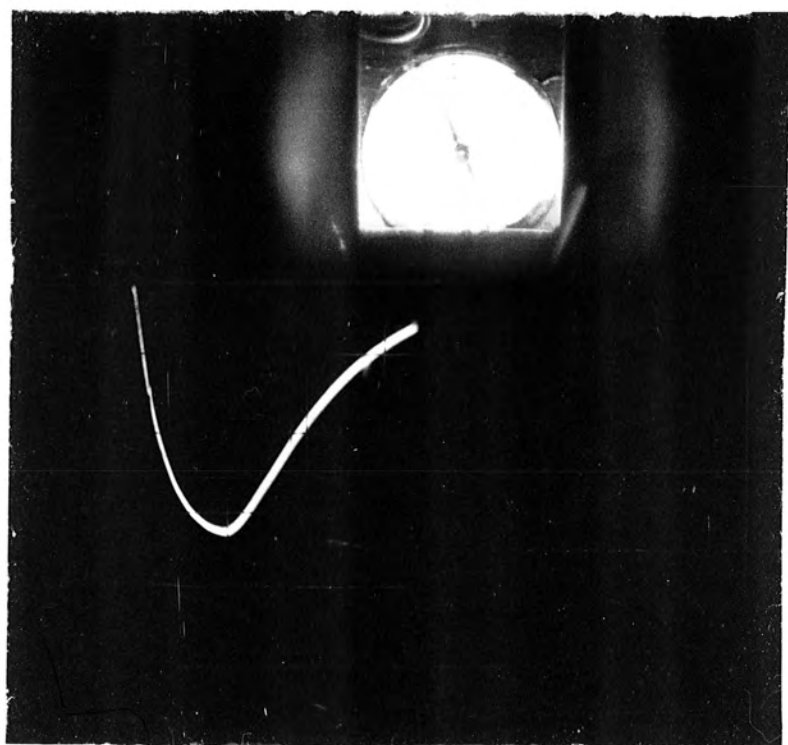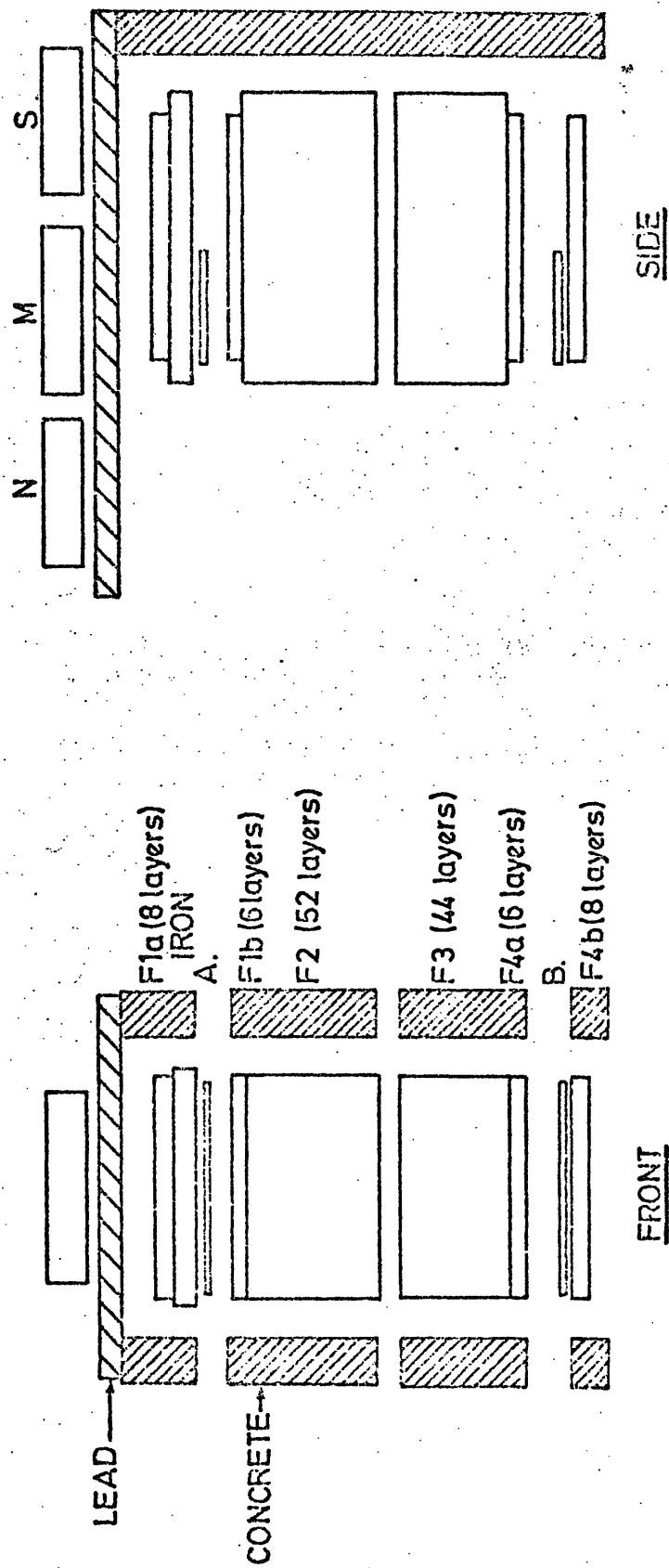
Figure 3.11   Scale diagram of the flash tube chamber.

two plastic scintillators A and B, of area 1.05 m^2 and thickness 5 cm, each viewed by five 53 AVP photomultiplier tubes and one 56 AVP tube. These two plastic scintillators, in coincidence, were used to select single particles (muons) traversing the chamber and is called the single particle selection system.

The steel plates, flash tubes and plastic scintillators are contained in an inner framework of steel girders, while around the chamber itself is a larger enclosure consisting of 30 cm thick wall of barytes concrete and a roof of 15 cm of lead supported by steel plates of thickness 1.3 cm. This absorber cuts out the soft components of EAS while allowing penetrating particles to pass through the chamber.

Above the lead there are three large liquid scintillators which form an EAS selection system. These scintillators are each of area 1.24 m^2, depth 15 cm, and are each viewed by two EMI 9583B photomultiplier tubes. The performance of these liquid scintillators are described in detail by Ashton et al. (1965).

The whole chamber is light-tight, allowing the use of a camera without a shutter. This means that the camera is continuously sensitive, the film being wound by one frame after each event.

When a trigger occurs a high voltage pulse is applied to the electrodes, creating the necessary electric field across the neon flash tube such that in tubes containing ionisation due to recent passage of a charged particle, the neon gas will break down and a visible discharge will occur in the tube.

This high voltage pulse is produced in the following way:

The master 5 volt trigger pulse triggers a thyristor, producing an output pulse of + 300 V magnitude. This pulse is fed to a high voltage pulse transformer, the output of which produces a trigger pulse for the "Trigatron" spark gap.

A voltage of 16 KV is supplied across the main spark gap. The pulse applied to the electrodes is approximately rectangular of height 8 KV and length of $10\mu s$.

A block diagram of the electronic circuits used in the EAS selection system (liquid scintillators) and the flash tube chamber calibration telescope (plastic scintillators) is shown in figure 3.12.

3.6   Response of the proportional counter to EAS particles

In single particle calibration runs for the proportional counter the minimum energy for muons and electrons to meet the triggering requirements are 24 MeV and 7.8 MeV respectively. These are calculated using the energy range relation of muons given by Serre (1967) and assuming 2 MeV g^{-1} cm^2 energy loss due to electrons, the amount of matter in the vertical beam being 3.9 g cm^{-2} of equivalent water.

Thus the expected integral rate of muons and electrons in calibration runs are 7.5×10^{-3} cm^{-2} s^{-1} st^{-1} and 3.8×10^{-3} cm^{-2} s^{-1} st^{-1} respectively, integrating the measured differential rate of these components given by Fizzini et al.(1968), at sea level.

Therefore the median Lorentz factor for a single particle in a calibration run is 29.5.   Mitra and Rosser (Galbraith, 1958) have measured the energy spectrum of electrons in EAS at sea level as

EAS SELECTION SYSTEM

NORTH E/F — E/F → ADD → AMP → DISC

MIDDLE E/F — E/F → ADD → AMP → DISC → COIN. → F.O. →▷ F/T TRIGGER / ▷ C/S TRIGGER

SOUTH E/F — E/F → ADD → AMP → DISC

E/F = EMITTER FOLLOWER
F/O = FAN OUT
F/T = FLASH TUBE
C/S = CYCLING SYSTEM

SINGLE PARTICLE SELECTION SYSTEM

A_1 E/F — A_2 E/F → ADD → AMP → DISC.

B_1 E/F — B_2 E/F → ADD → AMP → DISC.

→ COIN. → DISC. → F.O. → SCALER

30 SECOND DELAY

→ F/T TRIGGER
→ C/S TRIGGER
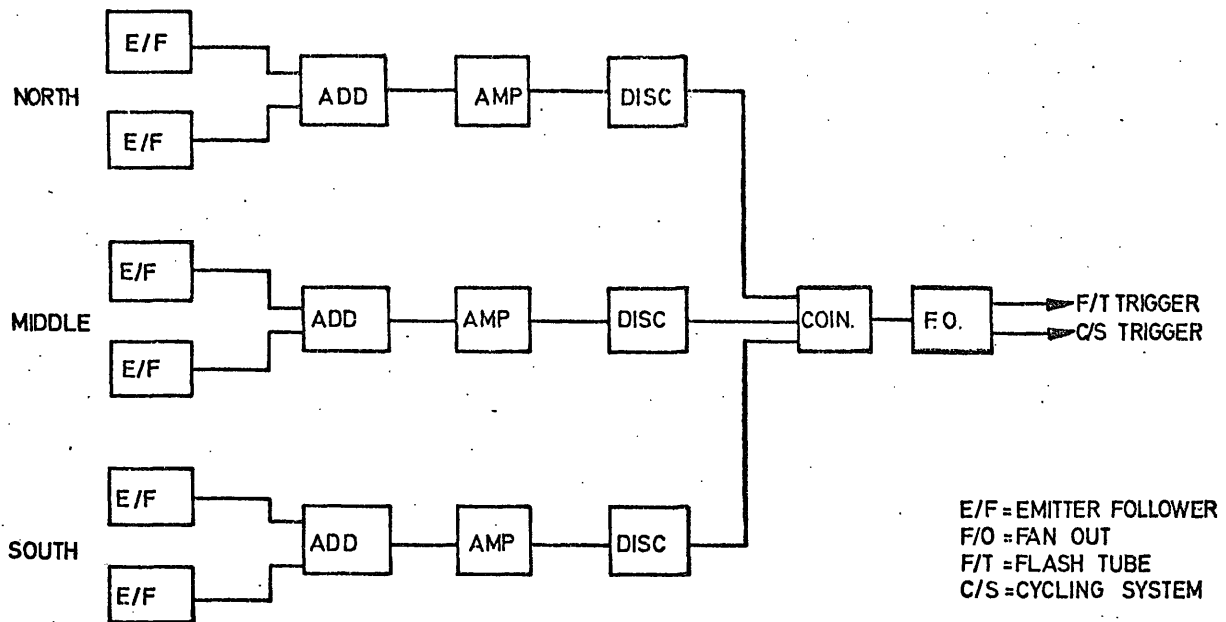
E/F = EMITTER FOLLOWER
F.O. = FAN OUT
F.T. = FLASH TUBE
C.S. = CYCLING SYSTEM
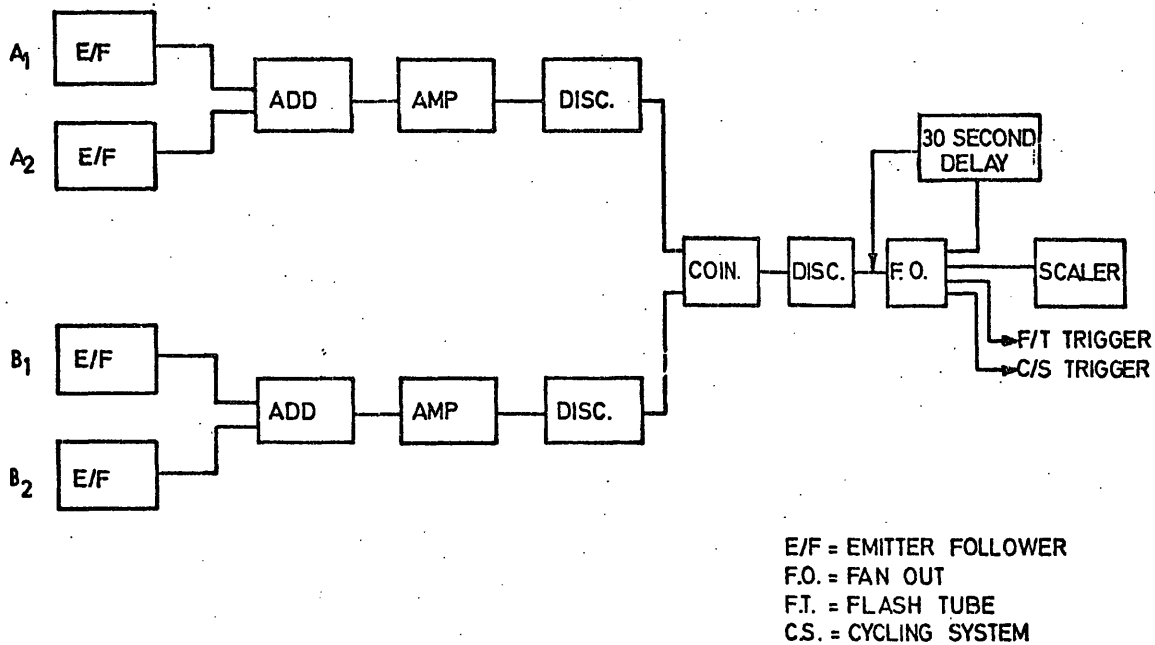
Figure 3.12 Block diagrams of the electronics used in the EAS selection system (liquid scintillators) and the flash tube chamber calibration telescope (plastic scintillators).

$N(>E) = K(E + E_c)^{-S}$ with $S = 1.1 \pm 0.3$ and E_c the critical energy of electrons being 114 MeV.

Taking $S = 1.1$ and $E_c = 114$ MeV one finds the medium energy of EAS particles (electrons) being 100 MeV corresponding to a median Lorentz factor equal to $\simeq 200$.

From figure 3.5 one can derive the most probable energy loss due to a single particle ($\gamma = 29.5$) and EAS particles ($\gamma = 200$). This indicates that EAS particles deposit more energy than single particles in traversing the proportional counter with a ratio equal to 1.27.

$R_{EAS} = 1.27 \, R_S$ where R_{EAS} and R_S are the response of the proportional counter to an EAS particle (electron) or single particle respectively.

Thus to obtain the density spectrum from the measured pulse height spectrum in the EAS experiment, the observed pulse heights have been divided by $1.27 \, R_S$, where R_S is the mean pulse height at the working voltage of the proportional counter as measured in a single particle calibration run (shown in figure 3.8). This then divided by the internal area of the counter, i.e. divided by $0.14 \, m^2$ (assuming a uniform distribution of particles over the area of the counter).

Since in run E, as mentioned earlier, pulse length distributions were measured it was necessary to measure the pulse height - pulse length distribution. The measurement was carried out using the following procedure:

Every time a cosmic ray particle (irrespective of direction) having traversed the counter produces a pulse which was measured through a fan out by an oscilloscope and at the same time the corresponding pulse length was measured using another oscilloscope. A scatter plot of pulse length

against pulse height was plotted and is shown in figure 3.13b. Figure 3.13a shows the electronic circuit diagram used to convert pulse height to pulse length.

The effective range in the EAS experiment was limited to $20\mu s$, equal to the delay time between the passage of EAS particles through the master trigger scintillation counters and the application of the high voltage pulse to the chamber. It was found that the rise time of the pulse due to EAS particles is longer than the single particle rise time, obtained from the proportional counter. Thus it was decided to measure the pulse height distribution of the proportional counter directly in the F and G series. This prevents uncertainties in deriving the density spectrum due to the width of scatter plot as can be seen in figure 3.13b.

The pulse length distribution obtained in the E series was converted to a pulse height distribution using the solid line drawn in figure 3.13b. This was done after correcting for the difference in rise rime between single particles and EAS particles. The corrected pulse height distribution was converted to the measured density spectrum of EAS by dividing the distribution by the area of the proportional counter.

3.7 Results

The experiment was carried out in the period of March 1972 to January 1974. As mentioned earlier the experimental data obtained in the three different runs were called the E, F and G series.

The data of the E series covers the density range of $\Delta = 40 - 700 \ m^{-2}$. The data of F and G series covers the
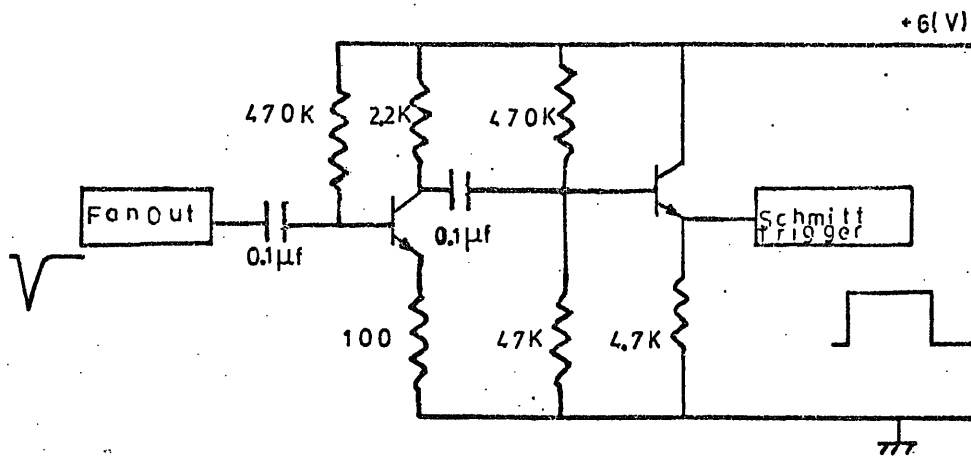
<u>Figure 3.13a</u>   The circuit used to convert pulse height to pulse length.
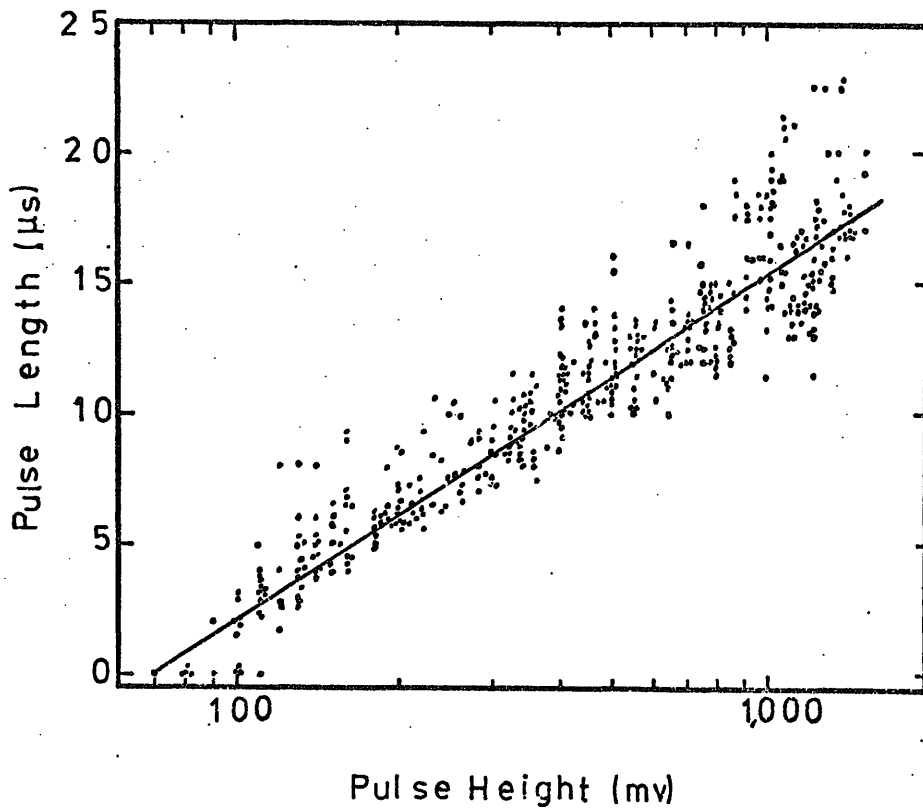
<u>Figure 3.13b</u>   Scatter plot of the pulse length as a function of pulse height. The solid line shows the best line through the measured points.

density ranges of $\Delta = 300 - 5,000$ m^{-2} and $\Delta = 500 - 5,000$ m^{-2} respectively. Figure 3.14 demonstrates the differential density spectrum obtained in all three series. As can be seen from this figure, the results obtained in the E series is shown separately. The data of the F series and G series were added to each other in the range of $\Delta > 500$ m^{-2}. Figure 3.14 shows that the experimental data of all three series are consistent with each other. A total number of 92 events with $\Delta > 1,000$ m^{-2} (in F series and G series) was observed. This was obtained in a sensitive time of 6870.7 hrs.

The slope γ_d of the observed differential spectrum was calculated using a chi-square test. It was found that

$$\gamma_d = -2.45 \; {\scriptstyle +0.05 \atop \scriptstyle -0.06}$$ for the density range of $\Delta = 40 - 800$ m^{-2}.

The value of the slope of the spectrum was found as $\gamma_d = -3.15$ $+0.43 \atop -0.60$ in the range of $1,000 < \Delta < 5,000$ m^2. The chi-square probabilities at these values are 20% and 75% respectively. The errors give 5% points. The probability that the whole spectrum in the density range of $\Delta = 40 - 5,000$ m^{-2} fits a single power law with the slope of -2.50 was calculated to be 0.8%.

The solid lines in figure 3.14 are drawn with slopes of -2.45 for $40 < \Delta < 800$ m^{-2} and -3.15 for $\Delta > 1,000$ m^2.

The Poissonian fluctuations were unfolded from the observed density spectrum for the region of $\Delta > 300$ m^{-2}. The results are shown in figure 3.14. It can be seen that the effects of accounting for Poisson fluctuation neither effects the slope of the spectrum, the position of the change in the slope at $\Delta \simeq 1,000$ m^{-2} nor the absolute intensity of
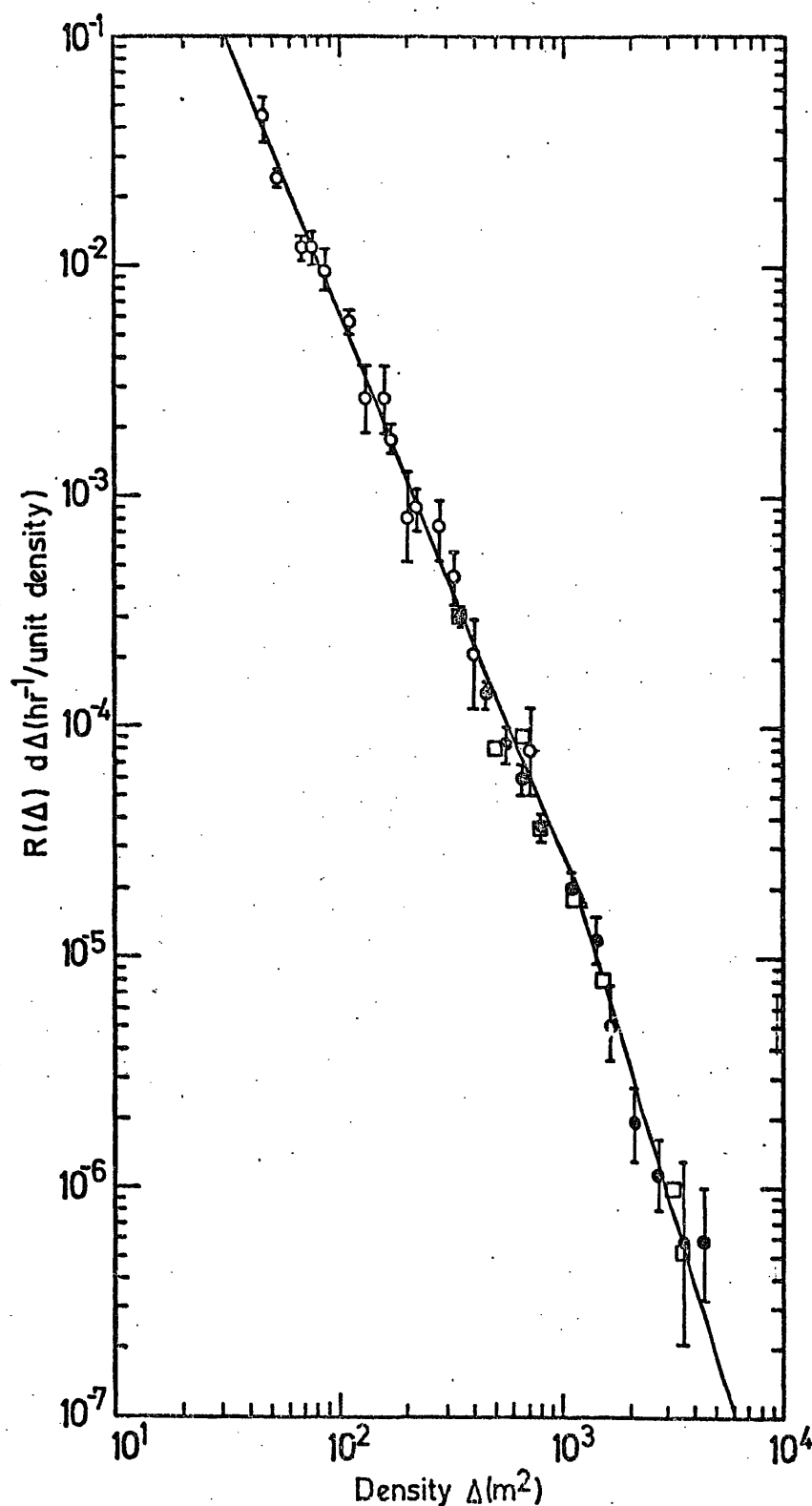
Figure 3.14   The differential density spectrum measured in the present experiment. ϕ = obtained in run E, ϕ = obtained in runs F and G, $\square$ = the corrected spectrum after unfolding the Poissonian fluctuations. It is seen that the effects of accounting for Poisson fluctuations neither effects the shape of the spectrum, the position of the change in slope at $\Delta \gtrsim 1,000$ m^{-2} nor the absolute intensity. The solid lines have a slope of -2.45 for $\Delta <$ 1,000 m^{-2} & -3.15 for $\Delta > 1,000$ m^{-2}. One unit of density is one particle m^{-2}.

the observed spectrum.

The measured integral density spectrum of EAS is shown in figure 3.15. This shows the overall results obtained in all the three series E, F and G. The solid spectrum drawn in figure 3.15 is the best fit through the experimental points and follows as:

$$R(>\Delta) = 411.0 \; \Delta^{-1.50 \pm 0.05} \; hr^{-1} \text{ in the range of } 40 < \Delta \leq 800 \; m^{-2}$$

$$R(>\Delta) = 1.310^4 \; \Delta^{-2.0 \; \pm \; {}^{0.38}_{0.28}} \; hr^{-1} \text{ in the range of } 1000 \leq \Delta < 5000 m^{-2}$$

These results indicate that the integral density spectrum of EAS at sea level has a slope of -1.50 in the density range $\Delta = 40 - 800 \; m^{-2}$. This is approximately consistent with most of the experimental data obtained previously in this range of density. The slope of the spectrum was found to be -2.0 in the range of $\Delta > 1000 \; m^{-2}$.

Greisen (1960) gives the following expression for the integral density spectrum of EAS at sea level in the range of $\Delta = 1 \div 10^4 \; m^{-2}$.

$$R(>\Delta) = 540 \; \Delta^{-(1.3 \; + \; 0.055 \; \log \Delta)} \; hr^{-1}$$

This suggests a gradual change in the slope of the density spectrum starting from $\gamma = 1.30$ at $\Delta = 1 \; m^{-2}$ to $\gamma = -1.46$ at $\Delta = 1,000 \; m^{-2}$. The absolute rate given by Greisen, is higher compared with the present experiment with a ratio of 2.0 at $\Delta = 100 \; m^{-2}$.

Cocconi (1949) and Cocconi and Tongiorgi (1949), using G-M tubes, give the following expression for the sea level density spectrum as given by Norman (1956).
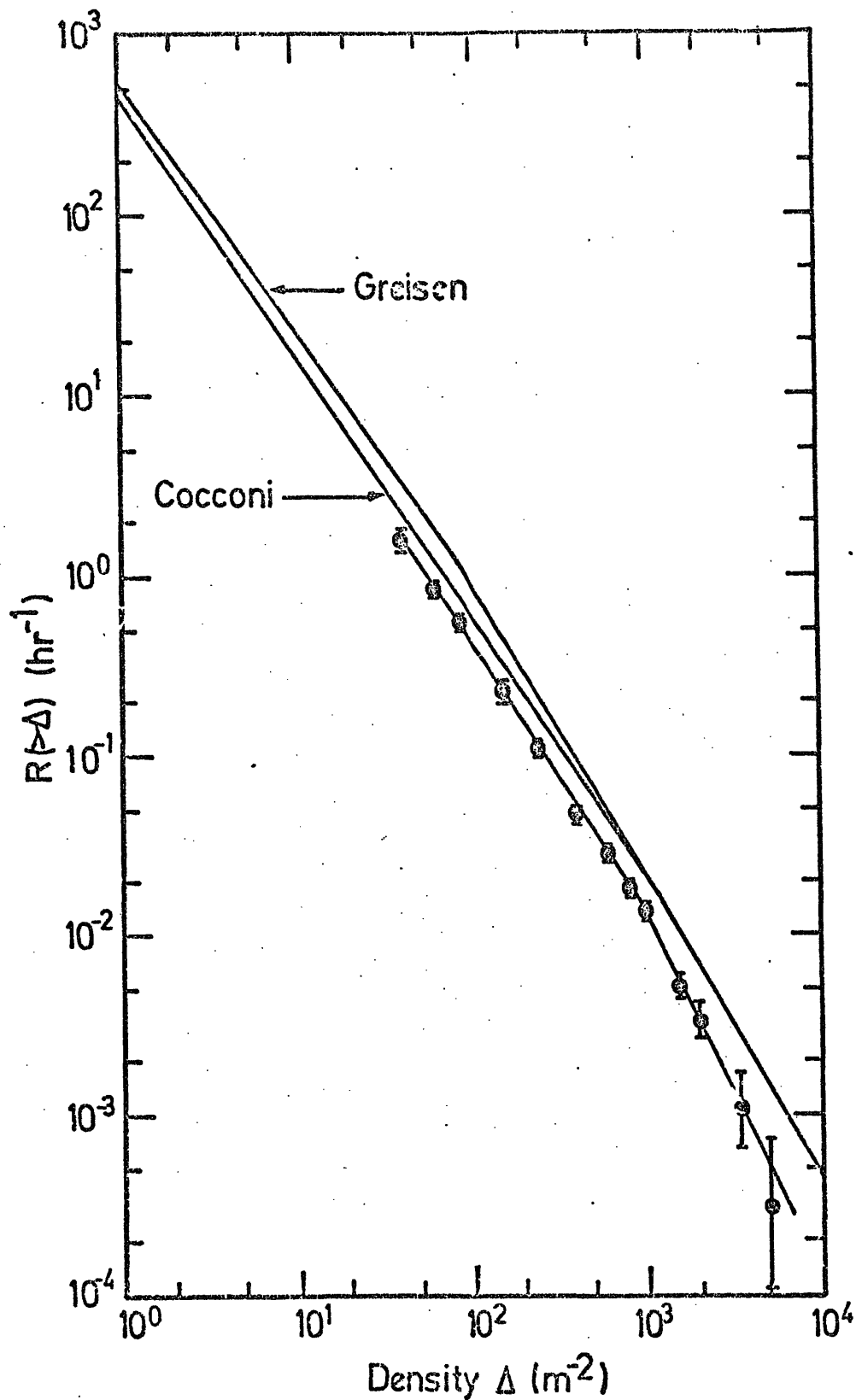
Figure 3.15   Integrate density spectrum obtained in the present experiment. The dashed curve is drawn through the experimental points. It has a slope of -1.5 for $\Delta < 800$ m^{-2} and a slope of -2.0 for $\Delta > 1,000$ m^{-2}. The solid curves are due to Greisen (1960) and Cocconi and Cocconi and Tongiorgi (1949).

$$R(>\Delta) = 460 \ \Delta^{-1.45} \ hr^{-1} \quad \text{in the density range } \Delta = 1\text{-}1{,}000 \ m^{-2}$$

This is in better agreement with the present results both in absolute rate and slope. The rate of the spectrum at $\Delta = 100 \ m^{-2}$ as given by this expression is higher than the present results by a factory of 1.4. Thus if one takes the average measured rate between the present results and those of Greisen it approximately agrees with the absolute rate as given by Cocconi and Cocconi and Tongiorgi in the range of $40 < \Delta < 1{,}000 \ m^{-2}$. The difference in the measured absolute rates of the spectrum could be attributed to instrumental effects (see Appendix C) and also to the trigger-ing system of EAS (see Prescott, 1956).

3.8 Derivation of the number spectrum from the measured density spectrum

3.8.1 The predicted electron density spectrum

The relationship between the measured density spectrum and number spectrum was pointed out in chapter 2. Thus it is of great interest to find out what peculiarity in showers is required to produce the observed density spectrum.

Assuming the lateral structure function of EAS particles is independent of shower size thus

$$R \ (>\Delta) = \int_0^{\infty} 2\pi r \ dr \ R(> \frac{\Delta}{\rho(r)}) \quad \text{where } N = \frac{\Delta}{\rho(r)} \ , \ R(> \Delta) \text{ is}$$

the integral density spectrum of EAS, $R(> \frac{\Delta}{\rho(r)})$ is the integral number spectrum and r is the core distance.

Measurements of the integral number spectrum have been summarised by Hillas (1970b). The results of the summary can

be parameterised in the following expressions, i.e. case (a)
and case (b).

Case (a)

$$R(>N) = 52.0 \ N^{-1.50} \ m^{-2} \ s^{-1} \ st^{-1} \quad \text{for} \quad N < 5.10^5$$

$$R(>N) = 36{,}920.0 \ N^{-2.0} \ m^{-2} \ s^{-1} \ st^{-1} \quad \text{for} \quad 5.10^5 < N < 3.10^7$$

$$R(>N) = 6.76 \ N^{-1.50} \ m^{-2} \ s^{-1} \ st^{-1} \quad \text{for} \quad N > 3.10^7$$

Case (b)

$$R(>N) = 52.0 \ N^{-1.5} \ m^{-2} \ s^{-1} \ st^{-1} \quad \text{for} \quad N < 5.10^5$$

$$R(>N) = 36{,}920.0 \ N^{-2.0} \ m^{-2} \ s^{-1} \ st^{-1} \quad \text{for} \quad N > 5.10^5$$

For both cases in the number spectrum it is assumed that
$R(>5.10^9) = 0.0$. This assumption does not change the
results for densities of $\Delta < 10{,}000 \ m^{-2}$.

For ease of calculation it is assumed in the above
expressions, that the kinks in the number spectrum are
absolutely sharp. A wider transition region for the change
in slope of the number spectrum does not change significantly
the results of the present calculations.

The integral Was calculated numerically for both cases
(a) and (b) of the number spectrum. For each case, three
lateral structure functions of electrons were assumed.
These are given by Greisen (1960), Kiel group (Hillas, 1970a)
and Sydney group (Hillas, 1970a) and are called ρ_G, ρ_K and
ρ_S respectively. The analytical expressions for these
functions are as follows.

$$\rho_G(r) = \frac{0.4}{r_1^2} \left(\frac{r_1}{r}\right)^{0.75} \left(\frac{r_1}{r+r_1}\right)^{3.25} \left(1 + \frac{r}{11.4\, r_1}\right) \text{ where } r_1 = 79m \text{ at}$$
$$\text{sea level.}$$

$$\rho_K(r) = 1.08.10^{-2} (r + 1.1)^{-1.5} \exp\left(-\frac{r}{120}\right)$$

$$\rho_S(r) = 2.12.10^{-3} (r + 1)^{-1.0} \exp\left(-\frac{r}{75}\right)$$

The lower limit of the integral is taken to be $r = 0.1$ m instead of $r = 0.0$. It will be shown in section 3.8.2 that this assumption does not change the results (see figure 3.17). The upper limit of the integral, r_{max}, varies with the assumed form of the structure function and the value of the minimum electron density Δ . This variation is such that $\rho(r_{max}) = \frac{\Delta}{5.10^9}$ where $\rho(r_{max})$ is the assumed lateral structure at $r = r_{max}$ and 5.10^9 is the maximum value for shower size.

The results of integration is expressed in units of $s^{-1}st^{-1}$. It is assumed that the effective solid angle of EAS particles is 0.75 st corresponding to $n = 9$ in $I = I_0 \cos^n \vartheta$. The result $n = 9$ is obtained in a separate experiment and will be described in chapter 5.

The calculated values of the integral density spectrum of EAS were multiplied by $(3,600 \times 0.57) = 2,052$. This gives the integral rate of EAS at sea level expressed in units of hr^{-1}. Figure 3.16 shows the results of the 6 predicted density spectra. The integral rates are plotted as $R(> \Delta) \times \Delta^{+1.5}$. The results of the present experiment is shown in figure 3.16 to be compared with the predicted spectra.

It can be seen that none of the 6 predicted spectra fit the observed spectrum in the present experiment. This comparison suggests that a change in the shape of the lateral
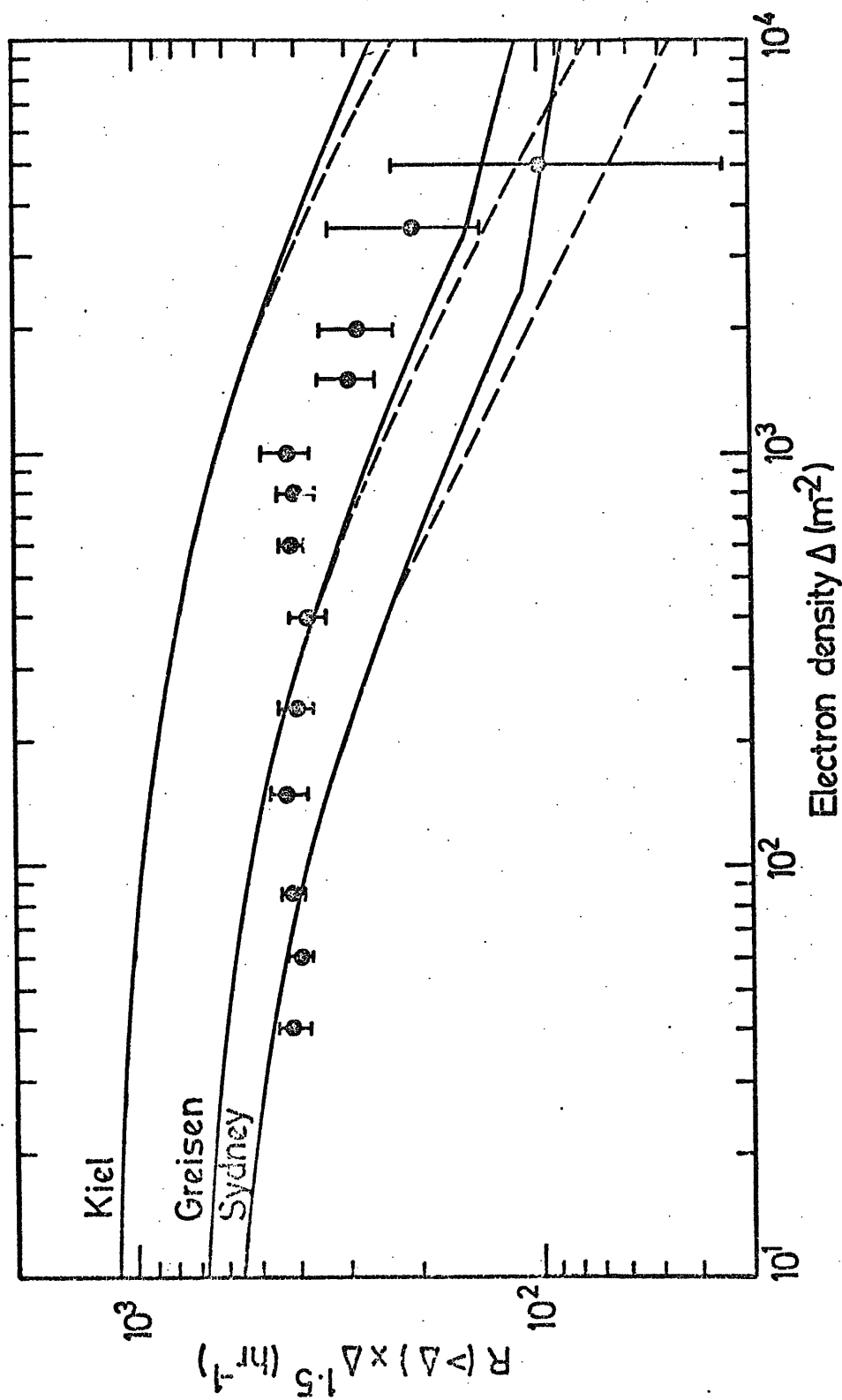
Figure 3.16   Integral density spectrum of EAS obtained in the present experiment. The solid (dashed) curves are the calculated spectra taking case a (case b) of the number spectrum and the lateral structure functions as given by Greisen, Kiel group and Sydney group as shown for each curve. It can be seen that none of the six calculated spectra fit the experimental data.

distribution function with shower size seems to be required to fit the measurements.

A chi-square test was carried out between NKG formula (Greisen, 1956) and each of the three selected structure functions in order to find out the best values for the age parameters of each of the assumed functions. The results show that the best values of S are 1.25, 1.20 and 1.40 for Greisen, Kiel and Sydney functions respectively.

Higher densities are produced by larger showers. Thus according to the observed density spectrum, the larger showers observed at sea level tend to be older (larger value of age parameters) to see at what core distances and at what shower size this occurs, the distributions of the shower sizes and the distribution of the core distances of EAS for a particular observed density were calculated. The procedure of the calculations and the results of the calculations will be explained in the following section.

3.8.2 Distribution of the core distance and size of EAS producing a given electron density

The rate of triggers for which the local electron density exceeds Δ_e and whose core falls at distance $> r$ is given by:

$$R\ (> r, > \Delta_e) = \int_{r}^{r_{max}} 2\pi r'\ I(\ > \frac{\Delta}{f(r')}) \ dr'$$

The rate of triggers of electron size $> N$ producing a local electron density is given by:

$$R\ (> N, > \Delta_e) = \int_{r_{min}}^{r_{max}} 2\pi r'\ I(\ > \frac{\Delta}{f(r')}) \ dr'$$

where $N = \dfrac{\Delta}{f(r)}$ and $f(r')$ is the structure function

of electrons.

The above integrals were evaluated numerically for different values of Δ_e. For each value of Δ_e, the functions were calculated for all six cases. These are two cases a and b for the assumed number spectrum given by Hillas (1970b) and three forms of the lateral structure functions given by Greisen (1960), Kiel group and Sydney group (Hillas, 1970a). The analytic expressions for these functions are the same as given in the previous section. Figure 3.17 shows the rate of EAS producing a given electron density and whose core falls at core distance $>$ r meter. This is calculated taking the Greisen lateral structure function for both cases (a) and (b) of the number spectrum.

Figure 3.18 demonstrates the rate of EAS of size $>$ N producing a given electron density. The calculation is based on the Greisen lateral structure function and cases (a) and (b) of the number spectrum.

To see the effect of the assumed lateral structure function on median core distances and median shower sizes of triggers producing an electron density Δ see tables 3.3 and 3.4 respectively. Minimum shower sizes shown in table 3.4 have been calculated at r = 0.1 m.

3.8.3 Derived number spectrum

It was mentioned in section 3.8.1 that according to the measured density spectrum a change in the slope of the lateral distribution function with shower size would seem to be required.
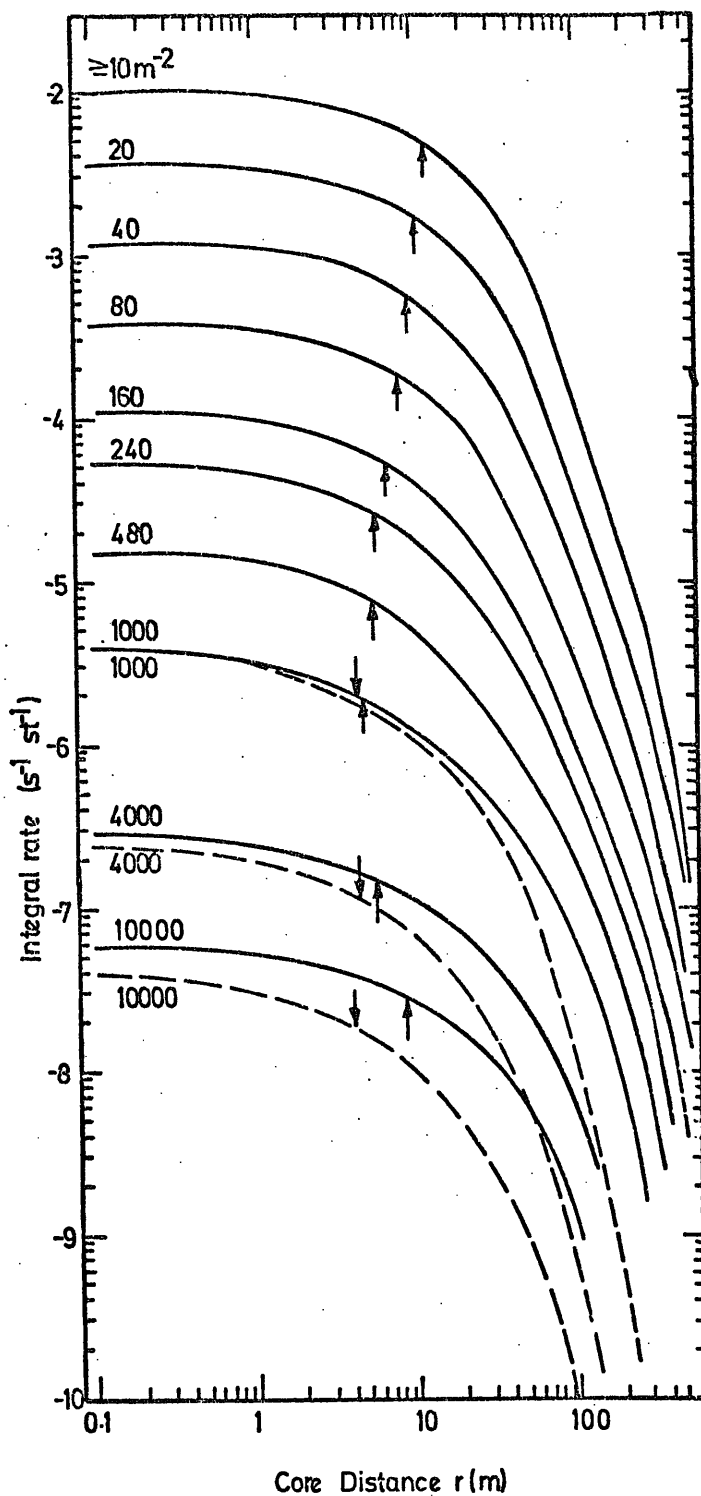
Figure 3.17   The rate of EAS which produce a local
electron density (m^{-2}), as indicated for
each curve, whose core fall at distance
$> r$ metres from the detector calculated
taking lateral structure function given by
Greisen for both case (a) of the number
spectrum (solid curves) and case (b) of the
spectrum (dashed curves). Median core
distances are shown by arrows.
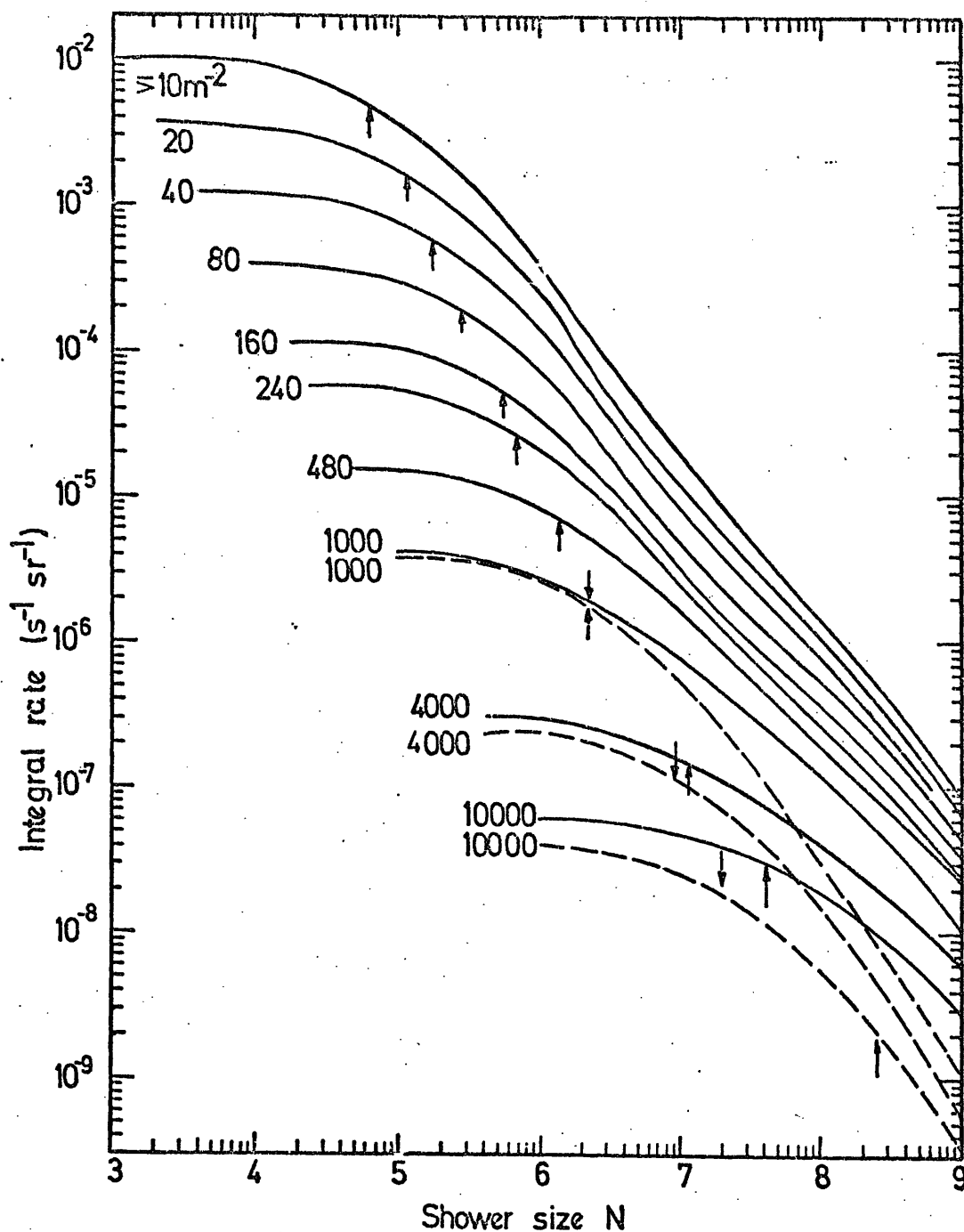
Figure 3.18   The rate of EAS of electron size $> N$ producing a local electron density (m^{-2}), as indicated calculated taking the lateral structure function given by Greisen for both case (a) of the number spectrum and case (b) of the number spectrum (dashed curves).   Median shower sizes are shown by arrow.

Minimum observed density (m^{-2})	Median Core distances (m)					
	Greisen		Kiel		Sydney	
	case(a)	case(b)	case(a)	case(b)	case(a)	case(b)
10	12	12	7	7	16	16
40	9.5	9.5	5.5	5.5	13	13
80	8.	8.	4.5	4.5	10	10
160	6.5	6.5	4.3	4.3	8.2	8.2
480	5.5	5.5	3.2	3.2	7.5	7.5
1000	4.5	4.5	2.5	2.5	8.	7.
4000	5.5	4.5	2.	2.	13.	7.
10000	8.5	4.5	3.5	2	14.	7

Table 3.3   The median core distances (m) calculated for structure functions given by Greisen, Kiel group and Sydney group assuming number spectrum given by Hillas for both cases (a) and (b) (see the text) as a function of minimum electron density (m^{-2}).

Minimum observed density (m^{-2})	Median shower sizes (the minimum sizes are shown in brackets)					
	Greisen case(a)	case(b)	Kiel case(a)	case(b)	Sydney case(a)	case(b)
10	6.10^4	6.10^4	2.10^4	2.10^4	$1.1.10^5$	$1.1.10^5$
	(10^3)	(10^3)	$(1.2.10^3)$	$(1.2.10^3)$	(5.10^3)	(5.10^3)
40	$1.8.10^5$	$1.8.10^5$	$7.0.10^4$	$7.0.10^4$	3.10^5	3.10^5
	$(3.2.10^3)$	$(3.2.10^3)$	$(4.8.10^3)$	$(4.8.10^3)$	(2.10^4)	(2.10^4)
80	$2.7.10^5$	$2.7.10^5$	10^5	10^5	5.10^5	5.10^5
	$(8.8.10^3)$	$(8.8.10^3)$	$(9.5.10^3)$	$(9.5.10^3)$	$(4.2.10^4)$	$(4.2.10^4)$
160	$5.0.10^5$	$5.2.10^5$	2.10^5	2.10^5	$8.5.10^5$	$8.5.10^5$
	$(1.7.10^4)$	$(1.7.10^4)$	$(1.8.10^4)$	$(1.7.10^4)$	$(8.2.10^4)$	$(8.2.10^4)$
480.	$1.3.10^6$	$1.3.10^6$	$4.2.10^5$	$4.2.10^5$	$3.5.10^6$	$3.5.10^6$
	(5.10^4)	(5.10^4)	$(5.6.10^4)$	$(5.6.10^4)$	$(4.2.10^5)$	$(4.2.10^5)$
1000	$2.3.10^6$	$2.2.10^6$	$9.8.10^5$	$9.8.10^5$	5.10^6	$4.3.10^6$
	(10^5)	(10^5)	$(1.2.10^5)$	$(1.2.10^5)$	$(5.2.10^5)$	$(5.2.10^5)$
4000	$1.1.10^7$	$9.5.10^6$	$3.5.10^6$	3.10^6	$3.3.10^7$	$1.8.10^7$
	(4.10^5)	(4.10^5)	$(4.6.10^5)$	$(4.6.10^5)$	(2.10^6)	(2.10^6)
10000	4.10^7	$1.9.10^7$	$7.5.10^6$	$6.5.10^6$	10^8	4.10^7
	(10^6)	(10^6)	$(1.2.10^6)$	$(1.2.10^6)$	$(5.2.10^6)$	$(5.2.10^6)$

Table 3.4 The median and minimum shower sizes producing a given electron density (m^{-2}) calculated for structure functions given by Greisen , Kiel group and Sydney group for either cases (a) and (b) in number spectrum given by Hillas (see the text). The numbers written in brackets show the minimum shower sizes.

Such a measurement has in fact been made by Vernov et al.(1970) as shown in figure 3.19. According to the results of Vernov et al.the age parameter is found to have a value of about 1.2 in the size range $10^5 - 10^6$ with evidence for S increasing to $\simeq 1.3$ in the size range $10^6 - 10^7$. In extrapolating S to lower shower sizes asymtotic values of 1.4 (curve 1 of figure 3.19) and 1.3 (curve 2 of figure 3.19) at $N = 10^3$ have been assumed. See figure 3.16 for justification for making this assumption.

Assuming an age dependence, as given by the smooth curves 1 and 2 in figure 3.19, the integral density spectrum was calculated. This was done using the NKG formula (see chapter 2) and a modified number spectrum to that given below to get a fit to measurements over the range 1- 5,000 m^{-2}. Since the density spectrum has not been measured for $\Delta < 40$ m^{-2} in the present work the spectrum was extrapolated to $\Delta = 1$ m^{-2} such that the resulting spectrum was approximately parallel to the formula given by Greisen (1960) in the density range $\Delta = 1 - 500$ m^{-2}.

The resulting best estimate of the sea level number spectrum is shown in figure 3.20.

$$R(>N) = 3.0 \; N^{-1.3} \; m^{-2}s^{-1}st^{-1} \qquad N \lesssim 7.10^5$$

$$R(>N) = 36{,}920.0 \; N^{-2.0} \; m^{-2}s^{-1}st^{-1} \qquad 7.10^5 \lesssim N < 3.10^7$$

$$R(>N) = 6.76 \; N^{-1.5} \; m^{-2}s^{-1}st^{-1} \qquad N > 3.10^7$$

This is of the same form as that given by Hillas (1970b) for $N > 7.10^5$. The difference for $N < 7.10^5$ increases as N
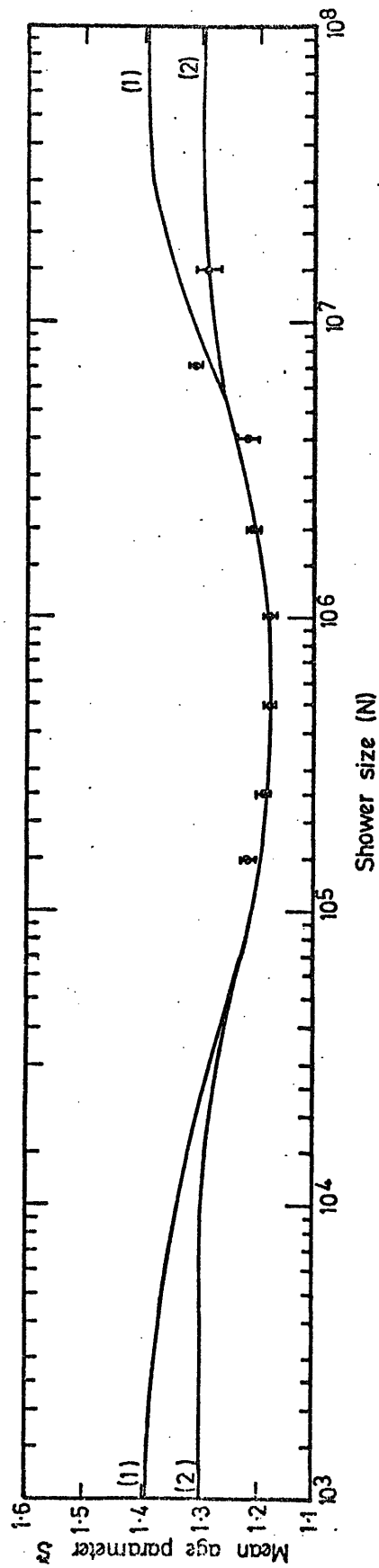
Figure 3.19 The dependence of the mean age parameter on shower size measured by Vernov et al.(1970) at sea level. The curves are drawn through the experimental points of Vernov et al. extrapolated asymptotically at both sides to $S = 1.4$ (curve 1) and $S = 1.3$ (curve 2).

decreases. For $N = 10^4$ the difference is a factor of 2.8. Figure 3.20 shows the predicted number spectrum and the results of direct measurements of the number spectrum as given by Hillas (1970b).

The resulting predicted density spectrum is shown in figure 3.21 where it is seen that the result is not sensitive to the asymtotic values of S in the range 1.3 - 1.4 at small and large shower sizes, as shown in figure 3.19.

Taking the derived number spectrum, as given above, and the age parameter dependence (see curve 2 of figure 3.19) the median core distances, the median shower sizes and the minimum shower sizes producing a given electron density were calculated. The results of the calculation are shown in table 3.5.

The experimental data shown in figure 3.20 are the median shower sizes (table 3.5) capable of producing the measured densities. The errors are relatively the same as given in figure 3.21.

3.9 Primary energy spectrum derived from measured density

3.9.1 Relationship between primary energy and shower size

In order to compute the primary energy spectrum from the measured size spectrum one must know the relation between shower size N and primary energy E_p. The problem has been approached in different ways, some of which are now discussed:

(i) The track-length integral

A semi experimental solution of the problem has been given by Greisen (1956), utilizing the altitude variation of the shower counting rates and the concept of track length.
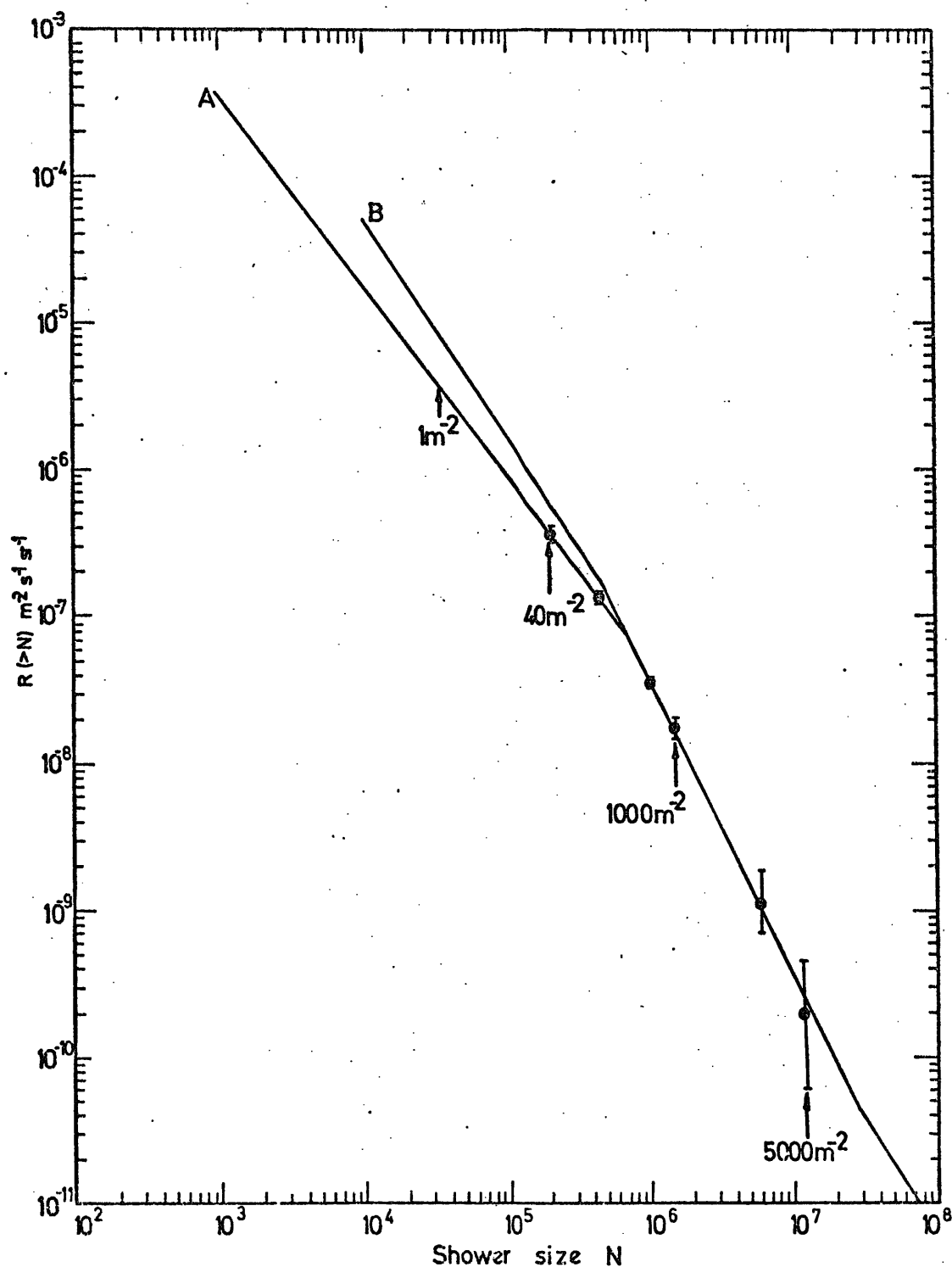
Figure 3.20   Integral number spectrum of EAS at sea level. A = derived from the measured density spectrum, B = summary of Hillas (1970b). ⊕ are the median shower sizes capable of producing the indicated densities.
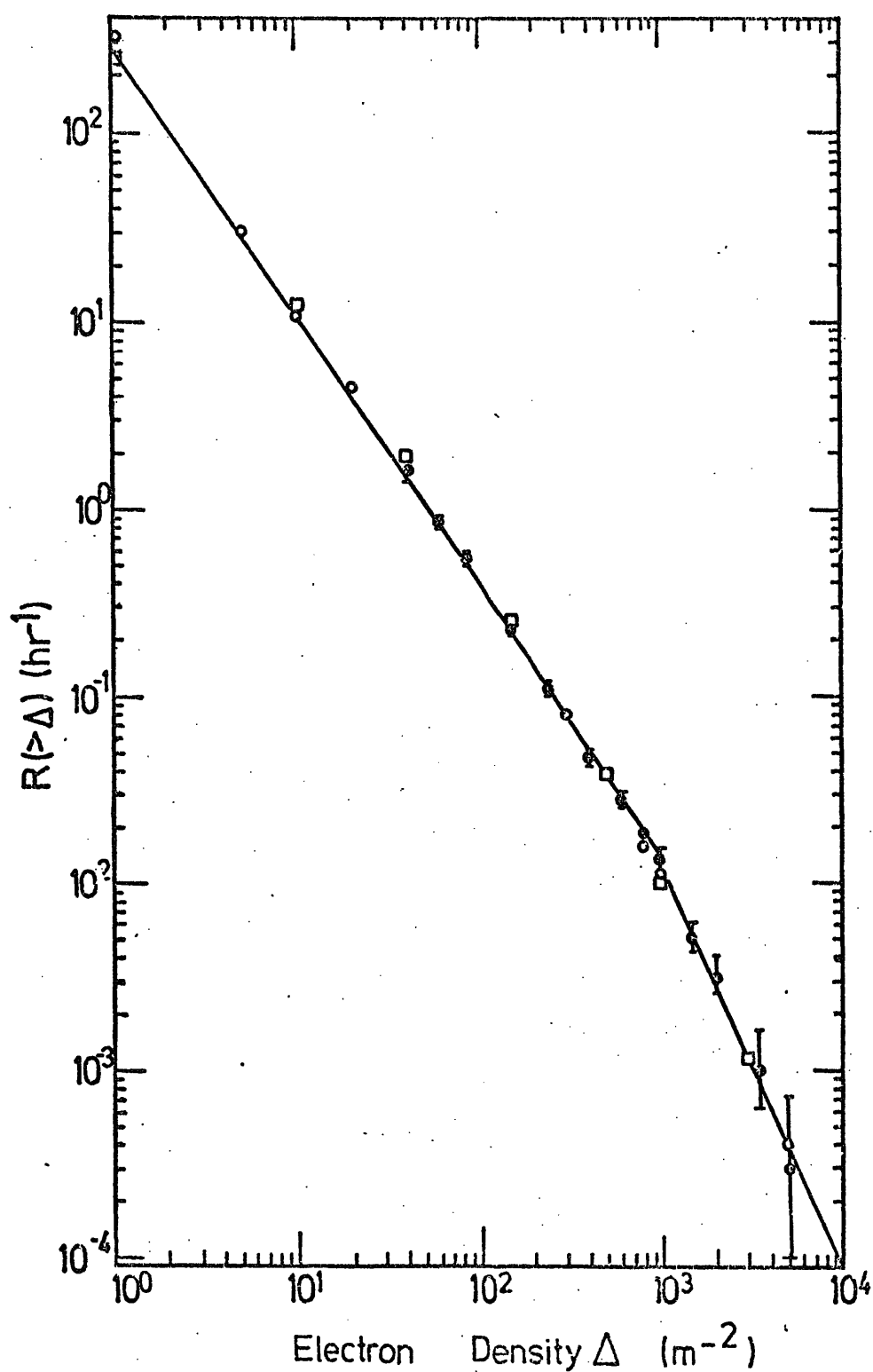
Figure 3.21 · Comparison between the measured integral density spectrum (ϕ) and the predicted spectrum calculated based on an age dependence, obtained by Vernov et al. (1970) extrapolated to age parameter S = 1.3 (o) and S = 1.4 (□). The solid spectrum is the best curve through the predicted points.

Minimum observed density (m^{-2})	Median core distance(m)	Median shower size	Minimum shower size
1	30	$3.5 \cdot 10^4$	$8 \cdot 10^2$
10	15	$1.5 \cdot 10^5$	$1.7 \cdot 10^3$
40	11	$2.1 \cdot 10^5$	$5.5 \cdot 10^3$
300	6	$7 \cdot 10^5$	$3 \cdot 10^4$
1,000	3.5	$1.5 \cdot 10^6$	$8 \cdot 10^4$
3,000	3.5	$4.8 \cdot 10^6$	$2.1 \cdot 10^5$
5,000	5	$1.2 \cdot 10^7$	$4 \cdot 10^5$
10,000	7.8	$4 \cdot 10^7$	$7 \cdot 10^5$

Table 3.5   The median core distances (m) and median
shower sizes producing a given electron density (m^{-2})
calculated for an NKG structure function with age
dependences as shown in figure 3.19 (curve 2) taking
derived number spectrum from measured density spectrum.
The minimum shower sizes calculated for showers falling
at core distances of $\geq$ 0.1 m.

Greisen calculates the track length integral, $E_0 \int N \, dt$, which yields the total energy dissipated in ionization by the charged particles in EAS. (E_0 is the critical energy, t is measured in radiation lengths, and N is the shower size observed at the level of observation; it is assumed that E_0 represents accurately the average energy dissipation per radiation length for all charged particles). The above integral gives 11.5 GeV per electron at sea level, with an uncertainty of the orders of 25%. Adding the energy dissipation due to muons, nuclear excitations and low energy nucleons, neutrinos and evaluating the integral below sea level, Greisen obtains 14 $\pm$ 3 GeV per electron at sea level for $N = 10^5$ and $N = 5.10^5$. The altitude variation was based on measurements of the frequency of showers with density exceeding $\simeq 50 \ m^{-2}$, equivalent to $N = 10^5$. Cocconi (1961) obtains 12 GeV per particle at sea level for $N = 3.5.10^5$.

(ii)   Model Calculation

The relation between E_p and N has been investigated assuming a model for shower development throuth the atmosphere. This has been obtained solving the diffusion equations (Ueda, 1960) or by Monte-Carlo calculations (de Beer et al.1966, Bradt and Rappaport 1967). In model calculations one faces serious problems due to the lack of precise knowledge of the characteristics of high energy interactions as well as the primary mass composition.

Bradt et al.(1965) have measured the integral size spectra of EAS as a function of zenith angle,or effective atmospheric depths at Mt. Chacaltaya ($530 \ g \ cm^{-2}$). Cutting the spectra at constant intensities they produce the longtitudinal development

of EAS as shown in figure 3.22. The smooth curves are drawn by Bradt et al.to fit the data points. La Pointe et al.(1968) have extrapolated the measured longtitudinal development of EAS for higher primary energy and they produce the longtitudinal development of EAS at a constant intensity cut of 10^{-15} cm^{-2} s^{-1} st^{-1}. The data of La Pointe et al.at this intensity are plotted in figure 3.22 and an approximate curve to fit this data is drawn through them. All the smooth curves have been extrapolated down to the depth of 1,030 g cm^{-2} (sea level) and are shown in figure 3.22. The number in the right row of the graph shows the constant intensity cut as given by Bradt et al.and La Pointe et al.in units of cm^{-2} s^{-1} st^{-1}. The values attached to each curve indicate the primary energy in (eV) obtained by means of figures 3.23 and 3.25 as will be described.

Bradt et al, also produced the integral intensity as a function of shower size at the maximum in the longtitudinal development. This is shown in figure 3.23. It can be seen that the maximum of showers at constant rates of 10^{-9} cm^{-2} s^{-1} st^{-1} and 10^{-10} cm^{-2} s^{-1} st^{-1} have an error. This is due to the lack of information on the longtitudinal development at these two rates for atmospheric depths of less than about 450 g cm^{-2}, as it is seen from figure 3.22. The experimental point at a rate of 10^{-15} cm^{-2} s^{-1} st^{-1} in figure 3.23 is taken from the longtitudinal development of EAS, at this rate, as given by La Pointe et al.

Figure 3.24 demonstrates the relationship between shower maximum and the size at sea level. This graph has been produced using figure 3.22 (which gives the intensity of EAS at sea level) and figure 3.23 (which gives the intensity at
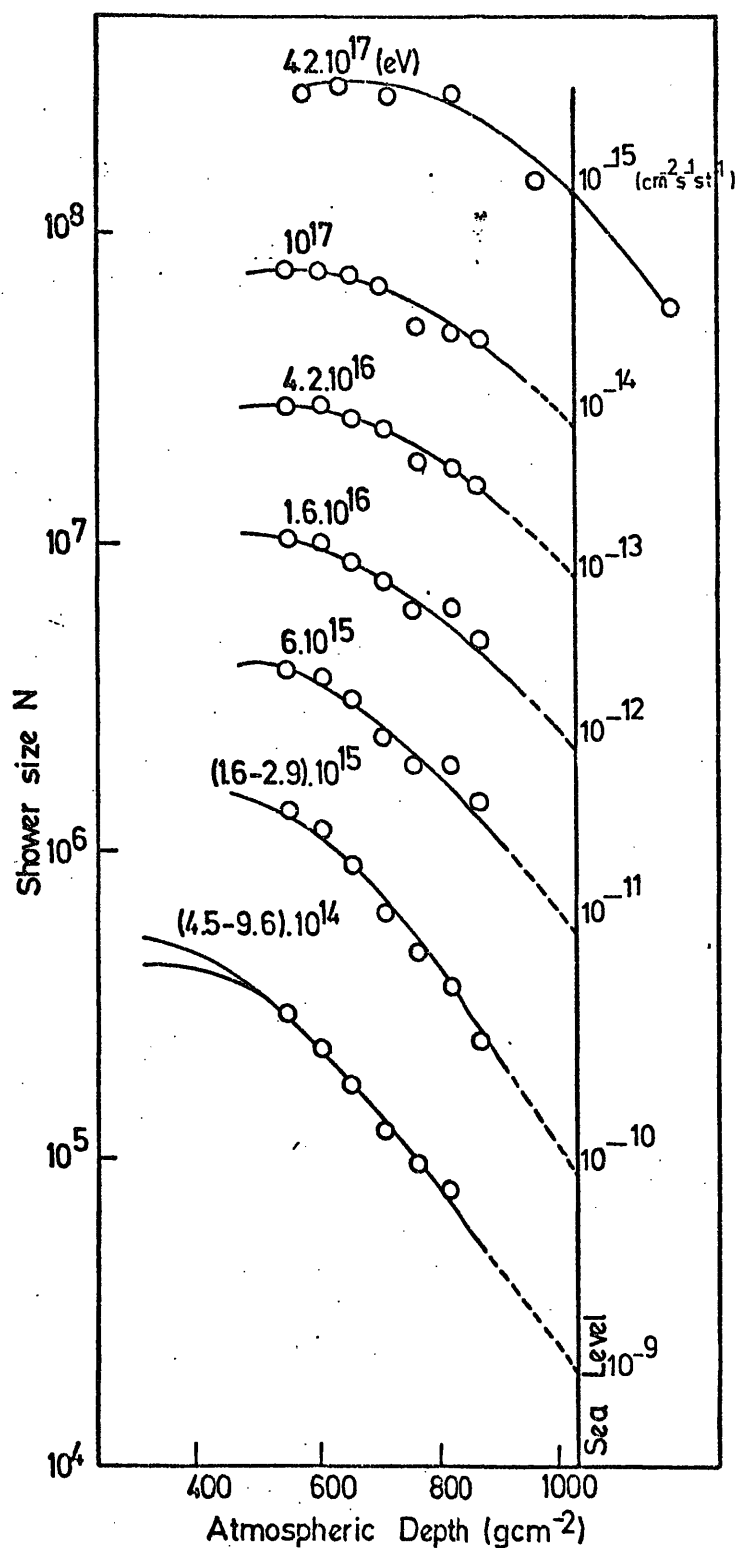
Figure 3.22   Longtitudinal development curves obtained from
constant intensity cuts on the plots of the size
spectra obtained for various zenith angles or
effective atmospheric depths.   The smooth curves
are shown to fit the data points of Bradt et al.
(1965) and are extrapolated to sea level(dashed
curves).   The points on intensity cut of 10^{-15}
$cm^{-2}s^{-1}st^{-1}$ are due to La Pointe et al.(1968)and
a smooth curve is drawn through them. The numbers
in the right of the graph are the constant inten-
sity cuts in units of $cm^{-2}s^{-1}st^{-1}$. The numbers
attached to each curve indicate primary energy.
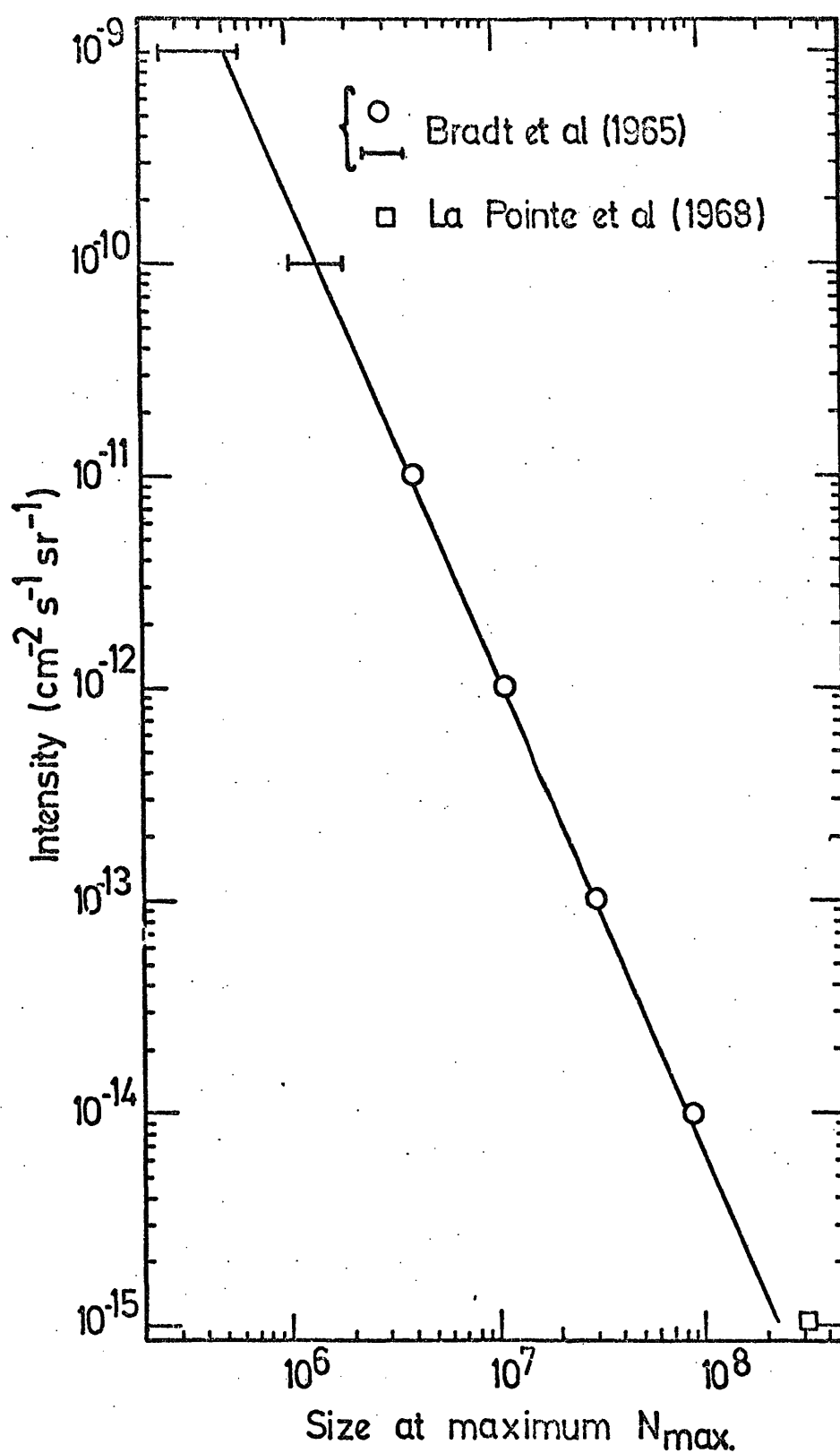
Figure 3.23   Integral intensity as a function of
shower size at the maximum in the
longtitudinal development curves of
figure 3.22.
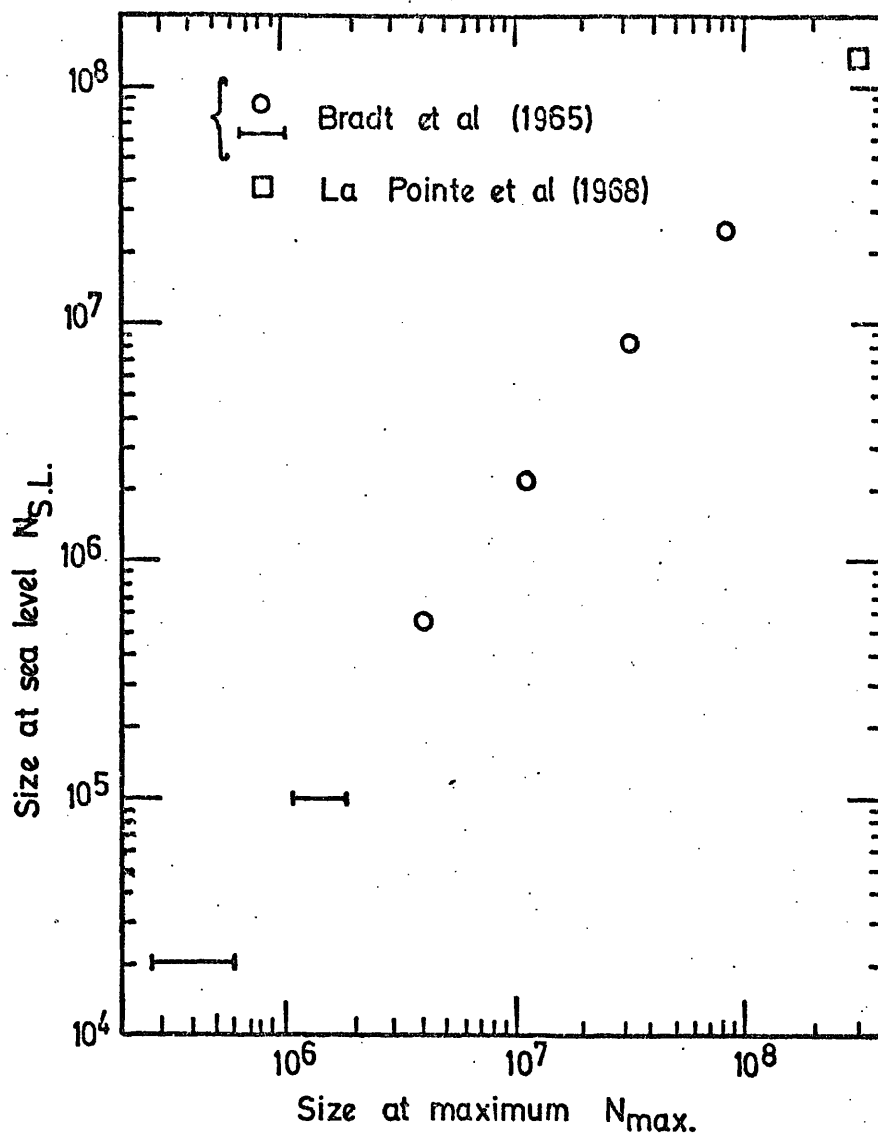
Figure 3.24   Size at maximum - size at sea level
relationship obtained from the meas-
ured EAS development by Bradt et al. and
La Pointe et al.

shower maximum).

The next step is to know the relationship between E_p and N_{max}. La Pointe et al.have calculated the E_p - N_{max} relationship and their results are shown in figure 3.25. Nikolski (Hayakawa, 1969) measuresthe energy flow of different components of EAS at 650 g cm^{-2} depth. He finds that 3.510^5 particles are produced by $(6 \pm ^{1.8}_{1.1}) 10^{14}$ eV primary. Using the shower development of Bradt et al.this size corresponds to 7.510^5 particle at maximum . This is shown in figure 3.25. Given the relation between N_{max} and $N_{S.L}$ (see figure 3.24) and the relation between N_{max} and E_p as given in figure 3.25 the size at sea level as a function of primary energy E_p were derived and the results are shown in figure 3.26. The results of the Monte-Carlo calculation of Bradt and Rappaport (1967) and the semi-experimental results of Greisen (1956) and Cocconi (1961) are given in figure 3.26.

As figure 3.26 shows all the data are not consistant with each other. This is due to the different assumptions for the model of high energy nuclear interaction and also the effect of inherent fluctuations in the shower development.

Kempa et al.(1974) have produced an E_p - N_{SL} relationship. Their results indicate that a discrepancy exists in the E_p - $N_{S.L}$ convertion depending on the procedure by which this convertion is obtained. For example at $E_p = 10^{16}$ eV the ratio of $E_p/N_{S.L}$ varies between 4.8 GeV to 12 GeV. Curve (b) of figure 3.26 is taken from Kempa et al. This is produced by Kempa et al.taking the shower development of Bradt et al.and La Pointe et al.and assuming 2 GeV/particle for E_p/N_{max} ratio. It can be seen that this is approximately
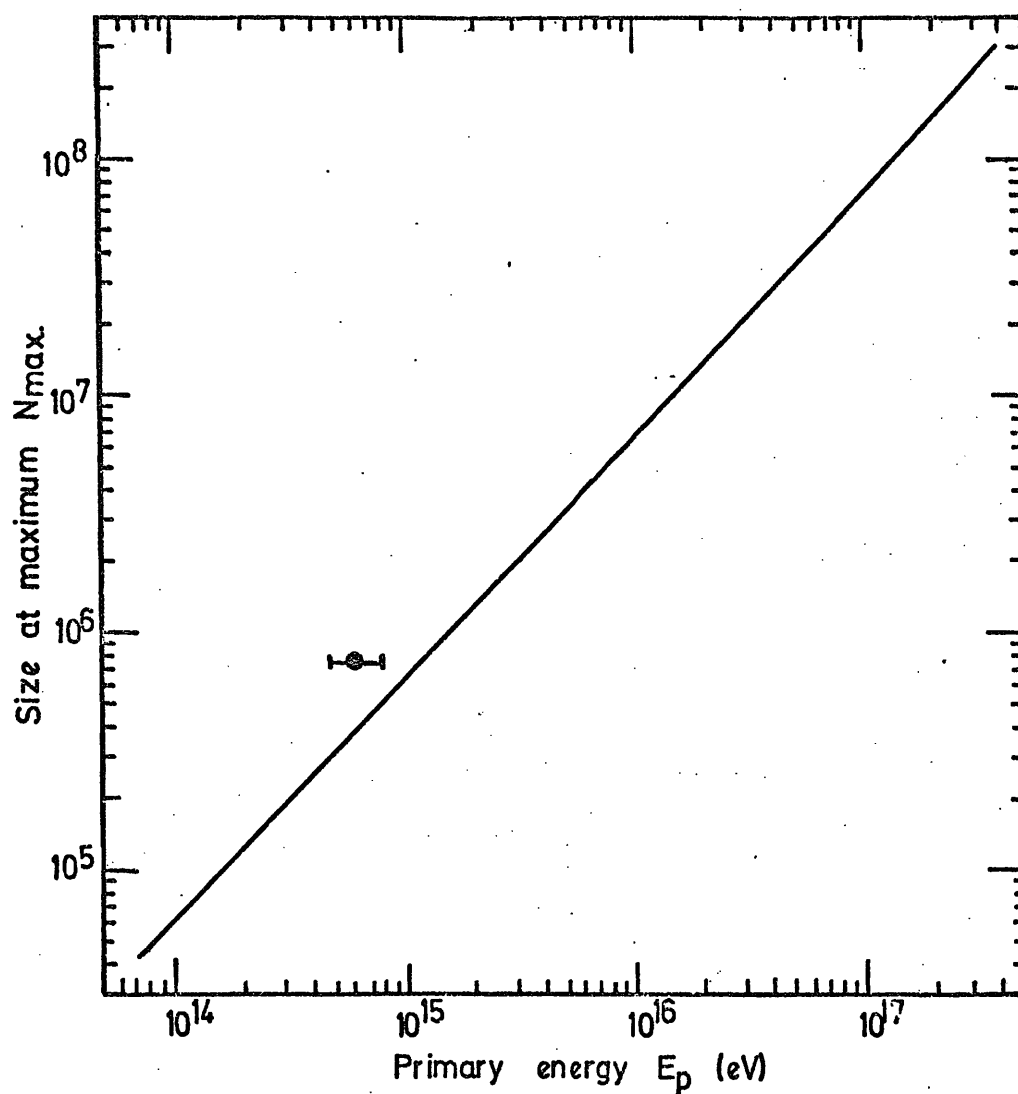
Figure 3.25   Conversion of size at maximum N_{max} to primary energy as given by La Pointe et al. (1968). —●— is derived from Nikolski (1962).
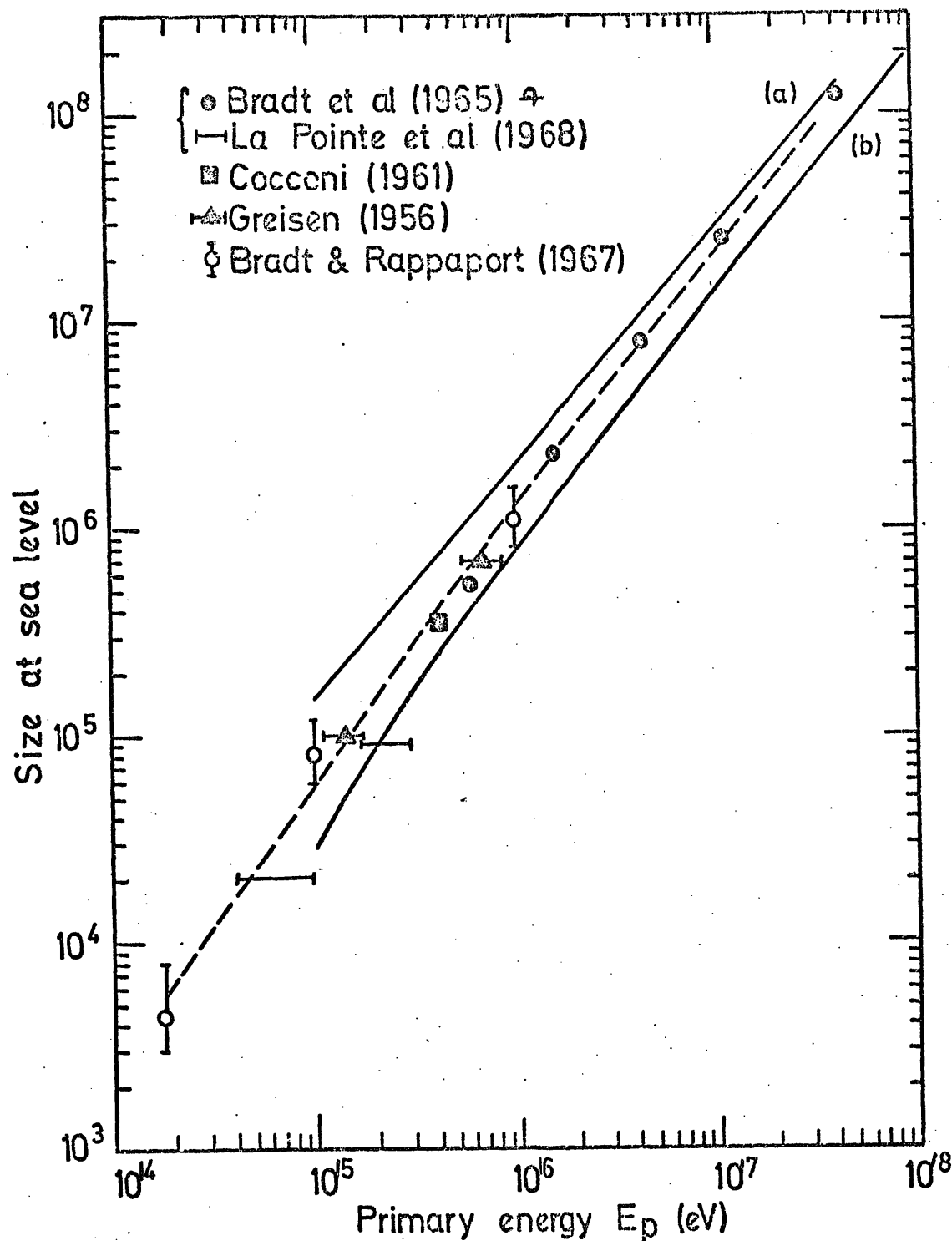
Figure 3.26   Conversion of size at sea level (1030 g cm^{-2})
to primary energy.   The data of Bradt et al.
(1965) and La Pointe et al. (1968) are taken
from the longtitudinal development of EAS as
given by figures 3.22 and 3.23 and using the
primary energy, size at maximum relationship as
given by La Pointe et al. in figure 3.25
The data of Cocconi and Greisen have been obtained
from measurements of the energy flow of different
components of EAS at sea level.   Bradt and
Rappaport (1967) have obtained their results by
Monte-Carlo calculation.   Solid curves designated
(a) and (b) are given by Kempa et al. (1974).
The dashed curve is drawn through the data by eye.

parallel to the dashed curve drawn through the data of
figure 3.26. The difference in absolute ratio of E_p/N_{max}
is because La Pointe et al.have assumed 1.7 GeV/particle at
shower maximum. Curve (a) of figure 3.26 is due to Kempa et
al. This is based on a model calculation with an $E^{1/4}$
multiplicity law.

3.9.2 Results

Taking the derived number spectrum from the measured
density spectrum as given in figure 3.20 and the E_p - $N_{S.L}$
relationship as given by the dashed curve in figure 3.26,
the integral primary energy of cosmic rays has been calculated
and is shown in figure 3.27. Assuming the E_p - $N_{S.L}$ relation
as given by curves (a) and (b) of the figure 3.26, the primary
energy was derived. This is shown in figure 3.27 and gives
upper and lower limits to the derived energy spectrum.

Table 3.5 shows the median shower sizes that produce
local electron densities of $\Delta > 1 \text{ m}^{-2}$ and $\Delta > 5,000 \text{ m}^{-2}$.
These median sizes were converted to primary energies using
figure 3.26. These are taken as the lower and upper limits
of the energy in energy spectrum of cosmic rays as shown in
figure 3.27. The primary energy spectrum plotted in figure
3.28 is the same as the one which is plotted in figure 3.27.
The ordinate of the graph shows $R(> E)$ E   in units of
eV cm^{-2} s^{-1} st^{-1} and is compared with the survey of Kempa et
al.(1974).

3.10 Conclusion

The density spectrum of EAS at sea level was measured
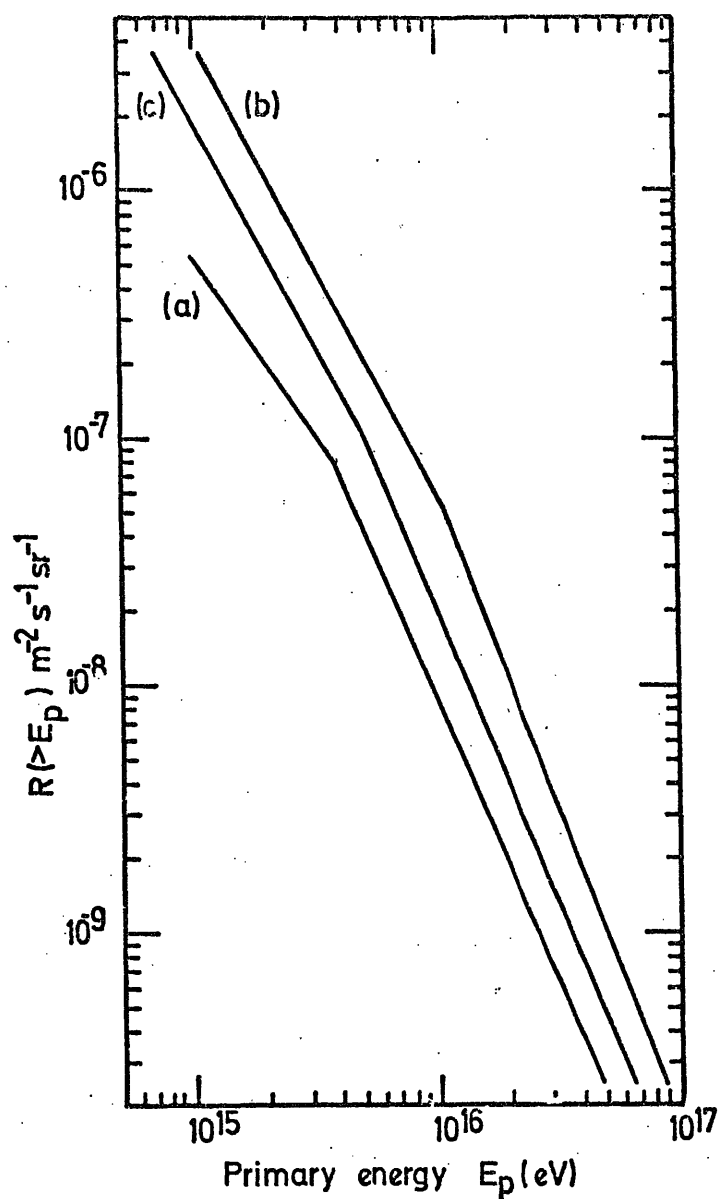
Figure 3.27   Integral primary energy spectrum derived from the measured density spectrum. Solid spectrum (c) is derived using the dashed curve of figure 3.26 and the spectra designated (a) and (b) are derived using curves (a) and (b) of figure 3.26 respectively.

Figure 3.28   Integral energy spectrum
of cosmic rays in the range
$10^{10} - 10^{20}$ eV. ●●=The derived
spectrum from the measured
density spectrum.   The big
box showing the limits of the
derived spectrum and the rest
of the points and lines are
the same as given in figure
2.8.
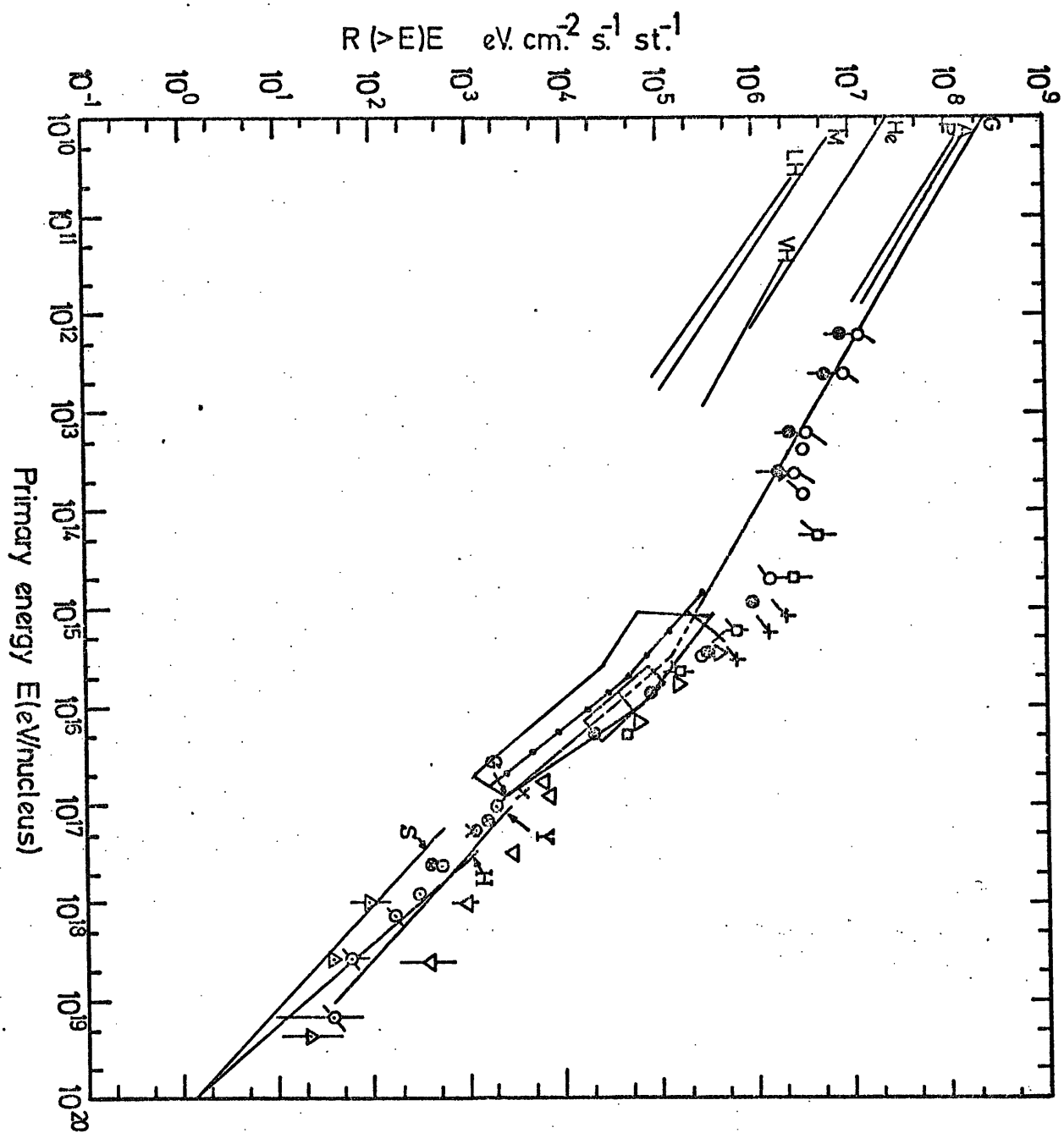
using a single proportional counter, using three liquid
scintillation counters as an EAS trigger. The results of
the measured spectrum can be described by

$$R(> \Delta) = 411 \ \Delta^{-1.5} \qquad hr^{-1} \qquad 40 < \Delta \lesssim 800 \, m^{-2}$$

$$R(> \Delta) = 1.3 \cdot 10^{4} \ \Delta^{-2.0} \ hr^{-1} \quad 1{,}000 < \Delta < 5{,}000 \, m^{-2}$$

This result shows that the slope of the density spectrum
changes from -1.5 to -2.0 at $\Delta \simeq 1{,}000 \, m^{-2}$. Taking the
measured size spectrum, by direct methods, as given by Hillas
(1970b) and assuming three forms of the lateral structure
functions, as given by Greisen (1960), Kiel group (Hillas,
1970a) and Sydney group (Hillas, 1970a), the predicted density
spectrum was calculated. Since the situation of the number
spectrum at sea level for $N \gtrsim 10^{7}$ is not clear two cases
(a) and (b) were assumed for the size spectrum. The analytical
expressions for cases (a) and (b) of the number spectrum are
as follows:

Case (a)

$$R(> N) = 52.0 \qquad N^{-1.5} \qquad m^{-2} \, s^{-1} \, st^{-1} \qquad N < 5 \cdot 10^{5}$$

$$R(> N) = 36{,}920.0 \ N^{-2.0} \qquad m^{-2} \, s^{-1} \, st^{-1} \ 5 \cdot 10^{5} < N < 3 \cdot 10^{7}$$

$$R(> N) = 6.76 \qquad N^{-1.5} \qquad m^{-2} \, s^{-1} \, st^{-1} \qquad N > 3 \cdot 10^{7}$$

and Case (b)

$$R(> N) = 52.0 \qquad N^{-1.5} \qquad m^{-2} \, s^{-1} \, st^{-1} \qquad N < 5 \cdot 10^{5}$$

$$R(> N) = 36{,}920.0 \ N^{-2.0} \qquad m^{-2} \, s^{-1} \, st^{-1} \qquad N > 5 \cdot 10^{5}$$

Thus 6 different forms of the density spectra were calcul-

ated. It was concluded that none of these 6 predicted spectra could fit the measured density spectrum. This result showed that a change in the shape of the lateral structure function with shower size would seem to be required. Taking the age dependence of the structure function as given by Vernov et al.(1970) and extrapolating the measured age parameter to S = 1.3 and S = 1.4 at small and large shower sizes the best number spectrum was derived. The derived number spectrum from the measured density spectrum can be expressed by

$$R(> N) = 3.0 \quad N^{-1.3} \quad m^{-2} \, s^{-1} \, st^{-1} \quad \text{for} \quad N \lesssim 7.10^5$$

$$R(> N) = 36{,}920.0 \, N^{-2.0} \quad m^{-2} \, s^{-1} \, st^{-1} \quad \text{for} \quad 7.10^5 \lesssim N < 3.10^7$$

$$R(> N) = 6.76 \quad N^{-1.5} \quad m^{-2} \, s^{-1} \, st^{-1} \quad \text{for} \quad N > 3.10^7$$

Taking this number spectrum and assuming the NKG formula as the structure function of electrons with age parameter varying as given by Vernov et al. the density spectrum was calculated. This spectrum fits the measured spectrum in the density range $\Delta = 1 - 5{,}000 \, m^{-2}$.

The derived number spectrum was converted to the primary energy spectrum using an $E_p - N_{S.L}$ relationship. It is noticed that the absolute rate, slope and the position of the kink in the primary spectrum depends on the assumed relationship between E_p and $N_{S.L}$. This is partly due to the inherent fluctuation in the EAS development and partly due to the lack of precise knowledge of the parameters of nuclear interaction.

The primary spectrum, however, indicates a change of slope in the energy range $(4 - 10) \, 10^{15}$ eV. The slope

changes from $\simeq -1.7$ for $E_p \lesssim 4.10^{15}$ to $\simeq -2.3$ in the energy range of $10^{16} - 10^{17}$ eV.

CHAPTER 4.

THE MUON COMPONENT CLOSE TO THE CORE OF EAS

4.1 Introduction

The amount of information about the primary particles and the properties of high energy collisions carried by the muon component is much higher than the electronic component. The lateral density of muons and thus the total number of muons of energy $\geq E_\mu$ are amongst the parameters which have been measured quite often. A comparison between the measured and predicted lateral density of muons shows that the former is narrower than the latter assuming standard models (CKP) for high energy collisions. The widening of the distributions could be due to an increase in the transverse momentum of produced pions, P_t, or an increase in the height of production. The interesting fact is that the width of the muon lateral distribution depends on the mean value of P_t of pions produced in the last interaction and the height of the muon origin on the multiplicity in the very first interactions in a shower. Thus the study of low energy muons, coming from pions produced in interactions with energy of $\simeq 10^{12}$ eV for which the transverse momentum is known, makes it possible to gain information about the multiplicity law of high energy interactions.

In the present work the density spectrum of low energy muons has been measured using a flash tube chamber. These measurements give information about the lateral distribution of muons and the flux of muons in EAS.

4.2   Properties of the flash tube chamber

4.2.1   The sensitive time of flash-tubes

When a charged particle passes through the gas of a flash
tube it ionizes the gas.   Thus if a high voltage is applied to
the tube after an appropriate time delay t_D any electron remain-
ing in the tube may initiate a discharge.   The probability that
the tube flashes is obviously, a function of the time delay and
is called the efficiency - time delay (η - t_D) relationship.

The relationship between η and t_D has been treated theoret-
ically by Lloyd (1960).   Lloyd found it convenient to plot η
as a function of t_D for a parameter, a f_Q, where a is the internal
tube radius in cm, f is the probability of one electron initiat-
ing the discharge and Q is the number of ion pairs per centimetre
produced initially in the tube.   The values of a and f are deter-
mined purely by the dimensions and the gas filling of the tubes.

Incoherent cosmic ray muons were selected by the single
particle selection system (see figure 3.12) to measure the η - t_D
relationship.   The measurement was carried out for different
values of t_D.   In each trigger the passage of a muon through the
flash tube chamber was photographed and thus a series of events
were obtained for each value of t_D.   In each event the total
number of flashes in F2 and F3 were counted, projecting the
negative films onto a scanning table, for acceptable events.
An acceptable event was an event in which not only the track of
a single particle must traverse the whole of F2 and F3, but must
also appear in F1 and F4.   The second condition was applied,
since Ashton et al. (1971) have shown that a tube may flash with
lower η if it traverses the region of fringing field down the
front of back edges of the electrodes in F2 and F3.

The measured number of flashed tubes on a track divided by the total number of layers in F2 and F3, i.e. divided by 96, gives the layer efficiency η_L . The internal efficiency η_I is defined as the ratio of the separation of neighbouring flash tube axes to the flash tube internal diameter multiplied by η_L

$$\eta_I = \frac{1.81}{1.58}\eta_L = 1.145\eta_L$$

The dependence of η_I on t_D was measured by Saleh (1973) for the chamber and is shown in figure 4.1. He found that a value of afQ = 9 $\pm$ 1 is the best fit to the experimental points. Thus afQ = 1.0 $\pm$ 0.1 is the best value for quarks of charge $e/3$ assuming the Lorentz factor of quarks and single particles are the same (see Ashton et al., 1971 for the variation of η_L against the momentum of ionizing particles).

4.2.2   Response of the chamber to single particles

Since one of the aims of the present work is to search for quarks (see chapter 8) it is necessary to choose a time delay for which the passage of a quark with charge $e/3$ through the chamber could be recognisable. The optimum t_D was found to be 20μs which makes it possible to distinguish the track of a charge $e/3$ particle from that of a charge e particle. This gives an acceptable efficiency for quark tracks and enables them to be distinguished from random alignments of spurious flashes in the chamber.

To obtain detailed information about the efficiency, η , of the flash tubes, for charge e particles a time delay of t_D = 20 μS was selected and for each event the total number of flashed tubes in F2 + F3 for acceptable events (an acceptable event has the same criteria as described in section 4.2.1) were counted.
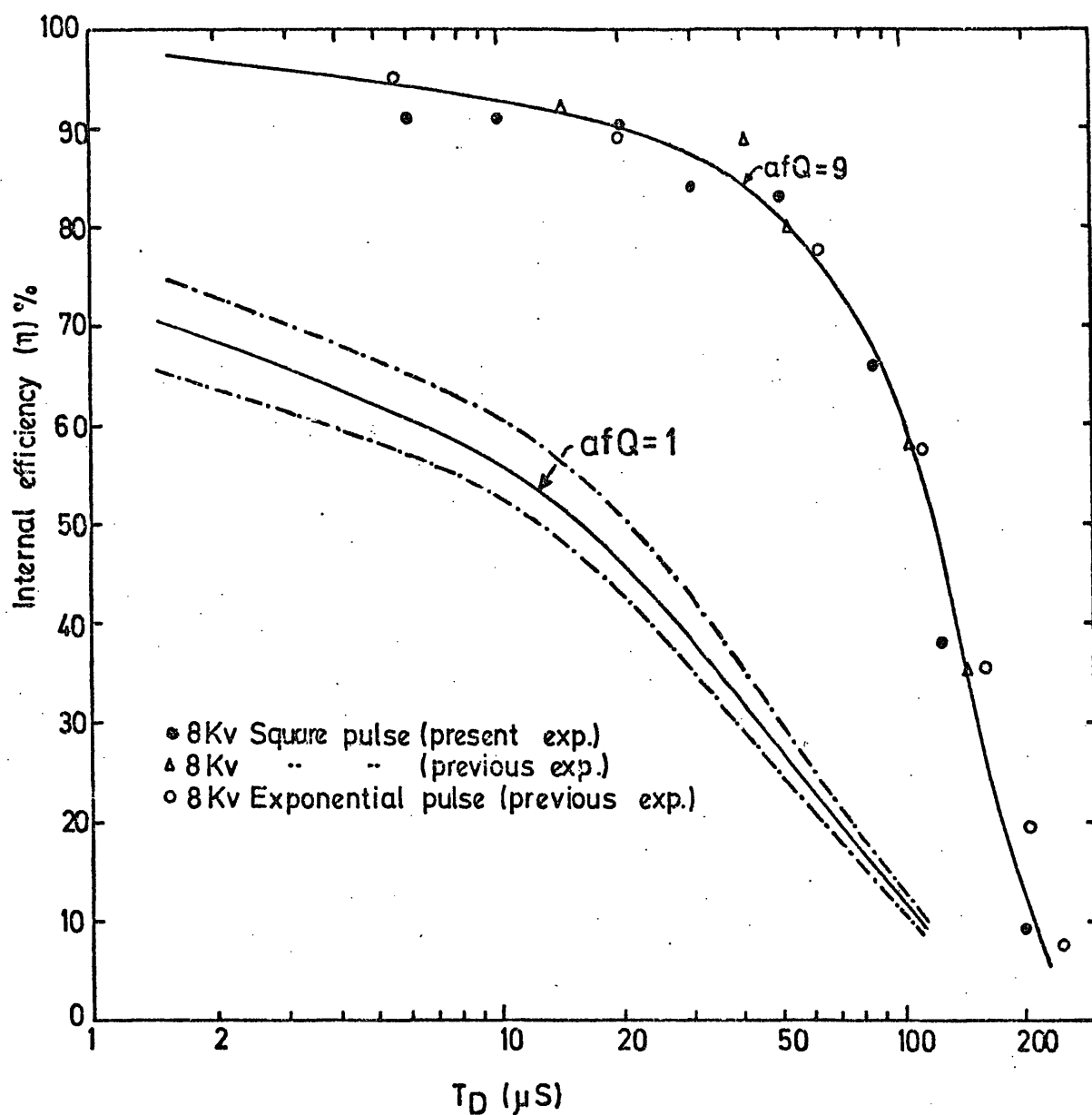
Figure 4.1 The variation of the internal efficiency of the flash tubes as a function of time delay, T_D. The points refer to experimental measurements. The full curve is the theoretical prediction with $af_1Q_1=9$, and corresponds to the best fit to the experimental points. Also shown is the $af_1Q_1=1$, which corresponds to a particle of charge $e/3$. The curves —·— indicate the latitude of uncertainty.

The results of measurements for 1,046 triggers is shown in figure 4.2. The mean number of flashed tubes is found to be 74.77 $\pm$ 0.14 with standard deviation σ = 4.6. The 20 μS time delay was used for all EAS runs in the present work.

4.3 The measured muon density spectra in EAS

4.3.1 Introduction

With the local electron density trigger determined by the EAS selection system (see figure 3.12) the density spectra of muons in the E and F series were measured. The analysis procedure consisted of projecting the negative of the film onto a scanning sheet. This gives a reduced image of real space in the ratio 1 : 20.

In each event the number of acceptable muon tracks were counted to obtain the frequency distribution of muons having a particular density as it is observed in the chamber.

An acceptable event was one which satisfied the following criteria (i) The muons pass through an arbitary level defined to be the middle of F2.

(ii) The muons are parallel to each other to within $\pm$ 5° in the projected plane.

(iii) The muons have a track length of $\geq$ 60 cm in real space.

The above criteria confirm that the measured particles are muons and thus exclude any bias produced by interactions in the scheilding when electronic detectors (eg. scintillators) are used to measure muon densities. Events in which the whole or a part of the chamber (in the middle of F2 and 60 cm on either side of it) are obscured by bursts, such that it makes measurement
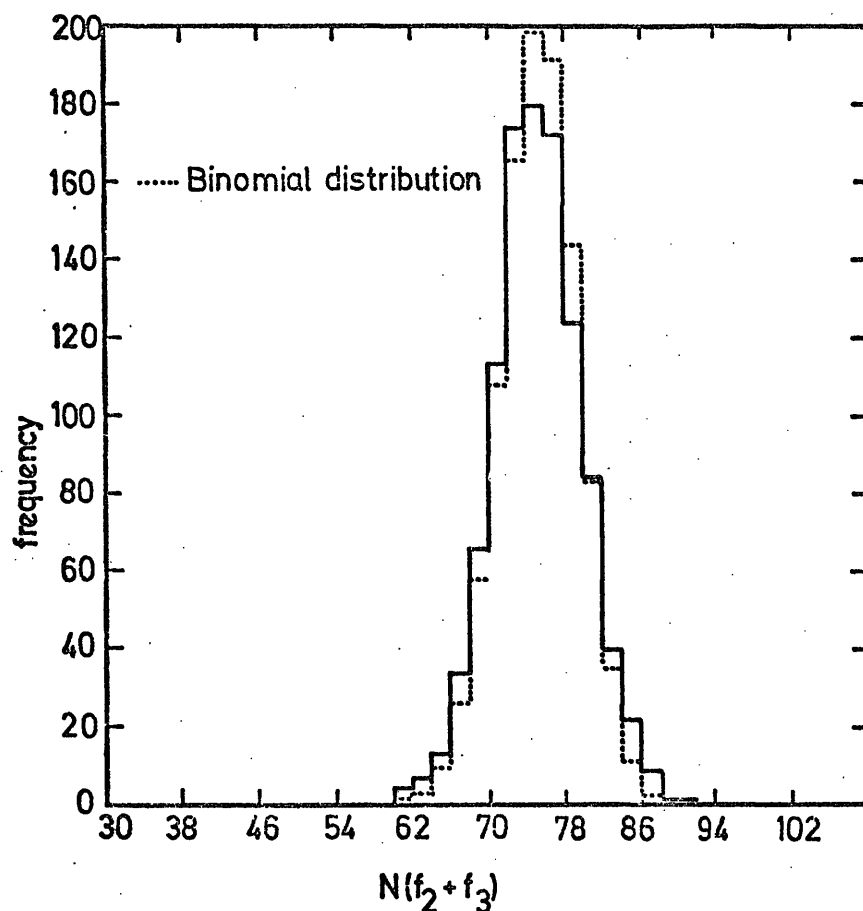
Figure 4.2   The single particle calibration
distribution. The distribution of
the numbers of flashes ($N(f_2+f_3)$).
along a track for 1,046 events for
which the time delay T_D was 20 μs.
The dashed histogram refers to the
expected binomial distribution.
The mean value of $N(f_2+f_3)$ obtained
was 74.77 ± .14. Maximum value of
$N(f_2+f_3)$ = 96.

impossible or inaccurate, have been rejected in the analysis

of the data. Figure 4.3 shows a scale diagram of the front

view of the chamber and gives an example of a typical event,

with four muons having traversed the middle of F2.

According to the criteria mentioned above the acceptable

muons have an energy threshold of 0.2 GeV. This is calculated

using the range - energy relationship as given by Serre (1967).

4.3.2 Results

A total number of 7137 triggers in the E series (films E23 -

E69) and 4,516 triggers in F series (films F1 - F40) were analysed.

The basic experimental data are shown in table 4.1. It can be

seen that the efficiency of detecting muons (defined as the

ratio of the number of measurable events to the total number of

triggers) is 82% and 59% for the E series and the F series resp-

ectively.

The deviation of the efficiency from unity is mainly due

to the reasons mentioned earlier (see section 4.3.1). The

limitation of the experimental apparatus, however reduces the

efficiency since events with $N_\mu \gtrsim 35$ muons crossing the flash

tube area (2.95 m^2) have been rejected in the analysis. This

effect is not significant since the density spectrum of muons

falls off very rapidly.

Since the electron density of the F series is higher than

the E series the median core distance of the former is less than

the latter and therefore the relative number of hadrons in the

F series is more than in the E series (see chapter 6). This

results in a decrease in the efficiency from 82% in the E series

to 59% in the F series.

LEAD

F1a

IRON

F1b

F2   A   B

F3

F4a

F4b
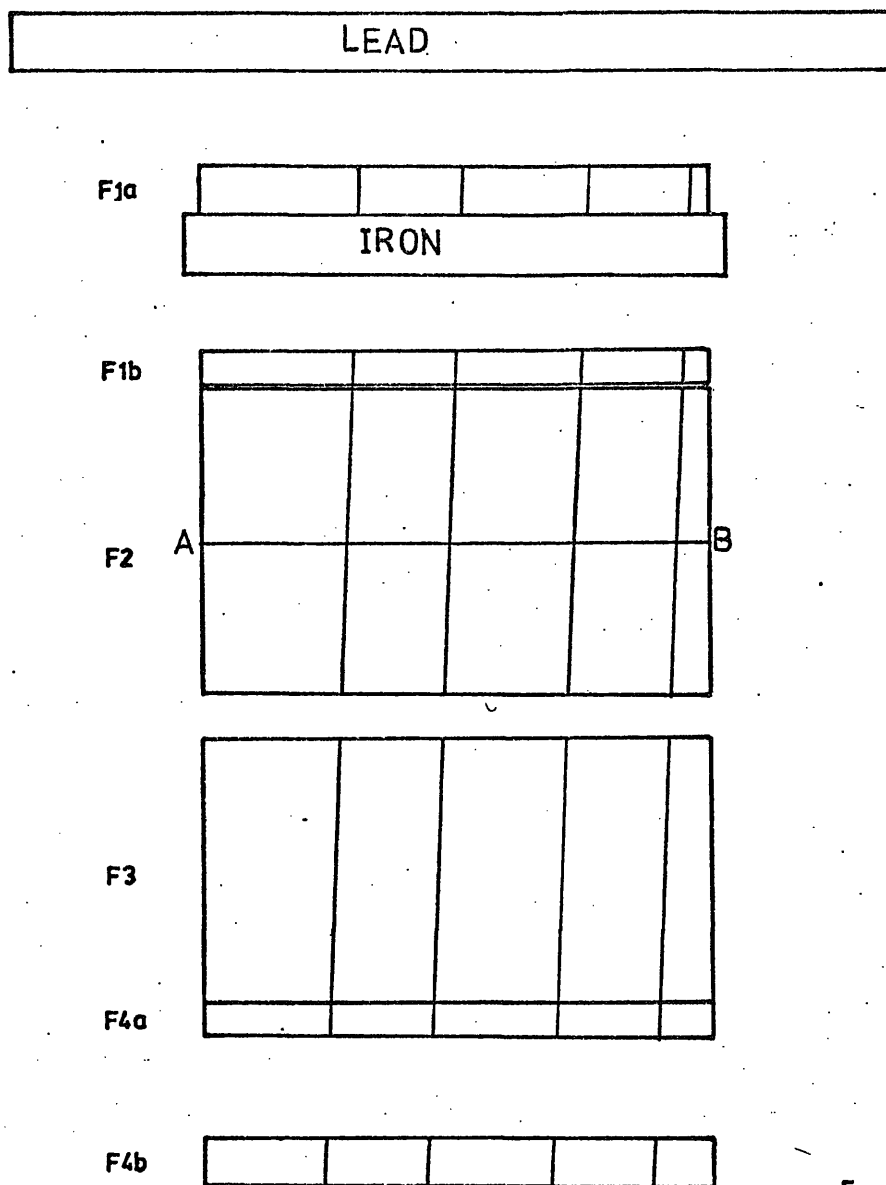
20cm.
20cm.

Figure 4.3   Scale diagram of the front
view of the chamber showing
the passage of muons through
the middle of F2 (line AB).

Film series	Total number of triggers	Total running time (hrs)	Rate (hr^{-1})	Total number of measure-able events	Events with no muons	Events with one muon	Events with >1 muon
E	7,137	1,347.5	5.3	5,857	1,442	1,500	4,415
F	4,516	5,419.6	0.82	2,680	322	376	2,358

Table 4.1   Basic experimental data obtained in muon density spectra.

The measured frequency distribution of muon density obtained in the E series and the F series are shown in figures 4.4 and 4.5 respectively.

The front view of the flash tube chamber and some examples of the events observed in the analysis of the muon density spectra are shown in plates 4.1 to 4.3.

4.3.3 The effect of background muons

A possibility which could affect the measured frequency distribution of the muons in EAS is the incoherent muon component of cosmic rays. The integral rate of muons of $E \geq 0.2$ GeV is $8.3.10^{-3}$ $cm^{-2}s^{-1}st^{-1}$ according to Hayman and Wolfendale (1962). The aperture of the chamber for acceptable events $\Omega = \frac{A1 \ A2}{d^2}$ where $A1 = A2 = 2.95$ m^2 and $d = 120$ cm, thus $\Omega = 6.1.10^4$ cm^2 st. Therefore the rate of single muons through the chamber is 506 s^{-1}.

Simple calculations show that the total number of single muons incident on the chamber in the $20\mu s$ period before the application of the high voltage to the electrodes is 62 and 28 for the E series and the F series respectively. Thus the effect of the incoherent muons in the measured distribution is negligible. In particular one should note that muons in EAS are parallel to each other.

The effect of the hadronic component of EAS and single particles are also insignificant in simulating the measured spectra. Since on the one hand the rate of this component compared with the muon component is very small and on the other hand there is a large probability that these particles interact in the lead and iron absorbers of the chamber.

<u>PLATE 4.1</u>

Front view of the flash
tube chamber

PLATE 4.2   Event E.66 - 35

An event showing three muons
having traversed the flash
tube chamber
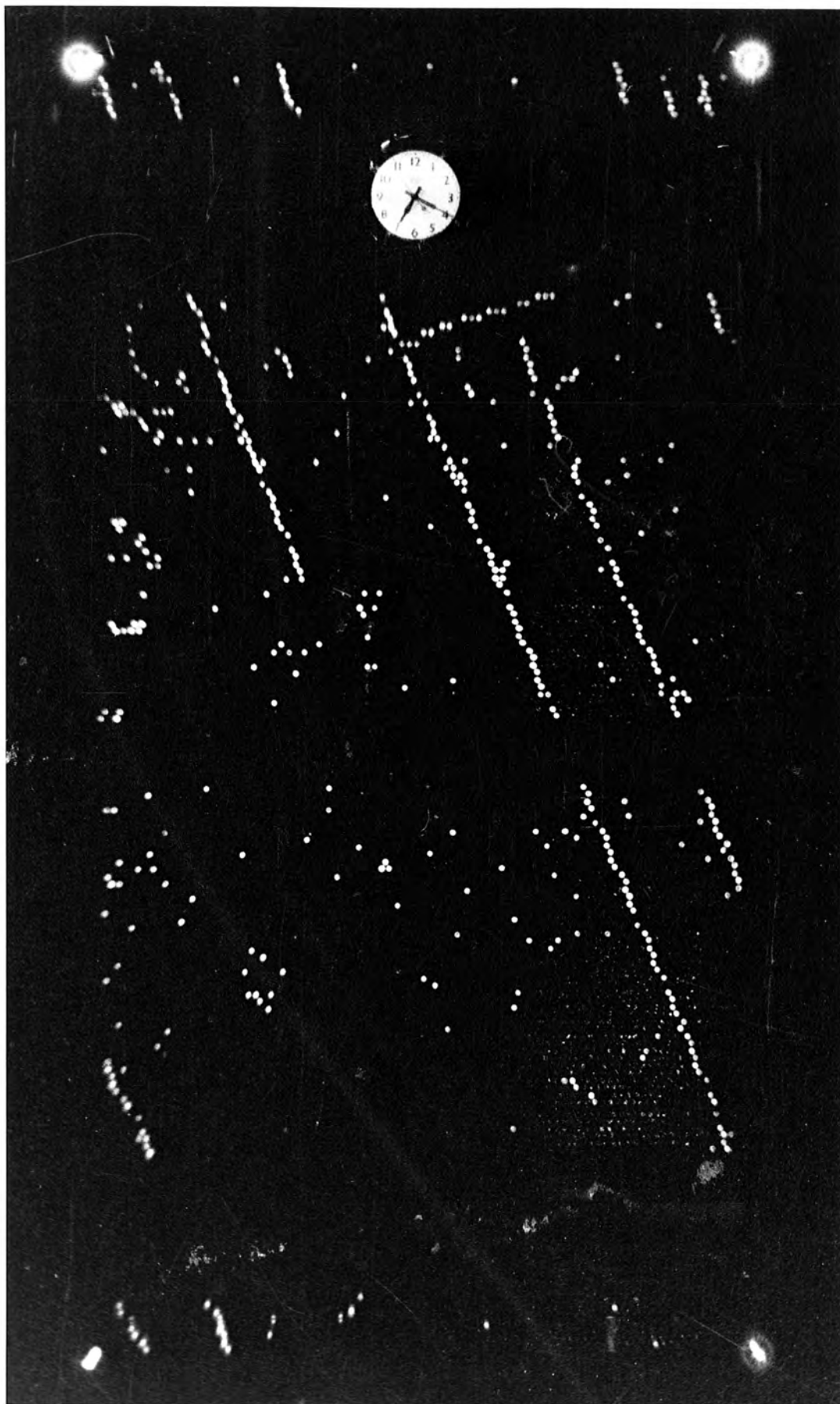
PLATE 4.3   Event E67 - 42

An event showing seventeen muons

having traversed the flash

tube chamber
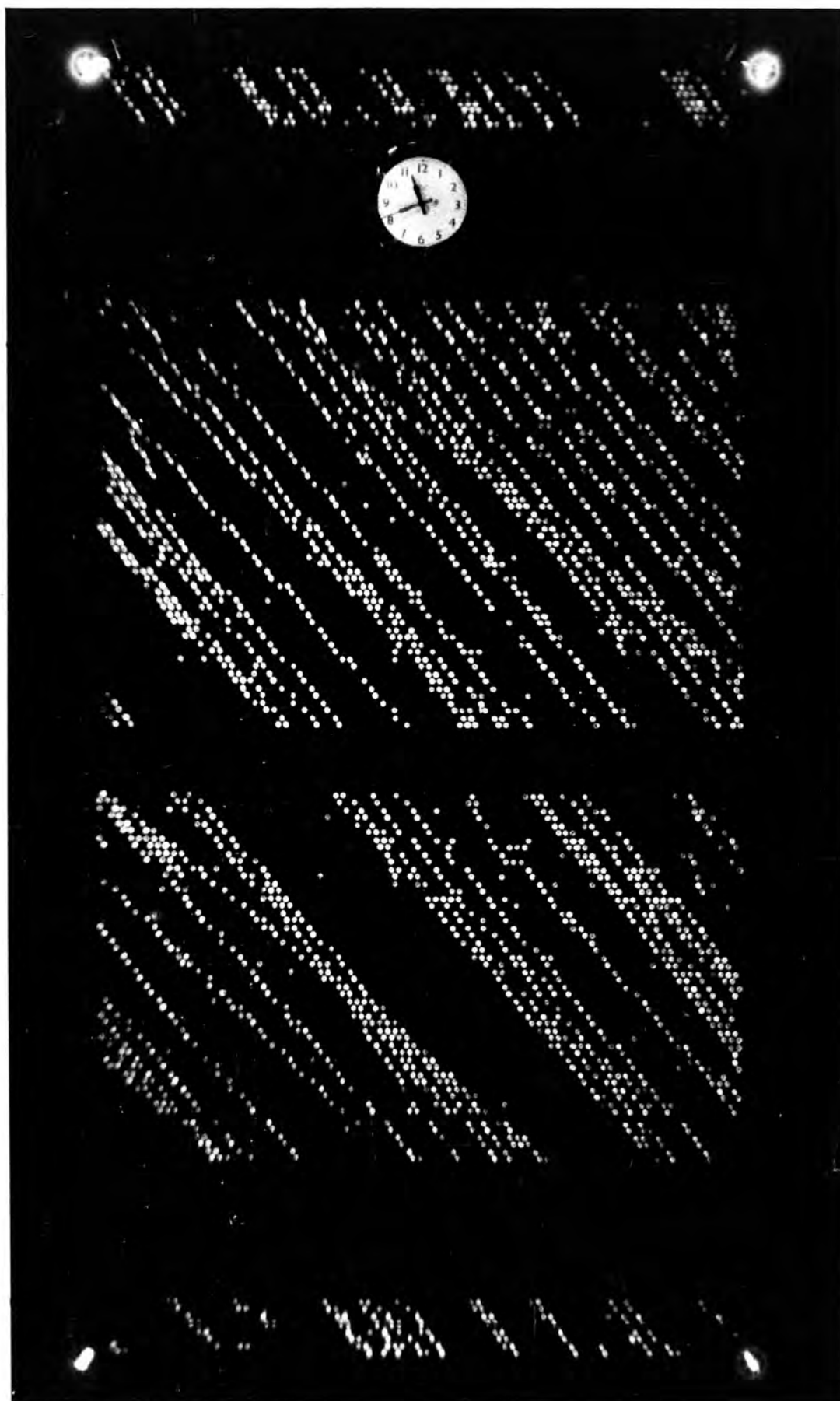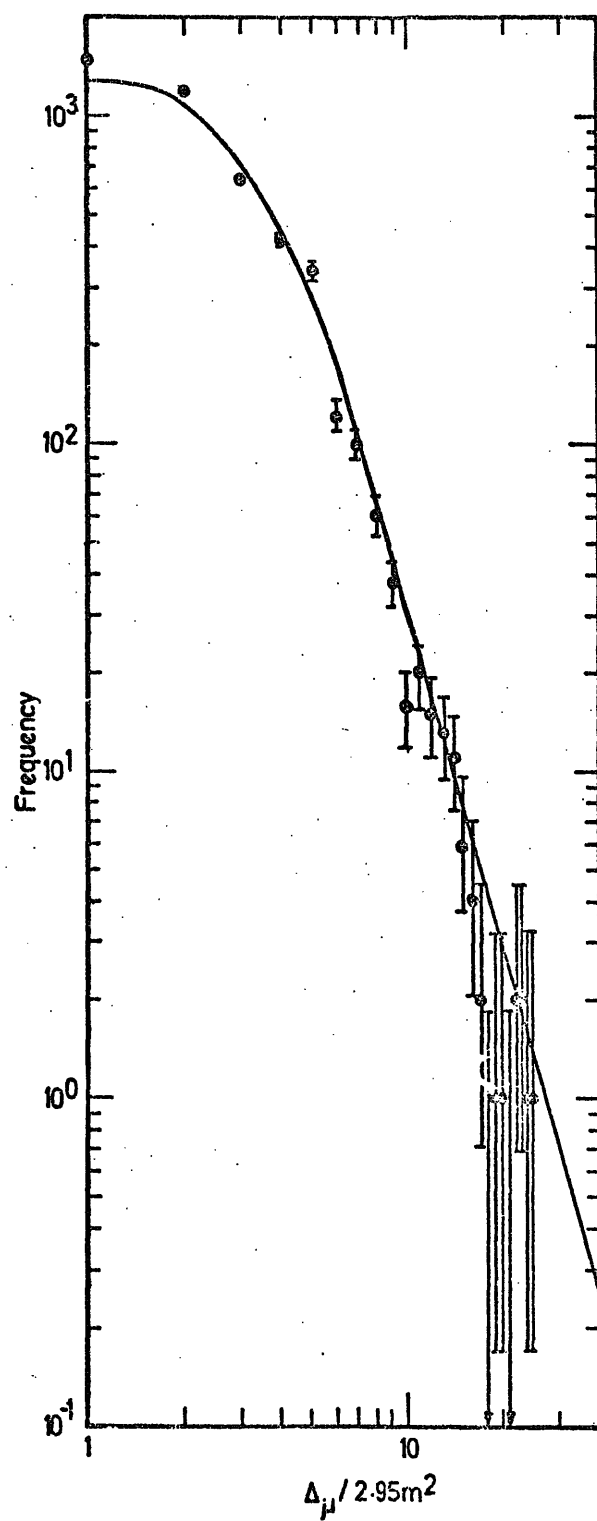
Figure 4.4   The differential density spectrum of muons measured in the E series. The solid curve is calculated for $\Delta_e \gtrsim 20$ m^{-2}.
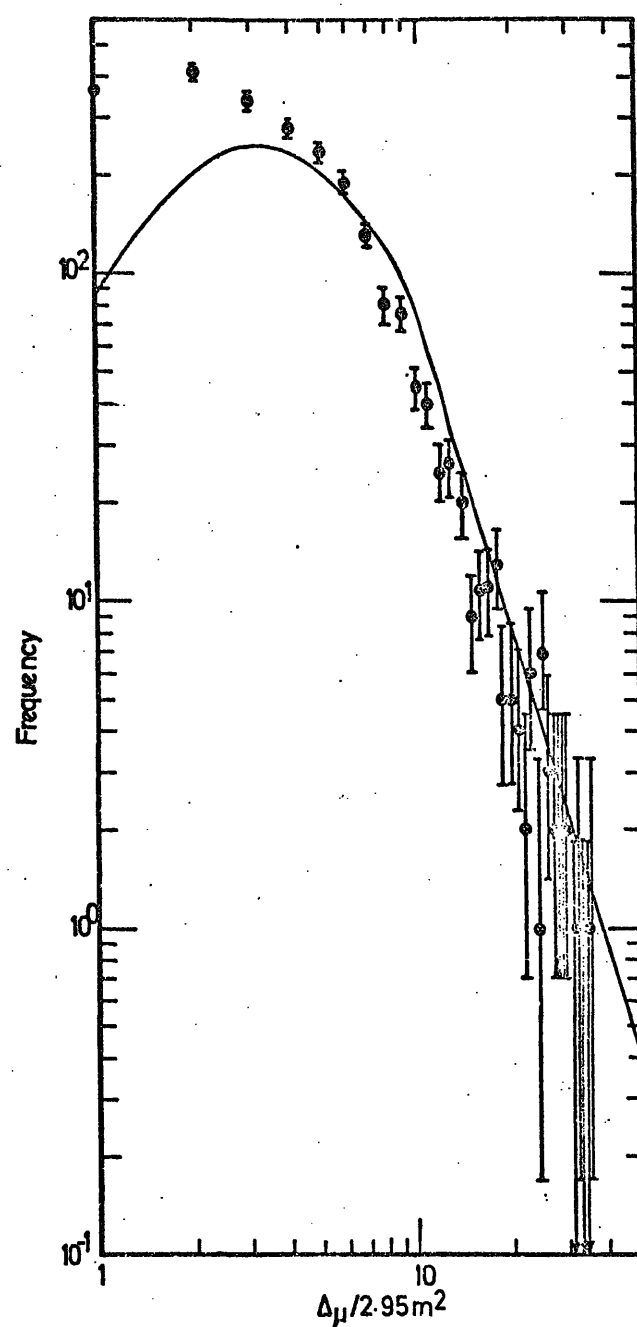
Figure 4.5   The differential density spectrum
of muons measured in the F series.
The solid curve is calculated for
$\Delta_e \geq 80 \ m^{-2}$.

4.4 Prediction of muon density spectra in EAS selected by a local electron density trigger

The calculations were carried out numerically. The sea level number spectrum used is the same as was derived from measuring the density spectrum of EAS (see chapter 3), i.e. of the form

$$R(>N) = 3.0 \quad N^{-1.3} \quad m^{-2}s^{-1}st^{-1} \quad \text{for} \quad N \leq 7.10^5$$

$$R(>N) = 3,6920.0 \quad N^{-2.0} \quad m^{-2}s^{-1}st^{-1} \quad \text{for} \quad 7.10^5 < N \leq 3.10^7$$

$$R(>N) = 6.76 \quad N^{-1.5} \quad m^{-2}s^{-1}st^{-1} \quad \text{for} \quad N > 3.10^7$$

The lateral distribution functions for electrons and muons at sea level that were used were those of Greisen (1960). Namely, for electrons:

$$\Delta_e(N,r) = \frac{0.4N}{r_1^2} \left(\frac{r}{r_1}\right)^{0.75} \left(\frac{r_1}{r+r_1}\right)^{3.25} \left(1 + \frac{r}{11.4 \ r_1}\right) \ m^{-2}$$

where r_1 is the cascade unit in air (= 79 metres), and for muons:

$$\Delta_\mu(\geq E_\mu, N, r) = \frac{14.4}{(1+\frac{r}{320})^{2.5}} \left(\frac{N}{10^6}\right)^{0.75} \left(\frac{51}{E+50}\right)\left(\frac{3}{E+2}\right)^{0.14r^{0.37}} m^{-2}$$

where N is the electron size, r is the core distance in metres and E is the minimum energy threshold of muons in GeV. The value of E = 0.2 GeV was used in the present calculations.

The rate of triggers where the local electron density exceeds Δ_e, and the muon density at the detector exceeds Δ_μ is given by:

$$R(\geq \Delta_\mu , \geq \Delta_e) = \int_{r_{min}}^{r_{max}} 2\pi r \; I\left(\geq \frac{\Delta_e}{\rho_e(r)} , \left(\geq \frac{\Delta_\mu}{\rho_\mu(r)}\right)^{1.33}\right) dr$$

where $N = \dfrac{\Delta_e}{\rho_e(r)}$, $\rho_e(r)$ is the lateral structure function

for electrons and $\rho_\mu(r)$ is the lateral structure function for

muons. N is related to the muon density by the formula:

$$N = \left(\frac{\Delta_\mu}{\rho_\mu(r)}\right)^{1.33}$$

The integral was evaluated from $r_{min} = 0.1$ m to r_{max}.

The value of r_{max} was defined such that $\Delta_e = 5.10^9 \rho_e(r_{max})$,

i.e. a cut-off of $N = 5.10^9$ is assumed for shower size. The

results of the calculations for a range of Δ_e are shown in

figure 4.6.

The frequency distribution of triggers as a function of the

number of muons crossing 2.95 m^2 (equal to the area of the flash

tube chamber) for different electron density trigger are calcul-

ated. The results are shown in figure 4.7.

It can be seen that the muon density (differential) spectra

follow as

$$I(\Delta_\mu) d\Delta_\mu = 1.77.10^{-2} \; \Delta_\mu^{-3.22} \; s^{-1}st^{-1}/(2.95 \; m^2) \; \text{for} \; \Delta_\mu \geq (\Delta_\mu)_t$$

where Δ_μ is the number of muons crossing 2.95 m^2 and $(\Delta_\mu)_t$

depends on the triggering requirements and increases as the

local electron density Δ_e increases (see figure 4.6).

It is believed that selecting a lateral structure function

as was found in chapter 3, derived from the measured density

spectrum of EAS, does not change the results of the present

Figure 4.6 The predicted integral muon density spectra in EAS selected by the local electron density requirement as indicated for each curve in units of particles m^{-2}. The curves bend over at low Δ_μ when the Δ_e trigger requirement is more important in determining the trigger than the recorded muon density.

Figure 4.7   The predicted differential muon
density spectra in EAS selected
by a local electron density
requirement as indicated for each
curve in units of particles m^{-2}.
One unit density represents one
muon having traversed the area of
the chamber $(2.95\ m^2)$.

calculations significantly.

4.5   Comparison between the measured and predicted spectra

4.5.1   General remarks

For comparing the predicted spectra with what is measured in theE and F series of measurements one must know (i) the total effective running time, (ii) the effective solid angle and (iii) the local electron density trigger.

(i) The total effective running time, t_{eff}, in each series is defined as the total running time multiplied by the efficiency of scanning (see section 4.3.2).   Thus t_{eff} = 1,104.9 hrs and 3,197.6 hrs for the E and F series respectively. Accordingly it is assumed that the events discarded in the analysis of the data do not introduce a change in the shape of the measured muon density spectrum.   The effect however does not change significantly the results of the E series since the efficiency is close to unity.   To examine the possible effect the measured rate per hour in both series are plotted in figure 4.8.   It can be seen there is good agreement between the two series for $\Delta_{\mu} > (\Delta_{\mu})_t$ which indicates that the way in which t_{eff} has been calculated is correct.

(ii) The effective solid angle is found to be 0.628 st, 0.57 st and 0.52 st for the E, F and G series respectively, as will be described in chapter 5.   For the present calculations the mean solid angle of the three series, i.e. $\bar{\Omega}$ = 0.57 st has been assumed.

(iii) The shape of the muon density spectra is very sensitive to the local electron density trigger for the low density region, i.e. for $\Delta_{\mu} \lesssim (\Delta_{\mu})_t$
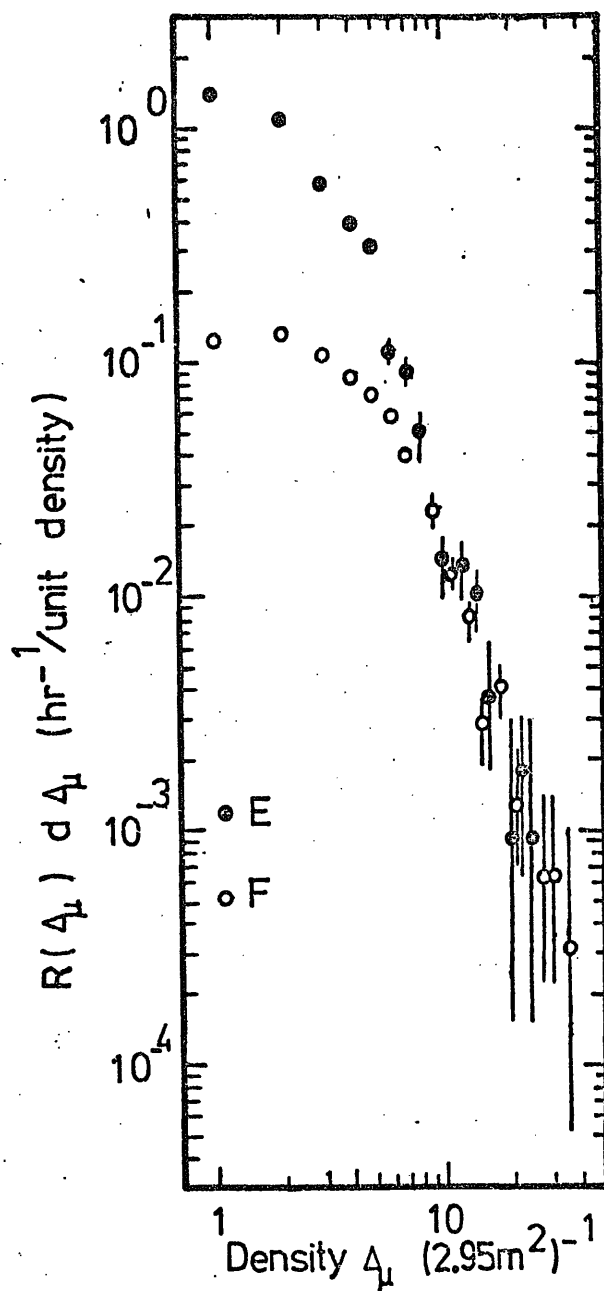
Figure 4.8 The differential muon density spectra (per hour) obtained in the E series (⊕) and the F series (⌀). Unit density corresponds to 1 muon having traversed the area of the flash tube chamber (2.95 m^2).

It was mentioned in chapter 3 that the minimum electron densities recorded by the EAS selection system are 40 m^{-2}, 160 m^{-2} and 511 m^{-2} for the E series, F series and G series respectively. For setting up the triggers the single particle pulse height for relativistic charged particles were determined in the E series and then the discriminator threshold of EAS selection system was set to correspond to 50 particles through each scintillator, i.e. a density per scintillator of 40 m^{-2}. Simpson (1964) has shown that the response of the liquid scint- illators, v , is related to the high voltage applied to the scintillator, V , by $v = KV^{7.2}$. Thus the supply voltage of the liquid scintillators were changed such that for the same discriminator threshold as set up in the E series, the triggering level corresponded to densities of 160 m^{-2} and 511 m^{-2} for the F series and G series respectively.

The measured rate of triggers are 5.3 hr^{-1}, 0.83 hr^{-1} and 0.17 hr^{-1} for the E, F and G series respectively. Table 4.2 shows the expected minimum electron density triggers for the above series for the measured trigger rates to be consistent with the density spectrum of EAS described in chapter 3 and obtained using a proportional counter.

The minimum densities calculated using the density spectrum given by Cocconi and Cocconi and Tongiorgi (1949) and Greisen (1960) are also shown in table 4.2.

It can be seen from this table, that the minimum density recorded by the liquid scintillators are higher than the values obtained if one uses the measured trigger rate and published density spectra. The difference is believed to be due to the interaction of photons in the scintillator as well as low energy

Film Series	Measured trigger rate (hr-1)	Electron density (m^{-2}) determined from the measured trigger rate and the sea level density spectrum			Electron density (m^{-2}) recorded by the scintillators.
		Proportional counter (chapter 3)	Cocconi et al. (1949)	Greisen (1960)	
E	5.30	16	20	25	40
F	0.83	60	80	100	160
G	0.17	180	233	280	511

Table 4.2   The electron density calculated in the E, F and G series using the measured rate and the integral density spectrum of EAS as given in chapter 3, Cocconi et al. (1949) and Greisen (1960). The densities recorded by the liquid scintillators above the chamber is given in the last column.

nuclear interactions.

For the present work it is assumed that the data of Cocconi and Cocconi and Tongiorgi are correct. Thus the minimum electron densities are 20 m^{-2}, 80 m^{-2} for the E series and F series respectively. It is noted that using the absolute rate of showers of a given density found by Cocconi et al.(1949) corresponds to the average rate found from the proportional counter measurements, described in chapter 3, and the survey of Greisen (1960).

4.5.2   The results of Comparison

The Poissonian fluctuations folded into the predicted differential spectra (figure 4.7) and the results are shown in figure 4.9.

As mentioned in section 4.5.1, the effective running times of the E series and F series are 1,104.9 hrs and 3,197.6 hrs respectively. The spectra obtained in figure 4.9 for $\Delta_e \geq 20$ m^{-2} and $\Delta_e \geq 80$ m^{-2}, corresponding to the E series and F series, multiplied by the effective running times of the corresponding series and by $\bar{\Omega} = 0.57$ st. The resulting spectra are demonstrated in figure 4.4 and 4.5.

It can be seen that there is good agreement between the predicted and measured spectra in the E series. The discrepency between the predicted and measured spectra obtained in the F series (figure 4.5), for low muon density region, is believed to be due partly to the inefficiency of the chamber in detecting muons produced by a high local electron density trigger.

The figure shows curves labeled 20, 40, 80, 160 on axes:
Y-axis: $R(\Delta\mu)d\Delta\mu$ ($s^{-1}st^{-1}$/unit density), ranging from 10^{-7} to 10^{-3}.
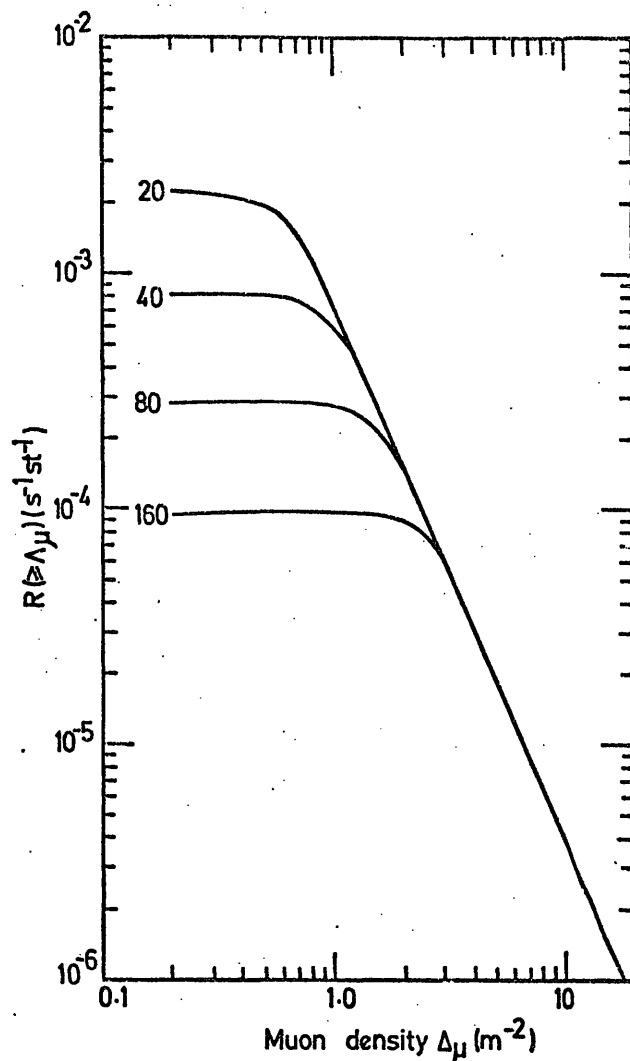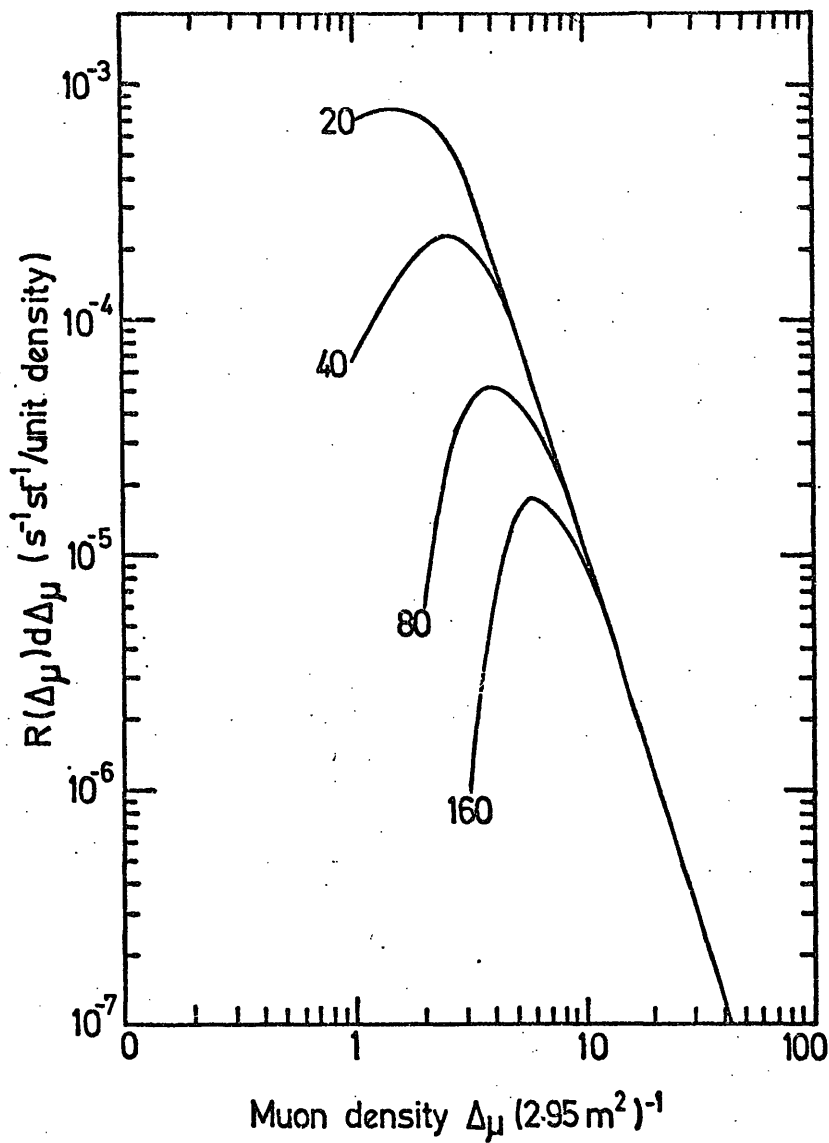X-axis: Muon density Δ_μ $(2.95m^2)^{-1}$, ranging from 0 to 100.
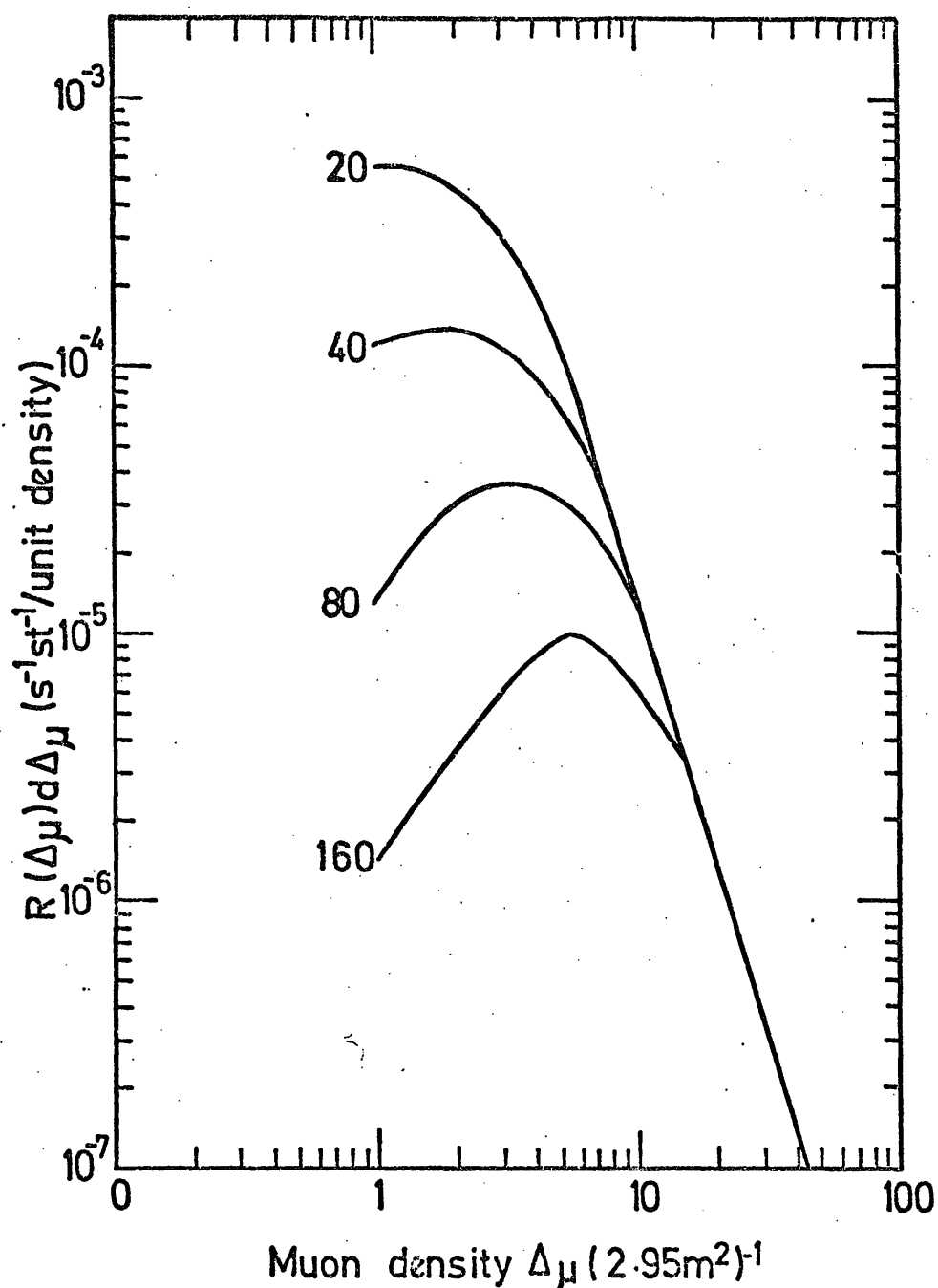
Table 4.9   The predicted differential muon density spectra in EAS selected by a local electron density requirement as indicated for each curve in units of particles m^{-2}. The Poissonian fluctuations have been folded into the spectra. One unit density represents a muon having traversed 2.95 m^2.

4.6 Distribution of the sizes and core distances of EAS producing a given muon density at the detector

It was seen in section 4.4 that there is a deficit in the frequency of low muon density events due to the characteristics of the trigger. To obtain more knowledge about the characteristics of EAS selected by the detector the rate of triggers, with local election density $\geq \Delta_e$ m^{-2} producing a minimum Δ_μ m^{-2} at the detector has been calculated by evaluating the following integrals, namely

$$R(\geq r, \geq \Delta_e, \geq \Delta_\mu) = \int_r^{r_{max}} 2\pi r' I(\geq \frac{\Delta_e}{\rho_e(r')} , \geq (\frac{\Delta_\mu}{\rho_\mu(r')})^{1.33}) \, dr' \quad \text{and}$$

$$R(\geq N, \geq \Delta_e, \geq \Delta_\mu) = \int_{r_{min}}^{r_{max}} 2\pi r' I(\geq \frac{\Delta_e}{\rho_e(r')}, \geq (\frac{\Delta_\mu}{\rho_\mu(r')})^{1.33} \, dr'$$

where $R(\geq r, \geq \Delta_e, \geq \Delta_\mu)$ is the rate of triggers produced by showers falling at a distance $\geq r$ from the core. $R(\geq N, \geq \Delta_e, \geq \Delta_\mu)$ is the rate of triggers produced by showers of size $\geq N$ and other terms have the same meaning as described earlier.

The functions are evaluated for local electron densities of 20 m^{-2}, 40 m^{-2}, 80 m^{-2} and 160 m^{-2}. The results are shown in figures 4.10 to 4.13. Figure 4.14 demonstrates the median shower sizes and the median core distances. These are plotted using figures 4.10 to 4.13.

In deriving the functions mentioned above the calculations are carried out taking the laterial density of muons as given by Clark et al. (1958) as given in chapter 2. The sea level number spectrum is taken from Hillas' survey of 1970b(for case a,

$\Delta e \geq 20$

$\Delta \mu \geq 1.0$

$\Delta e \geq 80m^{-2}$

2·0

4·0

6·0

8·0

10·0

15·0

20·0

25·0

30·0

$R(\geq r)(s^{-1} sr^{-1})$
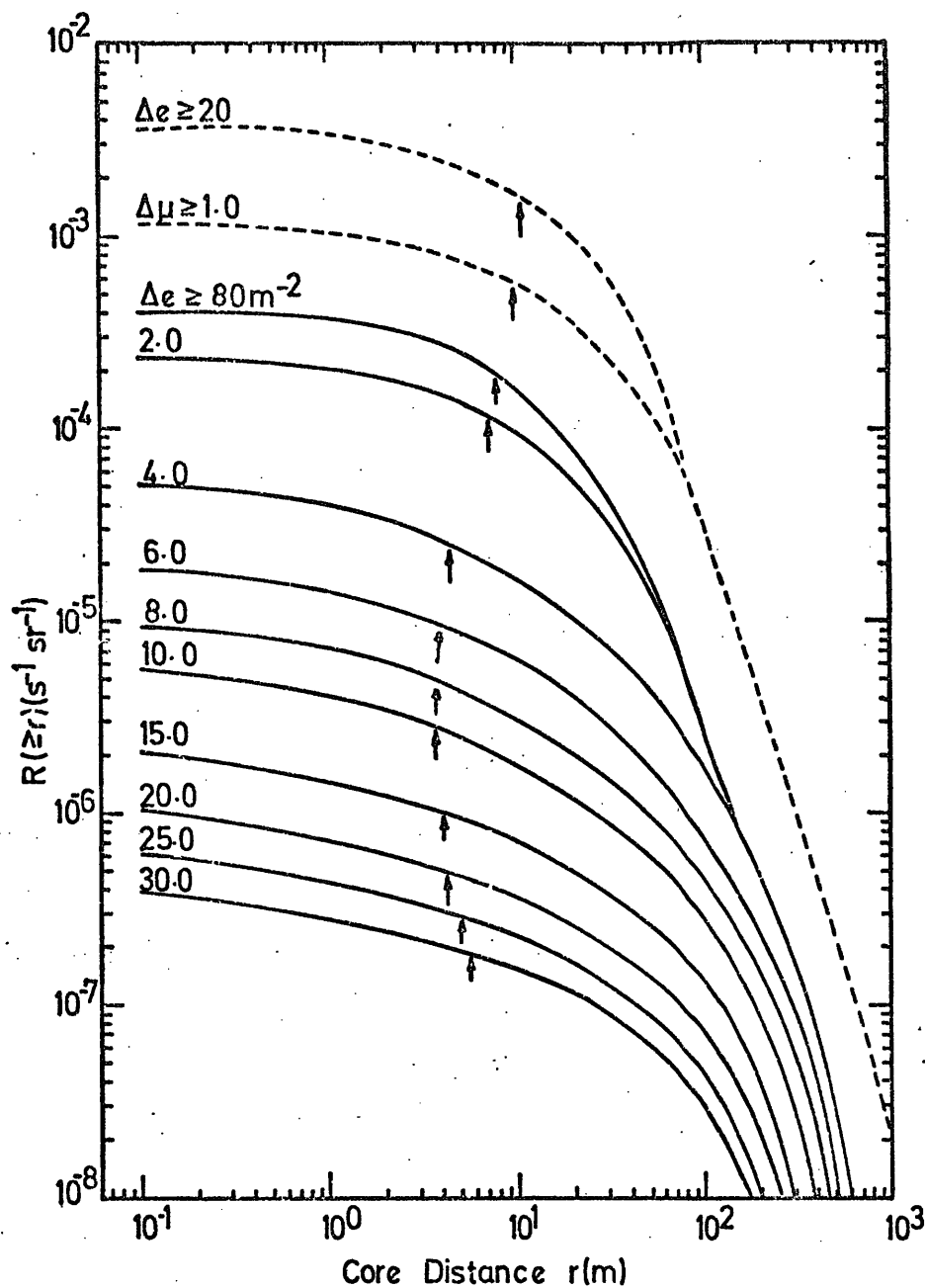
Core Distance r(m)

Figure 4.10   The rate of EAS which produce a local electron density ≥ 20 m^{-2} (dashed curves) and ≥ 80 m^{-2} (solid curves) and whose cores fall at a distance $\geq r$ metres from the detector. Median core distances are shown by arrows and the numbers attached to the curves indicate Δ_μ m^{-2}. Curves indicated by $\Delta_e \geq 20$ and $\Delta_e \geq 80$ are the rates of triggers as a function of core distance. The curves for $\Delta_\mu \geq 2$ m^{-2} are identical for both the electron density thresholds of $\Delta_e \geq 20$ m^{-2} and $\Delta_e \geq 80$ m^{-2} as at these muon densities Δ_μ determines the trigger requirement rather than Δ_e.
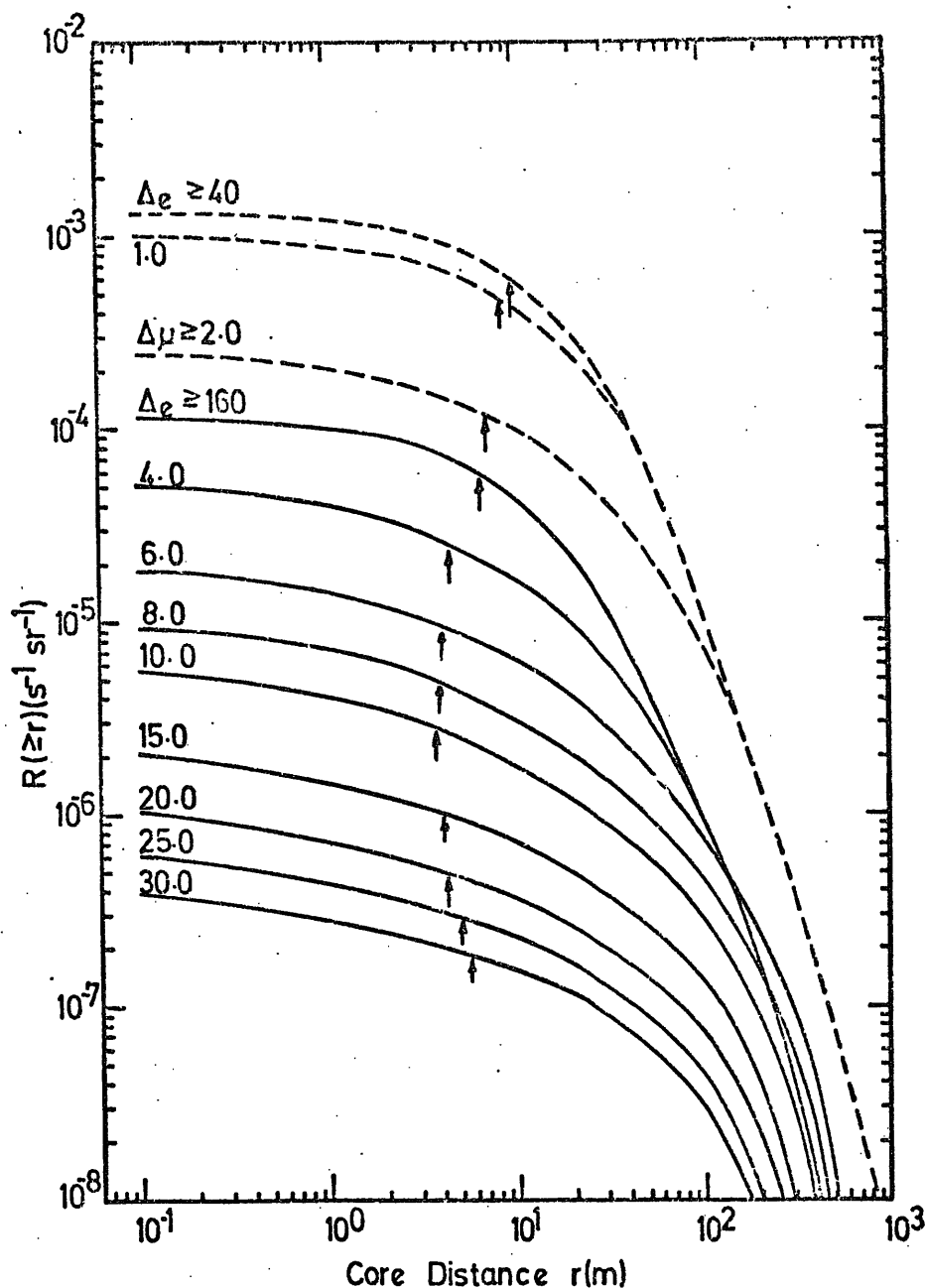
Figure 4.11 The rate of EAS which produce a local electron density ≥ 40 m^{-2} (dashed curves) and ≥ 160 m^{-2} (solid curves) and whose core fall at a distance $\geq r$ metres from the detector. Median core distances are shown by arrows and the numbers attached to each curve indicate Δ_μ m^{-2}. Curves indicated by $\Delta_e \geq 40$ m^{-2} and $\Delta_e \geq 160$ m^{-2} are the rate of triggers as a function of core distance. The curves for $\Delta_\mu \geq 4$ m^{-2} are identical for both the electron density thresholds of $\Delta_e \geq 40$ m^{-2} and $\Delta_e \geq 160$ m^{-2} as at these muon densities Δ_μ determines the trigger requirement rather than Δ_e.
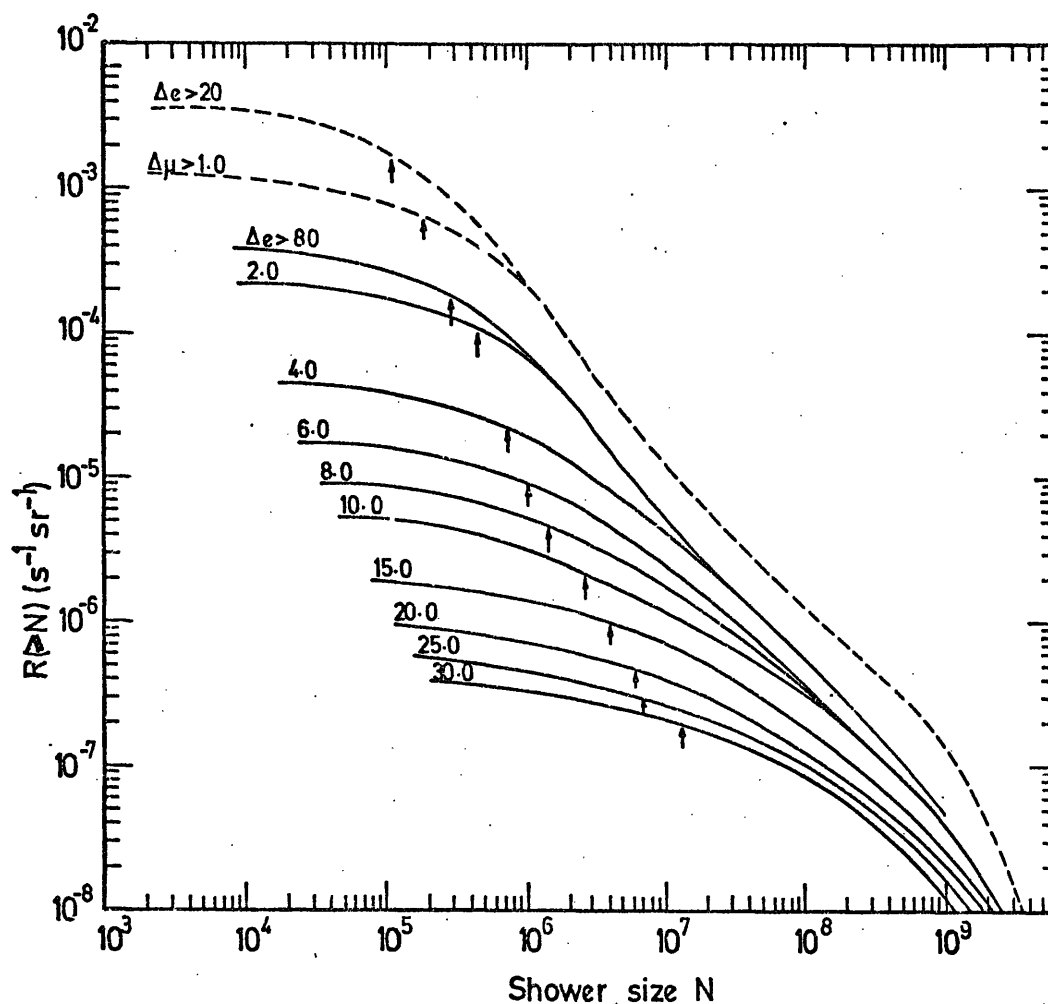
Figure 4.12   The rates of EAS of electron size$\geq$N producing a local electron density ≥ 20 m^{-2} (dashed curves) and ≥ 80 m^{-2} (solid curves) associated with different muon densities (m^{-2}). Median shower sizes are shown by arrows and the numbers attached to the curves indicate Δ_μ m^{-2}. Curves indicated by $\Delta_e \geq 20$ m^{-2} and $\Delta_e \geq 80$ m^{-2} are triggering rates. The curves for $\Delta_\mu \geq 2$ m^{-2} are identical for both the electron density thresholds of $\Delta_e \geq 20$ m^{-2} and $\Delta_e \geq 80$ m^{-2} as at these muon densities Δ_μ determines the trigger requirement rather than Δ_e.
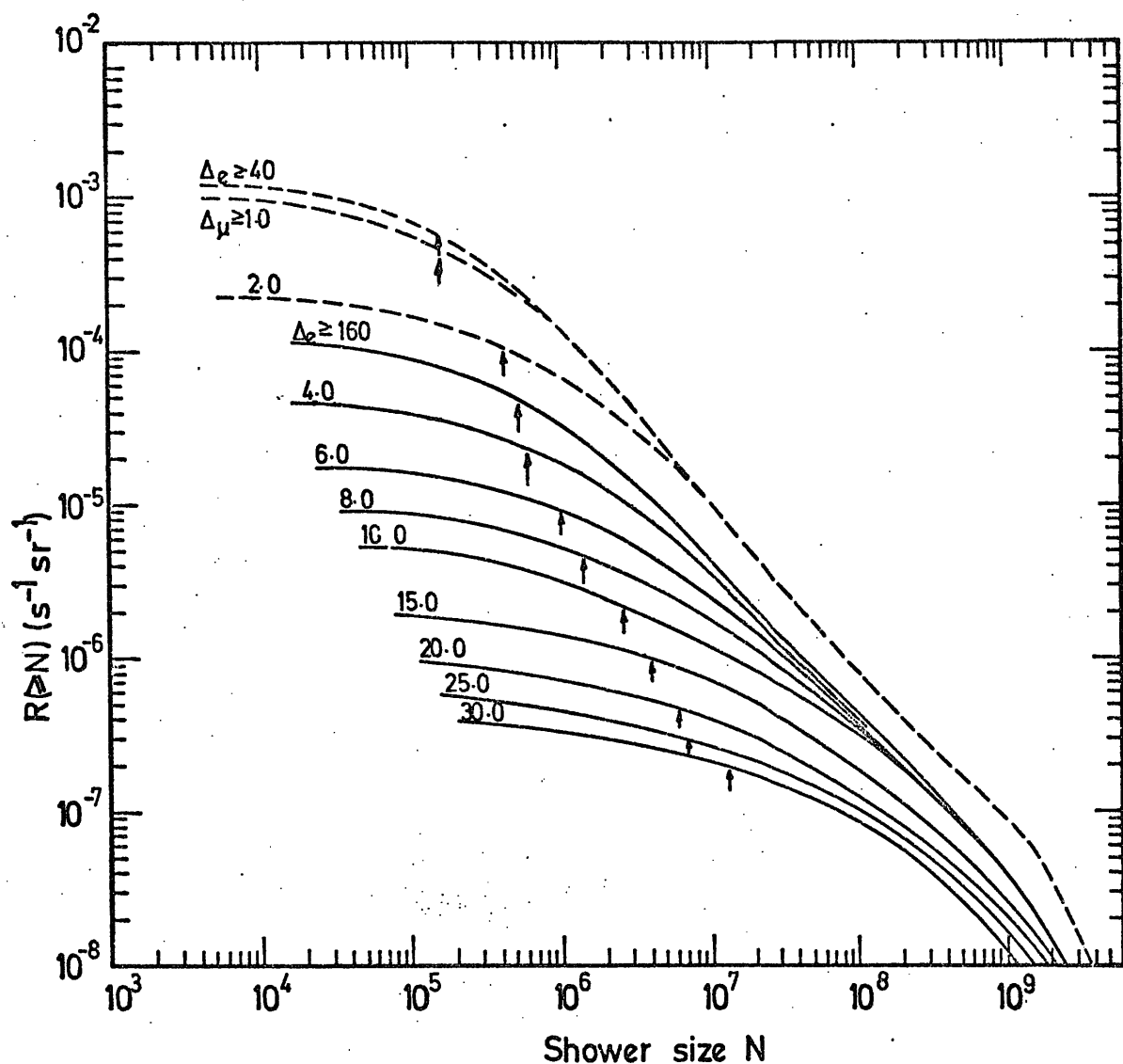
Figure 4.13   The rate of EAS of electron size $\geq$ N
producing a local electron density
≥ 40 m^{-2} (dashed curves) and
≥ 160 m^{-2} (solid curves) associated
with different muon densities (m^{-2}).
Median shower sizes are shown by arrows
and the numbers attached to each curve
indicate Δ_μm^{-2}.   Curves indicated by
$\Delta_e \geq 40$ m^{-2} and $\Delta_e \geq 160$ m^{-2} are
triggering rates.   The curves for
$\Delta_\mu \geq 4$ m^{-2} are identical for both the
electron density thresholds of $\Delta_e \geq 40$ m^{-2}
and $\Delta_e \geq 160$ m^{-2}, as at these muon densities
Δ_μ determines the trigger requirement rather
than Δ_e.
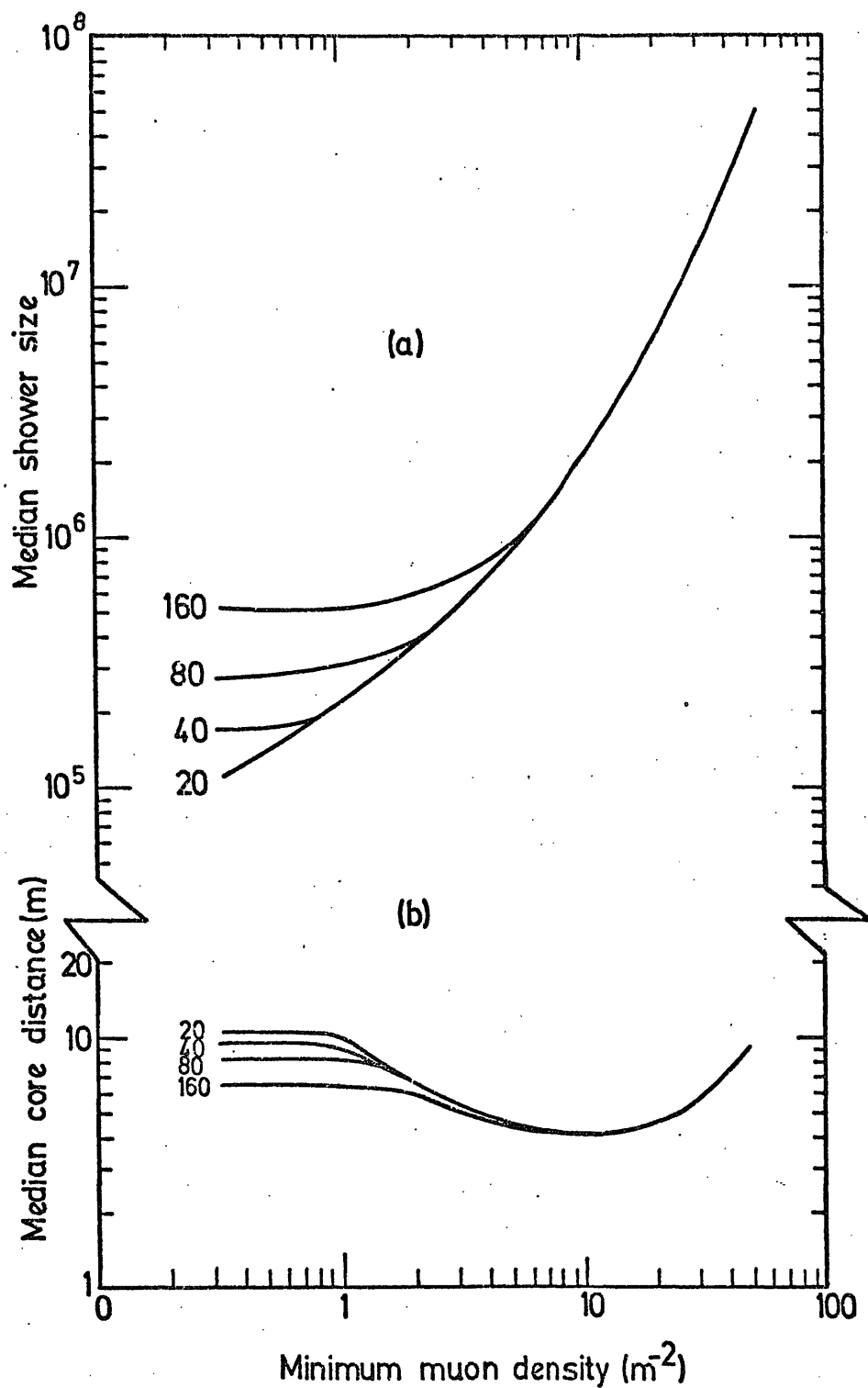
Figure 4.14   Median shower sizes (a) and median core distances (b) capable of producing a minimum muon density at a detector triggered by a predetermined local electron density (m^{-2}) as stated for each curve.

see chapter 3). The lateral density of electrons is taken from Greisen (1960). Using the number spectrum and lateral structure function, as given in section 4.4, does not change the results of these calculations significantly. In particular it does not change the calculated median shower sizes and median core distances.

4.7 Comparison with other experiments and discussion

4.7.1 Higashi et al. (1962)

Higashi et al. have measured the integral multiplicity spectrum of muons in EAS of E_μ >10 GeV by means of a cloud chamber situated underground. The chamber triggers by means of an EAS array on the ground. They found that γ =-2.6 for densities of $\Delta_\mu \gtrsim 7$ muon/m^2 in showers of size N $\geq 210^6$. Taking the integral slope of the number spectrum to be -2.0 and assuming the lateral structure of muons is independent of shower size, as has been found by Clark et al. (1958), Bennett et al. (1962) and Staubart et al. (1970) in a wide range of shower sizes, one obtains α = 0.77 in good agreement with direct experimental measurements. The value of α = 0.77 is obtained taking $N_\mu \propto N^\alpha$. Now since R ($\geq$ N) $\propto$ N$^{-2.0}$ for N $\geq 210^6$ thus R($\geq N_\mu$) $\propto$ N$^{-2.0/\alpha}$ $\propto N_\mu^{-2.6}$. This gives α = 0.77.

4.7.2 Betev et al. (1970)

The integral density spectrum of muons at 2,925 m above sea level has been measured by Betev et al. by means of an apparatus consisting of four hodoscoped G-M counter sets (each set containing ten G-M counters) located on the corners of an

(8×8) m^2 square under 30 cm of lead (equivalent to $E_\mu \gtrsim 600$
MeV). The corresponding mean number of muons in the shower was
$N_\mu \gtrsim 1.2 \cdot 10^6$. They found that different criteria for analysing
the data, depending on the number of counters giving no signal
in each set, give consistent results, except for one in which
the slope is significantly smaller than the rest. Excluding
this class, which is assumed to be due to the effect of electron
multiplication in the lead shielding they found an average
$\gamma = -2.35 \pm 0.05$.

Taking the slope of integral number spectrum equal to -2
one obtains $\alpha = 0.85$, a value which is very close to what has
been measured at sea level.

4.7.3 Firkowski et al. (1973)

These authors have measured the muon density spectrum for
muons of $E_\mu \gtrsim 5.6$ GeV in the density interval of 0.27 to 1.2
particles m^{-2}. Their experimental device consists of a set of
electron component detectors, a ground level muon detector with
energy threshold of $\simeq 0.5$ GeV and an underground muon detector
of energy threshold 5 GeV. A sample of 52,622 showers were
recorded by coincidence of any of eight out of thirty one detect-
ors (each of area 1.36 m^{-2}) and the results were used to obtain
the muon density spectrum.

They found $\gamma = -2.1 \pm 0.05$. The showers corresponding
to the measured density intervals are showers with primary
energy around 10^{16} eV. It is clear that they have found a
much flatter spectrum compared with the expected spectrum assuming
$\alpha = 0.75$. This could be due to the effect of multiplication
produced by bursts and δ rays in the muon detector shielding.

Giler et al. (1970) find a value of $\gamma = -2.39$ for an EAS model with multiplicity law $n_s \propto E^{1/4}$ and $\gamma = -2.21$ for a model with $n_s \propto E^{1/2}$. Thus Firkowski et al. explained their measured results assuming a fast increase of secondary particle multiplicities.

4.8   Conclusion

The density spectra of muons selected by local electron densities of $\Delta_e \geq 20$ m^{-2} and $\Delta \geq 80$ m^{-2} were measured using a flash tube chamber. Assuming the lateral density of muons is independent of shower size as given by Greisen, and taking the number spectrum as was found in chapter 3 (derived from the measured density spectrum of EAS) the muon density spectra were predicted. It was concluded that

(i)   There is good agreement between the measured and predicted spectra in particular for $\Delta_e \geq 20$ m^{-2}.

(ii)   The shape of the predicted and measured spectra of muons for high muon density region are independent of the local electron density requirement.

Some discrepancies were obtained for $\Delta_\mu \lesssim 5$ muons/2.95 m^2 in the local electron dnesity trigger of $\Delta_e \geq 80$ m^{-2}, between the measured and the predicted spectra. This could be attributed partly as a result of the bias imposed for low muon density region in analysing the data due to the obscurtion of the events by the bursts produced in the chamber. Thus one should operate the experiment with the muon density detector underground so that the nuclear particles would be absorbed in the overburden.

For the low electron density threshold and high muon density region, however, one concludes that the derived number spectrum

obtained in chapter 3 is reasonably accurate. The present results also suggest that not only the lateral structure function of muons is independent of shower size, but the form given by Greisen (1960) is valid down to an energy threshold of $\simeq$ 0.2 GeV.

Greisen (1960) gives the relation between number of muons N of $E_\mu >$ 1 GeV in a shower of size N

$$N_\mu \quad (> 1\text{GeV}) = 9.5 \cdot 10^4 (\frac{N}{10^6})^{0.75}$$

Murthy et al. (1968[b]) have calculated N_μ – N relationship assuming different models for nuclear interactions. Their calculations indicate that a model in which multiplicity follows as $n_s \propto E^{1/4}$ with production of nucleon – antinucleon pairs gives satisfactory results with the above expression. One should note that a model with multiplicity in the form of $n_s \propto E^{1/2}$ as given by Murthy et al. gives consistent results with the relationship given by Greisen. A standard CKP model, however, produces too low muons (by a factor of about 2) compared with Greisen's expression as found by Murthy et al.

CHAPTER 5

The absorption length of the electron-photon component of EAS as determined from both barometer coefficient and zenith angle distribution measurements.

5.1   Introduction

The measurement of the attenuation length of the shower particles and its dependence on the shower size gives rather important results about the development of EAS.   This quantity has been derived indirectly by measuring the zenith angle distribution of EAS and by measuring the barometric coefficient. These methods give the absorption length of the EAS spectrum rather than the attenuation length of the electron-photon component in showers of a given size.   In the next section the relationship between these two quantities is considered.

5.2   Theoretical Considerations

Assume that the primary energy spectrum is given by $R(> E) = A E^{-\gamma_1}$.   The shower development curve, produced by a primary of energy E, is shown experimentally (Bradt et al. 1965) and theoretically (Dixon et al., 1974) to attenuate with atmospheric depth (after the maximum of development), approximately, in an exponential form, i.e.

$$N(E, x) = N(E, 0) \, e^{-x/\lambda}$$

$$= B \, E^{\alpha} \, e^{-x/\lambda}$$

where $N(E,x)$ is the size of shower produced by a primary energy

E at depth x and λ is the attenuation length of shower particles. It is shown by model calculations (see Galbraith, 1958) that $N(E, 0) = B \, E^{\alpha}$, where α is close to 1.0.

Equating the integral size spectrum to the primary energy spectrum, one can write:

$$R(>N, x) = R(>E)$$
$$= A \, E^{-\gamma_1}$$

$$= A \left\{ \left[\frac{N(E, x)}{B \, e^{-x/\lambda}} \right]^{1/\alpha} \right\}^{-\gamma_1}$$

$$= A \, B^{\gamma_2} \, (N(E,x))^{-\gamma_2} \, e^{-x/\Lambda}$$

where γ_2 $(= \gamma_1 / \alpha$) is the exponent of the integral number spectrum at depth x. The absorption length of the EAS spectrum Λ is related to the attenuation length λ of the shower particles by

$$\Lambda = \lambda / \gamma_2$$

Thus a measurement of the barometric coefficient or the index n of the angular distribution of EAS (in the $I = I_0 \, \cos^n \vartheta$ relationship) of size $> N$ measures Λ (see Galbraith, 1958). This in turn could be related to the attenuation length of the shower particles (mainly electrons) by the above equation.

It is noted that the measurement of the barometric coefficient gives the absorption length of showers irrespective of the shower direction. Hodson (1953) and Kraybill (1949) have measured the altitude variation of the

rate of EAS. Greisen (1956) has calculated this variation

for the vertical showers, using a Gross transformation.

Using the measurements of Hodson and Kraybill he comes to

the conclusion that Λ for vertical showers is nearly the same

as the value of Λ found from the altitude dependence of all

showers irrespective of their zenith angle for atmospheric

depths close to sea level.

5.3   The method of zenith angle distribution

It was shown that muons observed in the chamber are

close to the core (see figure 4.14). Thus if one measures

the angular distribution of muons observed in the chamber

about the zenith one effectively determines the angular dist-

ribution of the axis of EAS. For this purpose the frequency

distribution of the acceptable muon tracks as a function of

their angles with respect to the vertical direction in the

front projected plane of the flash tube chamber was measured.

An acceptable track was one in which

(i) The track had crossed the top layer of F2 and the

layer positioned at one-third of the total depth of F2.

(ii)   The track being parallel within ± 5° with other muons

if they have been recorded by the chamber.   Figure 5.1 shows

the geometry used for the acceptable tracks.

The events were projected on the scanning sheet such that

the reconstructed events had a demagnification of 1:20 compared

to real space.   The angle between the direction of the accept-

able events and the vertical direction was measured.

The results of the measured angular distributions for

the E, F and G series are shown in figure 5.2.   These have

LEAD

F1a

IRON

F1b

A   B

C   D

F2

F3

F4a

F4b

20cm.

20cm.
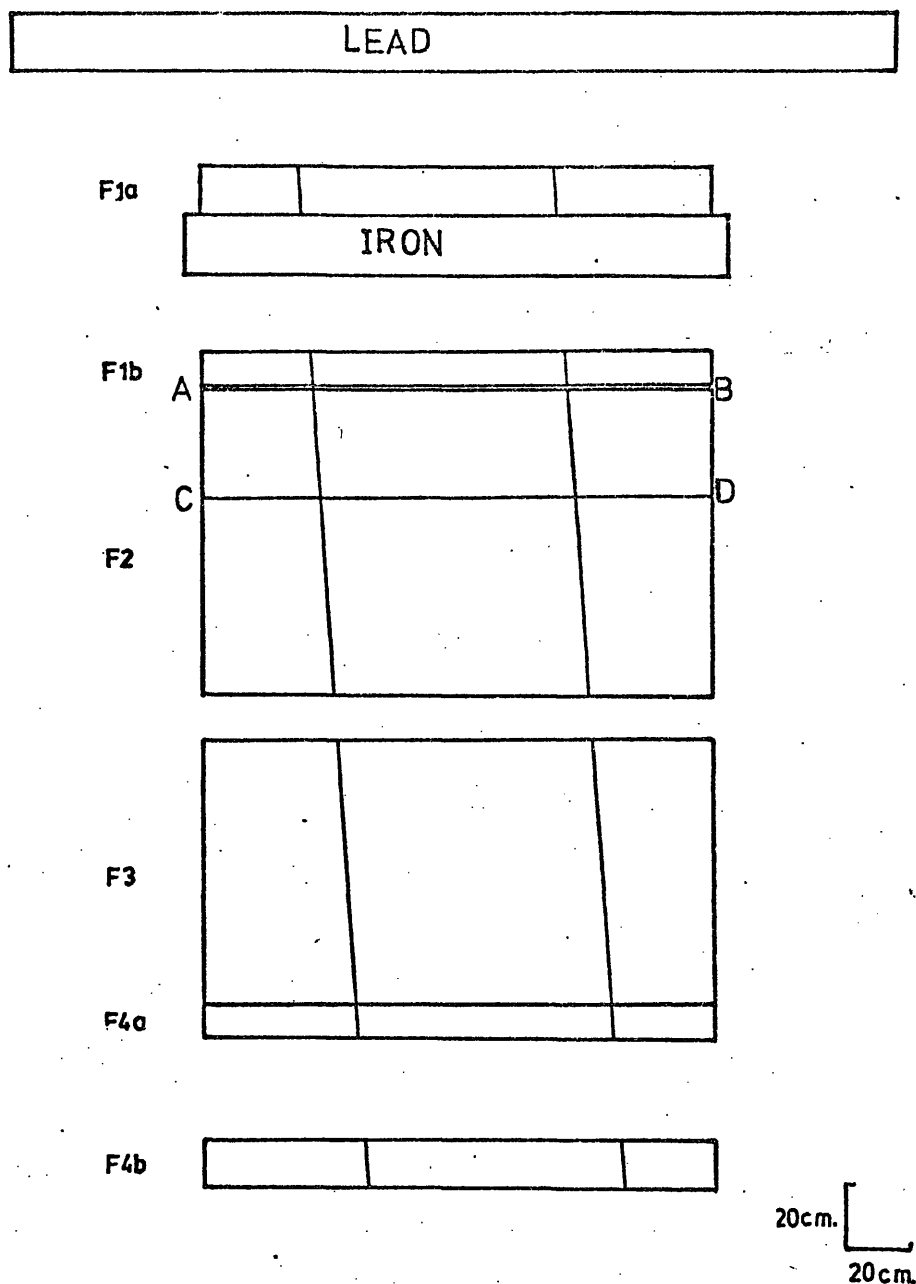
Figure 5.1   Scale diagram of the front view
of the chamber.   An example of
the passage of two muons through
the chamber and the geometry used
for acceptable tracks (ABCD) are
shown.   For a multiple (≥ 2) muon
event to be measured at least one
track should traverse both the
defining planes AB and CD and all
muon tracks should be parallel to
$\pm 5°$.
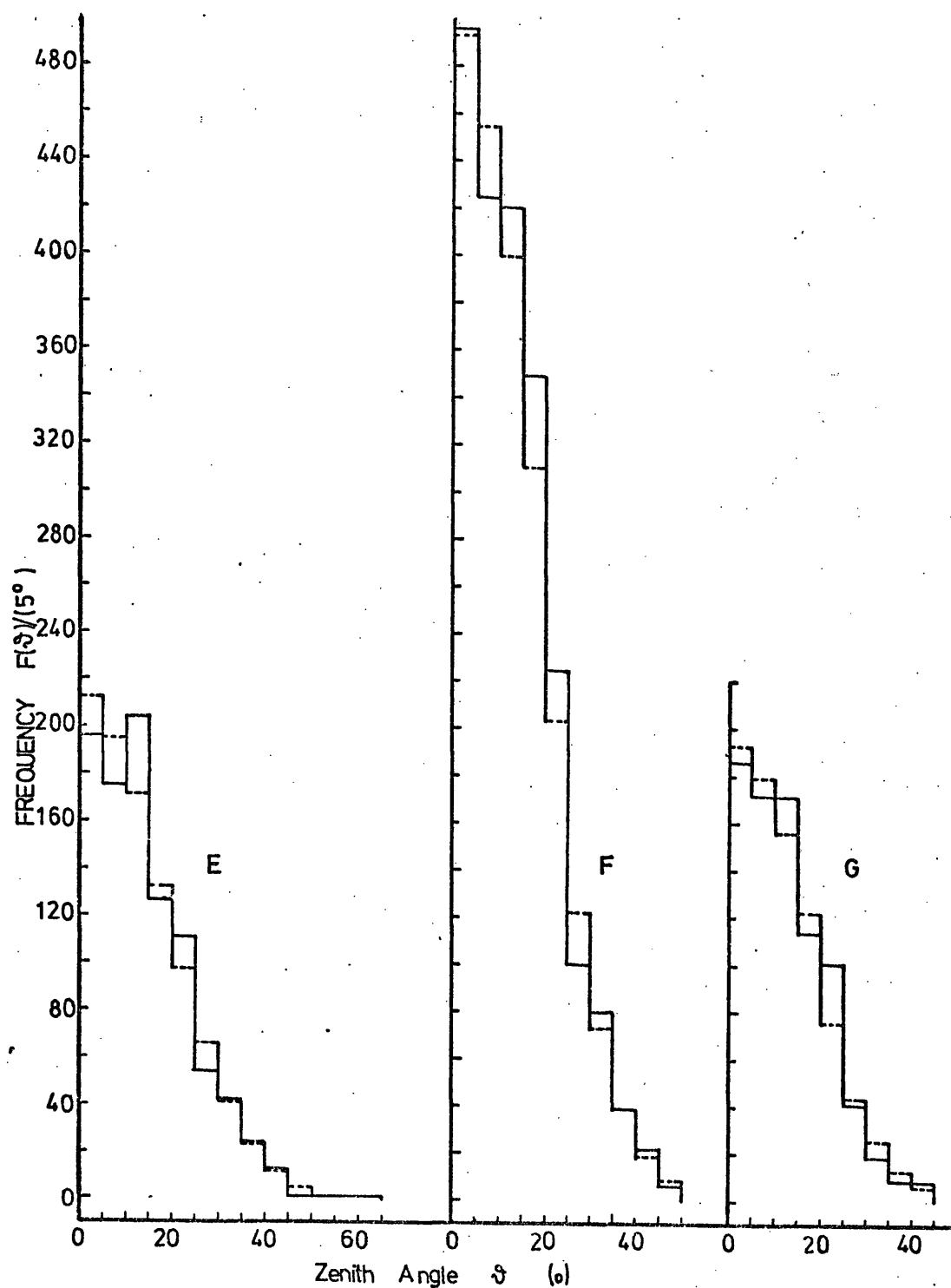
<u>Figure 5.2</u>   Frequency distribution of showers about
the zenith angle for the E,F and G
·series as indicated for each distribution.
The dashed distributions are the expected
ones for n equal to 8.0, 9.4 and 10.0
corresponding to the best fit values for
the E,F and G series respectively.

been obtained by analysing 1,441 triggers in the E series (films E39-E46), 2,890 triggers in the F series (films F1-F28) and 1,217 triggers in G series (films G1-G21). The measureable events were 949, 2,149 and 822 for the above mentioned series respectively.

The method introduced by Lovati et al. (1954) has been used to find the best n for each distribution, plotted in figure 5.2, assuming the angular distribution of EAS follows as $I = I_0 \cos^n \vartheta$ (The method will be described in Appendix B). The result of applying a chi-square test between the predicted distributions, with different n, and the observed distributions, show that $n = 8.0 \pm^{1.4}_{1.2}$, $n = 9.4 ^{+1.0}_{-0.8}$ and $n = 10.0^{+1.9}_{-0.9}$ for the E, F and G series respectively.

Galbraith (1958) shows that $\Lambda = \frac{P_0}{n}$ g cm^{-2} where P_0 is the atmospheric pressure (1,030 g cm^{-2} in the present case) and n is the index in the $I = I_0 \cos^n \vartheta$ relationship. Thus Λ is equal to $128 ^{+23}_{-28}$ g cm^{-2} for the E series, $109 ^{+10}_{-9}$ g cm^{-2} for the F series and $103 ^{+10}_{-20}$ g cm^{-2} for the G series.

If the rate of EAS varies with ϑ as $R(> N_\vartheta, t) = R(> N_0, t) \cos^n \vartheta$ as shown in the present case, the solid angle for which the showers are detected is $\Omega = \frac{2\pi}{n+2}$ st.

Therefore Ω is equal to 0.63 st., 0.56 st. and 0.52 st. for the E, F and G series respectively. The average solid angle for all series is $\Omega = 0.57$ st.

5.4 The method of barometric coefficient

A change in the atmospheric pressure corresponds to the apparatus being situated at different atmospheric depths,

and a variation in the observed rate of EAS is expected.

The variation of the showers recorded by the chamber in the F series has been determined as a function of atmospheric pressure. The result is shown in figure 5.3. From this figure the barometric coefficient $\beta = -9.5 \pm 0.56$ % $(Cm\ Hg)^{-1}$.

Galbraith (1958) shows that $\Lambda = \dfrac{13.6}{\beta - 4\vartheta}$ g cm^{-2} at sea level. In this equation ϑ is the temperature coefficient and is -0.3%. C^{o-1} as given by Hodson (1951). This gives $\Lambda = 116\ ^{+6}_{-5}$ g cm^{-2} for the absorption length of the EAS spectrum recorded in F series. Saleh (1973) has measured the barometric coefficient for the E series as $\beta = -11.6\ ^{+}_{-}$ 0.86 % $(cm\ Hg)^{-1}$. Thus $\Lambda = 10.6 \pm\ ^{8}_{6}$ g cm^{-2} for this series.

Each series corresponds to a different local electron density trigger. Thus it is assumed that the measured values of Λ correspond to the median shower sizes capable of producing the observed densities. These are $1.5.10^{5}$, $2.7.10^{5}$ and $5.5.10^{5}$ for the E, F and G series. These values have been obtained by means of table 3.5. The results of the measured Λ and the corresponding shower sizes for the above mentioned series are shown in table 5.1.

5.5 Derivation of the attenuation length of shower particles λ.

As mentioned in section 5.2, $\lambda = \gamma_{2}\Lambda$ where γ_{2} is the slope of the integral number spectrum. In the present work the weighted value of γ_{2} appropriate to the distribution of shower sizes that trigger the detector should be used to correlate the measured Λ with the attenuation
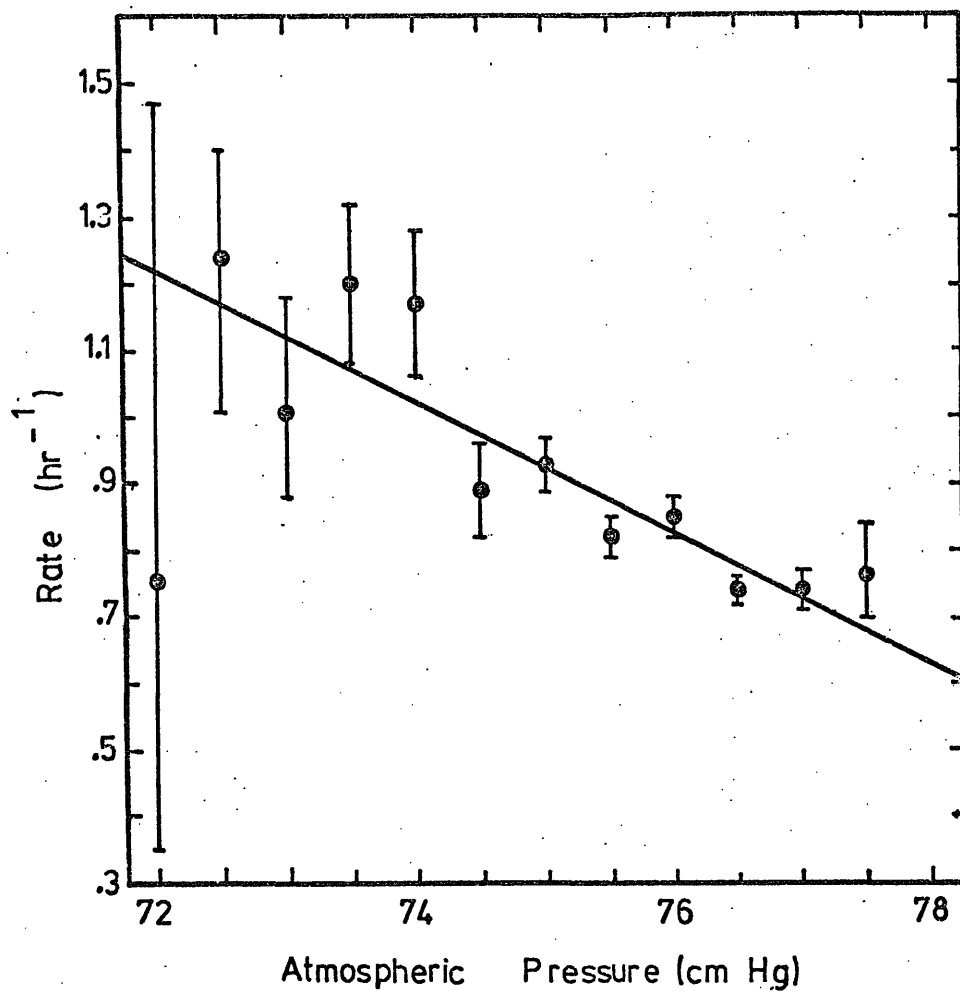
Figure 5.3   Rate of EAS as a function of
atmospheric pressure. The
solid line shows the best
line through the experimental
points. The graph is based
on 4516 showers recorded in
5,419.6 hours which produce
a local electron density ≥ 80 m^{-2}.

Film series	Median shower size	Weighted slope γ_2	Λ (g cm^{-2})		$\lambda = \gamma_2\Lambda$ (g cm^{-2})	
			The method of zenith angle	The method of barometric coefficient	The method of zenith angle	The method of barometric coefficient
E	$1.5.10^5$	1.38	$128\,^{+23}_{-28}$	$106\,^{+8}_{-6}$	$177\,^{+32}_{-37}$	$146\,^{+10}_{-9}$
F	$2.7.10^5$	1.53	$109\,^{+10}_{-9}$	$116\,^{+6}_{-5}$	$167\,^{+15}_{-14}$	$178\,^{+9}_{-8}$
G	$5.5.10^5$	1.64	$103\,^{+10}_{-20}$	–	$169\,^{+16}_{-33}$	–

Table 5.1   The measured and derived values of Λ and λ for the E, F and G series. The median shower sizes correspond to 20 m⁻2, 80 m⁻2 and 233 m⁻2 for the electron density triggers of the E, F and G series as were discussed in chapter 4.

length λ in showers of a given size. The weighted values of γ_2 for each series has been calculated using table 3.5 and the number spectrum obtained from the measured density spectrum, as described in chapter 3. The results show that γ_2 is equal to 1.38, 1.53 and 1.64 for the E, F and G series respectively. The values thus obtained for λ are tabulated in table 5.1. Figure 5.4 demonstrates the derived λ as a function of shower size for the above mentioned series.

It should be noted that the requirement of $\Delta_\mu \geq 1$ muon/ 2.95 m^2 in determining the absorption length of the EAS spectrum Λ , from zenith angle distribution measurements (see section 5.3), does not significantly change the median shower sizes and the weighted values of γ_2 given in table 5.1. This can be seen from figure 4.6.

5.6 Comparison with previous measurements

Tables 5.2 and 5.3 show the available experimental data on the measured absorption length of the EAS spectrum. These have been obtained from measurements of the zenith angle distribution of EAS (by the method of fast timing) and by the method of barometric coefficient. The last columns of these tables have been calculated by multiplying the measured absorption length Λ by the slope of the number spectrum at the corresponding size. The slope of the number spectrum is taken to be -1.3 for $N \leq 7.10^5$, -2.0 for $7.10^5 < N \leq 3.10^7$ and -1.5 for $N > 3.10^7$. These have been derived from a measurement of the density spectrum of EAS (chapter 3). (The data of Bennett et al., 1962 quoted in tables 5.2 and 5.3 and
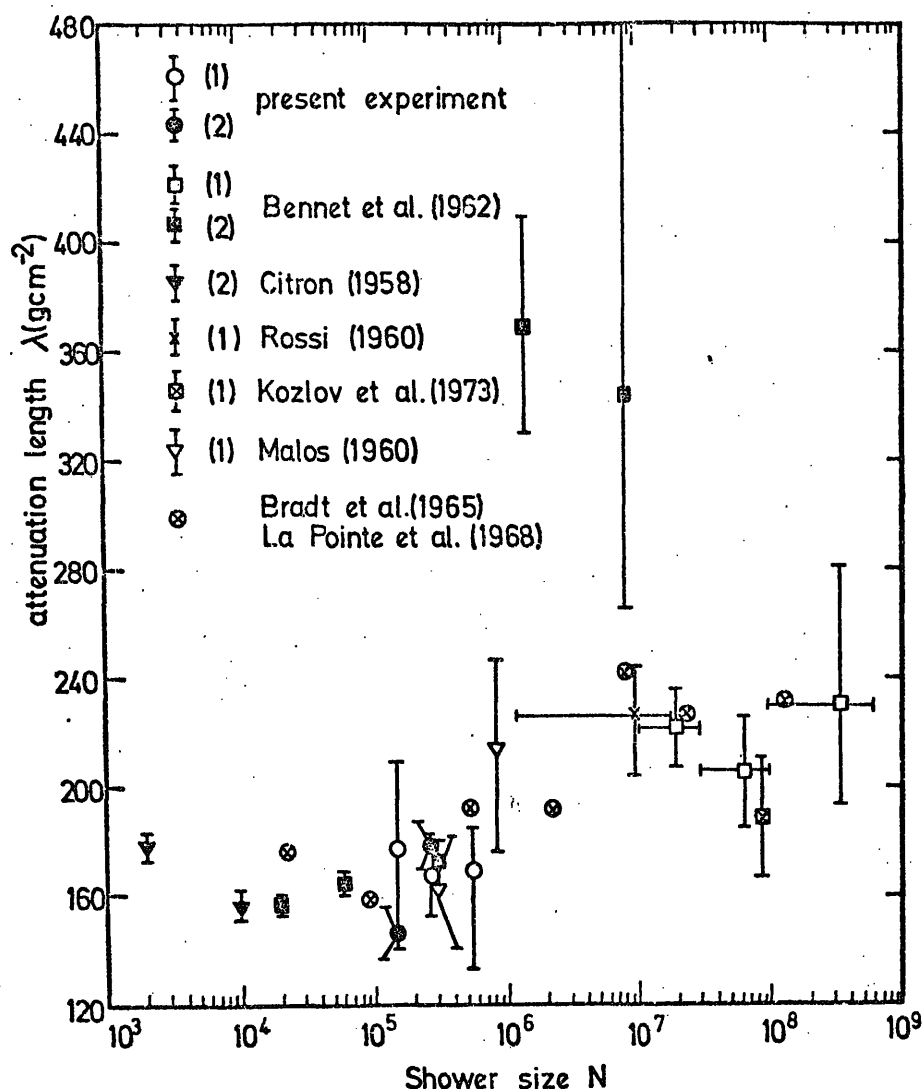
Figure 5.4   The measured attenuation length
of shower size, from measurement
of the zenith angle distribution
(1) and the barometric coefficient
(2) of EAS in the E, F and G series.
The results of other experiments
listed in tables 5.2 and 5.3 are
shown. The experimental data of
Bradt et al.(1965) and La Pointe et
al.(1968) have been calculated from
the shower development curves given
by these authors (see figure 3.22).
The results for λ given in this figure
are not directly comparable with the
summary of Murthy et al.(1968a) as
slightly different values have been
used for the exponent of the integral
number spectrum in deducing λ from the
measured Λ .

Author	Shower size	Λ g cm^{-2}	Shower attenuation length $\lambda = \gamma_2 \Lambda$ $(g\ cm^{-2})$
Bennett et al. (1962)	$(1-3)10^7$	$111+7$	222 ± 14
"	$(3-10)10^7$	137 ± 13	206 ± 20
"	$(1-6)10^8$	153^{+34}_{-23}	230^{+51}_{-35}
Rossi (1960)	$1.2.10^6-1.8.10^7$	113 ± 9	226 ± 18
Kozlov et al. (1973)	$8.5.10^7$	126 ± 15	189 ± 22
Malos (1960)	3.10^5	125^{+19}_{-17}	163^{+25}_{-22}
"	$8.5.10^5$	107^{+16}_{-19}	214^{+32}_{-38}

Table.5.2   The measured absorption length of number spectrum Λ deduced from zenith angle distribution. The attenuation length of the shower particles λ has been calculated multiplying Λ by the exponent of the integral number spectrum.

Author	Shower size	Barometric Coefficent β %(Cm Hg)$^{-1}$	Temperature Coefficient % Co^{-1}	Mass absorption β %(Cm Hg)$^{-1}$	Λ g cm^{-2}	Shower Attenuation length $\lambda=\frac{1}{2}\Lambda$ (g cm^{-2})
Bennett et al (1962)	2.10^4	-11.4 ± 0.2	-0.27 ± 0.02	-	120 ± 2	156 ± 3
"	6.10^4	-11.6 ± 0.2	-0.06 ± 0.03	-	127 ± 3	165 ± 4
"	3.10^5	-11.7 ± 0.3	$+0.12\pm0.05$	-	133 ± 5	173 ± 7
"	$1.4.10^6$	-10.1 ± 0.7	$+0.46\pm0.10$	-	185 ± 20	370 ± 40
"	8.10^6	-11.4 ± 2.0	$+0.66\pm0.30$	-	172^{+70}_{-40}	344^{+140}_{-80}
Citron(1958)	2.10^3	-	-0.12 ± 0.03	-10.6 ± 0.4	138 ± 4	178 ± 5
"	10^4	-	-0.34 ± 0.03	-12.1 ± 0.4	121 ± 3	157 ± 5

Table 5.3   The measured absorption length of number spectrum Λ deduced from the method of barometric coefficient.   The attenuation length of the shower particles λ has been calculated multiplying Λ by the exponent of the integral number spectrum (see the text).

shown in figure 5.4 were obtained at 260 m. above sea level).

Some of the dispersion of the experimental data of figure 5.4 (in particular for $N \gtrsim 10^6$) can be understood since different points were measured with apparatus of different geometry. Different experiments emphasize the particle densities at different distances from the axis of the shower. Now on the one hand the average age of the electronic component varies with radius (see section 2.2) and on the other hand the proportion of the muons among the particles recorded at large core distances increases. Thus one expects to over estimate the measured absorption length of the EAS spectrum recorded at large core distances. This effect could be seen in the measured data of Bennett et al., shown in figure 5.4, for $N > 10^6$, where the coincidence rate of showers recorded by three or four scintillators, a few hundred metres apart, have been measured as a function of barometric pressure.

The agreement obtained measuring Λ, by both methods, (zenith angle distribution and barometric coefficient) in the present experiment is expected, since Λ has been measured in showers which fall at median core distances varying from $\simeq 10$ m. to $\simeq 5$ m. for the E, F and G series.

5.7   Discussion

Shower development curves have been calculated theoretically by means of model calculations. In general the calculated attenuation length of shower particles λ, based on the standard CKP model, predicts a higher value for λ compared with the experimental data. The calculations also predict a rather

stronger dependence of λ on shower size than is indicated by the experimental data. Dixon et al. (1974) have calculated the attenuation length of shower particles under Approximation B for electromagnetic cascades using a standard CKP model. They show that $\lambda_B = 25.0$ Ln N + 95.0 g cm^{-2}. This indicates that λ varies from 383 g cm^{-2} at N = 10^5 to 555 g cm^{-2} at N = 10^6 which are much higher than the experimental results (see figure 5.4). Their calculations using Approximation A give even higher values for λ .

Kalmykov et al. (1971) have investigated the problem in more detail. Their calculations show that a model in which multiplicity varies as $n_s \propto (K E_0)^{1/2}$ for $K E_0 \geq 10^5$ GeV and $n_s \propto (K E_0)^{1/4}$ for $K E_0 < 10^4$ GeV predicts a value of $\lambda \simeq 220$ g cm^{-2} for showers in the range of $3.9.10^2 - 8.1.10^5$ at sea level λ has been calculated using the data in table 3 of Kalmykov et al. (1971). This is in better agreement with the data of figure 5.4 (although still too large) in this range of shower sizes. The calculations of Kalmykov et al. includes a mixed composition of primary particles for $E_0 < 3.5.10^6$ GeV per nucleon.

5.8 Conclusion

The absorption length Λ of the EAS number spectrum producing local electron densities of $\Delta_e \geq 20$ m^{-2}, $\Delta_e \geq 80$ m^{-2} and $\Delta_e \geq 233$ m^{-2} have been measured. The measured absorption length is related to the attenuation length of shower particles λ using the weighted value of the exponents of the integral size spectrum capable of producing these density thresholds at the detector. It is concluded that the attenuation length

remains fairly constant at about 170 g cm^{-2} for showers of size $N \simeq 10^5 - 6.10^5$ particles at sea level. The results are compared with other experimental data and reasonable agreement is obtained. The model calculations of Kalmykov et al. (1971) which assume a half law multiplicity in shower development for KE $\geq 10^5$ GeV predict $\lambda \simeq 220$ g cm^{-2} whereas the present measurements show the attenuation length to be 170 g cm^{-2} in the size range $1.5.10^5 - 5.5.10^5$.

CHAPTER 6

ENERGY SPECTRA OF HADRONS IN EAS

6.1 Introduction

It was mentioned in chapter 4 that a good fraction of
the events, obtained in the F series with $\Delta_e \geq 80$ m^{-2}, show
an interaction in the lead absorber above the chamber and in
the iron absorber inside the chamber. These interactions are
due to the existence of high energy hadrons in the core of EAS.

In the present experiment the lead and iron absorbers were
employed as thick targets for hadrons to interact and produce a
nuclear electromagnetic cascade in the targets. The width of
the produced bursts were measured in the flash tube layers below
the lead and iron absorbers. Neutral hadrons interacting in
the iron target were identified as producing no track in Fla
(see figure 3.11).

In a separate experiment the relationship between burst
width and burst size was determined. Thus the next step was
to estimate the primary energy from the measured burst size.
It is necessary therefore, in the analysis of the results of
the experiment to adopt some model for the interaction of the
hadrons in lead and iron absorbers so that a reliable estimate
of the particle energy can be made. It is obvious that one
should know the mass of the primary hadrons. It is assumed
that charged particle induced bursts are produced by pions and
neutral particle induced bursts are produced by neutrons.

6.2   Hadron-induced bursts

6.2.1   Electromagnetic cascade

The theoretical treatment of electromagnetic cascade in various media has been studied extensively by many workers. Broadly speaking there have been two lines of approach namely, (a) The Analytical Method and (b) The Monte-Carlo Method.

(a)   The Analytical Method

Mathematically it is very difficult to derive the number of electrons and photons at a given depth in a substance produced by a primary electron or photon of energy E_0.

Rossi (1952) has discussed the problem in detail considering the various processes such as pair production and Compton scattering for photons and bremsstrahlung and ionisation loss for electrons which occur during the development of the cascade. He introduces the following equations which are called diffusion equations, namely

$$\frac{\partial \pi(E,t)}{\partial t} = \int_E^\infty \gamma(E',t)\,\varphi_P(E,E')dE' + \int_E^\infty \pi(E',t)\,\varphi_E(E',E'-E)dE' - \int_0^E \pi(E,t)\,\varphi_E(E,E')dE'$$
$$- \epsilon(E)\,\frac{\partial \pi(E,t)}{\partial E}$$

$$\frac{\partial \gamma(E,t)}{\partial t} = \int_E^\infty \pi(E',t)\,\varphi_E(E',E)dE' - \int_0^E \gamma(E,t)\,\varphi_P(E,E')dE'$$

where,

$\pi(E,t)\,dE$ and $\gamma(E,t)$ are the numbers of electrons and photons between E and E + dE at depth t respectively.

$\varphi(E, E')$ is the differential probability per radiation length for an electron (photon) of energy E to produce a photon (electron) of energy E'.

To solve these diffusion equations certain simplifying assumptions have to be made. Two methods which introduce two different sets of assumptions are known as Approximations A and B respectively have been discussed by Rossi.

In Approximation A only the loss of energy due to pair-production for photons and bremsstrahlung for electrons have been considered, i.e. it is applicable to those energies large compared to the critical energy. Furthermore the radiation phenomena and pair - production have been described by their asymptotic formulae for complete screening.

Under Approximation B it is assumed that electrons lose their energy by collisions, taking a constant energy dissipation equal to the critical energy of an electron per radiation length. The Compton effect, however, is neglected and the asymptotic formulae for radiation and pair production are used.

It is interesting to note that under both Approximations A and B the cascade curves yield identical results for all materials provided thicknesses are measured in radiation lengths and energies in terms of the critical energy.

The methods of Approximations A and B which utilise what are known as functional transformations to solve the diffusion equations give a fairly complete solution to the problem in light elements. These methods, however, break down in light elements when the energy of the primary photon or electron is comparable to the critical energy. The method is also invalid for high Z materials since in heavy elements (i) the scattering of shower

particles is very large and (ii) the total photon absorption is strongly energy dependent.

The method applicable to high Z elements has been described by Ivanenkov (1957) and is known as the method of moments. Ivanenkov and Samasudov (1967a, 1967b) have produced a series of shower curves which apply to copper, iron, aluminium, lead and graphite absorbers. The curves cover a wide range of primary energies with different cut-off energies of produced particles. The curves have been calculated taking into account the energy dependence of the total photon absorption coefficient and also includes the effect of the increased track length due to multiple scattering of the shower particles.

The curves give 5 - 10% accuracy. The degree of accuracy obtained by the method of moments depends on the order to which the moments are calculated (Ivanenkov and Samasudov have calculated the first four moments to obtain the transition curve).

The results of shower curves (transition curves) calculated by Ivanenkov and Samosudov (1967a, 1967b) for photon initiated showers are plotted in figures 6.1 and 6.2 for lead and iron absorbers respectively. The energy cut-off for both curves are about 1 MeV.

Coats (1967) has surveyed the experimental results on electron-photon cascade showers and finds that experimental measurements of Murzin et al. (1963) and Takbaev et al. (1965), normalised to 100 GeV incident on an iron absorber, agree quite well with the theoretical curves due to Ivanenkov and Samosudov, as shown in figure 6.3a.

(b) The Monte-Carlo Method

This method gives fairly accurate results for shower
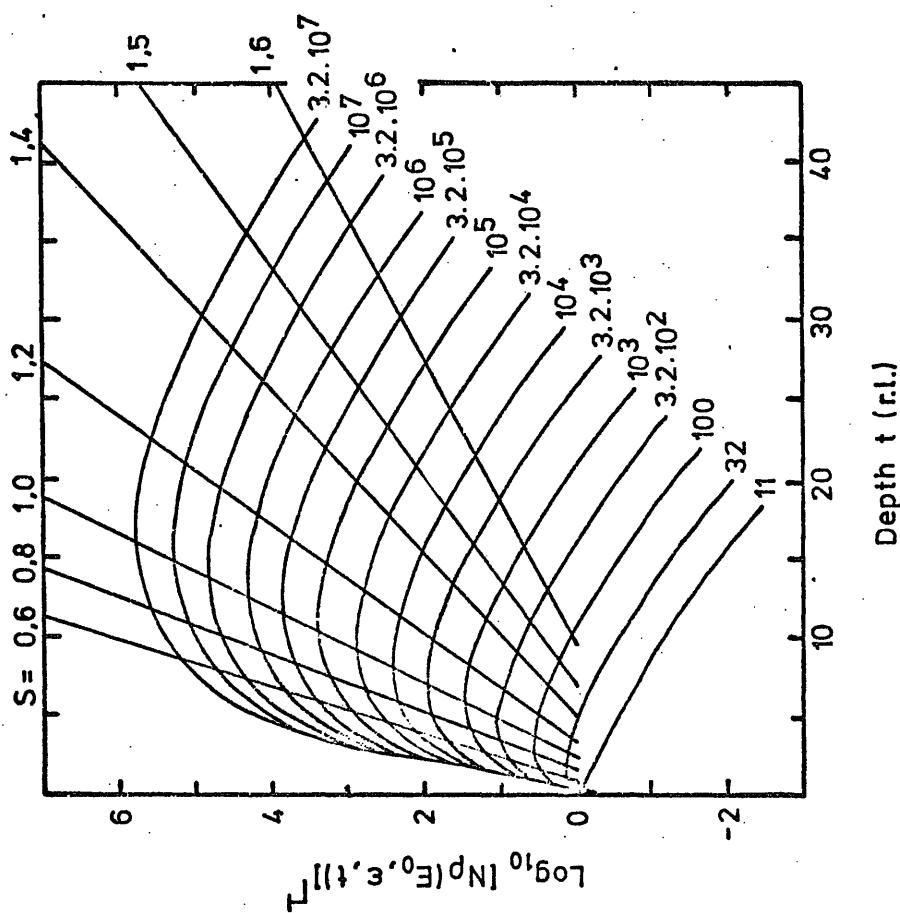
Figure 6.1 Transition curves for photon-induced cascades in lead, predicted by Ivanenkov and Samosudov. The numbers by each curve refer to the energy of the primary photon. All energies are in units of 0.437β, where β is the critical energy in lead and taken as 7.5 MeV. The cut-off energy ε is 0.35 or $\cong$ 1.16 MeV. Lines of constant S (age parameter) have been calculated from Approximation A.
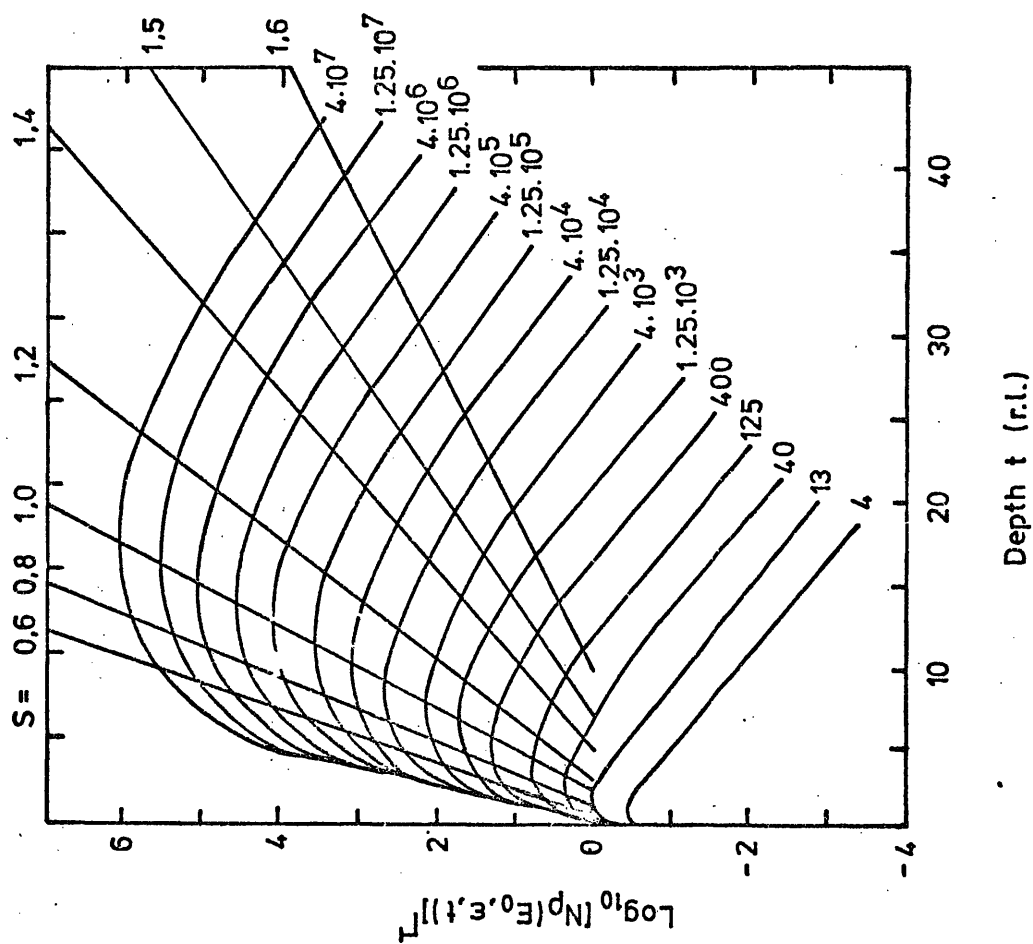
Transition curves for photon-induced cascades in iron, predicted by Ivanenkov and Samosudov. The numbers by each curve refer to the energy of the primary photon. All energies are in unit of 0.437β where β is the critical energy in iron and is taken as 21 MeV. The cut-off energy ε is 0.1 or 0.92 MeV. Lines of constant S (age parameter) have been calculated from Approximation A.
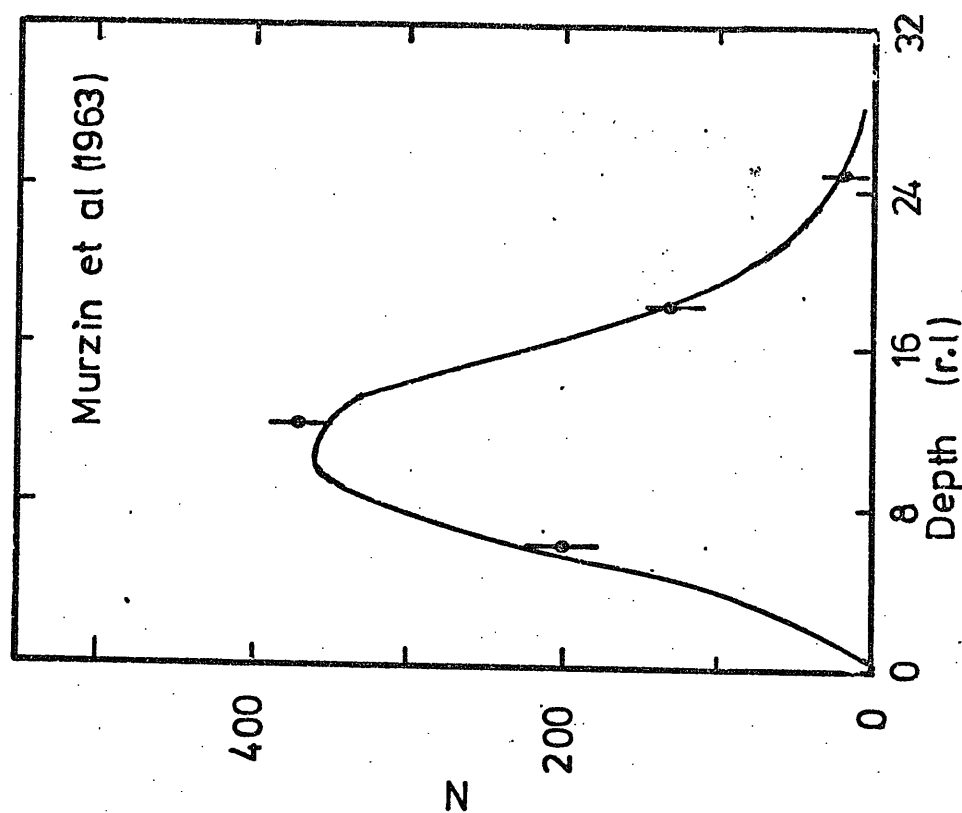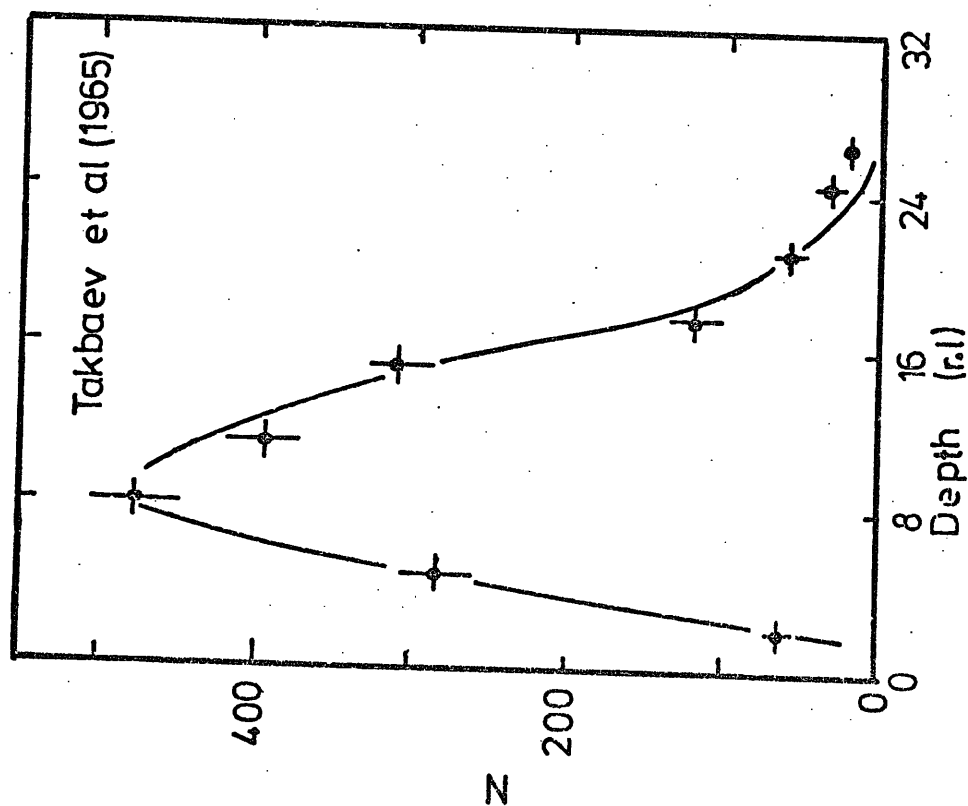
Figure 6.2

Figure 6.3a.   Comparison of the theoretical curves of Ivanenkov et al. (1959) with experimental results of Murzin et al.(1963) and Takbaev et al. (1965).
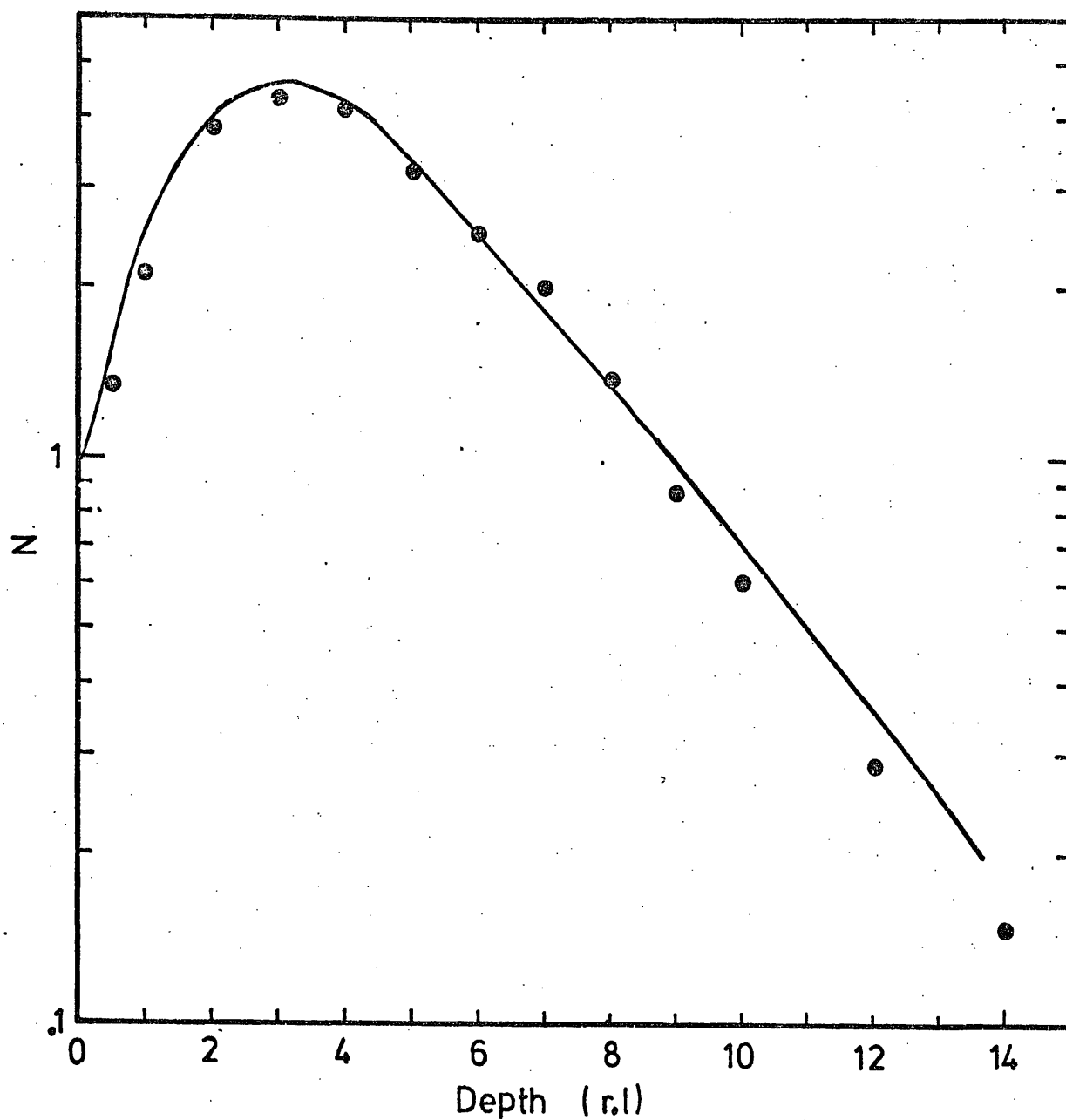
Figure 6.3b   Comparison of theoretical curve of Ivanenkov and Samusodov (1967a) with the Monte-Carlo calculations of Messel and Crawford (1970), shown by solid circles.   The comparison has been made for a 1 GeV photon incident on the lead absorber.   The cut-off energy E_c is 10 MeV.

development since one can follow the primary electron or photon continuously through the absorber. This means that one is able to use exact interaction probabilities.

Many groups have calculated the development of shower curves through a variety of targets which contain detailed information about the cascade, i.e. longtitudinal and lateral distribution of produced particles (Messel and Crawford, 1970).

Figure 6.3b shows a comparison between the Monte-Carlo simulation of Messel and Crawford, for a 1 GeV primary photon induced shower in lead, with the calculations of Ivanenkov and Samosudov, with energy cut-off of 10 MeV. As figures 6.3a and 6.3b indicate there is reasonable agreement between the transition curves calculated by Ivanenkov and Samusodov and Monte-Carlo simulation and experimental observation. Thus the calculation of Ivanenkov and Samusodov are assumed to be correct for cascade calculations.

6.2.2 Nuclear Model

An average treatment was introduced to follow the nuclear cascade produced by a primary charged pion incident vertically on the top of the lead and iron absorber. The properties of the model introduced for nuclear interaction can be summarised as follows.

(a) Energy loss of hadrons between successive nuclear interactions is negligible.

(b) In each interaction pions lose all their energy, i.e. the inelasticity of pions is taken to be equal to unity.

(c) The average multiplicity, n_S, is given by $n_S = 3 \ A^{0.19} \ E_o^{1/4}$ where A is the atomic weight of the absorber and E_o is the primary

pion energy in GeV.

(d) The secondary produced particles are pions, these being equal numbers of π^+, π^-, and π^0 mesons produced.

(e) The produced pions have on average equal energies and the energy distribution in the laboratory system is given by

$$S(E)\ dE = \frac{1}{E'}\ e^{-E/E'}\ dE,$$ where $S(E)\ dE$ is the differential probability of a secondary pion having energy E to $(E + dE)$ and E' is the average energy of the produced pions, i.e. $E' = \frac{E_0}{n_s}$.

The above mentioned properties of nuclear interactions are nearly the same as has been summarised by Cocconi (1965). The mass dependence of the multiplicity law (item c) is taken from a survey made by Jones et al. (1970). The distribution in energy of produced pions is the same as given by de Beer et al. (1966) for the forward direction in the laboratory system. The result is based on the CKP model (Cocconi, Koester and Perkins, 1961).

Knowing the properties of nuclear interactions, the nuclear cascade in the lead and iron absorber of the chamber has been determined by the following procedure.

The block of absorber was divided into four layers A, B, C and D each having equal thickness. The primary pion was allowed to interact in each of these layers with corresponding probabilities calculated from

$$P(x) = \left[1 - \text{EXP}\left(- x/\lambda_\pi\right) \right]$$ where $P(x)$ is the total probability that a pion interacts in a thickness x and λ_π is the interaction length of pions.

After the first interaction the total number of produced secondary charged pions with energies greater than 1 GeV and

the total number of produced secondary neutral pions of
$E \geq 0.2$ GeV were calculated (see item e of the nuclear model).
Thus the mean energy of charged pions with 1 GeV cut-off energy
is $(1 + E')$ and the mean energy of neutral pions with 0.2 GeV
cut-off energy is $(0.2 + E')$ where E' is the average energy
of produced pions in GeV (see item e of the nuclear model).
It was assumed that produced neutral pions decay immediately
to two photons of equal energies and the produced charged pions
are allowed to interact more in the absorber.   The average
depth of successive interactions was calculated from the
following ratio

$$\bar{x} = \frac{\int_0^{\infty,x} \exp(-x/\lambda_\pi) \, x \, dx}{\int_0^{\infty,x} \exp(-x/\lambda_\pi) \, dx} \quad \text{or}$$

$$\bar{x} = \lambda_\pi + \frac{x}{\exp(-x/\lambda_\pi) - 1} \quad \text{where x is the remaining}$$

thickness of the absorber after the first interaction (the
first interaction is assumed to occur at the middle of layers
A, B, C and D) and λ_π is the interaction length of pions.
The nuclear cascade was terminated when the number of produced
neutral pions with energy greater than 0.2 GeV fell below one.

The energy cut-off of 1 GeV for charged pions is based on
the fact that the inelastic cross section of interaction of
pions falls off rapidly for energies less than one GeV (Hayakawa,
1969).   The energy cut-off of 0.2 GeV was introduced for
neutral pions since photons, produced from the decay of π^o
almost at rest would not contribute significantly to the
electromagnetic cascade.

For primary protons the calculation was also carried
out for the iron absorber. The same model for nuclear
interaction, described above was adopted for the proton
induced cascade except that the inelasticity of protons in
iron was assumed to be 0.63, i.e. the multiplicity law for
protons follows as,

$$n_s = 3 \ A^{0.19} \ (K \ E)^{1/4}$$

where K = 0.63 and primary proton recoils with 37% of its
primary energy. The uncertainty arises in the average
value of K for protons. Bradt and Rappaport (1967) take
the inelasticity of protons to be a flat distribution ranging
from 0.25 to 0.75 for protons interacting with air nuclei.
Jones (1969) takes a beta distribution for the inelasticity of
protons. Jones et al. (1970) suggest that the inelasticity
depends on the mass number of the target and they measure the
inelasticity of protons interacting with iron nuclei to be
K = 0.63, a value which is adopted for the present calculations.

6.2.3 One dimensional calculation of the nuclear-electromagnetic cascade

The nuclear - electromagnetic cascade has been invest-
igated intensively in the past, longtitudinally and laterally,
and the results of calculation has been compared with experi-
ments to draw conclusions about the validity of the assumed
models for nuclear interactions at high energies (Jones, 1969
and Pinkau and Thompson 1966).

The average behaviour of the nuclear cascade mentioned in
6.2.2 determines the spectrum of produced neutral pions with
energy E as a function of depth, for a hadron incident on the
top of the absorber with energy E_0. Taking this calculation

and the transition curves of Ivanenkov and Samusodov (1967a, 1967b), for photon initiated showers in lead and iron absorbers (see figures 6.1 and 6.2), one can derive the expected number of particles below lead and iron absorbers as a function of primary energy. The results of calculations for charged pions incident on the top of lead and iron absorbers and for proton initiated bursts in the iron are plotted in figure 6.4. The calculation was carried out for 10, 50, 500 and 5,000 GeV hadron energies. Using the same procedure mentioned above, Saleh (private communication) has calculated burst energy relationship for proton incident on the top of lead absorber (15 cm depth). His results are also shown in figure 6.4.

6.2.4   Probability distributions

The average treatment introduced for the nuclear electro-magnetic cascade also gives information about the probability of observing a particular burst size below the lead and iron absorbers for different primary hadron energies E_o.

The variation of the produced burst size below the lead and iron absorbers as a function of the depth of the first interaction are shown in figures 6.5 and 6.6 respectively for different pion energies. As figure 6.6 shows there is no maximum for high energy primary pions, a fact which indicates that high energy pions incident on the top of the iron produce cascades which do not develop fully in the absorber. The flattening of burst size – energy relationship which occurs at high energy for the iron absorber also indicates that the shower can not develop fully (see figure 6.4). The integral probability of observing $\geq N$ particles below the lead and iron

The graph shows Burst Size N (vertical axis, 10^1 to 10^4) versus Energy E (GeV) (horizontal axis, 10^1 to 10^4).

Legend:

	Primary	Absorber
▣	Pion	Lead
●	//	Iron
◉	Proton	//
○	//	Lead
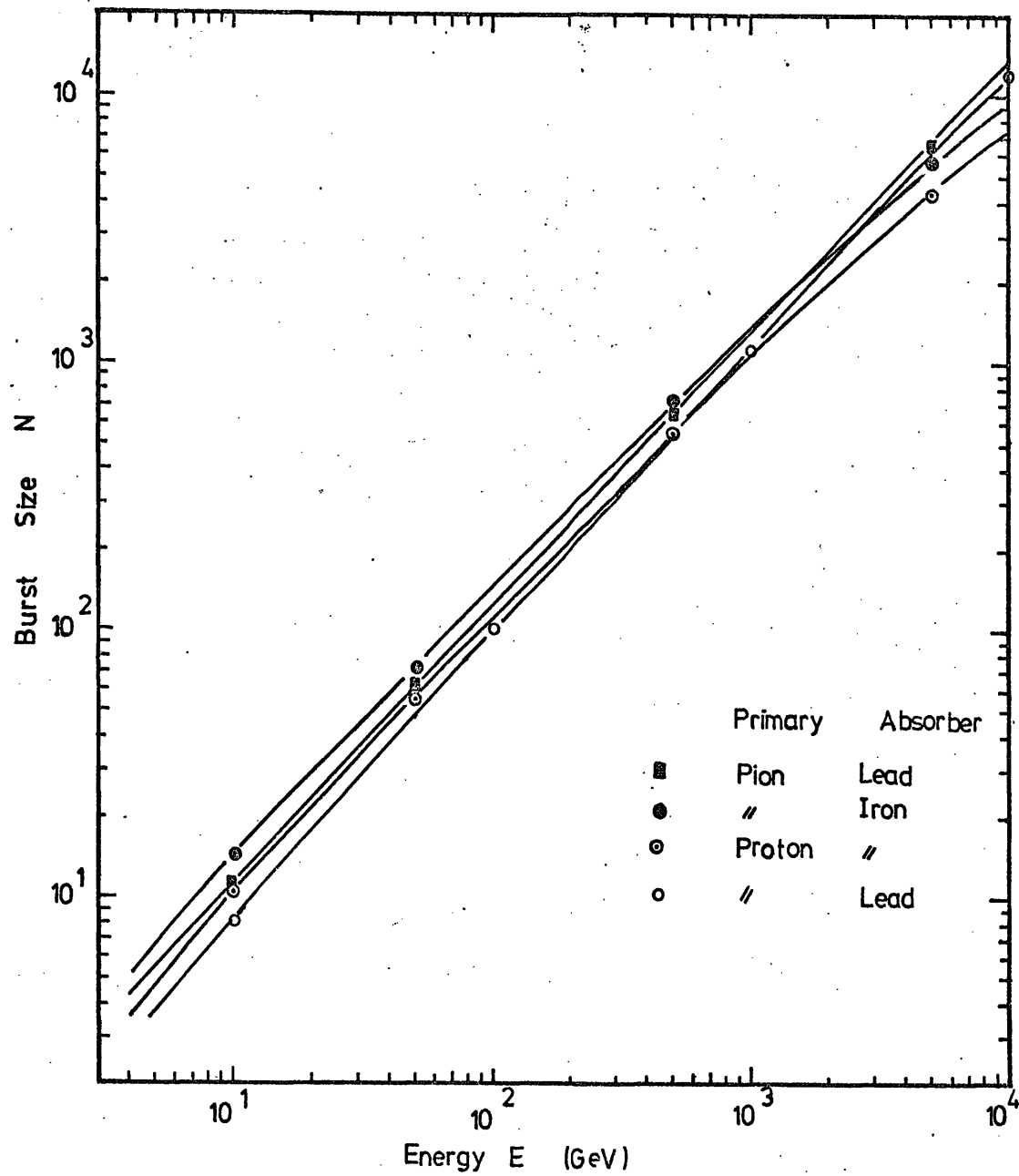
Figure 6.4   The calculated average burst size produced below a 15 cm. of lead or a 15 cm. of iron absorber as a function of primary pion or proton energy.
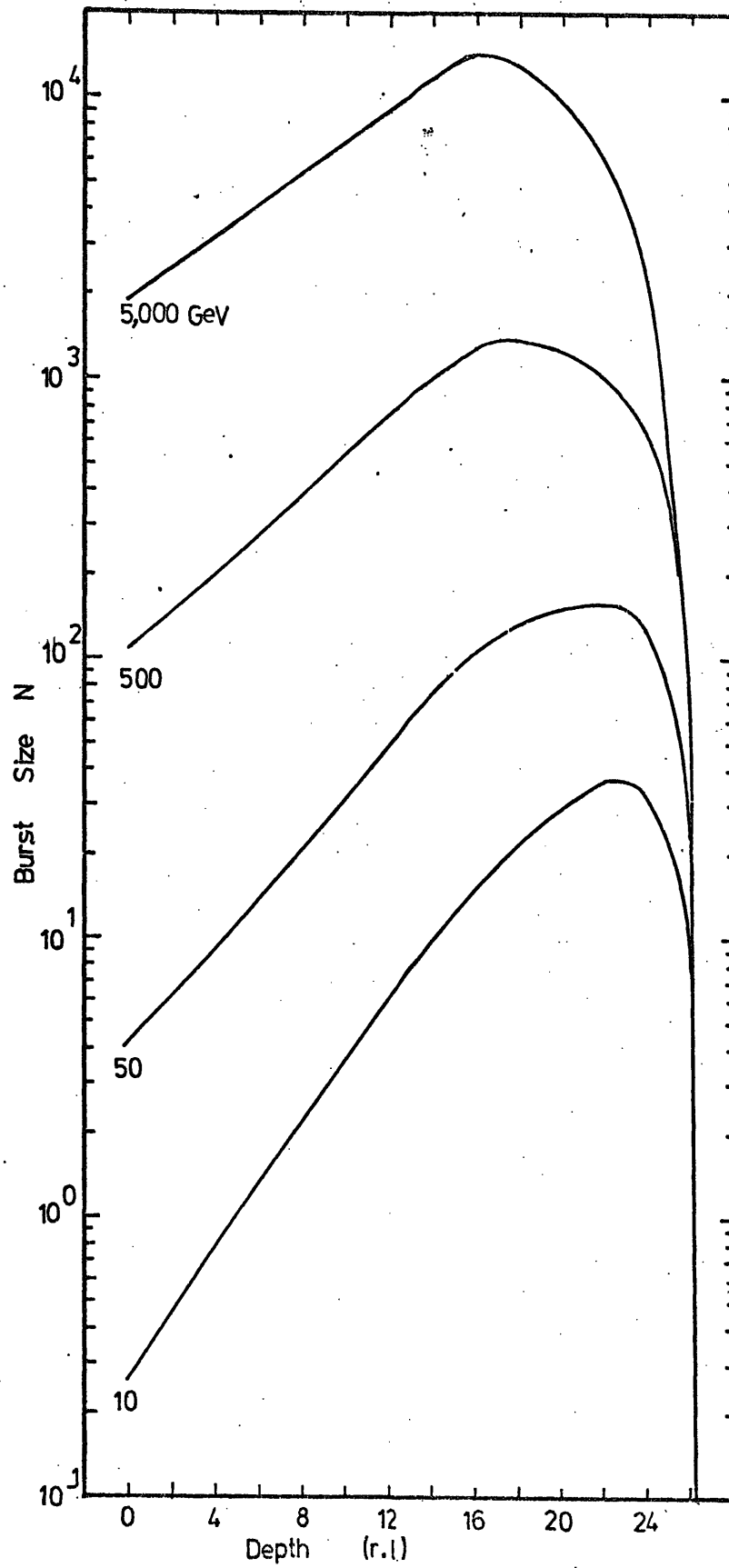
Figure 6.5   The calculated burst size, N, below 15 cm. of lead for an incident pion energy of E GeV (indicated for each curve) as a function of the depth of the first interactions.
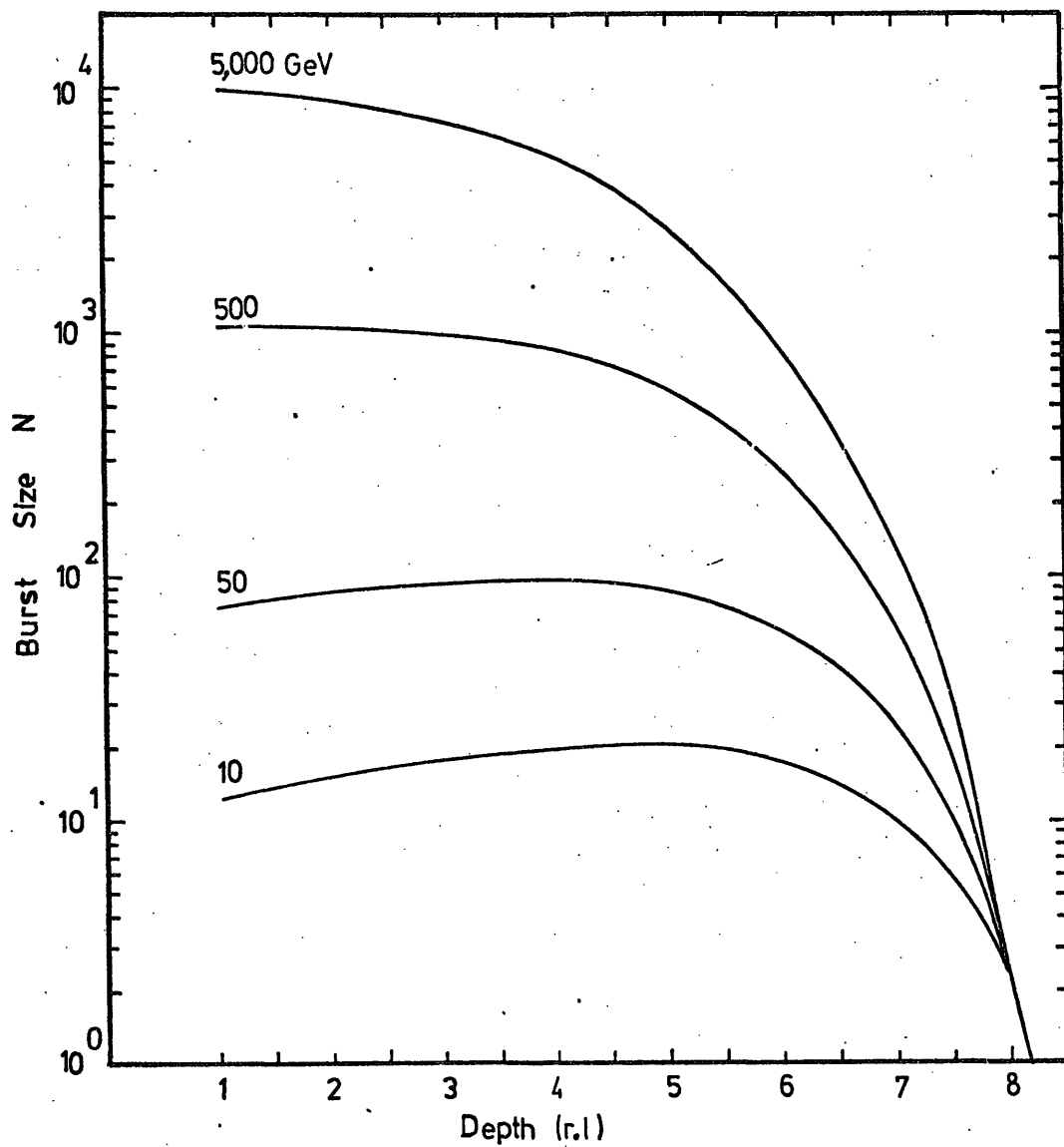
Figure 6.6   The calculated burst size, N, below 15 cm.
              iron for an incident pion energy of E GeV
              (indicated for each curve) as a function
              of the depth of the first interaction.

absorbers are shown in figures 6.7 and 6.8 respectively, for pion induced showers. To derive these curves the calculated probabilities are corrected for the probability of pions which do not interact in the lead and iron absorbers.

The numerical constants adopted for the present calculations, mentioned above, are shown in table 6.1.

6.3 Burst width - burst size relationship

6.3.1 Introduction

The problem of the nuclear - electromagnetic cascade discussed so far has been treated in one dimension. The produced secondary particles, however, deviate from the direction of the primary particle and thus the cascade develops laterally as well as longtitudinally. The procedure is the same as mentioned in chapter 2 for the development of EAS in the atmosphere. Thus one expects to be able to measure the width of the produced bursts below the target if one employs a visual detector to study the burst phenomena.

The burst width is the parameter measured in the present experiment to derive the energy spectra of hadrons in EAS in the F series. The widths of the bursts produced, in the lead and iron absorbers of the flash tube chamber, were measured in the top layers of Fla and Flb respectively (see figure 3.11). This measured parameter was then converted to burst size which was used to determine the energy spectra of hadrons in EAS. Thus it is essential to obtain the relationship between burst width and burst size below the lead and iron absorbers. The results of the relationship between burst width and burst size are taken from Saleh (private communication) and will be described in the next section.
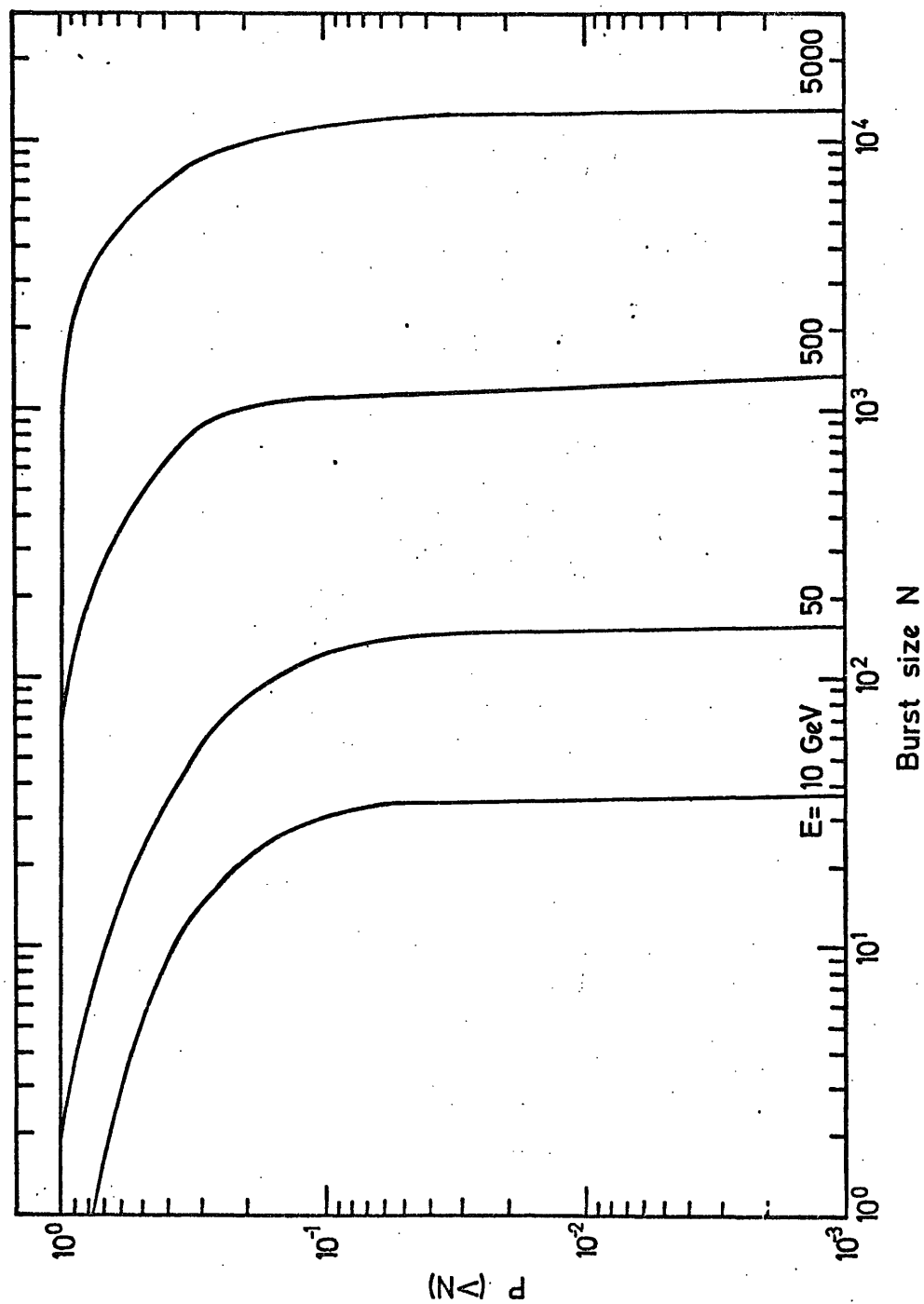
Figure 6.7 The calculated probability of observing a burst of size ≥ N below 15 cm of lead for a pion with energy E GeV (indicated for each curve) incident on the top of lead absorber.
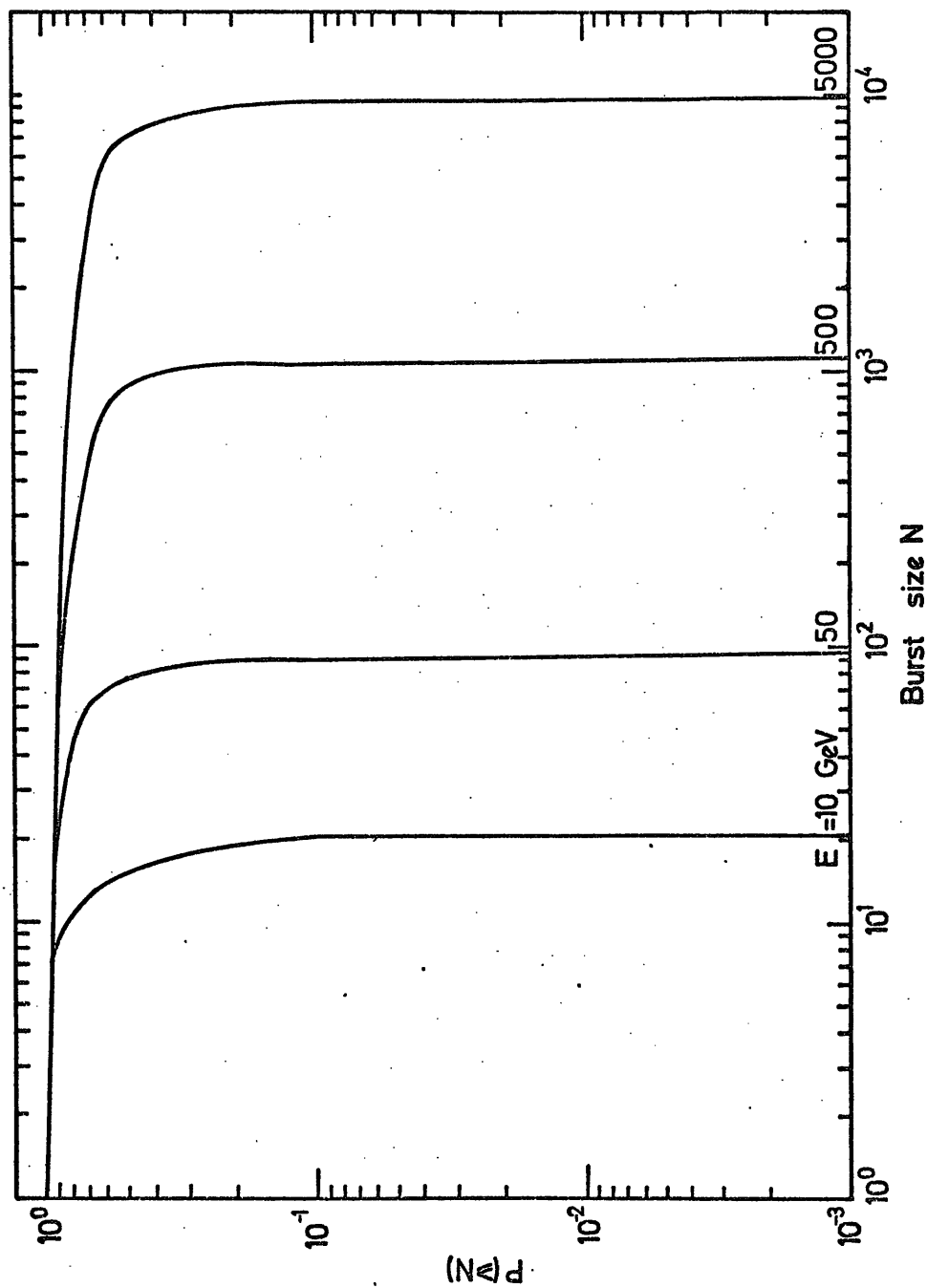
Figure 6.8   The calculated probability of observing a burst of size ≥ N
below 15 cm. of iron for a pion with energy E GeV (indicated
for each curve) incident on the top of the iron absorber.

Substance	Density (g cm^{-3})	Radiation length x_0 (g cm^{-2})	Pion interaction length	Proton interaction length
Lead	11.34	6.5	34.54 x_0	33.08 x_0
Iron	7.6	14.1	11.60 x_0	9.94 x_0
Aluminium	2.70	24.5	5.37 x_0	4.25 x_0
Glass	2.50	26.3	5.01 x_0	3.95 x_0

Table 6.1   A list of numerical constants used in the present calculations.

6.3.2 Experimental arrangement

The flash tube chamber was modified such that the burst
size produced in the lead absorber could be measured. This
was done by positioning a plastic scintillator (called scint-
illator c) below the lead absorber. Since there was enough
space between the lead and Fla (see figure 3.11) there was
no need to change the dimensions of the chamber. The flash
tube layer Fla was also brought forward by 15 cm so as to
completely cover the iron absorber in order to facilitate the
identification of neutral hadrons producing bursts in the iron.
A scale diagram of the modified chamber is shown in figure 6.9.
The plastic scintillators A and C were first calibrated by
means of a G-M telescope using the same procedure as described
in chapter 3 for the calibration of the proportional counter.
The mean pulse height of the single particle distribution was
used to determine the relative energy loss of a single particle
in traversing scintillators A and C.

The triggering requirement was a burst of particles
recorded by either plastic scintillators A or C with a minimum
size. For each trigger the pulse heights due to the passage
of the burst through the plastic scintillators A and C was
photographed by an open camera looking at an oscilloscope.
At the same time the pulse height due to the passage of a
hadron or EAS particle through scintillator M was also recorded
on the same film. In each trigger the flash tubes were also
triggered after a time delay of 20μs (the same as was used
in the EAS run for the F weries) and photographed. The logic
diagram for the electronics used in the experiment is shown

S   M   N

F1a (8 layers)
IRON
C.
A.
F1b (6 layers)
F2 (52 layers)
F3 (44 layers)
F4a (6 layers)
B.
F4b (8 layers)

LEAD

CONCRETE→

FRONT

SIDE

Scale:- 0 ___ 50cms.
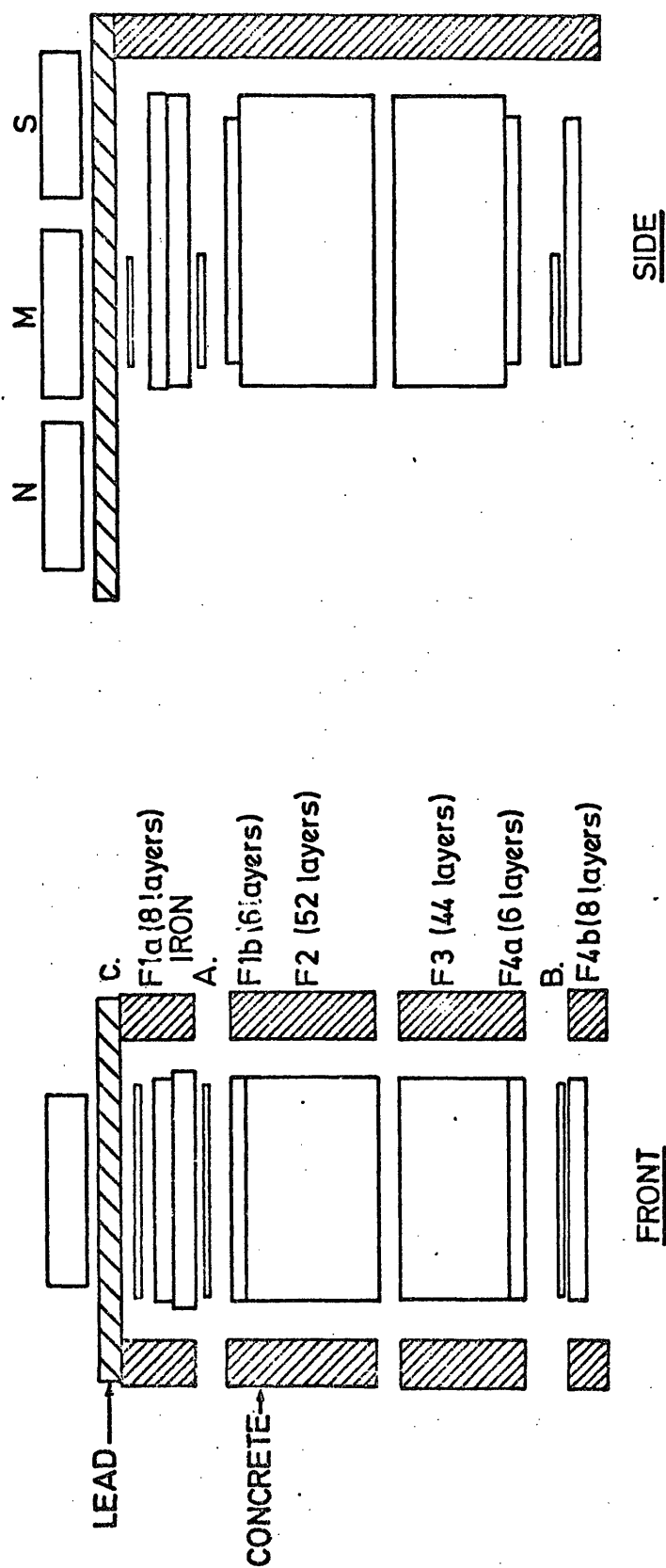
Figure 6.9   Scale diagram of the modified flash tube chamber.

in figure 6.10.

6.3.3 Results

The experiment was carried out for a minimum burst size
ranging from 20 particles up to a few thousand particles.

Since for a certain burst size there is a bias towards
smaller widths, a correction was applied to the measured
burst widths.

An acceptable event is defined as an event in which the
full width of the burst is measurable in the top layers of
Fla and Flb for bursts produced in the lead and iron absorbers
respectively. The width of the burst is defined as the width
in which all the flash tubes are flashed. After plotting the
scatter plot of the measured bursts width - burst size for
lead and iron absorbers, the experimental points were binned
and their means found. A correction was applied to the burst
width distribution as mentioned above to account for the
decreasing probability of being able to record the burst width
as the latter increased. The correction factor was $(\frac{D-d}{d})$ where
d is the measured width and D is the width of the flash tube
chamber. The results of the burst size - burst width relation-
ship are shown in figure 6.11 for the lead and iron absorbers.

6.4 Measured energy spectra of hadrons in EAS

6.4.1 Basic data

The F series films were scanned using an enlarger which
gave an image size of 1:20 compared to real space. The
criteria for accepted events was the same as mentioned in section
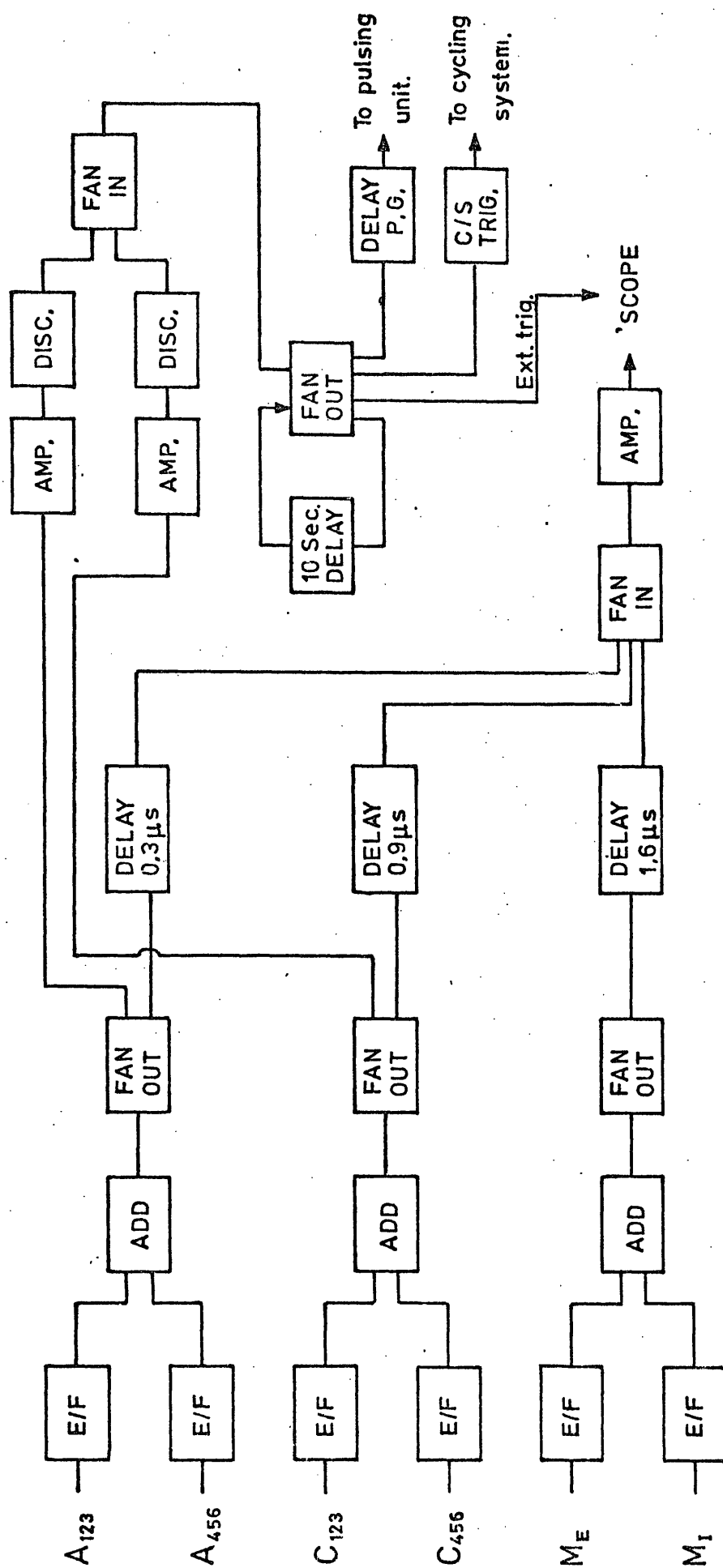
Figure 6.10   Experimental logic for the vertical burst experiment.
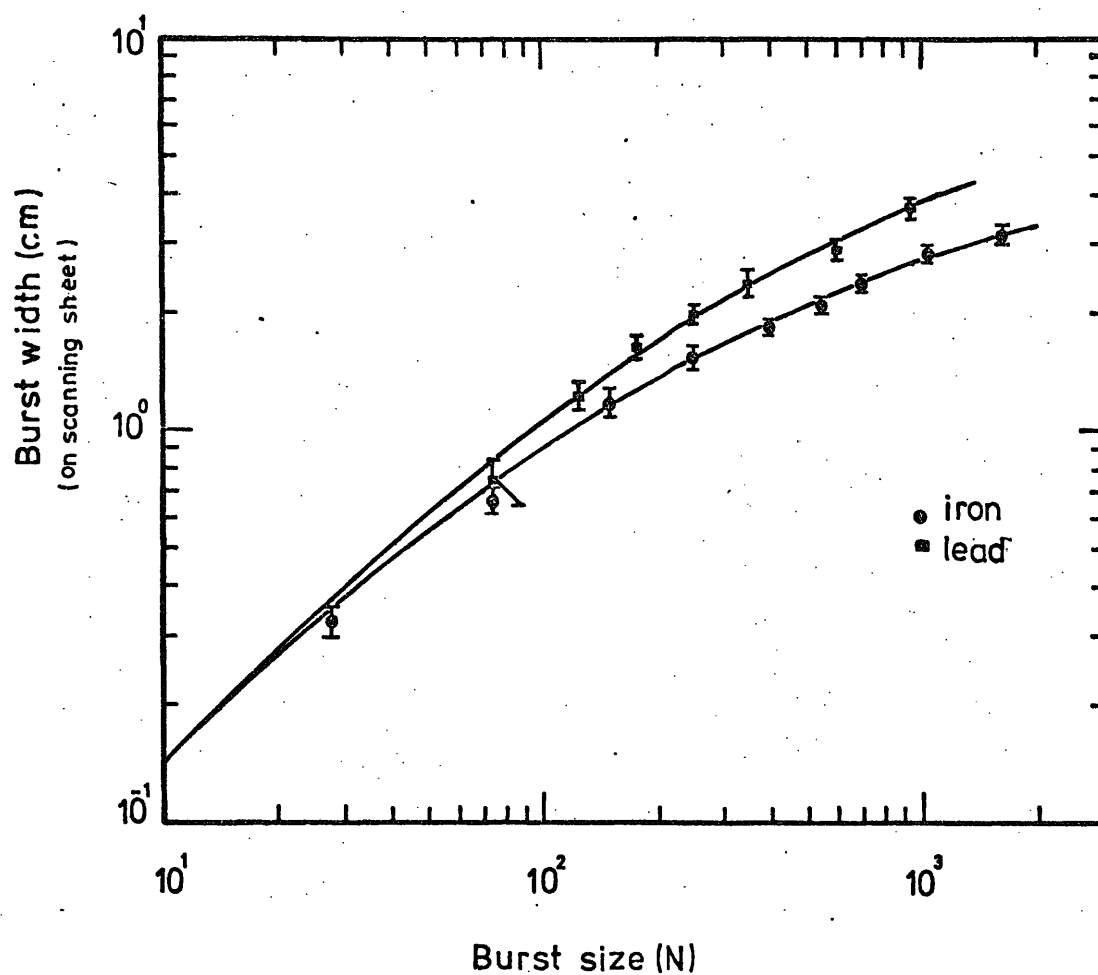
Figure 6.11   The measured burst width - burst size relationship
below the 15 cm. of lead and 15 cm. of iron
absorber.   1 cm. on the scanning sheet corresponds
to 20 cm. in real space.   Time delay = 20 µs
between the occurrence of the burst and the applic-
ation of the high voltage pulse to the flash tubes.

6.3.3, for bursts produced in the lead and charged bursts produced in the iron. Bursts in the iron were recognised as being produced by neutral hadrons if the axis of the burst lay within the dimensions of the chamber and showed no track in Fla (see figure 3.11). For each acceptable event a scale diagram of the event was drawn on the scanning sheet (scale of 1:20) and the burst width of the event was measured.

The following types of burst were observed in the present experiment.

(a) Bursts produced in lead, absorbed by iron.

(b) Bursts produced in lead, developing in iron.

(c) Charged bursts produced in iron

(d) Neutral bursts produced in iron.

(e) Charged and neutral bursts produced in flash tubes.

(f) Bursts produced in the iron which miss Fla, since Fla does not cover all the area of the iron absorber, and develop from the top of F2 and do not show any width in Flb. This type of burst simulates neutral hadron - induced bursts but they are recognisable due to the peculiar shape they produce in the chamber (a step shape of burst).

(g) Events with several primary hadrons.

Examples of bursts observed in the F series are shown in plates 6.1 to 6.4.

A total number of 4,401 events obtained in running time of 5,256.8 hrs were scanned. The results of the measured burst width spectra obtained in the lead, iron and the neutral hadron - induced bursts in iron are shown in figure 6.12. Table 6.2 shows a summary of the experimental data.

Neutral Bursts in Iron

Charged Bursts in Iron

All Bursts in Lead

Burst Width (cm)

FREQUENCY
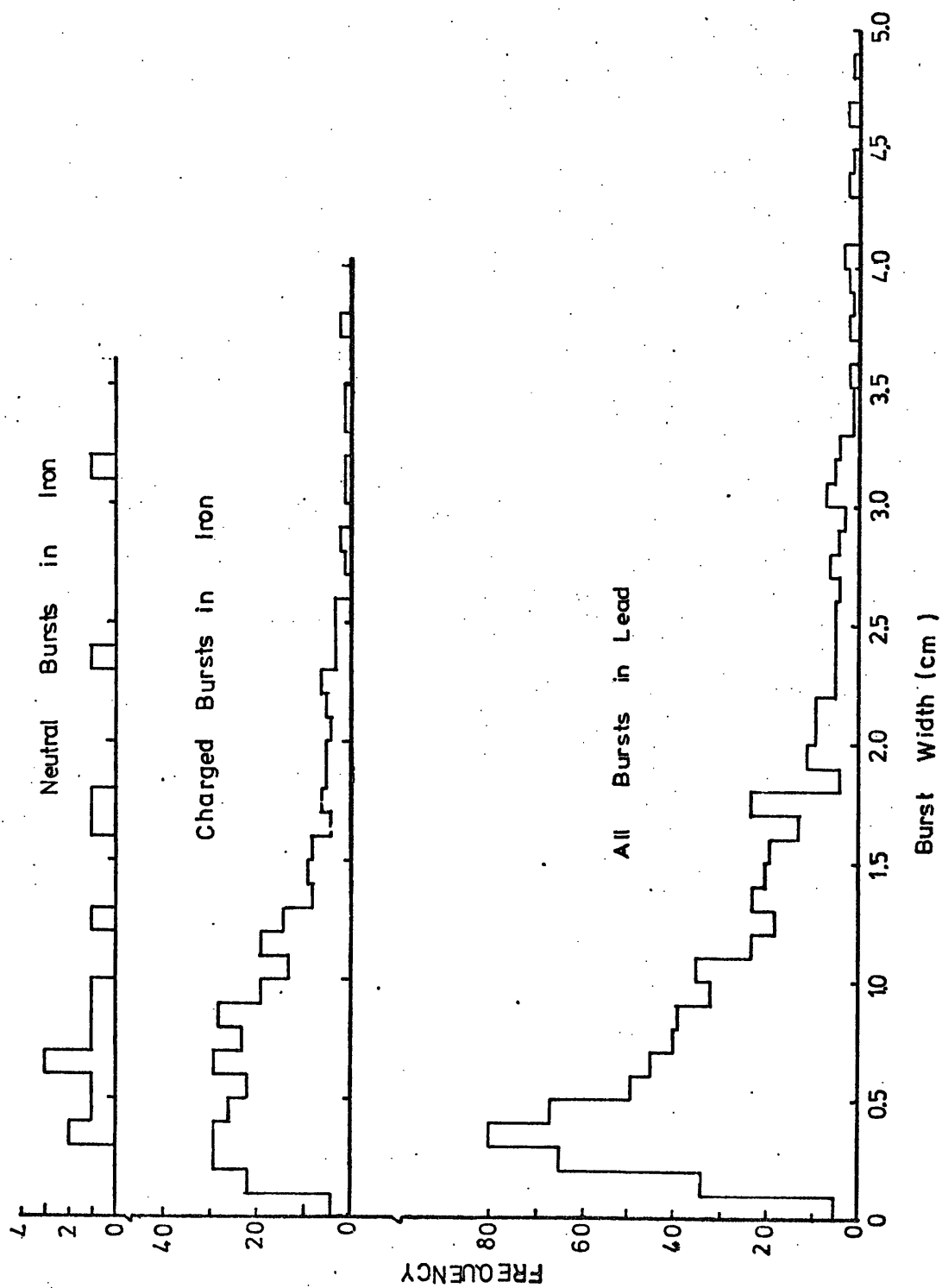
Figure.6.12

The measured burst width spectra for bursts observed under the lead and iron absorbers. 1 cm. on the scanning sheet corresponds to 20 cm. in real space.

PLATE 6.1   Event F35 - 92

A charged particle burst produced
in the lead

N = 225 particles

E = 180 GeV.
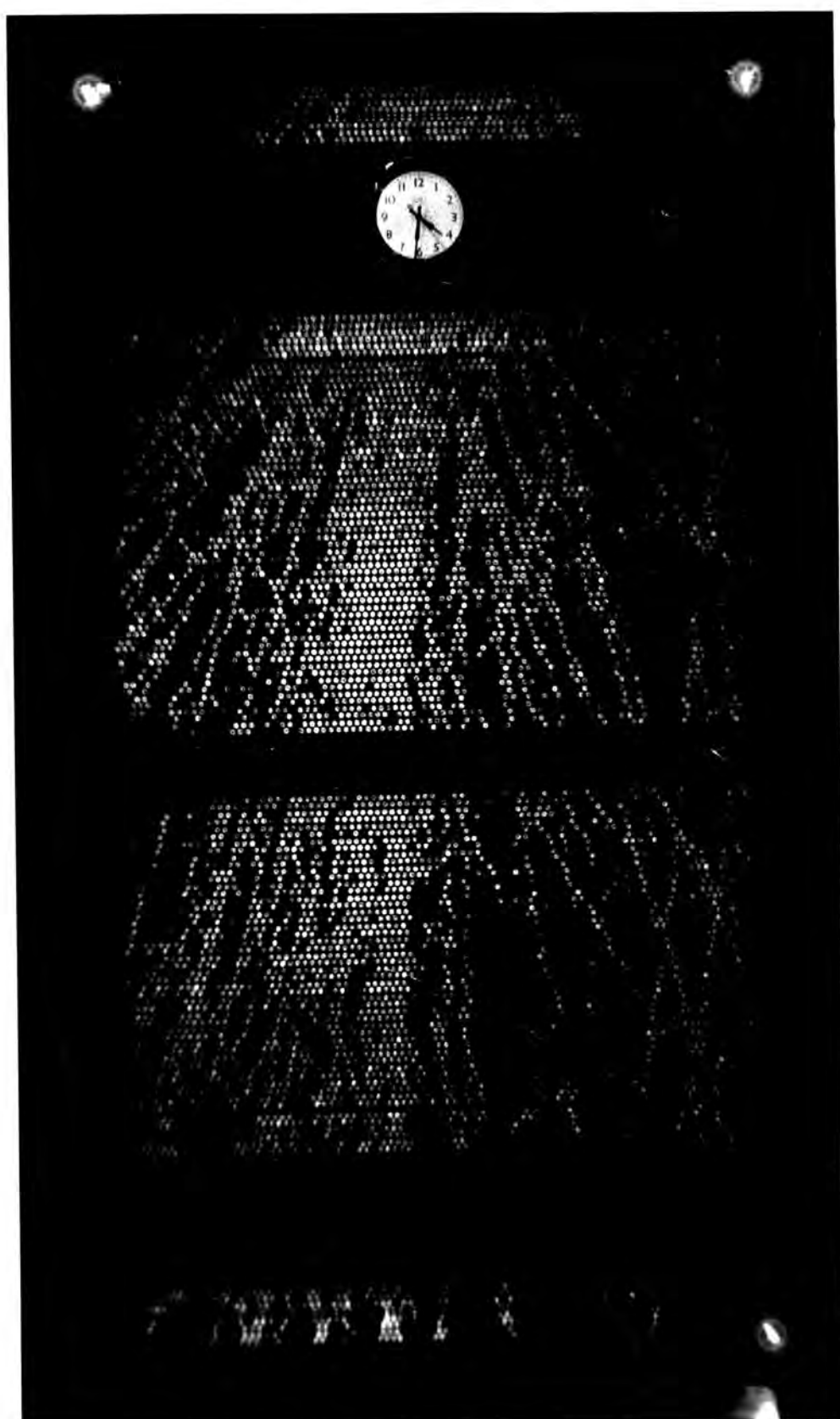
PLATE 6.2   Event F15 - 31
                A charged particle burst
                produced in the iron

                N = 225 particles
                E = 160 GeV.
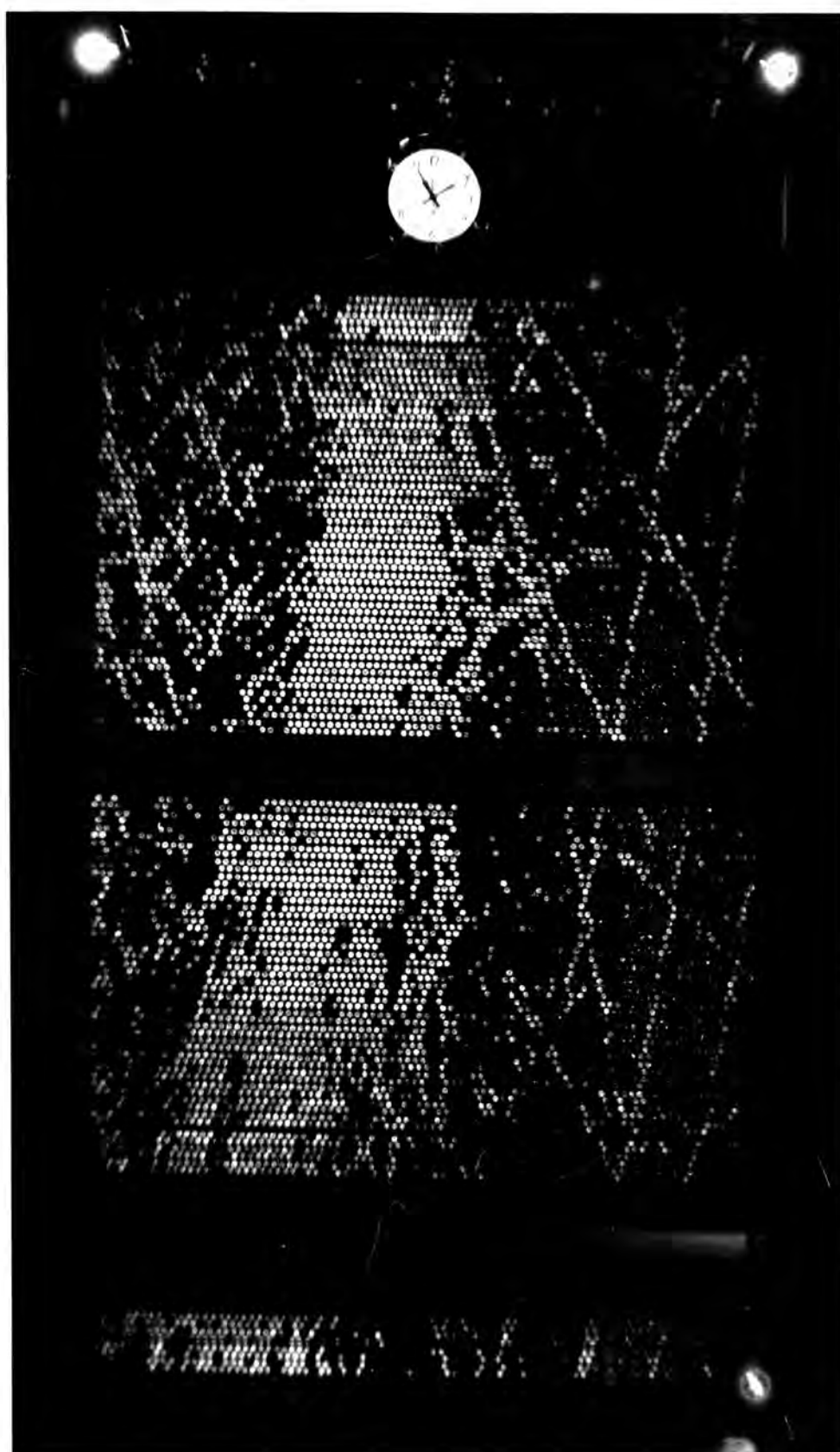
PLATE 6.3   Event F30 - 19

A neutral burst produced in
          the iron

N = 118 particles

E = 108 GeV

6.4.2   Energy spectra of charged and neutral hadrons

The measured burst width spectra below the lead and iron, plotted in figure 6.12, have been converted to burst size spectra by means of the measured burst width - burst size relationship shown in figure 6.11.   From the derived burst size spectra, the energy spectra of hadrons observed in EAS for the F series were calculated.   This was done using the calculated burst size - energy relationship for pion induced bursts in the lead and iron absorbers and the burst size - energy relationship for proton induced bursts in the iron absorber (see figure 6.4).   The former was used to estimate the energy spectra of charged hadrons in EAS and the latter to derive the energy spectrum of neutrons in EAS.   The results are shown in figures 6.13 and 6.14, in differential and integral form respectively.   The spectra, shown in figures 6.13 and 6.14, have been corrected for the aperture of the chamber, i.e. the measured frequency of burst width, d, has been increased by $\frac{D}{D-d}$, where D is the full width of the flash tube layer.

6.4.3   The Corrected energy spectrum of neutral hadrons

The presence of the penetrating component of EAS, in layer Fla of the chamber, could simulate a neutral hadron induced burst in iron, as being a charged hadron.   Thus the measured spectrum of neutral hadrons shown in figures 6.13 and 6.14 (solid curves) should be corrected for this effect. For this purpose the number of tracks, observed in Fla, which could account for a hadron induced burst below iron (except the main track) were counted, as a function of hadron energy.
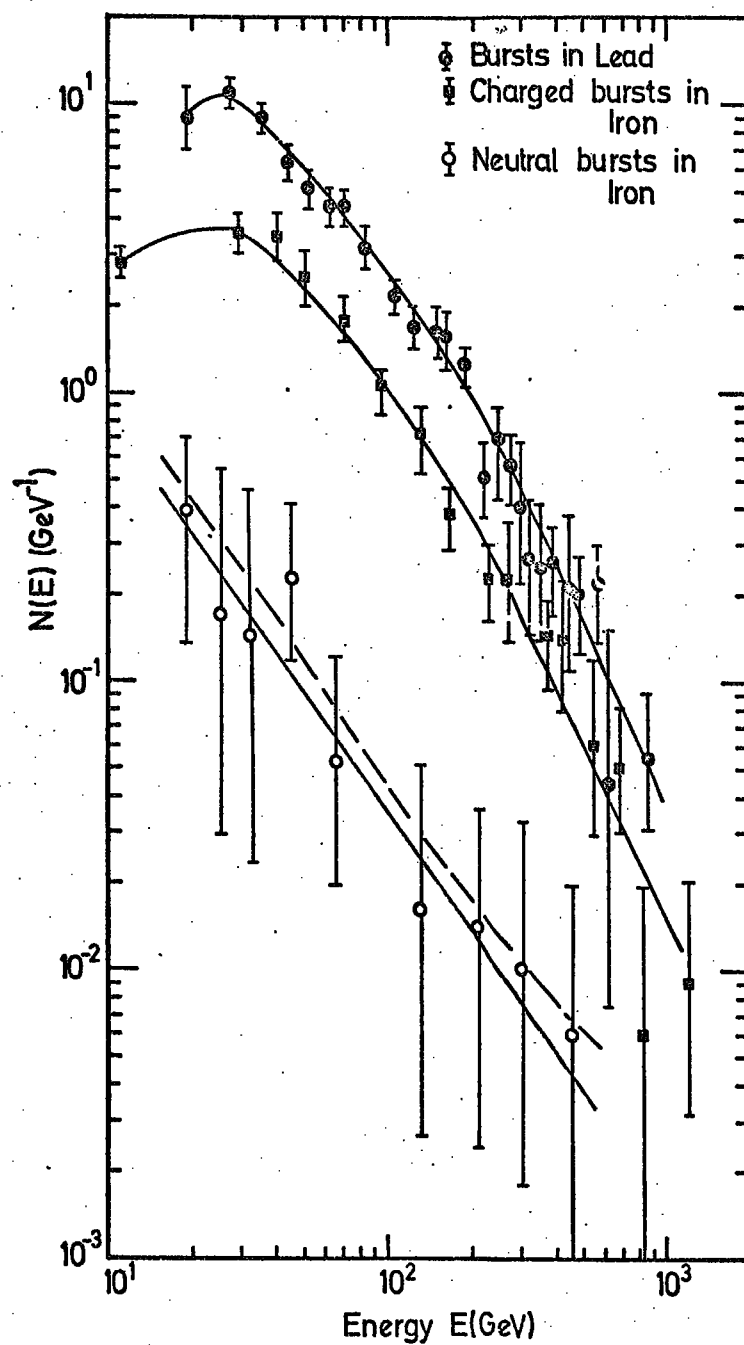
Figure 6.13   Differential energy spectra of all hadrons, charged hadrons and neutral hadrons measured below lead and iron respectively. The dashed spectrum shows the corrected neutral spectrum (see the text).
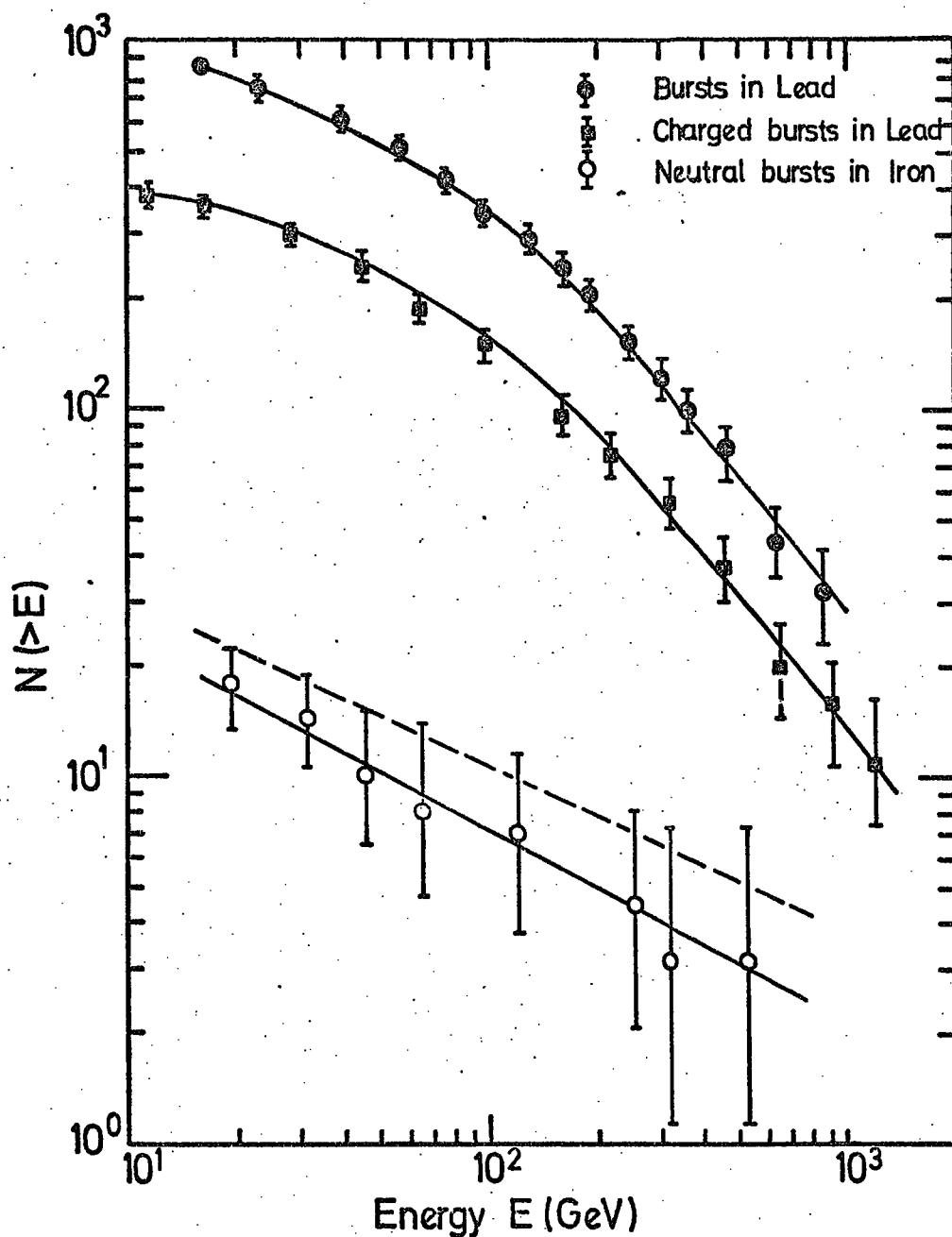
Figure 6.14. Integral energy spectra of all hadrons, charged hadrons and neutral hadrons measured below lead and iron respectively. The dashed spectrum shows the corrected neutral spectrum (see the text). For $E \gtrsim 200$ GeV the charged hadron spectrum can be represented by $E^{-1.15\pm0.16}$.

The results are shown in figure 6.15. It can be seen, that as the energy of hadrons increases, the resolution of the chamber in identifying neutral hadrons decreases. The spectra of neutral hadrons were corrected, using figure 6.15. The results of the corrected spectrum is shown in figures 6.13 and 6.14 (dashed curves).

6.5 Predicted rate of hadrons in region of EAS with a given minimum local electron density

The energy spectra of hadrons in EAS, detected using a local electron density, could be derived using the following measured parameters of EAS:

(a) The lateral density of electrons.

(b) The lateral density of hadrons of a given energy as a function of shower size.

(c) The differential number spectrum of EAS.

The lateral electron density of EAS is taken from the empirical formula given by Greisen (1960), see section 2.2. The analytical formula of the integral number spectrum, derived measuring the density spectrum (see section 3.8.3), was differentiated, namely

$$R(N) \; dN = 4.50 \; N^{-2.3} \; dN \; m^{-2} \; s^{-1} \; st^{-1} \quad N \leq 7.10^5$$

$$R(N) \; dN = 5.56.10^4 \; N^{-3.0} \; dN \; m^{-2} \; s^{-1} \; st^{-1} \quad 7.10^5 < N \leq 3.10^7$$

$$R(N) \; dN = 10.14 \; N^{-2.5} \; dN \; m^{-2} \; s^{-1} \; st^{-1} \quad N > 3.10^7$$

and is assumed for the present calculations. The calculations were also carried out using the differential number spectrum in the form of

$$R(N) \; dN = 78.26 \; N^{-2.5} \; dN \; m^{-2} \; s^{-1} \; st^{-1} \quad N \leq 5.10^5$$

$$R(N) \; dN = 5.56 \; 10^4 \; N^{-3.0} \; dN \; m^{-2} \; s^{-1} \; st^{-1} \quad 5.10^5 < N \leq 3.10^7$$

$$R(N) \; dN = 10.14 \; N^{-2.5} \; dN \; m^{-2} \; s^{-1} \; st^{-1} \quad N > 3.10^7$$
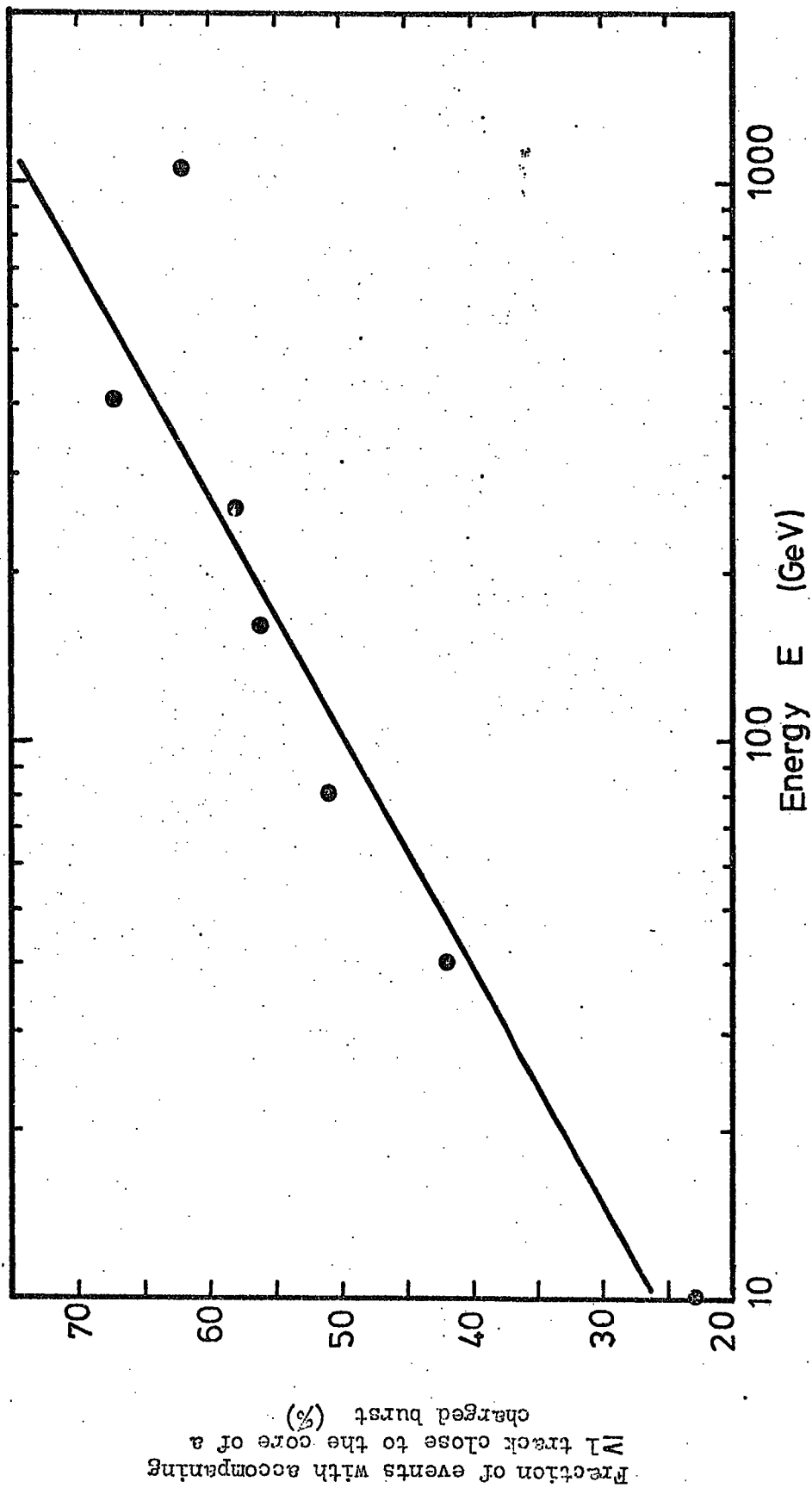
Figure 6.15   Fraction of bursts (%) in which charge of primary hadron could not be defined uniquely as a function of hadron energy. The solid line is the best line through the experimental points.

which is calculated using the survey given by Hillas (1970b).

The lateral density of hadrons, $n(E,r,N)dE \, dr$, of energy $(E, E+dE)$ at core distance of $(r, r+dr)$ in a shower of size N was measured by Kameda et al. (1965). They present their results as

$$n(E,r,N) \, dE \, dr = 0.35 \, N^{0.35} \, E^{-1.2} \exp\left(-\frac{r}{r_0}\right) dE \, dr$$

where $r_0 = 2.4 \, N^{0.32} \, E^{-0.25}$ with E in units of 100 GeV and r in metres.

Integrating the above expression over all core distances one obtains the number of hadrons of ≥ 100 GeV in a shower size N, namely

$$n(N, \geq 100 \text{ GeV}) = 14.2 \left(\frac{N}{10^5}\right)^{1.0 \pm 0.15}$$

In their paper, Kameda et al. give the following expression for the flux of hadrons of $E \geq 100$ GeV in a shower of size N particles,

$$n(N, \geq 100 \text{ GeV}) = 7.2 \left(\frac{N}{10^5}\right)^{0.99}$$

Thus it is necessary to modify the lateral density of hadrons given by Kameda et al. such that it gives 7.2 hadrons of $E \geq 100$ GeV in a shower of 10^5 particles. The modified expression for the lateral density of hadrons has been calculated and the result is as follows

$$n(E,r,N) = 6.26 \cdot 10^{-3} \, N^{0.35} \, E^{-1.2} \exp\left(-\frac{r}{r_0}\right) \text{ m}^{-2} \text{ GeV}^{-1}$$

where $r_0 = 0.19 \, N^{0.32} \, E^{-0.25}$ with E in GeV and N is the shower size in units of single particles.

Integrating the above expression over all core distances, for a fixed shower size, one obtains the energy spectrum of

hadrons in EAS. The slope of the integral energy spectrum of hadrons is found to be -0.75, as reported by Kameda et al., a value which is not consistent with the results of most other workers (see table 2.3). This also is inconstent with the predicted slope, obtained from the Monte-Carlo simulations performed by Bradt and Rappaport (1967) and Grieder (1972), giving -(1 - 1.2) for the slope of integral energy spectrum of hadrons in EAS in the range of E $\simeq$ 100 - 1,000 GeV. The expression given by Kameda et al., however, gives a shower dependence which is consistent with other workers (see table 2.3). Therefore it was assumed that the size dependence, and the expression given for r_0, in the lateral density of hadrons given by Kameda et al., are correct and the following parametarised expression was assumed to represent the lateral density of hadrons.

$$\Delta_h (E,r,N) = A \ N^{0.35} \ E^{-\alpha} \exp\left(-\frac{r}{r_0}\right) \ m^{-2} \ GeV^{-1}$$

where $r_0 = 0.19 \ N^{0.32} \ E^{-0.25}$ with r in metres, E in GeV and N in units of single particle.

To derive the differential energy spectrum of hadrons associated with a local electron density trigger Δ_e , the following integral was evaluated, numerically.

$$R(E, \geq \Delta_e) \ dE = \int_{r=0}^{r_{max}} \int_{N_{min}}^{N_{max}} 2\pi r_0 \Delta_h(E,r,N) \cdot R(N) dE \ dN \ dr$$

where R(N) dN is the differential number spectrum, r_{max} is taken to be 100 m, i.e. the density of hadrons for r $\geq$ 100 m becomes negligible, N_{min} is the minimum shower size at core distance r capable of producing an electron density

(calculated from the lateral density of electrons) and N_{max}
was assumed to be 5.10^9.

To fit the present measurements the value of α was allowed
to vary from 1.5 to 2.2 in stages of 0.05 and for each value
of α the constant A, in the parametarised lateral distribu-
tion of hadrons, was normalised such that one gets 7.2 hadrons
of ≥ 100 GeV in showers of $N = 10^5$ particles. The results
of calculations for different values of local electron density
trigger, for $\alpha = 1.75$ which gives the best fit to the slope of
the measured spectrum for $E \geq 200$ GeV, are plotted in figure
6.16. The integral energy spectra of hadrons for different
Δ_e, for $\alpha = 1.75$, are also plotted in figure 6.16.

The results of calculations shown in figure 6.16, have been
produced using the number spectrum derived from the measured
density spectrum of EAS. The same calculations have also been
carried out taking the number spectrum given by Hillas (1970b).
Figure 6.17 shows the results. These have been calculated
for $\alpha = 1.80$ (which gives the best fit to the slope of the
measured spectrum for $E \geq 200$ GeV) in the modified expression
of Kameda et al.

Comparing the calculated energy spectra of hadrons given
in figures 6.16 and 6.17, it can be seen that the shape of the
predicted spectra are almost the same. This is expected
since the number of hadrons of energy $\geq E$ is nearly independent
of shower size (Kameda et al.). The absolute rate of hadrons
found using Hillas's number spectrum is higher compared with
the one which is found using the number spectrum obtained from
measuring the density spectrum. The ratio is $\simeq 1.7$ for
$\Delta_e \geq 20$ m^{-2} and decreases to $\simeq 1.0$ for $\Delta_e \geq 480$ m^{-2}.
The function given by Kameda et al. is valid for $100 < E < 1,000$
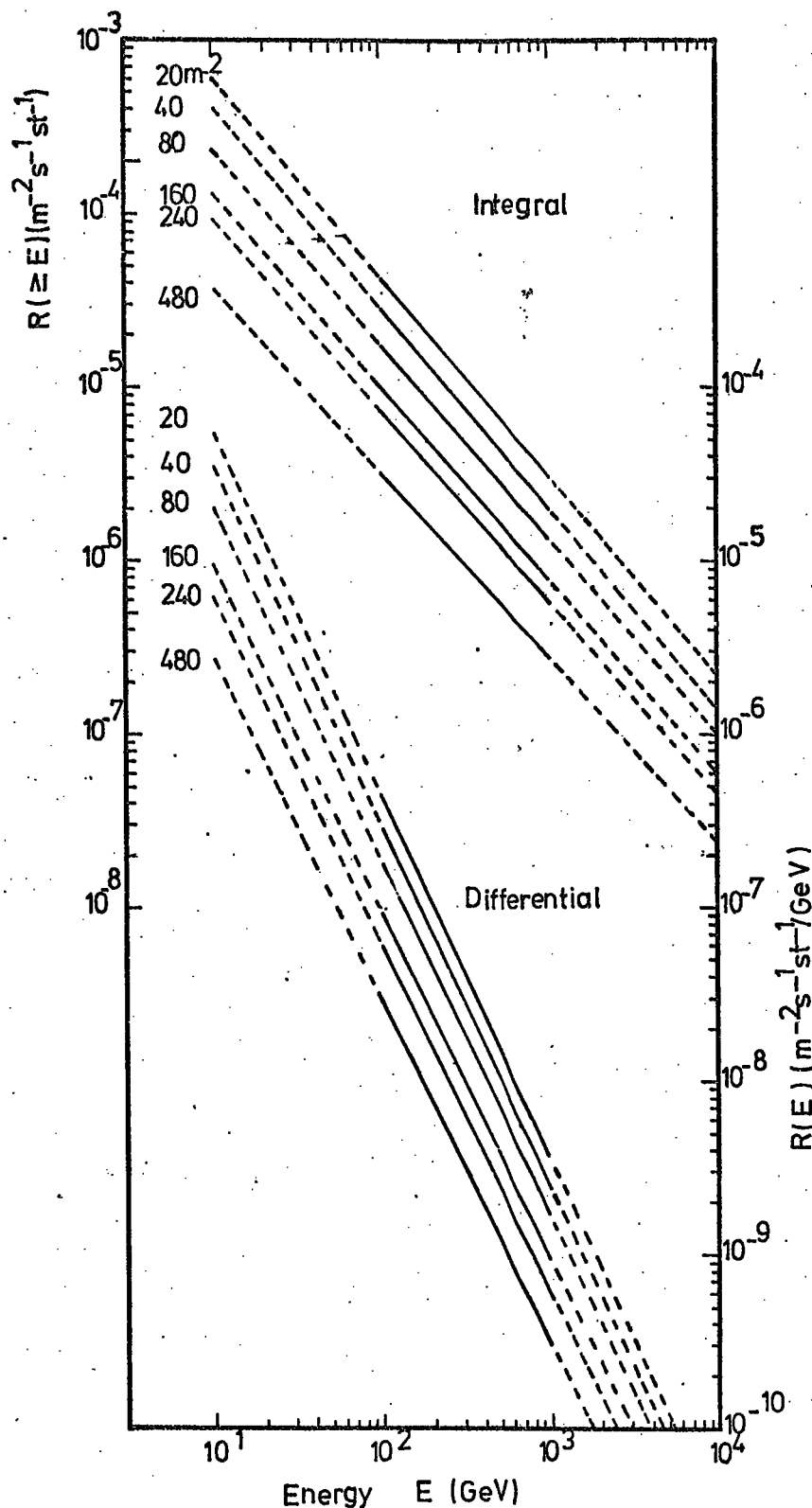
Figure 6.16. The predicted integral and differential spectra of hadrons for different values of minimum electron densities, indicated for each spectrum. The calculations are carried out, taking $\alpha = 1.75$ in the parametarised expression of Kameda et al.(1965) The expression given by Kamed et al. is normalised such that it gives 7.2 hadrons of $E \geq 100$ GeV in a shower of 10^5 particles (see text for further details). Sea level number spectrum found from density spectrum measurements assumed.
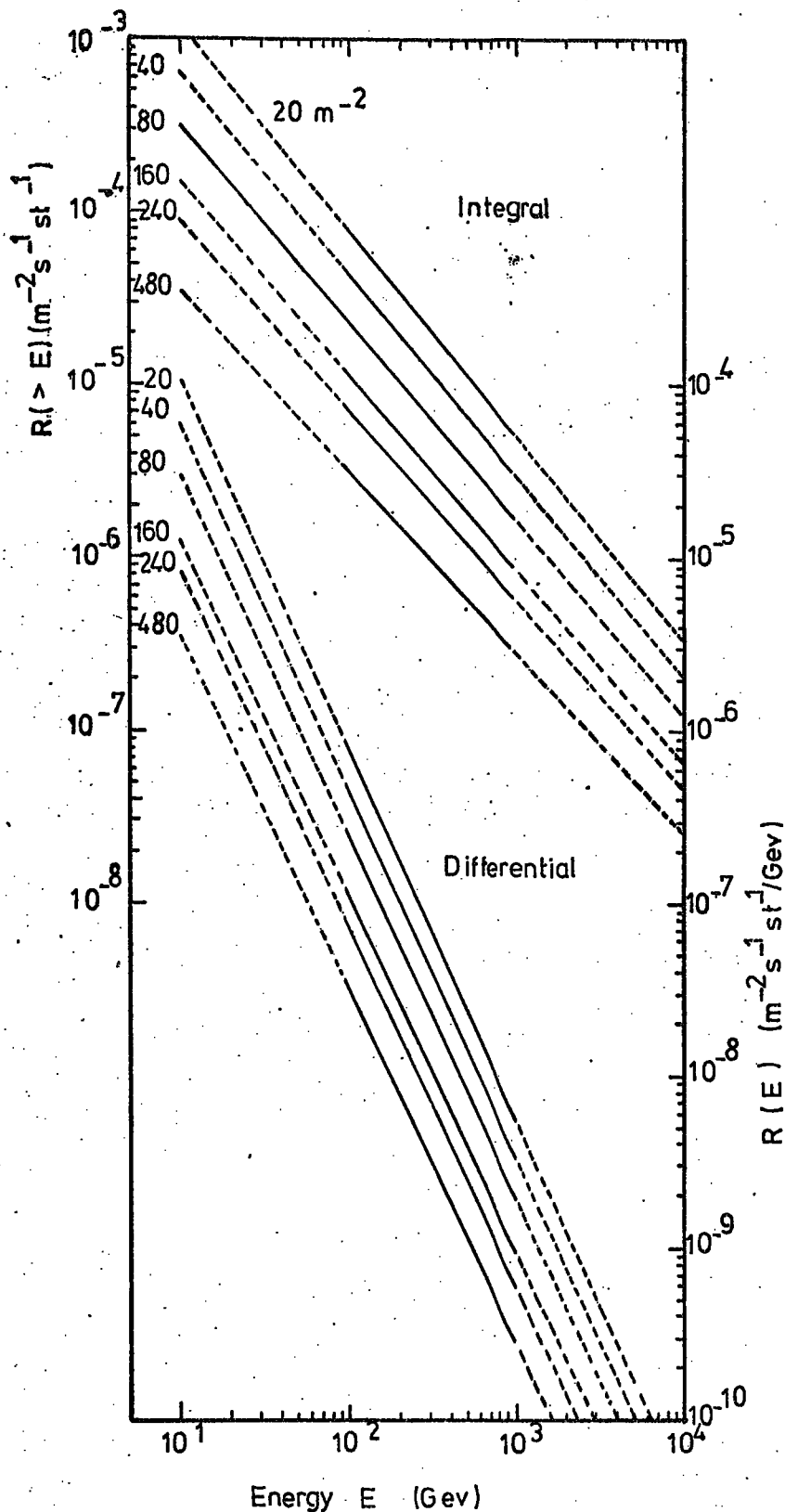
Figure 6.17   The predicted integral and differential
spectra of hadrons for different values of
minimum electron densities, indicated for
each spectrum.   The calculations are carried
out, taking $\alpha = 1.80$ in the parametarised
expression of Kameda et al. (1965).   The expres-
sion given 7.2 hadrons of $E \geq 100$ GeV in a
shower of 10^5 particles (see text for further
details).   Sea level number spectrum found
from Hillas (1970b) summary assumed.

GeV, thus the predicted spectra for $E < 100$ GeV and $E > 1,000$ GeV have been shown as dashed lines in figures 6.16 and 6.17.

6.6 Distribution of the rate of EAS producing hadrons of energy $\geq E$ in regions of EAS with a given minimum local electron density.

The integral rate of EAS, as a function of shower size and core distance, producing hadrons of energy $\geq E$ GeV at a detector, triggered by a local electron density of $\Delta_e \geq 80$ m^{-2} are calculated. The results of the calculations are shown in figures 6.18 and 6.19. The assumed functions for the measured parameters of EAS, in these calculations, are the same as given in section 6.6.

It can be seen from figure 6.18, that the median core distance decreases to one metre, for showers producing hadrons of $E > 2,000$ GeV. This is consistent with the fact that energetic hadrons are coliminated near the core of showers.

6.7 Comparison between the measured and predicted spectra

The measured integral spectra of hadrons (charged) indicate that, the spectra obtained under lead and iron absorbers are parallel, within experimental errors. The measured integral spectra have a slope of -1.15 ± 0.16 for energies of $E \gtrsim 200$ GeV (see figure 6.14). Taking $\alpha = 1.75$, in the modified hadron lateral density function due to Kameda et al. (1965), one obtains the slope of integral energy spectra of hadrons to be $\simeq -1.15$ (see figure 6.15). Thus according to present measurements, and assuming the lateral density of hadrons given by Kameda et al. is correct, it can be seen that the slope of the integral energy spectra of hadrons in a shower of size N
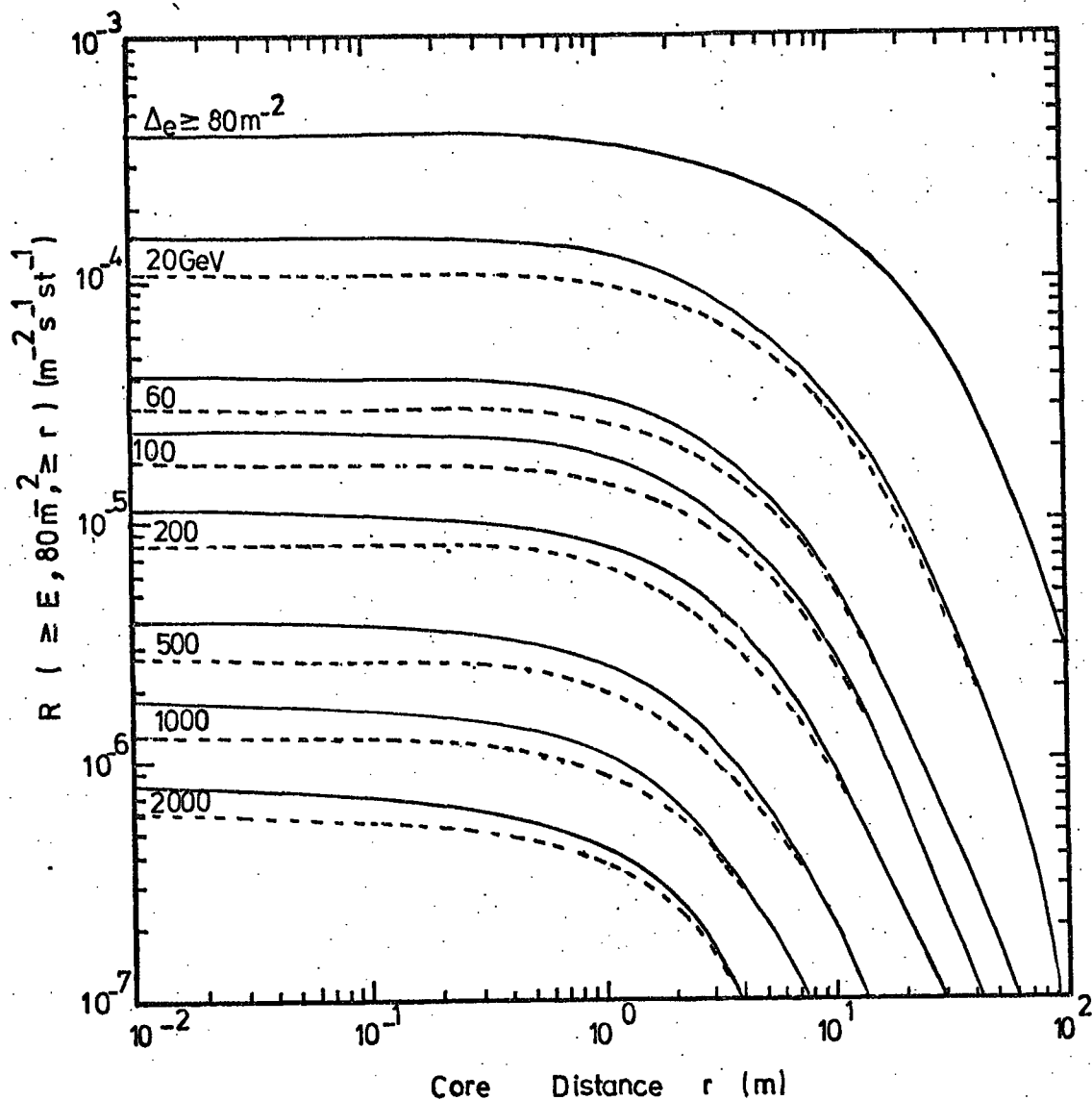
Figure 6.18   The calculated rate of EAS falling at core
                distances $\geq$ r meters in a detector producing
                hadrons of energy $\geq$ E GeV.   The first curve
                ($\geq$ 80 m^{-2}) shows the characteristic of the
                trigger.   Calculated using the Hillas (1970b)
                summary of the sea level number spectrum.
                The dashed curves are calculated using the
                sea level number spectrum found from the
                measured density spectrum.
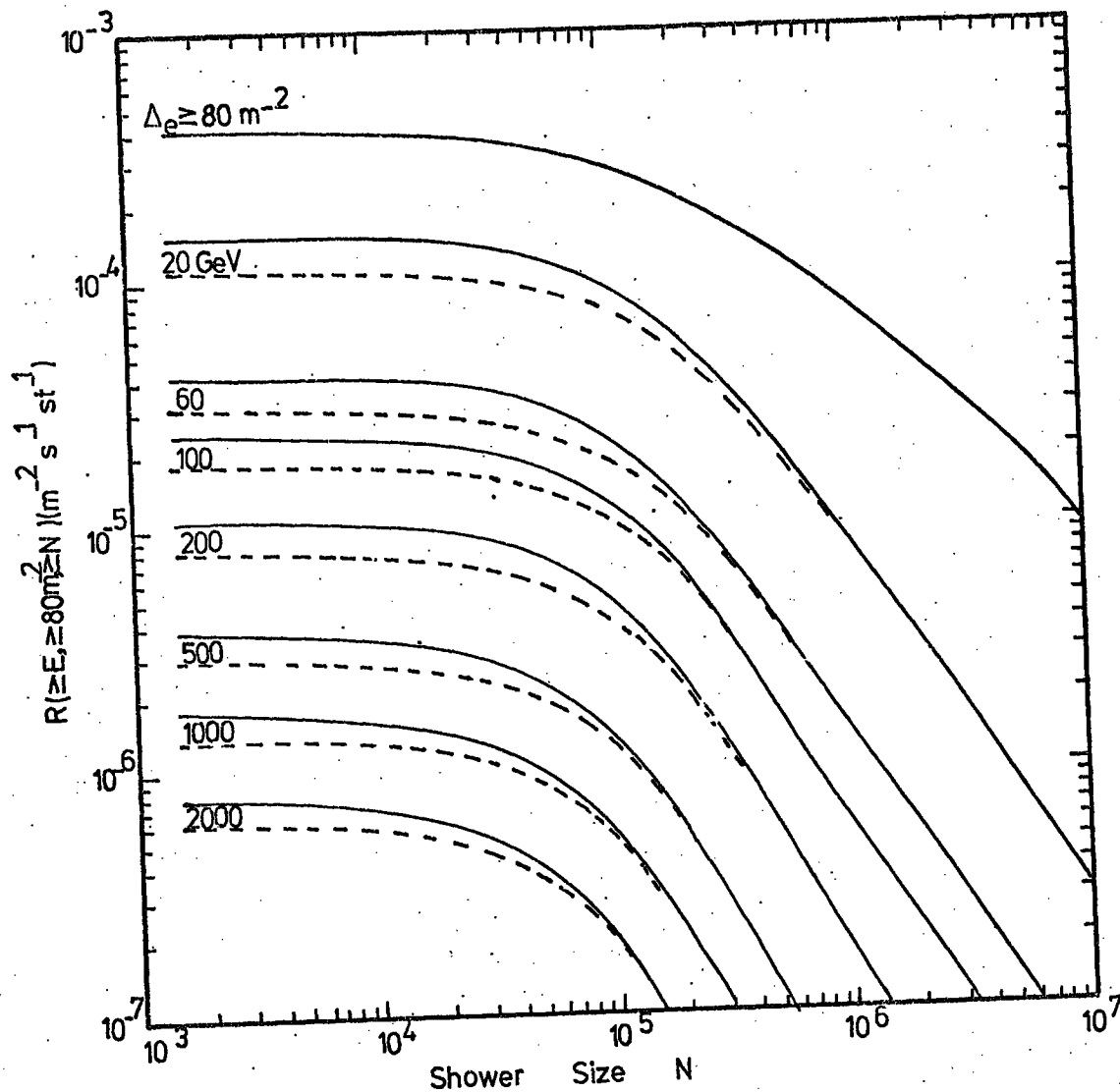
<u>Figure 6.19</u>   The calculated rate of size ≥ N producing hadrons of energy ≥ E GeV in a detector. The first curve (≥ 80 m-2) shows the characteristic of the trigger. Calculated using the Hillas (1970b) summary of the sea level number spectrum. The dashed curves are calculated using the sea level number spectrum found from the measured density spectrum.

is -1.25 (assuming the lateral density of hadrons follows as $\Delta_h(E, r, \text{\&.}) \propto E^{-\alpha}$, it can easily be shown that the energy spectra of hadrons in a shower of size N follows as $n(>E, N) \propto E^{-(\alpha - 0.5)}$).

Theoretical values of the exponent given by other authors are -1.0 (Bradt and Rappaport, 1967), -1.21 (Thielheim and Beiersdorf, 1969) and -1.1 (Murthy, 1967). Measurements resulted in -1.08 to -1.19 (Chatterjee et al., 1968), -1.2 (Tanahashi, 1965), -0.8 to -1.3 (Vernov et al., 1960) and -1.2 (Bohm et al., 1968). These predictions and measurements cover an energy range of E > 100 GeV up to about 2 TeV. At very high energies (>1TeV) the slope of energy spectrum, however, steepens as a consequence of finite primary energy.

The present measurement indicate a steeper slope than most other workers, being about 10% higher. This could be due to the way in which the lateral density of hadrons, due to Kameda et al., has been parametarised.

The measured spectra show that the spectra flattens for E $\lesssim$ 200 GeV. The decrease in the slope for hadrons of energy E $\lesssim$ 100 GeV is shown in the prediction of Thielheim and Beiersdorf and Grieder (1970) as well as in the measurements of Tanahashi (1965) who attributed it to the increasing decay probability of pions.

According to figure 6.14 the total number of hadrons of E $\gtrsim$ 200 GeV incident from the atmosphere on the detector is 353. This is calculated by adding the numbers observed to interact in the lead and iron and then correcting this number due to the probability of interaction (see table 6.1). This is obtained in 5,258,8 hrs. The area of the layer Fla is 2.57 m^2 and the effective solid angle (to be described in

chapter 7) is 0.57 st. Thus the rate of measured hadrons of $E \geq 200$ GeV is $1.27.10^{-5}$ m^{-2} s^{-1} st^{-1} in region of EAS of local electron density ≥ 80 m^{-2}.

According to figure 6.16, the integral rate of hadrons of E 200 GeV, for $\Delta_e \geq 80$ m^{-2}, is 8.10^{-6} m^{-2} s^{-1} st^{-1}. This is smaller than the measured rate. The discrepancy obtained could be partly due to the way in which the expression given by Kameda et al. has been normalised.

Thus the present measurements suggest that for $E > 200$ GeV

$$\Delta_h(E,r,N) = 0.22 \ N^{0.35} \ E^{-1.75} \ \exp(-\ r/r_0) \ \text{m}^{-2} \ \text{GeV}^{-1}$$

where $r_0 = 0.19 \ N^{0.35} \ E^{-0.25}$ with E in GeV and N in units of single particles.

The total number of hadrons of $\geq E_0$ GeV in a shower of size N is

$$n(\geq E_0, N) = \int_{E_0}^{\infty} \int_{r=0}^{\infty} \Delta_h(E,r,N) \ 2\pi r \ dr \ dE$$

Substituting the expression, given above, in this function

$$n(\geq E_0, N) = 0.04 \ N^{0.99} \ E_0^{-1.25} \quad \text{where N is}$$

in units of single particles and E_0 is in GeV.

6.8   Conclusion

The energy spectra of hadrons in regions of EAS of local electron density ≥ 80 m^{-2} was derived. This was done by measuring the burst width distribution of hadron induced cascades, in the lead and iron absorbers, of the flash tube chamber. It was found that the slope of the integral spectra of hadrons in regions of EAS of local electron density ≥ 80 m^{-2} is -1.15 ± 0.16 for the energy range $E \simeq 200 - 1,000$ GeV.

The measured spectra have been related to the spectra

in a shower of fixed size. For this purpose the lateral density of hadrons, measured by Kameda et al. (1965), was folded into the derived number spectrum, obtained from measuring the density spectrum of EAS as was explained in Chapter 3. The function given by Kameda et al. was modified such that the resulting spectra fit the measurement for E $\geq$ 200 GeV in the present experiment. Integrating the modified expression of the lateral density of hadrons, over all core distances, it was found that

$$n(\geq E_o, N) = 0.04 \ N^{0.99} \ E_o^{-1.25} \quad \text{where } n(\geq E_o, N)$$

is the total number of hadrons of $\geq E_o$ GeV (for E_o in energy range of $\simeq$ 200 - 1,000 GeV) in a shower of size N particles at sea level. (It was shown that if the number spectrum, obtained from the summary of Hillas (1970b) is used in the calculations then it does not change the above results significantly). The expression given above is valid for $2.10^4 < N \lesssim 4.10^5$ using figure 6.19, which shows that in regions of EAS of local density ≥ 80 m^{-2}, hadrons of energy $\geq$ 200 GeV accompany the electron-photon shower in 80% of the triggers in this size range.

CHAPTER 7

FURTHER DISCUSSION OF THE MEASUREMENTS ON

HADRONS IN EAS

7.1 Introduction

In deriving the energy spectrum of hadrons described
in chapter 6, it was assumed that all charged particle induced
bursts are produced by charged pions. In this chapter the
significance of muon - induced bursts on the measured spectra
has been considered. Subtracting the muon contamination from
the measured energy spectra of charged particle induced bursts
one can determine the charge to neutral ratio.

7.2 Ratio of the frequency of the bursts produced in the iron and lead absorbers

Taking the constant values for the interaction length of
pions in the lead and iron (see table 6.1), the relative
frequency of the expected bursts produced in the iron to lead
is 0.45. Figure 7.1 shows the measured ratio as a function
of energy. It can be seen that good agreement between the
measured and predicted ratio (dashed line) is obtained.

One expects to see a different ratio if the rate of muon-
induced bursts is significant.

7.3 Angular distribution of hadrons in EAS

The angular distribution of charged particle induced
bursts in the iron has been measured. For measurement the
following criteria were adopted.

i) The bursts have energies of E< 500 GeV (a pion with 500
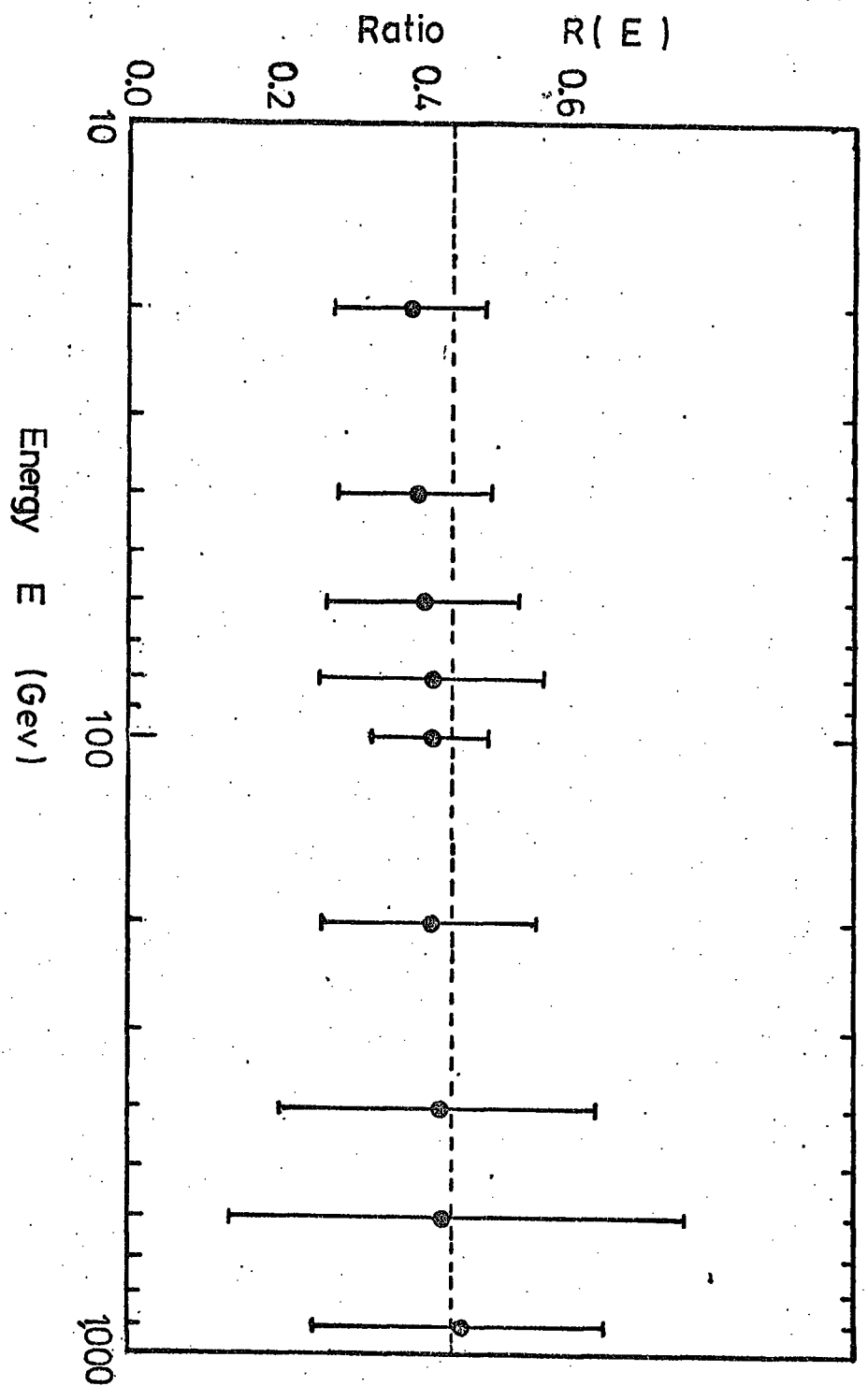
Ratio of the observed bursts produced in the lead and iron
absorbers as a function of hadron energy incident on the
top of the absorbers. The dashed line shows the predicted
ratio.

GeV energy interacting in iron produces a burst width of 2 cm. below the iron as measured on the scanning sheet, i.e. 40 cm. (width in real space).

ii)   The core of the bursts do not pass within 1 cm. as measured on the scanning sheet from either side of the chamber.

The projected angular distribution of hadrons satisfying the above criteria were measured and the results are shown in figure 7.2.

Assuming the angular distribution of hadrons in EAS follows as $I = I_0 \cos^n \vartheta$, in real space, and adopting the method due to Lovati et al. (1954), which predicts the angular distribution in a given projected plane (see Appendix B), the best value for n from the measured angular distribution was calculated using a chi-square test, to be $n = 9 \pm 2$.

It is interesting to note that measuring the angular distribution of hadrons in EAS gives information about the attenuation length of hadrons in EAS.   From the present measurement the attenuation length, $\lambda_H = \frac{1,030}{n}$ g cm^{-2} , is calculated to be $\lambda_H = 114 \, ^{+23}_{-20}$ g cm^{-2} for showers of size $N = 2.7 \cdot 10^5$ (equal to the median shower size producing a local electron density $\Delta_e \geq 80$ m^{-2}) which is larger than the value of $85 \, ^{+15}_{-10}$ g cm^{-2} measured by Kameda et al. (1965).   These authors measured the angular distribution of hadrons in EAS and they gave $n = 12 \pm 2$ for showers of size $N = 4 \cdot 10^4 - 4 \cdot 10^6$.

Assuming $n = 9$ the effective solid angle Ω , for hadrons is $\Omega = \frac{2\pi}{n + 2}$ or $\Omega = 0.57$ Sr.

7.4   Bursts in glass

A class of bursts observed in the flash tube chamber were the bursts produced in the chamber as a result of interaction
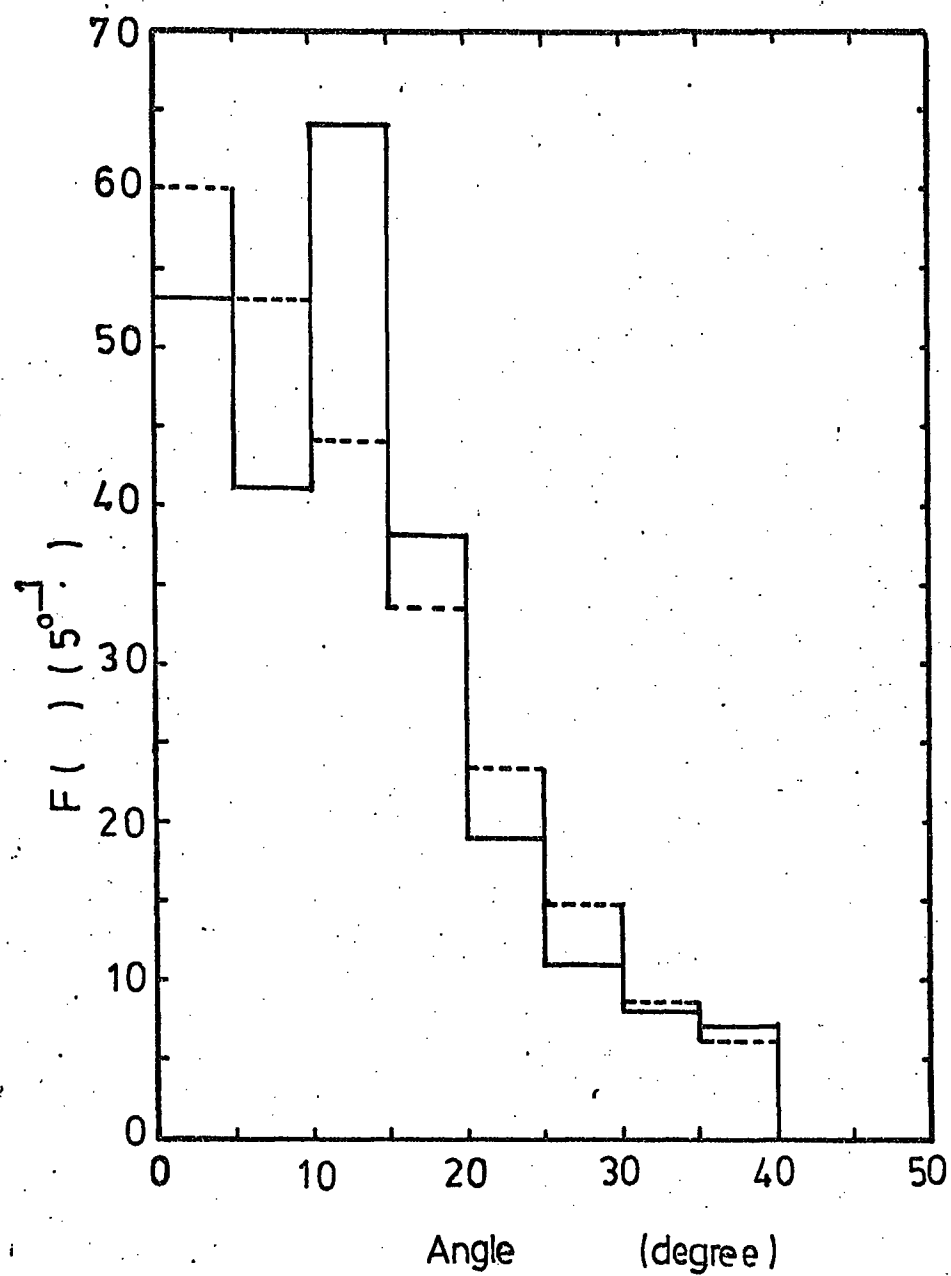
Figure 7.2   Angular distribution of bursts observed
below iron.   The dashed distribution
has calculated for n = 9 after Lovati
et al. (1954).

with the glass of the flash tubes and the aluminium electrodes.
It was possible to measure the interaction length of particle-
induced bursts in the chamber. For this purpose all charged
particles producing a burst in F2 and F3 indicating a track in
Fla and Flb, i.e. passing through the lead and iron absorbers,
were considered. The distance between the point of interaction
and the top of F2 was measured (on a scanning sheet). The
measured frequency was then corrected for the aperture of the
chamber, based on the measured angular distribution of hadrons
(see section 7.3) and using the method of Lovati et al.(1954).

A total of 57 bursts produced by charged particles (satis-
fying the above criteria) in films F1-20 were observed. The
results are shown in figure 7.3. Taking the best line through
the corrected experimental points the interaction length of
particle producing bursts in the chamber is $\lambda = 115 \pm 50$ g cm^{-2}.
This value is not inconsistent with $\lambda_\pi = 131$ g cm^{-2} which is
expected for pions interacting the chamber assuming pion -
proton cross section $\sigma_{\pi p} = 22$ mb (Alexander and Yekutieli,
1961). Thus the particle - induced bursts in the chamber are
hadrons and so the muon contamination is not significant.
(A total of 15 bursts produced by neutral particles in the
chamber were observed, in films F1-F20).

It is interesting to note that, however muons have a very
low probability to produce bursts in light materials and also
the total amount of matter (in the vertical direction) in F2
and F3 in 91.5 g cm^{-2}. On the other hand it is recalled that
the probability of hadrons traversing the lead and iron absorbers
and then interacting in the chamber is only about 25% (see
table 6.1). Thus the latter could partly compensate the former
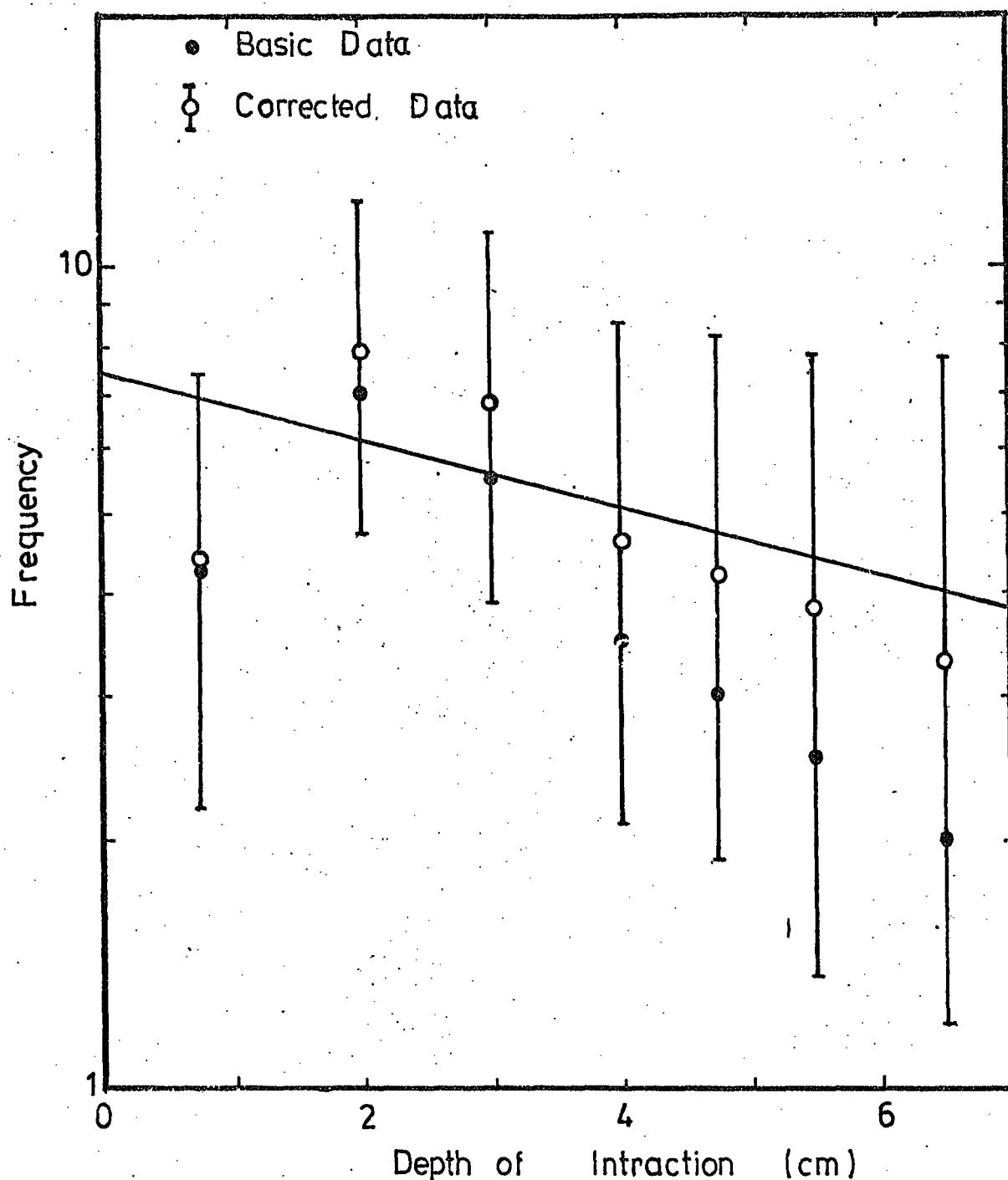
Figure 7.3   Frequency of bursts observed in F2 and F3 as
              a function of the distance between the point
              of interaction and the top of F2 measured on
              the scanning sheet (∅m.), 1 cm. on the scanning
              sheet corresponds to 20 cm. in real space.
              The data are corrected using the method of
              Lovati et al. (1954), see the text. The solid
              line is the best line through the corrected
              experimental points.

one.

7.5 Predicted rate of muon-induced bursts

The final attempt was to predict the rate of muons producing bursts in the chamber (iron absorber) and compare it with the observed burst spectrum.

For this purpose the integral energy spectrum of muons in EAS with local electron density of $\Delta_e \geq 80 \ m^{-2}$ was calculated, taking the number spectrum given by Hillas (1970b), the lateral electron density given by Greisen (1960) and the lateral muon density of energies $\geq E_\mu$ due to Greisen (1960).

$$R(\geq E_\mu, \geq 80) = \int_{r=0.1}^{r_{max}} \int_{N_{min}}^{N_{max}} 2\pi r \Delta_\mu (\geq E_\mu, r, N) \ R(N) dN \ dr$$

where $R(N) \ dN$ is the differential number spectrum, $\Delta_\mu(\geq E_\mu, r, N)$ is the lateral density of muons of energy $\geq E_\mu$ at core distance r is a shower of size N. N_{max} was taken to be 5.10^9, N_{min} is the minimum size capable of producing a density of $80 \ m^{-2}$ at core distances r, calculated from the electron structure function, and r_{max} is the maximum core distance for a shower of size 5.10^9 particles capable of producing $80 \ m^{-2}$.

The lateral density of muons of energy $\geq E_\mu$ is extrapolated from about 20 GeV, where it is confirmed by experimental data, up to the highest energies. (The results of Monte-Carlo simulations by Goorevich and Peak (1973) show that the density of muons of $E_\mu \geq 100$ GeV at r = 10 m in a shower of size 2.10^7 particle is not inconsistent with the Greisen formula).

Hanson (Private Communication) has calculated the burst size spectrum below a thick iron absorber for an assumed muon

energy spectrum incident on the top of an absorber. Since muons have a large attenuation length the produced burst spectrum is independent of absorber thickness for thick absorbers up to a limiting energy which is approximately equal to the minimum energy cascade which can develop to shower maximum in the whole depth of the absorber, i.e. up to about 1,000 GeV for the iron absorber (see figure 6.2).

The calculated differential muon spectrum was folded into the calculation of Hanson and thus the rate of muon-induced bursts in the iron, were obtained. The results are shown in figure 7.4. Comparing the predicted rate of muon-induced bursts with the measured spectra of hadrons, shown in figure 7.4, one can see that the former is smaller (10%) than the latter for burst sizes > 30 particles.

7.6   Charge to neutral ratio

It was shown that the rate of muon-induced bursts in the measured energy spectra of hadrons is not significant for the high energy region (see figure 7.4). Thus using figures 6.13 and 6.14 one can determine the charges to neutral ratio, f, as a function of hadron energy. The results are shown in table 7.1a. It can be seen that f decreases as hadron energy increases for E $\gtrsim$ 50 GeV. The results shown in table 7.1 have been obtained using the corrected neutral spectrum but still f is too large, compared with the experimental data of Kameda et al. (1965) and Vatcha and Sreekantan (1973). The results obtained by these authors are given in tables 7.1b and 7.1c.

The large value for f obtained in the present experiment is possibly due to the lack of resolution of the chamber in
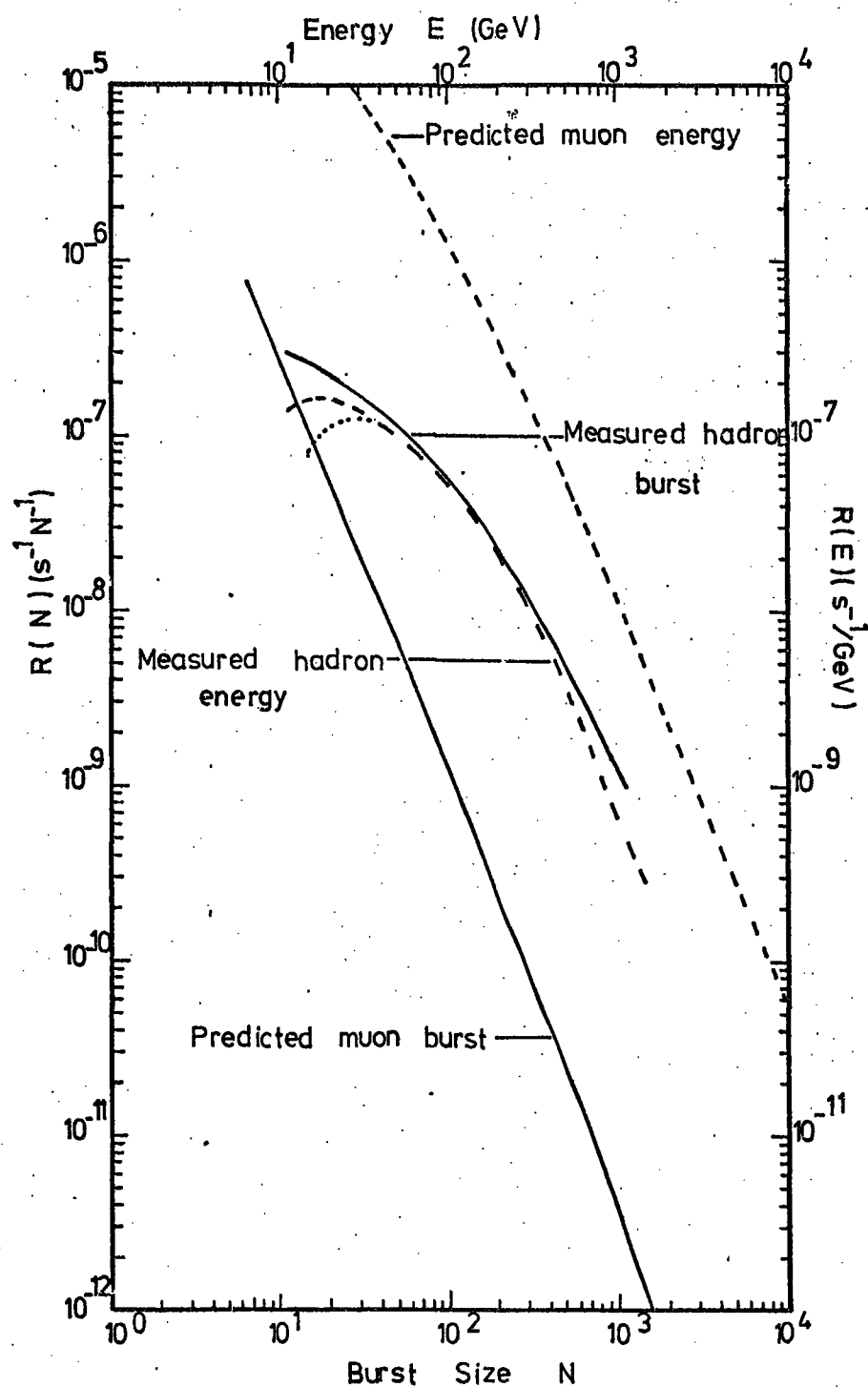
Figure 7.4 Comparison between the measured burst spectrum below iron with the predicted burst spectrum due to muon-induced bursts in iron. The dashed curves show the predicted muon and measured hadron energy spectra. The dotted curve shows the measured energy spectrum after subtracting the muon contimination. It is seen that bursts of size ≲ 13 particles produced predominantly by muons.

(a)

Energy E (GeV)	Ratio of charged to neutral hadrons f	
	$f(E)$	$f(\geq E)$
30	15 ± 25	17 ± 4
50	20 ± 19	17 ± 5
100	25 ± 28	13 ± 5
300	20 ± 32	8 ± 4
500	11 ± 13	6 ± 4

(b)

Energy E (GeV)	Ratio of charged to neutral hadrons f
For all energies	4.5 ± 0.5
$E < 500$	6 ± 1
$E \geq 500$	$2.5 \, {}^{+1.5}_{-0.5}$
$E \geq 1,000$	1.5 ± 0.5

(c)

Energy E (GeV)	Ratio of charged to neutral hadrons f			
	observed, f		calculated, f	
	$N < 3.10^5$	$N \geq 3.10^5$	Without $N \bar{N}$	with $N \bar{N}$
25	6.2 ± 1.3	3.0 ± 0.3	200	2.4
50	3.8 ± 0.9	2.6 ± 0.3	130	1.5-3
100	1.9 ± 0.6	1.8 ± 0.4	65	1.2-2.2
200	1.2 ± 0.8	1.2 ± 0.8	25	1.1-1.9

Table 7.1   Charge to neutral ratio measured (a) by present experiment, (b) by Kameda et al.(1965) and (c) by Vatcha and Sreekahtan (1973). The predicted ratio for the absence and presence of N-$\bar{N}$ in EAS components are shown in (c) calculated for 800 g cm^{-2} elevation by Vatcha and Sreekantan (1973). Since the rate of muon contamination is $\lesssim 10\%$ for hadrons of $E \gtrsim 30$ GeV thus the calculated charge to neutral ratio shown in table (a) have not been corrected for muon contamination.

identifying neutral hadrons associated with high local electron density.

7.7 Discussion

The measured parameters of hadrons in EAS which are more sensitive, to different assumptions of high energy collision, are (i) number of hadrons of energy > E and (ii) the charge to neutral ratio (see Grieder 1970-1973).

(i) The number of hadrons of energy $\geq$ 200 GeV in the shower of size range $N = 2.10^4 - 4.10^5$ was derived (see section 6.8). This is shown in figure 7.5. The experimental data of Kameda et al. (1965) and Tanahashi (1965) are shown in figure 7.5. It is seen that while there is good agreement between the present results and those of Kameda et al., there is some inconsistency for $N \lesssim 10^5$ between the present results and those of Tanahashi. This may be due to the analytic function given by Kameda et al. for the lateral density of hadrons being incorrect for the smaller shower sizes.

The Monte-Carlo calculations of Grieder (1970), for two of his models, and Bradt and Rappaport (1967) are shown in figure 7.5. The results of Grieder are based on the so-called SFB* and IDFB* models. The former model assumes a half law multiplicity, i.e. $n_s \propto E^{1/2}$. The latter model assumes that $n_s \propto E^{3/8}$. In both models the production of nucleon-anti-nucleon pairs ($N \bar{N}$) in high energy interactions has been assumed. It is seen from figure 7.5 that neither of these models agree with the experimental data. One should note that Grieder has calculated the number of hadron in EAS produced by a fixed primary energy. To convert primary energy to shower size 10 GeV/particle is assumed. This assumption however, is

The graph shows R(≥200GeV,N) plotted against shower size (N).

Legend:

Expt.
— Present work
---- Kameda et al (1965)
•—•— Tanahashi (1965)

Theo.
—·— Grieder (1970) IDFB*
——— // // SFB*

I Bradt & Rappaport (1967)
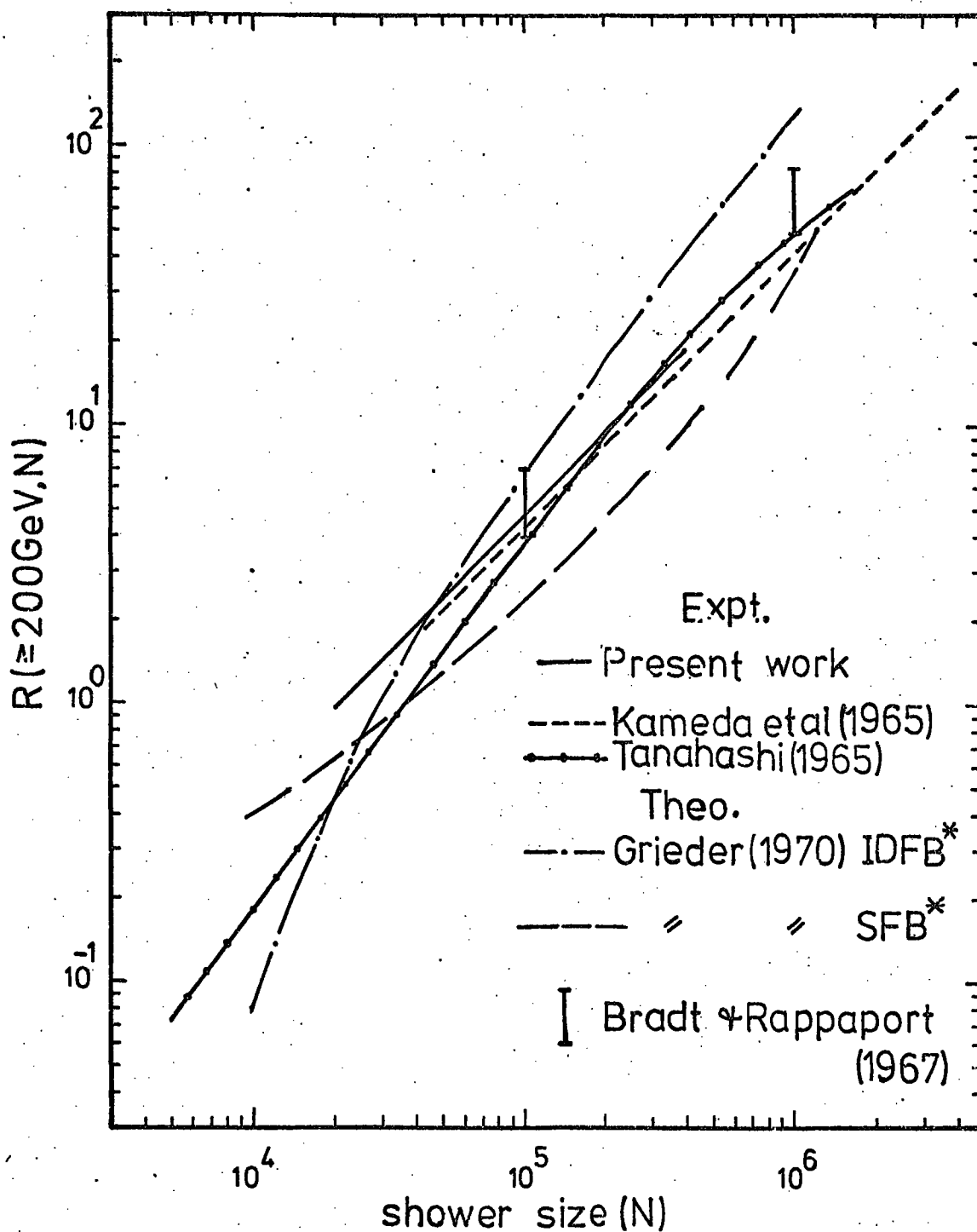
<u>Figure 7.5</u>　The measured and predicted (based on Monte-Carlo calculation) flux of hadrons of E ≥ 200 GeV at sea level as a function of shower size. The results of the present experiment cover size range of $2.10^4 - 4.10^5$.

believed to have a small effect in the size dependence of the number of hadrons.

The prediction of Bradt and Rappaport shown in figure 7.4, does not include N $\bar{N}$ production and represents two centre and isobar production for protons and iron nuclei. It can be seen that the results are not too sensitive to the mass of primary cosmic ray particles.

(ii) The charge to neutral ratio, f, obtained in the present experiment (see table 7.1a) indicates that f decreases as energy increases. This is consistent with the experimental results of Kameda et al. and Vatcha and Sreekantan (1973) as shown in tables 7.1b and 7.1c. Vatcha and Sreekantan (1973) have shown that the absence of N $\bar{N}$ production in high energy interaction produces a larger value for f compared with the results of present work.

7.8 Conclusion

The rate of muon-induced burst, in the measured energy spectrum of hadrons, described in chapter 6, was investigated. It was shown that the contamination of muons in the measured spectra of hadrons of high energy is not significant. The number of hadrons of E $\geq$ 200 GeV in shower of size N = 2.10^4 - 4.10^5 was determined and the results compared with model calculations. It was concluded that there is little sensitivity measuring the energy spectra of hadrons, at sea level, with the mass of primary cosmic rays. The charge to neutral ratio obtained in the present work gives a higher value than the experimental data of Kameda et al. (1965) and Vatcha and Sreekantan (1973). This could be explained as a result of the lack of resolution of the chamber in identifying neutral hadrons associated with high local electron density. The ratio obtained,

however, supports the production of N-$\bar{\text{N}}$ in high energy inter-
actions.

CHAPTER 8

SEARCH FOR QUARKS CLOSE TO THE
CORE OF EAS

8.1   The concept of quark theory

8.1.1   Introduction

Ever since the discovery of pion attempts have been made to understand the known so-called elementary particles in terms of elementary sub-units.   For doing this the investigation has been directed into two main branches, namely:

(i)   To get advantage of the symmetry properties of the strong interactions, which can lead to a grouping of particles into families with similar properties.

(ii)   To develop the so-called composite models of elementary particles, in which attempts have been made to reduce all the diversities of particles to bound states of a minimum number of fundamental particles or truely elementary particles.

It was the second branch (ii) which led Fermi and Yang (1949) to assume that all pions are the bound states of nucleon, antinucleon (N N̄) pairs.   After the discovery of strange particles by Rochester and Butler (1947) in Cosmic radiation the theory of Fermi and Yang was abandonded since it could not account for the strange particles.

Sakata (1956) proposed that sub-units were the triplet proton, neutron and lambda zero together with their antiparticles.   According to the Sakata model one could get a good description of the structure of mesons in terms of unitary

super multiplets but it failed to be consistent with the
observed octet and decimet multiplets of baryons as their
existance become firmly established experimentally. In the
Sakata model mesons are considered to be bound states of two
triplet particles and an anti-triplet particle. According
to group theory the direct product of triplets forming mesons
and baryons are:

Mesons. $3 \otimes \bar{3} = 8 \oplus 1$

Baryons $3 \otimes 3 \otimes \bar{3} = 15 \oplus 6 \oplus \bar{3} \oplus 3$

where $\otimes$ means direct product, $\oplus$ means direct sum and a
bar means anti-particle.

Gell-Mann (1964) and Zweig (1964, 1965) noticed that
although $3 \otimes 3 \otimes 3$ gives the wrong multiplet structure for
baryons the reduction $3 \otimes 3 \otimes 3 = 10 \oplus 8 \oplus 8 \oplus 1$ agreed with
the observations. Considering the Gell-Mann, Nishijima
relation which states $Q = T_3 + \frac{B+S}{2} = T_3 + \frac{Y}{2}$ where $Q =$
charge, $T_3 =$ third component of isospin, $S =$ strangeness and
$Y =$ hypercharge, then the fundamental triplet particle the
so-called quarks (after Gell-Mann) each carry baryon number
$1/3$ so as to be consistent to the conservation of baryon number
and the Gell-Mann - Nishijima relation. Table 8.1 shows the
quantum number of quarks. The fundamental triplet particles
are called p type, n type and λ type quarks.

The groups of eight and ten baryons (having spin $1/2 \hbar$
and $3/2 \hbar$ respectively) are demonstrated in figure 8.1. On
the right hand side of figure 8.1 the way in which each term
is made up of quarks are shown. The lightest particles are
at the bottom of figure 8.1 (The particles have been established

Triplet particle	T_3	B	S	Y	Q	Spin (in units of $\hbar$)
p	$\frac{1}{2}$	$\frac{1}{3}$	0	$\frac{1}{3}$	$+\frac{2}{3}$	$\frac{1}{2}$
n	$-\frac{1}{2}$	$\frac{1}{3}$	0	$\frac{1}{3}$	$-\frac{1}{3}$	$\frac{1}{2}$
λ	0	$\frac{1}{3}$	-1	$-\frac{2}{3}$	$-\frac{1}{3}$	$\frac{1}{2}$

Table 8.1   Quantum numbers of quarks.   The corresponding anti-quarks have quantum numbers of opposite sign

Triplet particle	Mass difference (GeV)	Decay scheme	Life time
p	M	stable	Infinite
n	M	$n \rightarrow p+e+ \bar{\nu}_e$	$\sim$ sec
λ	M+0.14	$\lambda \begin{cases} p+\pi^- \\ n+\pi^0 \end{cases}$	$\sim 10^{-10}$ sec

Table 8.2   Possible mass difference and decay schemes of quarks.

Baryon octet (J=1/2)

Ξ° Ξ^- $p\lambda\lambda$ $n\lambda\lambda$

Σ^+ Σ° Σ $pp\lambda$ $pn\lambda$ $nn\lambda$
        Λ° $pn\lambda$

P^+ N° ppn pnn

Baryon decuplet (J=3/2)

Ω^- $\lambda\lambda\lambda$

$\Xi^{\circ *}$ Ξ^{-*} $p\lambda\lambda$ $n\lambda\lambda$

Σ^{+*} $\Sigma^{\circ *}$ Σ^{-*} $pp\lambda$ $pn\lambda$ $nn\lambda$

Δ^{++} Δ^+ Δ° Δ^- ppp ppn pnn nnn
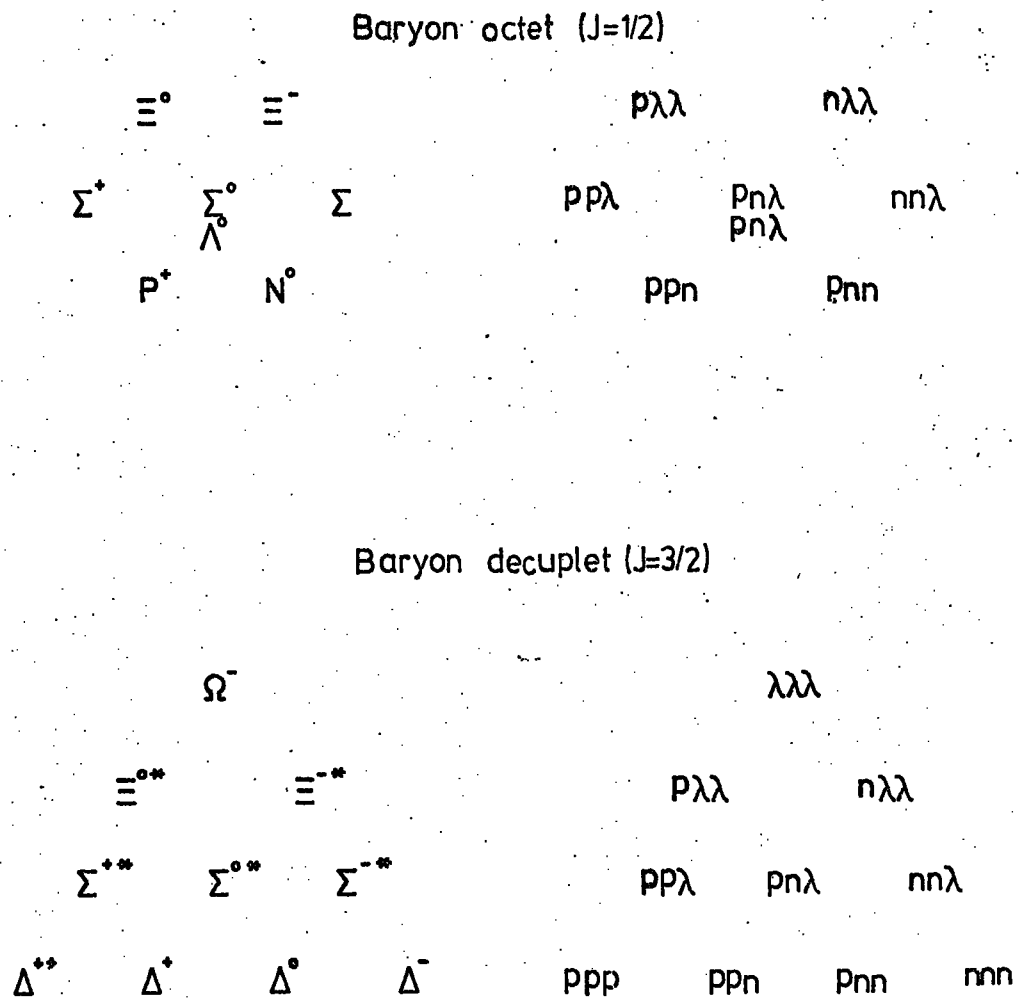
Figure 8.1   The construction of the baryon octed and
de cuplet from the three fractionally
charged particles.   The right hand side
shows the way in which each particle is
made of three quarks.

experimentally as given by the Particle Data Group, 1972).
Comparing the properties of elementary particles with their
expected quark compositions (figure 8.1) one can deduce the
mass difference and decay schemes of quarks. The results
are given in table 8.2.

8.1.2 The expected properties of free quarks

The predicted properties of quarks are; (a) The mass
of quark, (b) The cross section of quark production and
(c) The quark nucleon inelastic cross section and inelasticity.

(a) The mass of the quark.

In the non-relativistic model, for which the greatest
number of interesting results have been obtained, the quark
mass must be heavy. Morpurgo (1967) has obtained a rough
estimate of quark mass, considering mesons are formed by quark-
antiquark pairs of mass about 5 GeV/c^2 to several tens of
GeV/c^2 (The values obtained for the quark mass depends on the
square of the assumed range of the q $\bar{q}$ potential).

(b) The cross section of quark production

The possibe interactions producing quarks in high energy
nucleon-nucleon collisions are as follows (Ashton, 1973):

(1) $N + N \longrightarrow N + N + q + \bar{q}$

(2) $N + N \longrightarrow N + 3 q$

(3) $N + N \longrightarrow 3 q + 3 \bar{q}$

(4) $\pi + \pi \longrightarrow \pi + q + \bar{q}$

(5) $\pi + \pi \longrightarrow 2(q + \bar{q})$

Figure 8.2 demonstrates the threshold kinetic energy for quark production in N - N collisions and virtual π-π collisions as a function of quark mass as given by Ashton (1973). In this figure the full horizontal line represents the energy equivalent to 30 GeV colliding beams and the broken line is the approximate primary cosmic rays energy at which the electron density at the core of EAS is 1 m^{-2} at sea level or mountain altitude. It can be seen from figure 8.2, that the upper limits of the quark mass are $M_Q \leq 4.8$ GeV and $M_Q \leq 2.7$ GeV for proton beams of 70 GeV energy (Serpukov) and 28 GeV energy (CERN) respectively if quarks are produced according to process (1).

(c)   The quark-nucleon, inelastic cross section and inelasticity.

Comparing proton-proton and pion-proton scattering one can see that there are nine possible q q interactions in the former, whereas there are 3(q q) and 3(q $\bar{q}$) interactions in the latter. Thus considering q $\bar{q}$ and q q cross sections are equal at high energies, so the rate of proton-proton to pion-proton scattering cross sections is $9/6 = 1.5$. The experimental values for p - p and π - p (p stands for proton and π stands for pion) are $\simeq$ 33 mb and $\simeq$ 22 mb respectively. Thus one can conclude that quark-nucleon cross section is $\simeq$ 11 mb.

It is shown that the measured attenuation length of cosmic ray nucleons through the atmosphere is larger than their interaction length with atmospheric nuclei (see Cocconi, 1961). This suggests that on average nucleons lose 0.3 $\simeq \dfrac{2 M_\pi}{M_N}$ of their energy in nucleon-nucleon collisions. Assuming quarks
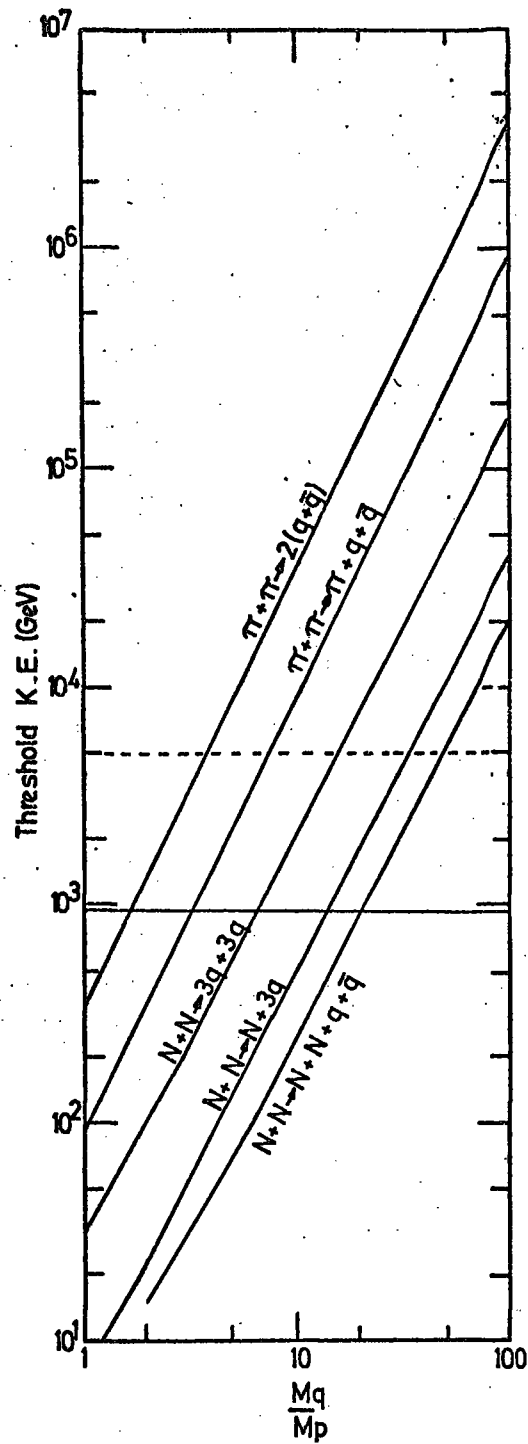
Figure 8.2   Threshold kinetic energy for quark production in nucleon collisions as a function of the quark mass. The full horizontal line represents the energy equivalent to 30 GeV colliding beams and the dashed line the approximate primary cosmic ray energy at which the electron density at the shower core is $1m^{-2}$ at sea level or mountain altitude.

are surrounded by a mesic field the relative energy loss of

a quark-nucleon interaction $\frac{\Delta E}{E} \simeq \frac{2\,M_\pi}{M_q} \simeq \frac{M_N}{M_q} \times 0.3.$

This suggests that the larger the quark mass the more material

it is likely to penetrate before being reduced to a non -

relativistic velocity.

8.1.3 Some of the achievements and difficulties in quark theory

In addition to the fact that quark theory gives a good

description of the structure of meson and baryon multiplets

it does explain the mass formula for the various isotopic

spin families that constitute the multiplets.   The theory

also gives the constant G_A, whose square determines the rate

of disintegration of $n \rightarrow p + \bar{e} + V$., as $5/3 = 1.67$ to be

compared with 1.26 as has been obtained experimentally.   The

ratio of the magnetic moment of neutron to proton is found

experimentally as $\frac{\mu_N}{\mu_p} = -0.685.$ The quark model suggests

that $\frac{\mu_N}{\mu_p} = -0.667$ which shows an agreement better than 2%.

The theory of quark, also, makes it possible to derive a large

number of relations among the cross sections for strong inter-

action, for instance the ratio of p - p to π - p cross

sections as mentioned in section 8.1.2.

The main difficulty which is considered in quark theory

is that fractionally charged particles have not yet been

observed.   This, however, is answerable if one suggests that

the mass of free quarks are higher than the power of present

accelerators.   It is hoped that further experiments with

accelerators and improvements in detection systems in cosmic

ray experiments will give the answer. The other serious difficulty of the model is suggested to be that of saturation, that is to say why $q \bar{q}$ and $q q q$ states produce the total mass of mesons and baryons respectively, while four quark states are presumably unstable. According to the theory of quantum electrodynamic the electron is a structureless particle and this has been confirmed experimentally. The problem which arises is that if fundamental particles carry fractional charges then why does the electron carry integral charge? If one considers Δ^{++} one comes to the conclusion that according to the quark theory the total wave function of Δ^{++} is symmetric which is not consistent with the Pauli exclusion principle (considering quarks are fermions).

These difficulties of the theory of the quark (SU3) has led theoreticians to modify quark theory. One can mention Coloured quarks (Nambu, 1966), which consideres quarks having red, yellow or blue colours. Another is the Charm quark in which an additional quantum number, the so-called charm, C, is to be added to the Gell-Mann - Nishijuma relationship (Tarjanne et al. 1963 and Bjorken and Glashow 1964) in which quarks can carry integral charge. Another theory is the Parton - model due to Feynman (1969) which has met some success in deep lepton-hadron inelastic scattering. This model assumes that hadrons are made up of fundamental triplet particles (constituent quarks or valence quarks) and a sea of quark-antiquarks (current quarks). All of these models, however, face some difficulties. One should notice that more degrees of freedom (like Coloured quarks) produce more selection rules.

8.2   Previous search for quarks

8.2.1   Search by accelerators

The search for quarks has been carried out, in the
produced particles in high energy collisions, by means of
accelerators.   The procedure is to measure the ionisation
loss of secondary particles either by means of visual detectors
(mainly bubble chambers or streamer chambers) or by electronic
detectors (mainly scintillators).   This method enables one
to distinguish between fractionally charged particles and
integral charged particles.   This is due to the fact that
energy loss is proportional to Z^2, Z being the charge of
particle.   For instance typical bubble densities are 2.2/cm
and 8.8/cm for charged particles of $^e/3$ and $^{2e}/3$ respectively
to be compared with 20/cm for a unit charged particle.   In
the second method (using electronic detectors, say scintillators)
one needs to use several layers of scintillators in order to
minimise the fluctuations in energy loss and other factors.
The next type of investigation has been to measure the mass
of the produced particles (irrespective of being fractional
or integral charged particles) at fixed momentum by means of
Cerenkov counters and by measuring the time of flight.

Since no evidence for the existence of fractionally charged
quarks has been obtained the experimenters give the upper
bounds of the differential cross section for quark production
in N - N collisions.   The results of CERN (Allaby et al, 1969)
and Serpukov (Antopov et al.,1969) are shown in table 8.3
(Landsberg, 1974).   A comparison has been made between the
upper bounds on the differential cross section for quark

Proton energy	Electric charge	P_Q GeV/c	ϑ_Q m rad.	Upper bound $\frac{d^2\sigma_Q(P_Q,\vartheta_Q)}{dP\,d\Omega}$ 90% C.L. cm^2 st^{-1} (GeV/c)$^{-1}$	Antiprotons $\frac{d^2\sigma}{dp\,d\Omega}(p_{\bar p}=P_Q,\vartheta_{\bar p}=\vartheta_Q)$ cm^2 st^{-1} (GeV/c)$^{-1}$	Antiprotons Effective number $N^{"}_{\bar p}{}^{"}$	Antineutrons $\frac{d^2\sigma}{dp\,d\Omega}(p_{\bar d}=P_Q,\vartheta_{\bar d}=\vartheta_Q)$ cm^2 st^{-1} (GeV/c)$^{-1}$	Antineutrons Effective number $N^{"}_{\bar d}{}^{"}$	Antihelium $\frac{d^2\sigma}{dp\,d\Omega}(p_{\overline{He}3}=P_Q,\vartheta_{\overline{He}3}=\vartheta_Q)$ cm^2 st^{-1} (GeV/c)$^{-1}$	Antihelium Effective number $N^{"}_{\overline{He}3}{}^{"}$
E=70 GeV		16.7	0	1.4·10⁻³⁵	1.6·10⁻²⁷	2.6·10⁸	1.7·10⁻³¹	2.8·10⁴	~9·10⁻³⁶	1
	−e/3	21.5	0	3.6·10⁻³⁷	7.9·10⁻²⁸	5.0·10⁹	5.0·10⁻³²	3.2·10⁵	~9·10⁻³⁶	57
Antipov et al. (1969)		26.7	0	7.1·10⁻³⁸	2.1·10⁻²⁸	6.9·10⁹	1.1·10⁻³²	3.4·10⁵	~2·10⁻³⁶	65
Serpukov					$\Sigma N^{"}\,\bar{}_{\bar p}{}^{"}$ = 1.2·10¹⁰		$\Sigma N^{"}\,\bar{}_{\bar d}{}^{"}$ = 6.9·10⁵		$\Sigma N^{"}\overline{He}3{}^{"}$ = 113	
		33.3	0	7.7·10⁻³⁶	6.10⁻²⁹	1.8·10⁷	1.8·10⁻³³	5.3·10²	—	—
	−2e/3	43.0	0	2.1·10⁻³⁷	6.4·10⁻³⁰	6.9·10⁷	1.1·10⁻³⁴	1.2·10³	—	—
		53.3	0	4.1·10⁻³⁸	1.1·10⁻³¹	6.2·10⁶	6.0·10⁻³⁷	35	—	—
					$\Sigma N^{"}_{\bar p}{}^{"}$ = 9.3·10⁷		$\Sigma N\bar{}_{\bar d}{}^{"}$ = 1.8·10³		$\Sigma N^{"}_{\overline{He}3}{}^{"}$ ~	
E=27 GeV	−e/3	10.9	0	7.2·10⁻³⁹	1.2·10⁻²⁹	5.0·10¹⁰	$\bar d/\bar p$·10⁻⁶	~5·10⁴	—	0.2-0.3
Allaby et al. (1969) CERN	−2e/3	14.7	6.5	5.2·10⁻³⁸	1.5·10⁻²⁹	6.0·10⁸	$\bar d/\bar p$·10⁻⁶	~5·10²	—	—

Table 8.3   Comparison of upper bound on the differential cross sections for quark production with the data on the yields of heavy strong interacting particles. ϑ = angle of emission of secondary particle, $P_Q = |q| P$ is the momentum of a quark with charge q. See the text for the rest of terms (Landsberg, 1974).

production with the data on the yields of heavy strong inter-acting particles $\bar{P}$, $\bar{d}$ and $\overline{He}3$ for the same values of the momenta and production angles at which quarks searches have been made. The effective numbers $N"\bar{p}"$, $N"\bar{d}"$ and $N"\overline{He}3"$ quoted in table 8.3 means that; if quarks had the same production cross section as $\bar{p}$, $\bar{d}$ and $\overline{He}3$ then the number of quarks that would be detected by the set-up during the search would be equal to $N"\bar{p}"$, $N"\bar{d}"$ and $N"\overline{He}3"$.

8.2.2 Search for quarks in stable matter

It was shown in table 8.2 that, one of the quarks are stable. Thus if quarks have been produced by cosmic radiation during the life of the earth one expects that quarks will be detectable in the earth. Let us assume that these quarks have been mixed through the top two kilometers of the earth's crust. Thus the density of quarks per nucleon is $\rho =$ ($\pi T/y N)\varphi$ where T = age of the earth, ($\simeq 1.5.10^{17}$ S) y = depth in g cm^{-2} corresponding to 2 km., N = number of nucleons per g , π comes from integrating over the isotropic incident flux and φ is the quark flux from cosmic rays cm^{-2} s^{-1} st^{-1}. Correspondingly, $\rho N = 2.4.10^{12}\varphi$. This indicates that if $\varphi < 5.10^{-11}$ cm^{-2} s^{-1} st^{-1} therefore $\rho N < 120$ quarks/g .

Several methods of searching for quarks have been tried namely; (a) Refined versions of the Millikan oil drop experiment (b) Magnetic levitometers and (c) Mass and optical spectroscopy.

(a) This method is essentially the same as was used by Millikan (1910), to measure the charge of the electron, using

different sources like sea water or graphite. The quark concentration (in units of quarks per nucleon) has been measured by Rank et al. (1968), Gallinaro et al. (1966) and Braginski et al. (1968) to be $\simeq 10^{-17}$, $\simeq 10^{-18}$, and $\simeq 10^{-17}$ respectively. Millikan (1910) has also reported one event within hundred events having a charge about 30% lower than the final value of the charge of an electron.

(b) In this method the test body is placed in a magnetic potential well and the charge of the body is measured by the body's motion under the influence of electric field.

Morp urgo et al. (1970) have examined 27 graphite grains of an average mass of 5.10^{-10} kg. Their results show that the concentration of quarks is < 1 per 2.10^{18} nucleons. Hebbard and Fairbank (1971) have studied niobium pellets which appeared to have a charge of $(-0.37 \pm 0.03)e$.

(c) A stable charged quark may form a quark hydrogen atom after capturing an electron of the hydrogen atom. The spectral series of such an atom should be detectable in a spectrum. The different groups searching for quarks by this method have been reported, in general, negative results (Skutnik 1970, Burbidge and Burbidge 1967, Sinanoglu et al. 1966). Rank (1969) has looked for spectral lines from quark-hydrogen atoms in samples of sea water, sea weeds, oysters, sea plankton and lake water. His results indicates that the upper limit of the concentration of $2e/3$ quarks is 10^{-18} quarks per nucleon in sea water and lake water and 10^{-17} quark/nucleon in 1 kg samples of oysters, sea weed and plankton.

8.2.3   Search for quarks in cosmic rays

A search for quarks in cosmic rays has been conducted
at sea level, underground and mountain altitudes ever since
the postulation of quark theory by Gell-Mann (1964).   This
covers searches for fractionally charged particles in unaccomp-
anied cosmic rays as well as in EAS.   The progress made has
been reviewed by Sitte (1970) and L. Jones (1971).

(a)   Search for quarks in unaccompanied cosmic rays

Mainly in these experiments the scintillation counters
have been employed to detect fractionally charged particles.
The scintillators select events where the energy deposited in
them is characteristic of that expected from incident particles
having fractional charges and discriminate against events where
the energy deposit is greater or equal to that expected from
integral charge particles.   These experiments, however, face
the problem of background effects due to electron photon showers
or the downward fluctuations in energy loss in the counter.
To reduce background effects different attempts has been made
such as selecting events which indicate the primary particle
has traversed a straight line through all layers of scintill-
ators (Kasha et al. 1967) or incorporating gas proportional
counters in their scintillator telescope (Garmire et al. 1968).
This has been done since proportional counters have a greater
sensitivity to γ-rays compared with scintillators.   The most
successful technique has been to use visual detectors in
conjunction with scintillators, for instance Ashton et al.(1968)
have used flash tubes as visual detector.   The quark limit
obtained by this method is less than about 10^{-10} cm^{-2} s^{-1} st^{-1}.

(b)   Search for quarks as delayed particles in EAS

Let us assume that a detector is situated at a distance
H from a high energy nuclear interaction in which quarks are
produced.   Thus the time difference, Δt, between the arrival
of particles travelling with the velocity of light and quarks
is

$$\Delta t = \frac{H}{\beta_q c} - \frac{H}{C} = \frac{H}{C}\left(\frac{1-\beta_q}{\beta_q}\right) \quad \text{where } \beta_q \text{ is the}$$

relative velocity of quarks with respect to light.   Taking
$\beta_q \simeq 1$ thus $\Delta t = \frac{H}{C}\frac{1}{2\gamma_q^2}$, where $\gamma_q = \frac{1}{\sqrt{1-\beta_q^2}}$.

If at the energy threshold for quark production (see section
8.1.2) the Lorentz factor of the c.m.s. of two colliding nucleons
is γ_c then $\Delta t = \frac{H}{C}\frac{1}{2\gamma_c^2}$, since if the quarks are produced

at rest in the c.m.s. then their Lorentz factor in the laboratory
system is given by $\gamma_q = \gamma_c$.   Taking H = 16.8 Km above sea
level, table 8.4 demonstrates the delay time expected at sea
level of heavy mass quarks arriving behind the shower front
for different processes of quark production.   (Ashton 1973,
private communication).

Although most of the experimenters give positive results
for detecting delayed particles but, due to uncertainties of
such experiments they have used their data to quote limits on
the quark flux.   Dardo et al. (1972) working at 70 m.w.e.
underground and Tonwar et al. (1971) at 2,150 m. above sea level
claimed a definite signal at flux levels of 10^{-8} and 10^{-9}
$cm^{-2} s^{-1} st^{-1}$ respectively.   These positive results are much
higher than the upper limit of the flux reported by Jones et al.

Production Process	Energy threshold in laboratory system for $M_q \gg M_N$ (GeV)	Delay time (ns)
$\pi + \pi \rightarrow \pi + q + \bar{q}$	$98 \; M_q^2/M_N$	$570/M_q^2$
$N + N \rightarrow N + 3q$	$4.5 \; M_q^2/M_N$	$10^4/M_q^2$
$N + {}_7N^{14} \rightarrow 3q + {}_7N^{14}$	$A^{1/3} \frac{3}{2} \frac{9M_q^2}{m}$	$31/M_q^2$
$N + N \rightarrow N + N + q + \bar{q}$	$2 \; M_q^2/M_N$	$2.1 \cdot 10^4/M_q^2$
$N + N \rightarrow 3q + 3q$	$18 \; M_q^2/M_N$	$1.56 \cdot 10^3/M_q^2$

<u>Table 8.4</u>   Delay time expected at sea level of heavy mass quarks relative to ultra relativistic particles from interactions taking place at an altitude of 16.8 km above sea level and at an energy close to the kinematic threshold. All masses in GeV/c^2 and A is the atomic weight of nitrogen. M_N is the mass of nucleon m is the mass of nitrogen and M_q is the mass of quark (Ashton, private communication).

(1967), Bjornboe et al. (1968) and White et al. (1970).

They carried out their experiments at 3,230 m. above sea level,

16 to 36 m.w.e. underground and sea level respectively. These

experimenters have given the upper limit for massive particles

as 10^{-10}, 3.10^{-10} and 4.10^{-11} cm^{-2} s^{-1} st^{-1} respectively.

The positive results of Dardo et al. and Tonwar et al. have

been criticised by Ashton (private communication).

(c) Search for quarks in EAS

Since EAS are produced as a result of the interaction of

primary cosmic rays of energy above $\simeq 10^{14}$ eV thus are potent-

ially important in the search for quarks. Some of the experi-

mental results obtained so far are shown in table 8.5. It

can be seen that apart from the result of the Sydney group the

rest give negative results on the detection of quarks. The

positive results of the Sydney group have been criticised by

a number of authors (Wilson 1970, Kiraly and Wolfendale, 1970,

Adair and Kasha 1969, Rahm and Sternheimer 1969, Rahm and

Louttit 1970 and Frauenfelder et al. 1970). The main critic-

ism was that the Sydney group do not adequately demonstrate

that the five events (quark candidates) were well separated

in ionisation density from the distribution due to plateau or

minimum ionising charged e particles.

8.3 Present experiment

8.3.1 Introduction

A quark search in the E series ($\Delta_e \geq 40$ m^{-2} as defined

by liquid scintillators above the chamber) experiment has

been carried out and in a total number of 12,057 triggers

20 tracks with low efficiency, in the region of $e/3$ fractionally

Author	Method of detection	Electron density threshold	Quark flux in units of $10^{-10} \text{cm}^{-2}\text{s}^{-1}\text{st}^{-1}$	
			$e/3$	$2e/3$
Cairns et al. (1969)	Cloud chamber	>154 m^{-2}	-	~ 5
Clark et al. (1971)	Cloud chamber	>86 m^{-2}	<0.3	<0.3
Evans et al. (1971/72)	High pressure Cloud chamber (28 atoms.He)	>60 m^{-2}	<40	-
Ashton et al. (1971)	Flash Tube Chamber	>40 m^{-2}	<2.6	-
Hazen et al. (1973)	Cloud chamber	$\gtrsim 80$ m^{-2}	<40	-

Table 8.5 Summary of the quark flux obtained in EAS, close to the core of showers, using visual detectors. All the results are given at the 90% confidence level except for the results of Cairns et al. (1969).

charged particles were observed (Ashton et al. 1973a).

From these 20 background tracks, after careful analysis, it was found that two of the low efficiency tracks, out of 20 observed tracks, satisfy the apparant criteria for being genuine quarks. These two candidates, however, could be the result of incoherent muons having traversed the chamber prior to the EAS trigger. It is supposed that the mass of quarks are very high. Thus if one looks at EAS of higher energies, compared with the E series experiment, one hopes to detect them if they are free quarks close to the core of EAS, arriving at sea level. Besides it was hoped that performing the experiment using a higher electron density trigger one can compare the number of low efficiency background tracks with the twenty low efficiency tracks observed in the E series experiment. This comparison enables one to have more information about the probability that the two quark candidates, observed in E series, are genuine. For this purpose the events observed in F series (with an electron density trigger of four times that of E series) experiment was investigated to search for fractionally $e/3$ charged particles. The median shower size of the F series is larger than the median shower size of E series (see table 3.5), i.e. is 4.10^5, as has been recorded by liquid scintillators. The median shower size is more likely to be $2.7.10^5$, as mentioned in chapter 4.

8.3.2   Basic data and analysis

The experimental data were obtained during June, 1972 to March, 1973. The frequency distribution of the total number of flashed tubes in F2 + F3 (see figure 3.11) for acceptable

tracks was obtained and the results are shown in figure 8.3.
An acceptable track is defined as one in which:

(a)   The track must traverse F2 + F3 and produces at least
one flash in the defining layers F1 and F4.

(b)   The track being parallel within $\pm$ 5° (in the projected
plane) with another track having a track length $\geq$ 60 cm. (in
real space).   This criterion was applied for tracks in which
the total number of flashed tubes in F2 + F3 was $\geq$ 60 flashes.

These criteria ensure that:

(a)   The possible observed low efficiency tracks have
passed through the chamber, by demanding that they have
traversed defining layers F1 and F4.   This means that back-
ground tracks due to edge effects (Ashton et al. 1971) which
could simulate quarks have been eliminated.

(b)   Reduces the possibility that, the observed low
efficiency, tracks are due to the passage of incoherent muons
preceding to the EAS trigger.

The negative of the films was first scanned and the events
satisfying the above criteria were selected.   Then the
negative of the films were projected having a scale 1:4.5
compared with real space and the total number of flashed tubes
in F2 + F3 were counted.   For each acceptable event a scale
diagram of the event was plotted.   Table 8.6 compares the
yield of measurable tracks obtained in the E series and F
series.   It is seen that the percentage of photographs showing
at least one measureable track are about the same in both
series.   Table 8.7 demonstrates the frequency of observing
more than one measurable track in an event obtained in the
F series.   One of the low efficiency tracks obtained in the
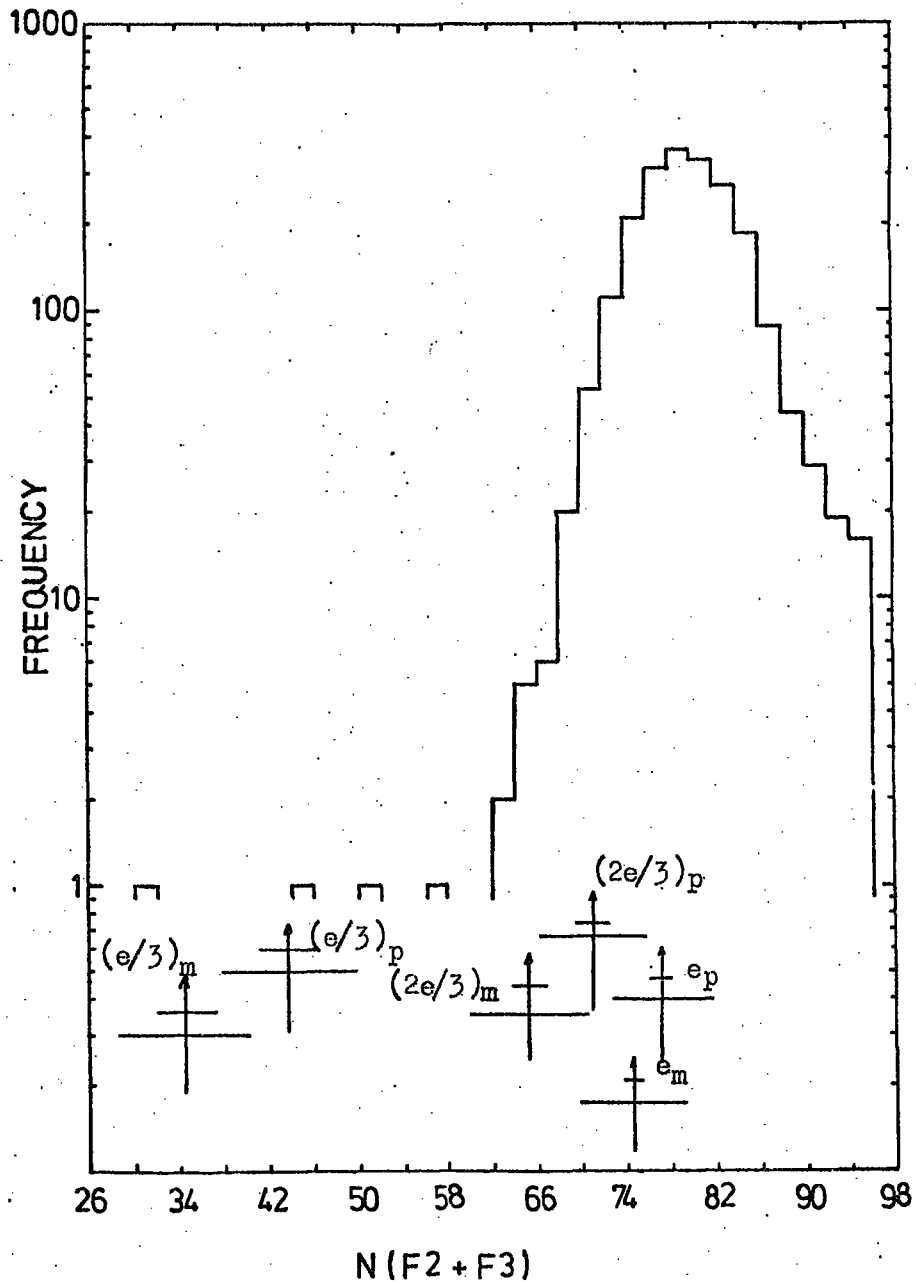
Figure 8.3   Frequency distribution of the observed
number of flashes in F2 + F3.   The arrows
indicate the expected number of flashes in
F2 + F3 for charge e, $^2e/3$ and $e/3$ particles.
The small bars indicate the uncertainty in
the position of the arrow and the large
bars the expected standard deviation of the
distribution.   Mean number of flashes in
F2 + F3 is 79.92 ± 0.19.   The standard
deviation of the distribution is 4.66.

EAS selection	Running time (hr)	Total number of photographs	Total number of measurable photographs	Rate of photographs that give at least one measurable track (%)	Total number of measurable tracks
F series (present experiment)	5,420 Films F1-F40	4,516	1,116	25%	2,077
E series (Ashton et al. 1973a)	2,570 Films E1-E69	12,057	2,753	23%	4,501

Table 8.6   The basic experimental data obtained in F series.   For comparison the results of E series (Ashton et al. 1973a) is also given.

Number of measurable tracks in a photograph n	Number of photographs N showing n measurable tracks	N x n
1	554	554
2	315	630
3	152	456
4	55	220
5	30	150
6	6	36
7	3	21
8	0	0
9	0	0
10	1	10
Total	1,116	2,077

Table 8.7   Frequency of observing $\geq$ one measurable track in the F series

F series is shown in plate 8.1 and one of the two candidates
for quark, observed in the E series is shown in plate 8.2.
A single low efficiency track (event F24-6) is observed which
does not pass through F4 and thus was excluded in being a
quark candidate.   The event is a multiple-scatter one and
is shown in plate 8.3.

8.3.3   <u>The resolving power of the chamber as a quark detector</u>

It is essential to see whether the chamber differentiate
between charged e particles compared with the hypothetical
fractional charged particles.

For single particles the median momentum of muons producing
calibration triggers is 2.1 GeV/c using the data of Hayman
and Wolfendale (1962).   Crispin and Fowler (1970) give the
most probable ionisation loss, I, in neon for primary muons.
This shows that I/I_m = 1.14 and I/I_p = 1.43, where I_m and I_p
are minimum and plateau ionisation losses.   According to
figure 4.1 the overall best fit to η_I - T_D measurements is
a $f_1 Q_1$ = 9 ± 1.   Thus the expected a $f_1 Q_1$ for I_{min} and I_p
charge e particles are $(\frac{9 \pm 1}{1.14}$ =) 7.9 ± 0.9 and ((7.9 ± 0.9) x
1.43 =) 11.3 ± 1.3 respectively.   Table 8.8 shows the expected
number of flashes for 96 layers (F2 + F3) of flash tubes.
The results of the calculations shown in table 8.8, are demon-
strated in figure 8.3.   It can be seen that the flash tube
chamber resolves $e/3$ charged particles from e charged particles.
Figure 8.3 indicates that fractional $e/3$ charged particles
should have 28-50 flashes in F2 + F3.   To convert the calcul-
ated values of a $f_1 Q_1$ (see table 8.8) to internal efficiency,
η_I, first the variation of η_I against time delay T_D for differ-

PLATE 8.1   Event F14 - 122

A low efficiency track
N(F2 + F3) = 44
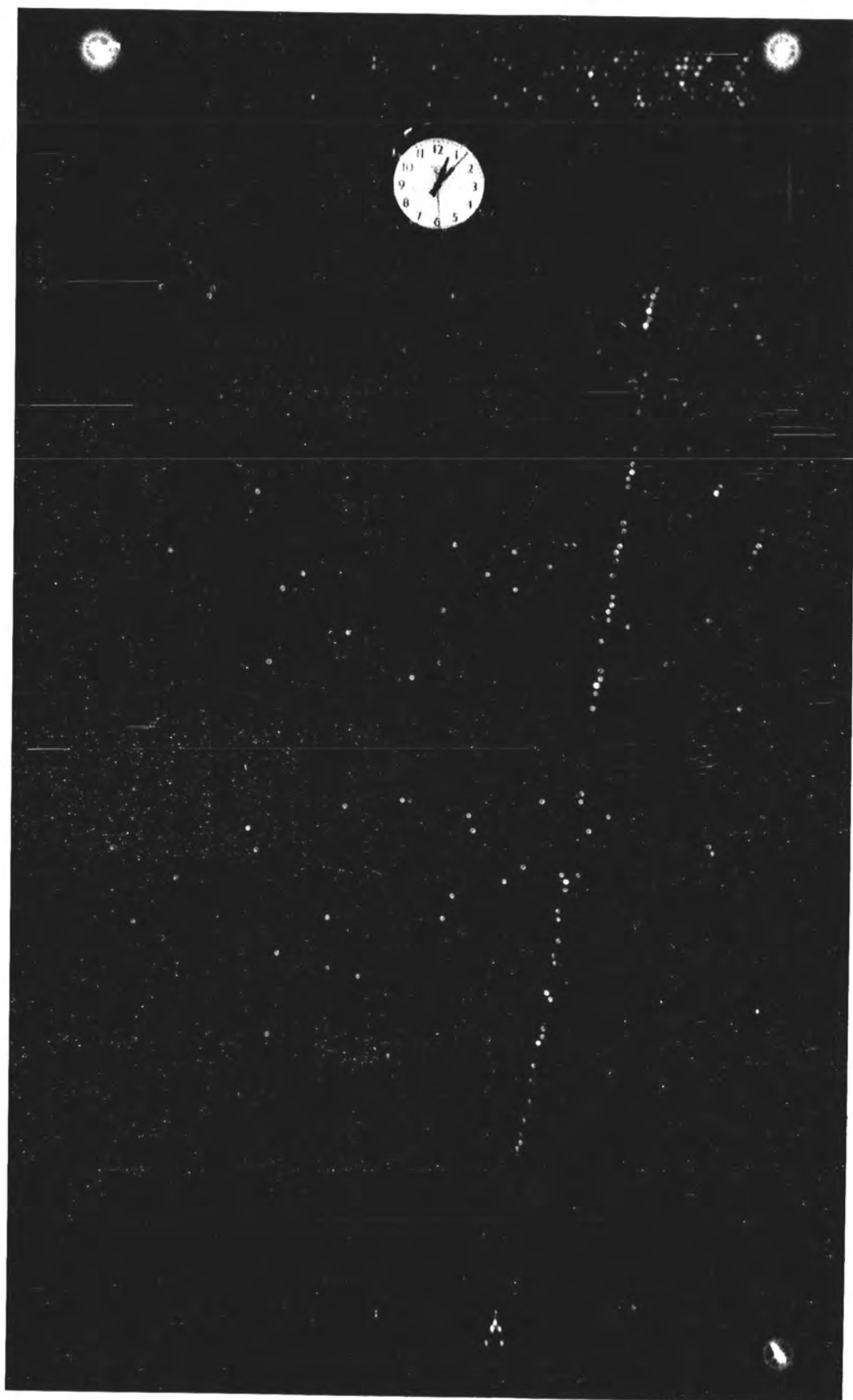
PLATE 8.2   Event E19 - 45

A quark candidate obtained
in the E series

$N(F2 + F3) = 28$
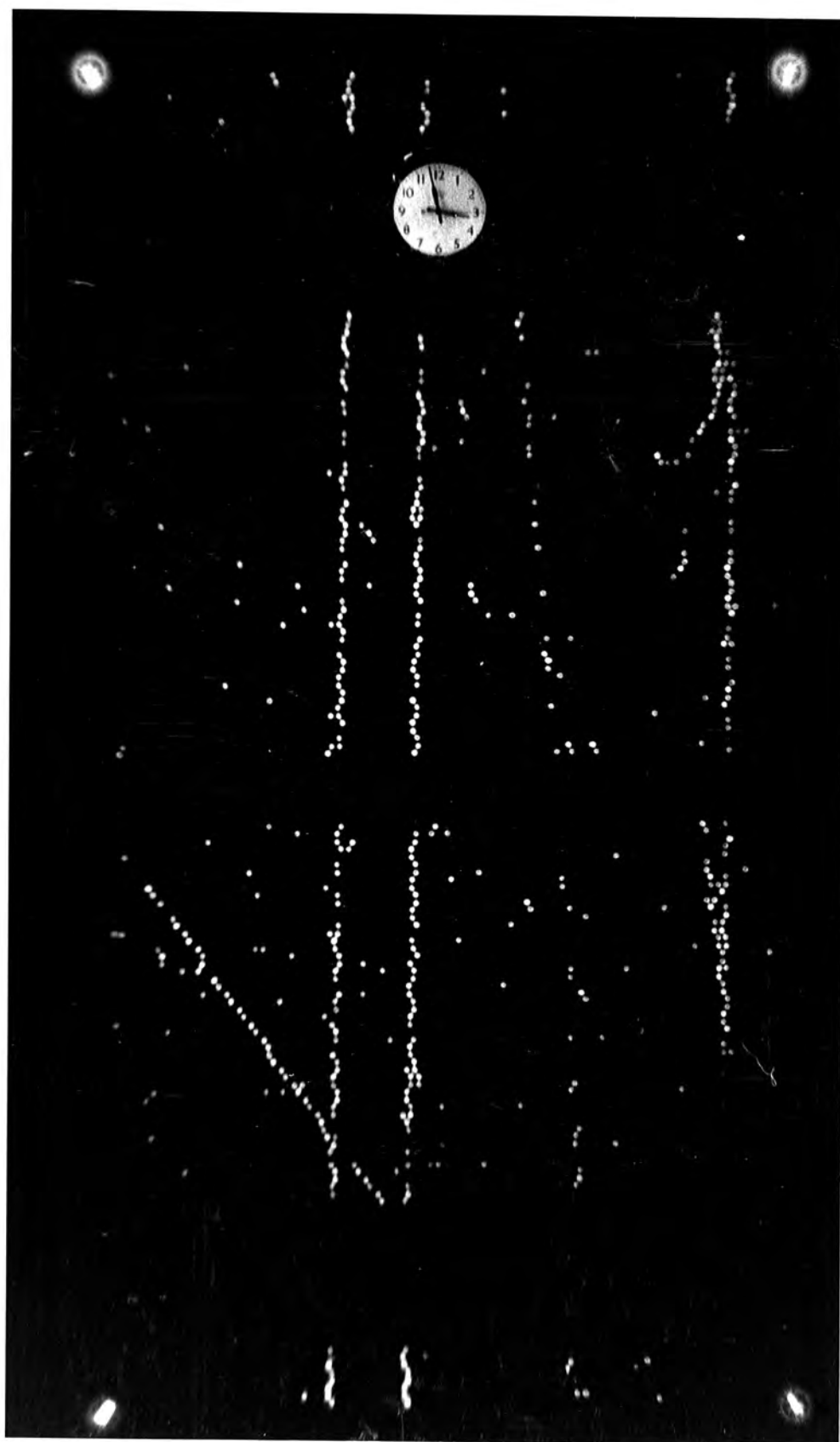
PLATE 8.3   Event F24 - 6

The low efficiency multiple-
scatter event.
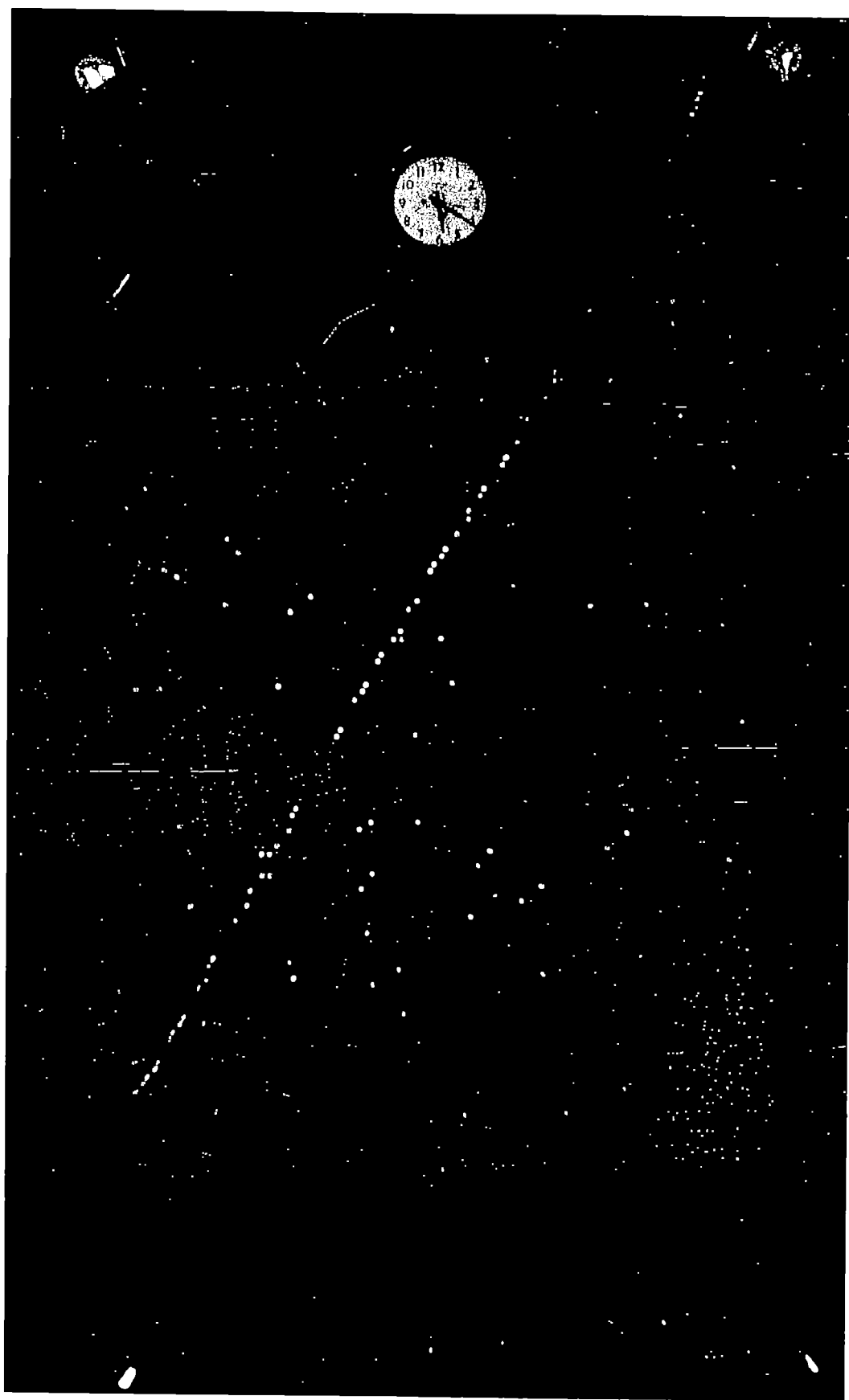
Charge	Energy loss	$a f_1 Q_1$	η_I for $T_D=20\mu s$ (%)	η_L (%)	Expected number of flashes for $(F2+F3)=96\eta_L$	Expected standard deviation of the distribution of flashes about mean ($96\,\eta_L$).
e	I_m	7.9±0.9	89±1	77.6±0.9	74.5±0.9	4.7
e	I_p	11.3±1.3	92±1	80.4±0.9	77.1±0.9	4.5
e/3	I_m	0.88±0.10	41±3	35.8±2.6	34.4±2.5	5.8
e/3	I_p	1.26±0.15	52±3	45.4±2.6	43.5±2.6	5.9
2e/3	I_m	3.25±0.40	78±2	68.0±1.7	65.2±1.6	5.3
2e/3	I_p	5.04±0.60	84.5±1.8	73.7±1.6	70.9±1.5	4.9

Table 8.8   The expected number of flashes and their standard deviations produced by minimum ionising (I_m) and plateau ionising (I_p) charged e, e/3 and 2e/3 particles in (F2+F3) for 20μs time delay.

ent a f_1Q_1 were calculated (Lloyd, 1960). Then the variation

of η_I against a f_1Q_1 at the fixed value of $T_D = 20\mu s$ was

obtained. From this variation the expected values of a f_1Q_1,

shown in table 8.8, were converted to η_I. Ashton et al (1973d)

have measured frequency distribution of the number of flashes

in F2 + F3 for different values of T_D, from which the standard

deviation of the distribution of flashes about the mean were

deduced (seventh column of table 8.8).

8.3.4   The expected number of knock-on electrons

To exclude the low efficiency background tracks from

genuine quarks in the chamber one must consider the following

points:

(a)   The track traverses F1 and F4 (to eliminate edge

effect).

(b)   The time elapsed between the observed low efficiency

tracks and the occurrence of the last trigger should be more

than about 3 min (Ashton et al. 1971, Saleh 1973). This

is approximately equal to the recovery time of flash tubes,

in which the tubes become efficient (at normal level) for

detecting ionising particles.

(c)   The track being parallel with other shower penetrating

particles.

In the present experiment all the three observed low

efficiency tracks, in the range of quark candidates (28 - 50

flashes in F2 + F3), satisfy conditions (a) and (b), mentioned

above.   None of them, however satisfy condition (c) and thus

all could be attributed to background tracks.

There is, however, a further test to differentiate between

charge e and charge e/3 particles.   This is the rate of knock-

on's (K.O's) per track. The probability of K.O. production
is proportional to Z^2, where Z is the charge of the primary
particle. Thus it is expected that the rate of K.O's prod-
uced by a charged $e/3$ particle would be equal to $1/9$ of that
produced by a charged e particle.

A K.O. is defined as (at least) a pair of adjacent flashes
on the track in F2 + F3. For three observed low efficiency
tracks the frequency of the observed K.O.'s were determined
and the results are shown in the fifth column of table 8.9.
One should notice that the single random background flashes
(in F2 + F3), which are attributed to radio activity in the
glass, could simulate the observed number of K.O.'s per track.
The total number of these spurious flashes in F2 + F3 were
counted, for events shown in table 8.9. The results of which
are indicated in table 8.9 (sixth column of table 8.9).
Ashton et al. (1973d) have demonstrated that the total number
of the observed spurious flashes are independent of time
delay. Thus the total number of simulated K.O.'s for each
event was calculated and then substracted from the total
observed K.O.'s, the results are shown in the seventh column
of table 8.9. This was done by the following procedure:

Total number of genuine K.O.'s = Total number of the
observed K.O.'s $- \dfrac{2 \times N(s.p) \times N(F2+F3)}{84.5 \times 96}$ where N(F2+F3) is

the observed flashed tubes in F2+F3 for the quark candidate,
N (s.p) is the observed number of random spurious flashes in
F2+F3 and the factor 84.5 is the average number of flash tubes
in each layer of the chamber. On the other hand the expected
number of K.O.'s (according to the above definition) for a
muon having traversed the chamber is 1.6 per track. (This

Event number	Total number of flashes in F2-F3 for quark candidates	Number of tracks observed in the chamber excluding the quark candidate	Angle between quark candidate and other tracks	Number of K.O's in F2+F3 along quark candidate	Number of single random background flashes in F2+F3	Total number of genuine K.O.'s in F2+F3 along quark candidate
F10-67	30	0	-	0	93	-
F14-122	44	0	-	1	67	0.12
F39-97	50	0	-	5	152	3.1

Table 8.9   Detail characteristics of quark candidates observed in the F series.

is equivalent to K.O.'s with energy $E \gtrsim 4$ MeV, which is equivalent to the range of two flashed tubes as will be described in chapter 9). Thus the expected number of K.O.'s/ track for a quark of charge $^e/3$ is $\simeq 0.18$/track. Therefore one concludes that only the event F10-67 and F14-122 (see table 8.9) could be accounted as background tracks simulating quarks. (It should be noted that the expected number of K.O.'s/ track for long time delay decreases due to the decrease in the detection efficiency of the chamber and is $0.4 - 0.8$ K.O.'s/ track for time delays ranging between $144-103\mu s$, Ashton et al. 1973 a).

A sample of the events, obtained in the F series was scanned and it was found that 9.1% of all photographs have only background flashes. Figure 4.1 suggests that incoherent muons traversing the chamber in the period of $103\mu s$ to $144\mu s$ ($41\mu s$ width) prior to the EAS trigger would produce 28-50 flashed tubes in F2+F3. The mean expected rate of incoherent muons through the chamber is 104.2 s^{-1}. This is equal to the rate of muons with energy ≥ 0.78 GeV multiplied by the aperture of the chamber. The rate of muons of $E \geq 0.78$ GeV is $6.3.10^{-3}$ cm^{-2} $s^{-1}st^{-1}$ as given by Hayman and Wolfendale (1962). This suggests that the expected rate of the incoherent muons simulating quarks for 4,516 events (films F1-F48) is ($4,516$ x $\frac{9.1}{100}$ x 41.10^{-6} s x 104.2 s^{-1} =) 1.8. This result is sufficiently close to the two observed background events to conclude that the events F10-67 and F14-122 were produced by background muons.

It is noted that if 9.1% of events showing only background flashes are calculated to be 1.8 background muons simulating quarks then the 25% (see table 8.6) showing measurable tracks

should contain 4.9 background muons, simulating quarks. None is observed which could be as a result of fluctuation as well as the effect of the obscuration of the chamber due to electron photon showers. These are produced in the chamber as a result of nuclear interaction of hadrons (in EAS), mainly with lead and iron absorbers.

8.3.5 The upper limit of the quark flux

As no genuine $e/3$ quark tracks have been found it is concluded that the upper limit of quarks through the chamber (1.57 m^2 st aperture) is $0.89.10^{-11}$ $cm^{-2}s^{-1}st^{-1}$ at the 90% confidence level. This limit accounts for the possible loss of 16% ($= 1 - e^{-0.18}$) genuine quarks which would produce side by side K.O.'s flashes on their tracks. Taking the inelastic cross-section of quarks to be 11 mb (see section 8.1.2) the upper limit of quarks incident on the top of the chamber is $5.5.10^{-11}$ $cm^{-2}s^{-1}st^{-1}$ at the 90% confidence level. Table 8.10 summarises the results obtained in the F series. The results of the E series is shown in table 8.10 to be compared with the present experiment.

8.4 Conclusion

The results of the present experiment indicates that the chamber is capable of detecting $e/3$ particles. No genuine quarks with charge $e/3$ have been observed. The upper limit for quarks in EAS of median shower size $2.7.10^5$ (capable of producing ≥ 80 m^{-2} local electron density) is found to be $5.5.10^{-11}$ cm^{-2} s^{-1} st^{-1} at the 90% confidence level. Comparing the observed number of 3 low efficiency background tracks with

EAS selection	Total number of triggers	Total number of tracks having 50 flashes in F2+F3	Number of quark candidates satisfying the required criteria	Quark flux
F series Films F1-F40	4,516	3	0	$< 5.5 \ 10^{-11} \mathrm{cm}^{-2} \mathrm{s}^{-1} \mathrm{st}^{-1}$ at 90% confidence level.
E series Ashton et al. (1973a) Films E1-E69	12,057	20	2	$<8.0.10^{-11} \mathrm{cm}^{-2} \mathrm{s}^{-1} \mathrm{st}^{-1}$ (based on two possible events)

Table.8.10   Summary of the results obtained in the present experiment (F series).

The results of E series (Ashton et al. 1973a) are shown for comparison.

20, as has been observed in the E series, indicates that the latter yielded a larger number per trigger than the former although this difference could be due to fluctuation. Accordingly it is suggested that further experiments should be carried out with the same or less electron density trigger as the E series. For further experiments, with the present flash tube chamber, one needs to modify the chamber such that the effect of background will be minimised. For this purpose it is suggested that one should increase the area of the plastic scintillators A and B so that the resulting telescope aperture covers the chamber sensitive volume. In this way one is enable to monitor the muons, and other penetrating particles, having traversed the chamber in the time period $0 - 200\mu s$ preceding the EAS trigger by means of a single particle indicator.

CHAPTER 9

PRODUCTION OF FORWARD AND BACKWARD MOVING

SECONDARIES BY PENETRATING PARTICLES

9.1   Introduction

The importance of K.O.'s as a test to identify genuine quarks from the background particles was discussed in chapter 8.   In this chapter the ability of the chamber in recording K.O.'s, produced by the muon component of the cosmic rays, has been considered.   For this purpose the energy spectrum of K.O.'s in wide range of energy has been measured.

An interesting type of events showing backward moving secondaries, produced by penetrating component of cosmic radiation has been observed.   A possible explanation for this type of event is given.

9.2   The method of the analysis of data

Using the single particle selection system (see figure 3.12) 4,237 events were obtained.   The negative of the films thus obtained (films C2-C22) were projected such that the constracted events having a ratio of 1:45 compared to the real space.   A K.O. defined as a recoiled track off the main primary track. The range of K.O.'s satisfying the following criteria were measured:

   (i) The K.O. have an apparent range of $\geq$ 3 flashed tubes.

   (ii) The apparent point of the K.O. production lay within F2 or F3.

To measure the range of K.O.'s (in the present experiment the range of K.O.'s in vertical plane have been measured) the

total number of flashed tubes and aluminium electrodes, along
the K.0. track, were counted. (The position of the electrodes
were drawn on the scanning table and thus enables one to count
the number of electrodes). The range of K.0.'s passing through
F4a and F4b (see figure 3.11) were measured up to the fourth
layer of F4b. For these cases 10 MeV energy loss was assumed,
for K.0.'s having traversed scintillator B.

For each measurable K.0. the projected recoiled angle
of K.0.'s were measured. The measurement carried out for
K.0.'s in which the first three flashed tubes were in straight
line. A scale diagram of all the measured K.0.'s were drawn.

The analysis carried out for 4,237 events of K.0.'s with
range $\geq$ 6 flashed tubes. A total number of 554 K.0.'s were
observed. Out of these 554 K.0.'s, the angular distribution
of 359 K.0.'s were measured. The measurements of K.0.'s
with range between 3-5 flashed tubes carried out for 574
triggers and 69 K.0.'s with this range were obtained. This
measured frequency normalised to 4,237 triggers to be comparable
with K.0.'s of range $\geq$ 6 flashed tubes. Table 9.1 shows the
results of the measured range distribution of the observed
K.0.'s. An example of an observed K.0. is given in plate 9.1.

The measured range distribution of K.0.'s converted to
the energy spectrum of K.0.'s using the range-energy relation-
ship of electrons as will be described in the following section.

9.3   Range-energy relationship

The range R of a particle travelling in a particular
absorber defines as the distance in which the particle can
traverse before it stops. This range is, obviously, a

PLATE 9.1   Event C5 - 29

An example of a K.O. observed
in the chamber

E = 55 MeV.
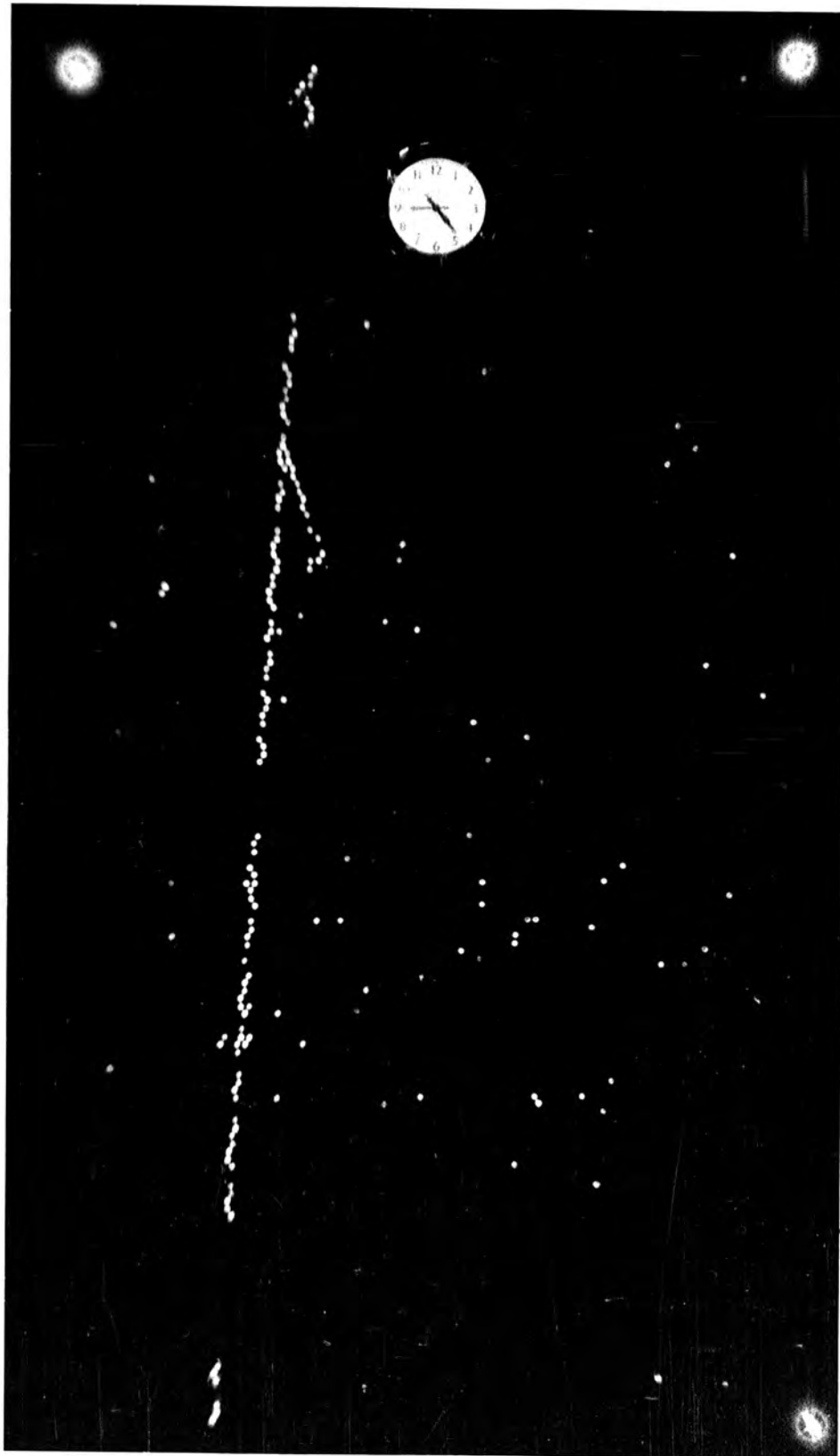
Range of K.O. (Number of flashed tubes)	Frequency
3-5	511
6	115
7	72
8	54
9	61
10	59
11	30
12	34
13	9
14	14
15-17	27
17-19	11
19-21	16
21-23	8
23-25	13
25-27	3
27-29	4
29-31	4
31-33	5
33-35	5
35-41	1
41-47	2
47-56	3
56-62	4

Table 9.1   Frequency distribution of the measured K.O.'s obtained, in analysing 4,237 triggers.

function of the primary energy of the particle and depends
on the way in which it loses its energy and follows as:

$$R = \int_0^{E_O} \frac{dE}{-dE/dx}$$ where $\frac{dE}{dx}$ is the total energy

loss per unit length.

The electron range is a somewhat indefinite concept
since at low energy region electrons diffuse through matter
and at high energy region the initial electron is soon obscured
by an accompanying shower of electrons. In particular, at
high energy region radiation losses makes the apparent range
of electrons to be shorter than the actual range.

The range of high energy electrons have been calculated
by Wilson (1951) for copper, lead and aluminium. Wilson
takes into account the radiation losses and the effect of
multiple scattering of the electrons. His calculations show
that the range R of electrons of energy E_O (in units equal to
L_n 2 times the ionisation loss in radiation length) follows
as:

$R = \log (E_O + 1)$ where R is the mean range in radiation
length.

In this formula the effect of multiple scattering has
been neglected. Wilson, however corrects the calculated
range for this effect and his results are shown in figure 9.1,
for aluminium absorber.

Berger and Seltzer (1964) have calculated the range
of electrons by Monte-Carlo method in different absorbers.
Tabata et al. (1971) give the results of the calculation of
Berger and Seltzer, for electrons in the range of 4-24 MeV
for aluminium. These are shown in figure 9.1. The experi-
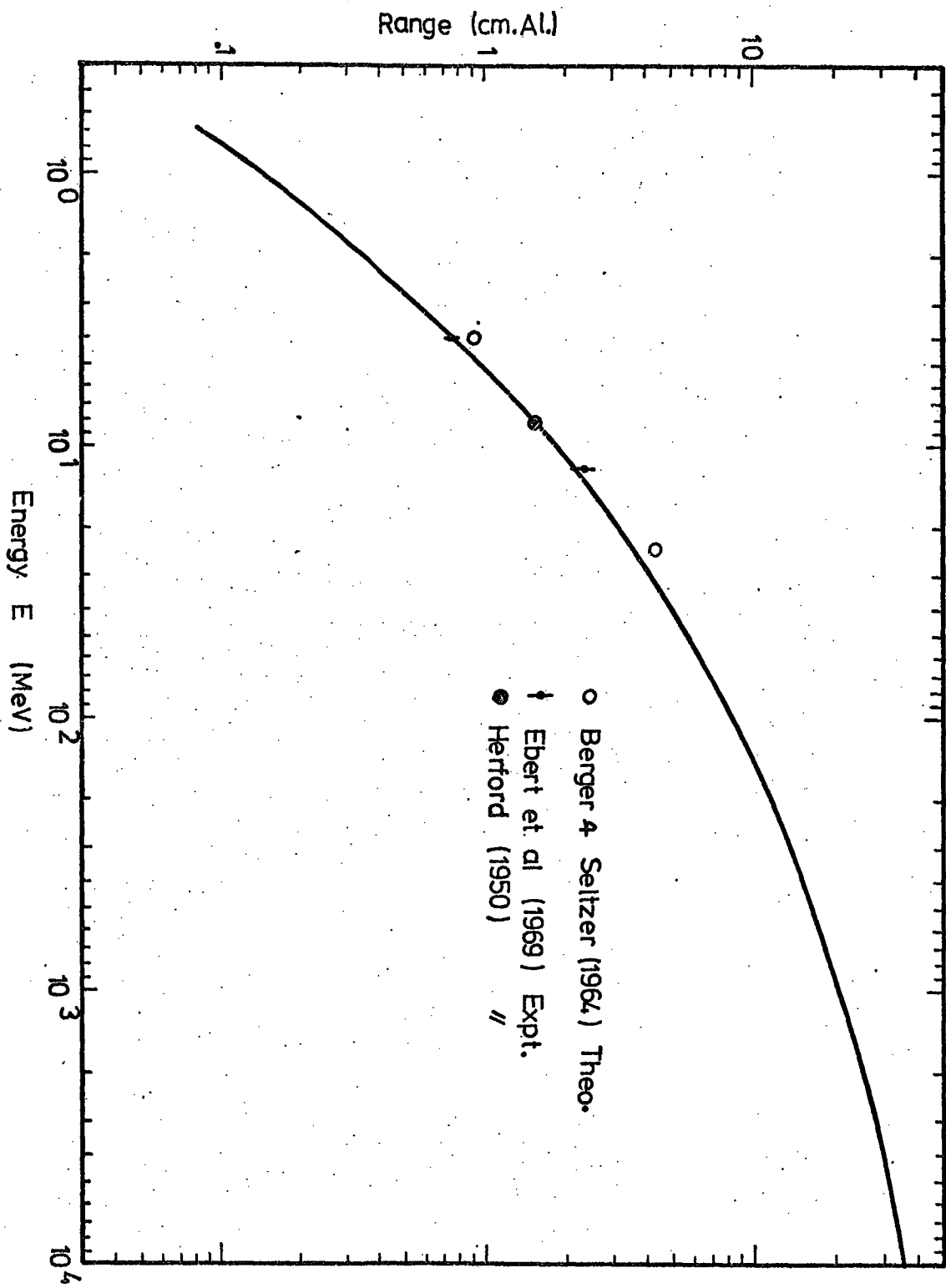
Figure 9.1   Range of electrons as a function of the electron energy
in aluminium. The solid curve shows the results of
the calculation of Wilson (1951).

mental results of Herford (1950) in the region of 4-12 MeV,
and Ebert et al. (1969), in the region of 4-24 MeV, also
are shown in figure 9.1. It can be seen that the results
of Wilson (solid curve of figure 9.1) is in reasonable agree-
ment with other workers in the energy region were the comparison
has been made.

To estimate the energy of K.O.'s from their measured range
in the chamber, it is assumed that the range of electrons in
aluminium and glass, for a fix electron energy, are the same.
This is due to the fact that the radiation length and critical
energy of these absorbers are nearly the same (see table 6.1).
The amount of glass for a particle having traversed one flash
tube is 0.314 cm. and the thickness of aluminium electrode is
0.122 cm. The production of K.O. in the gas of the tubes and
polythene sleeves of the tubes ($6.35.10^{-3}$ cm in thickness)
have been neglected.

Accordingly the measured range of electrons converted to
electron energy by means of figure 9.1. The differential
energy spectrum of K.O.'s thus obtained is shown in figure
9.2. Since some corrections must be made to these results,
as will be described later, thus the results shown in figure
9.2 is called, the apparent measured differential energy spec-
trum of K.O.'s.

9.4 Angular distribution of K.O.'s

It was mentioned earlier that low energy electrons
scatter through the absorber before they stop. This makes
the measurements of the angular distribution of K.O.'s to
be inaccurate in present experiments. To reduce this inaccur-
acy, only K.O.'s in which the first three flashed tubes, in
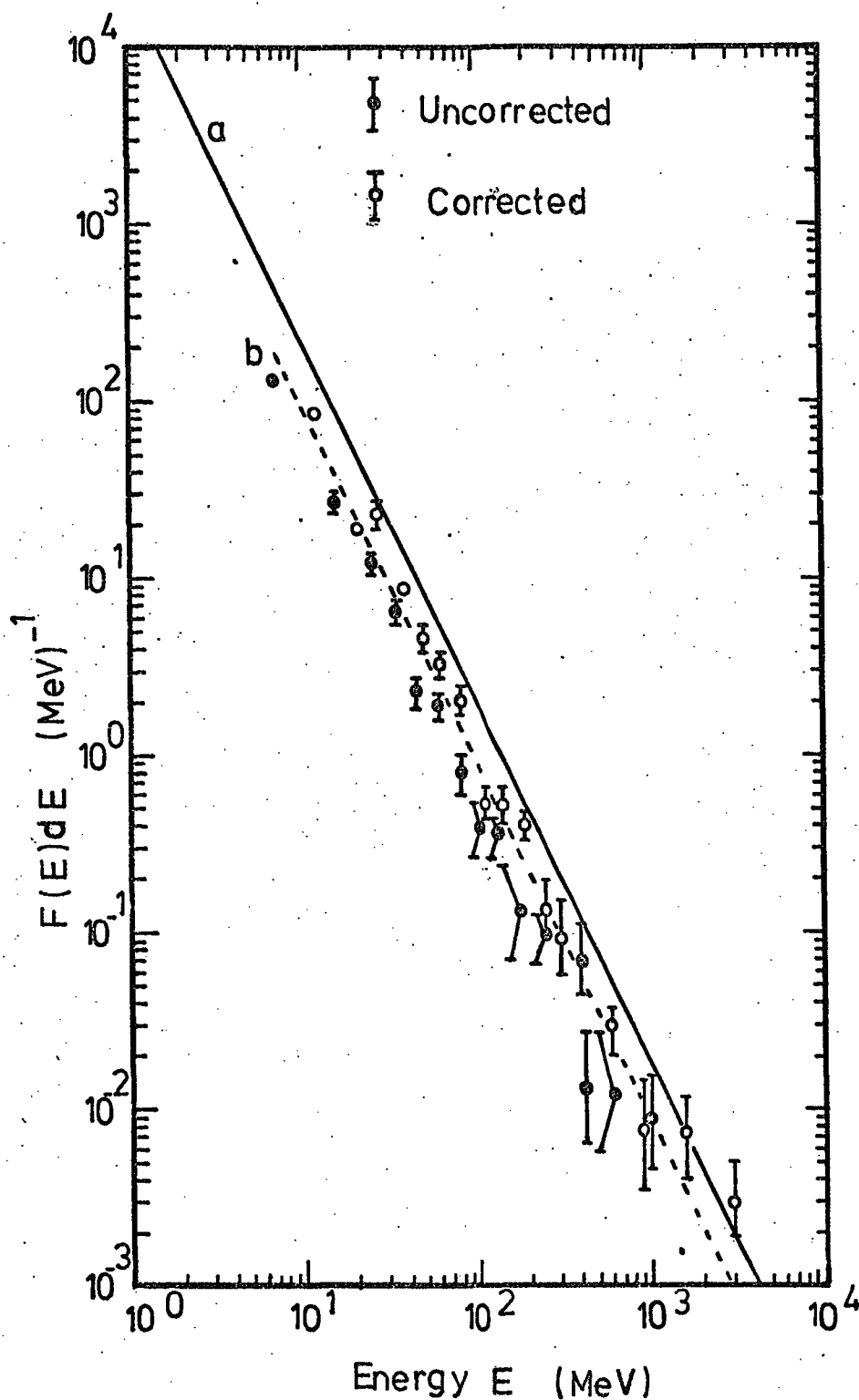
Figure 9.2   Measured differential energy spectrum of K.O.'s obtained for 4237 tracks (1 track =91.5 g cm^{-2} aluminium). The first point has been obtained analysing 572 tracks and is normalised to 4237 tracks. Solid curve (a) shows the predicted spectrum according to Bhabha theory (see the text). The dashed spectrum (b) shows the best line through the corrected spectrum (ϕ).
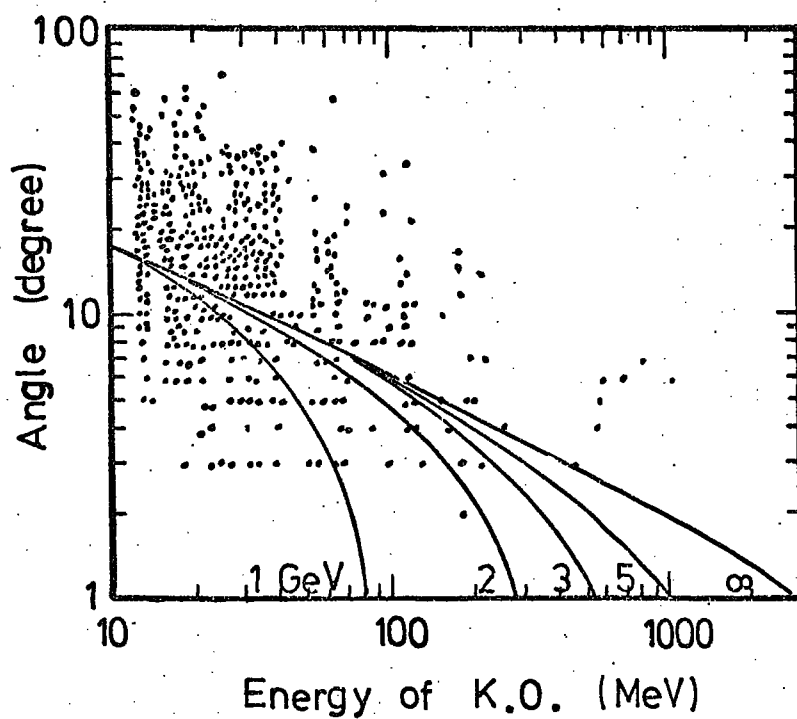
Figure 9.3   The measured projected angular distribution
of K.O.'s having range ≥ 6 flashed tubes.
The solid curves show the predicted angular
distribution of K.O. (in real space). The
primary muon energy (in GeV) is indicated
for each curve.

their ranges, were in the same line considered. Figure
9.3 shows a scatter plot of the measured angular distribution
of K.O.'s with range $\geq$ 6 flashed tubes.

If α is the recoiled angle (in real space) and E is
the K.O. energy produced by a muon of momentum p and mass
$m_\mu c^2$ then (Kannangara and Zivkovic, 1953)

$$E = \frac{2 \, m_e \, p^2 \cos^2\alpha}{m_e \sqrt{p^2 + m_\mu c^2 - p^2 \cos^2\alpha}}$$

The solid curves in figure 9.3 shows the angular distrib-
ution of K.O.'s for different muon energies. This figure
indicates that about more than a half of the experimental
data lie above the predicted curve of $E = \infty$. This disagree-
ment is mainly due to the effect of multiple scattering for
low energy electrons. At high energy region the disagreement
is due to ambiguity in the height of K.O. production, as will
be described in section 9.6.

9.5 Correction for the aperture of the chamber

Take the vertical distance of F2 + F3 to be equivalent
to 1 cm. of aluminium, and the distance between bottom of F3
to the fourth layer of F4a to be equivalent to L_0 cm. of
aluminium. Thus the probability of measuring a K.O., prod-
uced in F2 or F3, with range of 1 cm. of aluminium is (the
distance between K.O. production to the top of F2 is equiv-
alent to $(L + L_0 - 1)$ cm. of aluminium).

$$P(1) = \frac{(L + L_0 - 1)}{(L + L_0)}$$

P(1) was evaluated as a function of 1 . Using figure
9.1 the range 1 converted to K.O. energy (adding 10 MeV energy

loss due to scintillator B). The results are shown in figure 9.4.

9.6 Correction for energy of K.O.

It was shown in section 9.4 that the expected angular distribution of K.O.'s are very small, in particular for high energy region. This introduces a serious problem in measuring the actual range of K.O.'s, i.e. to identify accurately the point of K.O. interaction, due to the geometry of the flash tubes. An attempt has been made to estimate approximately the actual range of K.O.'s (in projected plane) from its measured range as follows:

Two typical muon tracks I and II were drawn on a scale diagram of the flash tube chamber (front view). It was assumed that muon tracks I and II interact at one of the points a, b, c, d, a', b', c' and d' (see figure 9.5) producing a K.O. of energy E_t'. The recoiled angle of K.O. was evaluated from figure 9.3 for $E_\mu = \infty$ and its range R_t was derived from figure 9.1. After drawing the K.O. track with range R_t the number of flashed tubes, where the K.O. track and the primary muon track were shared, counted. This then subtracted from the total number of flashed tubes expected for a K.O. of energy E_t'. This shows the apparent number of flashed tubes, R_a which would be observed in the analysis of the data. This procedure was done for all eight positions mentioned above. For each position two cases, depending on the K.O. produced in either side of the muon, were considered. Thus for each K.O. energy E_t' a total of 16 values of R_a were obtained. The mean of these 16 values of R_a and its error was calculated
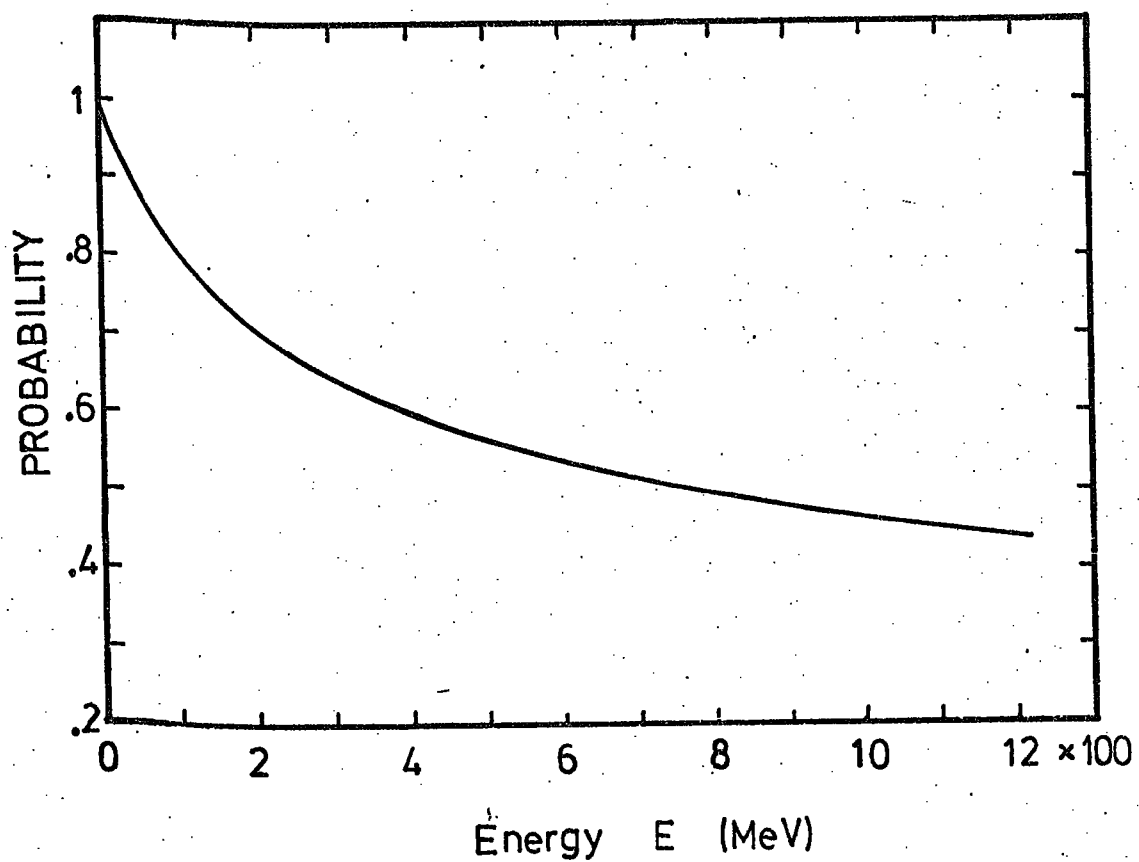
Figure 9.4   Probability of observing a K.O. with
              energy E (MeV) in the chamber.
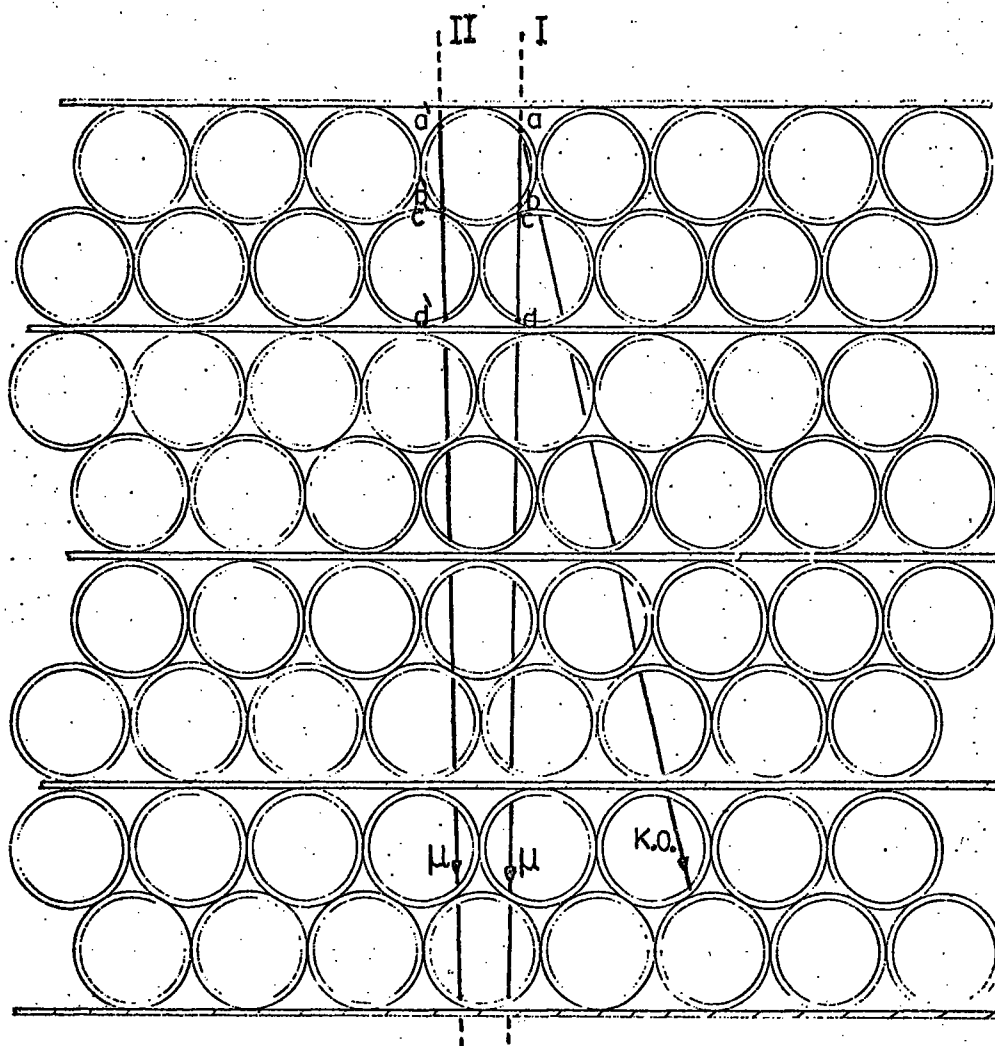
Figure 9.5   This figure shows the production of a K.O. by a typical muon track (I) at point a. The energy of K.O. is 16 MeV (equivalent to a range of 7 flash tubes). The angle of emission of K.O. is taken to be 14°, assuming the energy of muon is $E_\mu = \infty$. It can be seen that the first three flashed tubes have been shared between K.O. and the muon track (I). The energy of K.O. thus would be measured as 10 MeV (equivalent to a range of 4 flash tubes.).

and converted to E_a by means of figure 9.1. The variation of apparent K.O. energy E_a as a function of true energy E_t is plotted in figure 9.6. In these calculations it is assumed that K.O.'s do not go under any multiple scattering, such that it causes a change in the direction of initial K.O. track. Because the angle of recoiled K.O. is very small for energies of $E_t \gtrsim 1,000$ MeV, the calculation carried out only for one case in this energy region.

An example is given in figure 9.5 where a K.O. of energy of 16 MeV (equivalent to a range of 7 flashed tubes) has been produced at point a. It can be seen that the first three flashed tubes could be misidentified as due to the primary muon track. Thus in measurement, this K.O. would be considered to pass through 4 flash tubes, i.e. having an energy of 10 MeV.

9.7 The corrected differential energy spectrum of K.O.

The rate of measured K.O. at the measured apparent energy E_a first corrected for aperture by means of figure 9.4. This then corrected for estimating K.O. energy using solid curve of figure 9.6. The results of the corrected spectrum is shown in figure 9.2. The dashed line shown in figure 9.2 has been drawn through the corrected experimental points and follows a form of $F(E')dE' \propto \frac{1}{E'^2} dE'$, where E' is the energy of K.O.

9.8 Comparison between the measured and predicted energy spectrum of K.O.

The differential collision probability for particles of mass, m, and spin $1/2$ has been calculated by Bhabha (1938)

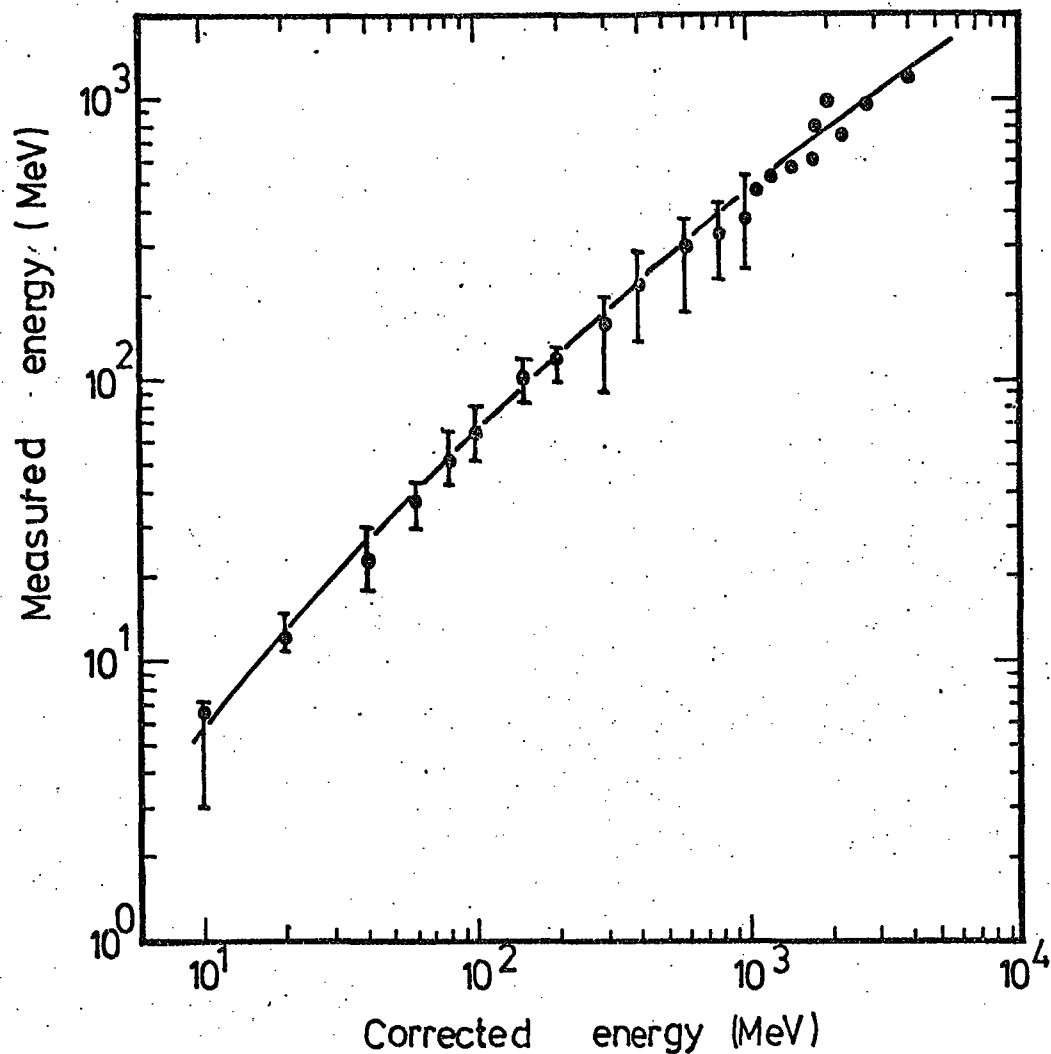Figure 9.6   This figure shows the relationship
between the measured (uncorrected)
and corrected energy of K.O.'s.
The arrows show the mean error of
each point obtained in averaging
16 different positions for K.O.
production (with the same angle).
The measurements for corrected energy
beyond 1000 MeV only have been carried
out for one position.   The solid curve
demonstrates the best curve through the
points.

and is (Rossi, 1952)

$$P(E, E') \, dE' = \frac{2c \, m_e c^2}{2} \quad \frac{dE'}{E'^2} \left(1 - \beta^2 \frac{E'}{E'_m} + \frac{1}{2} \left(\frac{E}{E + mc^2}\right)^2\right) g \, cm^{-2}$$

where $c = 0.15 \frac{Z}{A}$, $m_e c^2$ is the rest mass of electron, β is the relative velocity of the incident particle of energy E with respect to light, E' is the energy of K.O., E'_m is the maximum transferable energy and is given by,

$$E'_m = 2 \, m_e c^2 \quad \frac{(E^2 - m^2 c^4)}{(2 \, m_e c^2 \, E + m^2 c^4 + m_e^2 c^4)}$$

Figure 9.7 demonstrates E'_m as a function of muon energy for μ-e collisions.

The total probability of K.O.'s of energy E' in traversing a muon of energy E through F2 + F3 is (the vertical amount of matter in F2 + F3 is 91.5 g cm^{-2} and the average $\frac{Z}{A}$ of F2 + F3 is $\simeq 0.5$):

$$P_t(E, E') \, dE' = \frac{6.83}{\beta^2} \left[1 - \frac{2E'}{E'_m} + \frac{1}{2}\left(\frac{E}{E + mc^2}\right)^2\right] \frac{dE'}{E'^2} \, (MeV \cdot track)^{-1}$$

Since in the present experiment no information is available about the energy of the individual muons thus it is necessary to assume a form for the energy spectrum of muons at the point of K.O. production. This spectrum then should be folded into the function $P_t(E, E') \, dE'$ to obtain the predicted differential energy spectrum of K.O.'s.

The adopted energy spectrum of muons for present calculations is taken from Hayman and Wolfendale (1962). It is assumed that all K.O.'s have been produced at the centre of F2 + F3. The energy loss for muons from the top of the
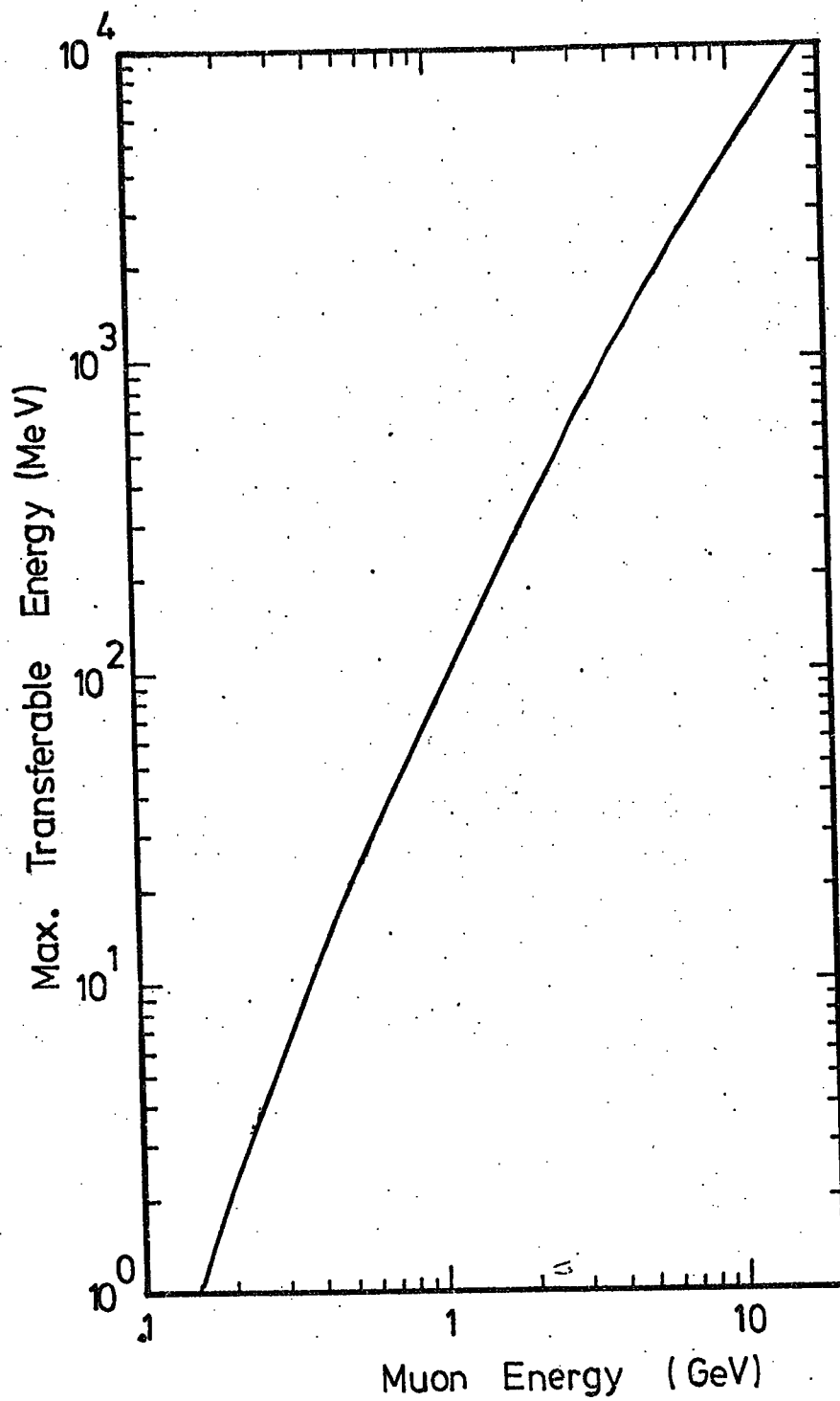
Figure 9.7   Maximum transferable energy to electron
              as a function of muon energy in μ-e
              collisions.

chamber to middle of F2 + F3 is 0.5 GeV. This is calculated
taking the range-energy relation as given by Serre (1967).
This then subtracted from the energy spectrum of Hayman and
Wolfendale to obtain the energy spectrum of muons at the centre
of F2 + F3. This then folded into the function $P_t(E,E')dE'$
calculating the following integral

$$N(E,E')dE' = \int_{E_\mu(min)}^{E_\mu(max)} N(E_\mu) \, P_t(E, E')dE' \, dE_\mu$$

where $N(E,E')dE'$ is the total number of K.O. and $N(E_\mu)dE_\mu$
is the energy spectrum of muons at the middle of F2 + F3.
E_μ (min) is the minimum muon energy capable of producing a
K.O. of energy E' and E_μ (max) assumed to be 30 GeV).
The above integral, calculated numerically and then the
results normalised to 4237 triggers. The solid curve in
figure 9.2 shows the expected differential energy spectrum of
K.O. produced by 4,237 triggers in the chamber.

It can be seen that the expected and measured spectra
are parallel within experimental errors. The absolute rate
of the predicted spectrum is nearly twice the observed rate.
The loss in the rate of the measured spectrum at low energy
region is mainly due to the effect of multiple scattering.
There is equal probability for K.O. to scatter in either side
of the initial electron track, i.e. toward the main muon
track or outward from it. This suggests that the K.O.'s
which have been scattered toward muon track would be indisting-
uishable from the main track and thus would be lost. The
other effects are the ambiguity in estimating energy of K.O.,
i.e., ambiguity in the point of interaction and possible

errors in the range-energy relationship. It should be noted that in present experiment the projected range of K.O.'s have been measured which introduces an uncertainty in estimating the measured K.O. energy. Because of these uncertainties the corrected experimental data normalised at arbitary point of $E' = 160$ MeV to the expected spectrum, i.e., the rate of the experimental points multiplied by 2.0. At each energy E' the measured rate after normalisation divided to the expected rate at the corresponding energy and the results are shown in figure 9.8.

Figure 9.2 shows that the measured spectrum is consistent with the predicted spectrum, based on Bhabha theory, for the measured energy range in this experiment. The increase in cross section production for $E' > 1$ GeV, as observed in this experiment, is due to the uncertainty in measuring $E_t' - E_a'$ relationship for high energy region (see section 9.6).

One should note that although probability of other processes than K.O., i.e. pair production and bremstrahlung, are much lower for low energy muons (less than a few ten of GeV) they become comparable or higher than K.O. cross section for muon energy of $\gtrsim 40$ GeV. The effect of these processes is believed to be not significant in present experiments (with 2.1 GeV. median muon energy).

9.9 Comparison with other experiments

Figure 9.8 demonstrates a survey of the experimental data as given by Allkofer et al. (1971) together with the results of present experiments. This figure shows the deviation of the experimental data from the theory of K.O. as

Author	Source of muons	Code
Present work	Cosmic rays	▨
Roe and Sozaki (1959)	Cosmic rays	◉
Deery and Neddermeyer (1961)	Cosmic rays	△
Chaudhuri and Sinha (1964)	Cosmic rays	O
Chaudhuri and Sinha (1965)	Cosmic rays	◉
Kearney and Haze (1965)	Cosmic rays	▲
Allkofer et al. (1971)	Cosmic rays	□
Backenstoss et al. (1963)	8 GeV muon from accelerator	▼
Kirk and Neddermeyer (1968)	10.5 GeV/c and 5.5 GeV/c muons from accelerator	▽

Table 9.2   This table serves as a key of figure 9.8.
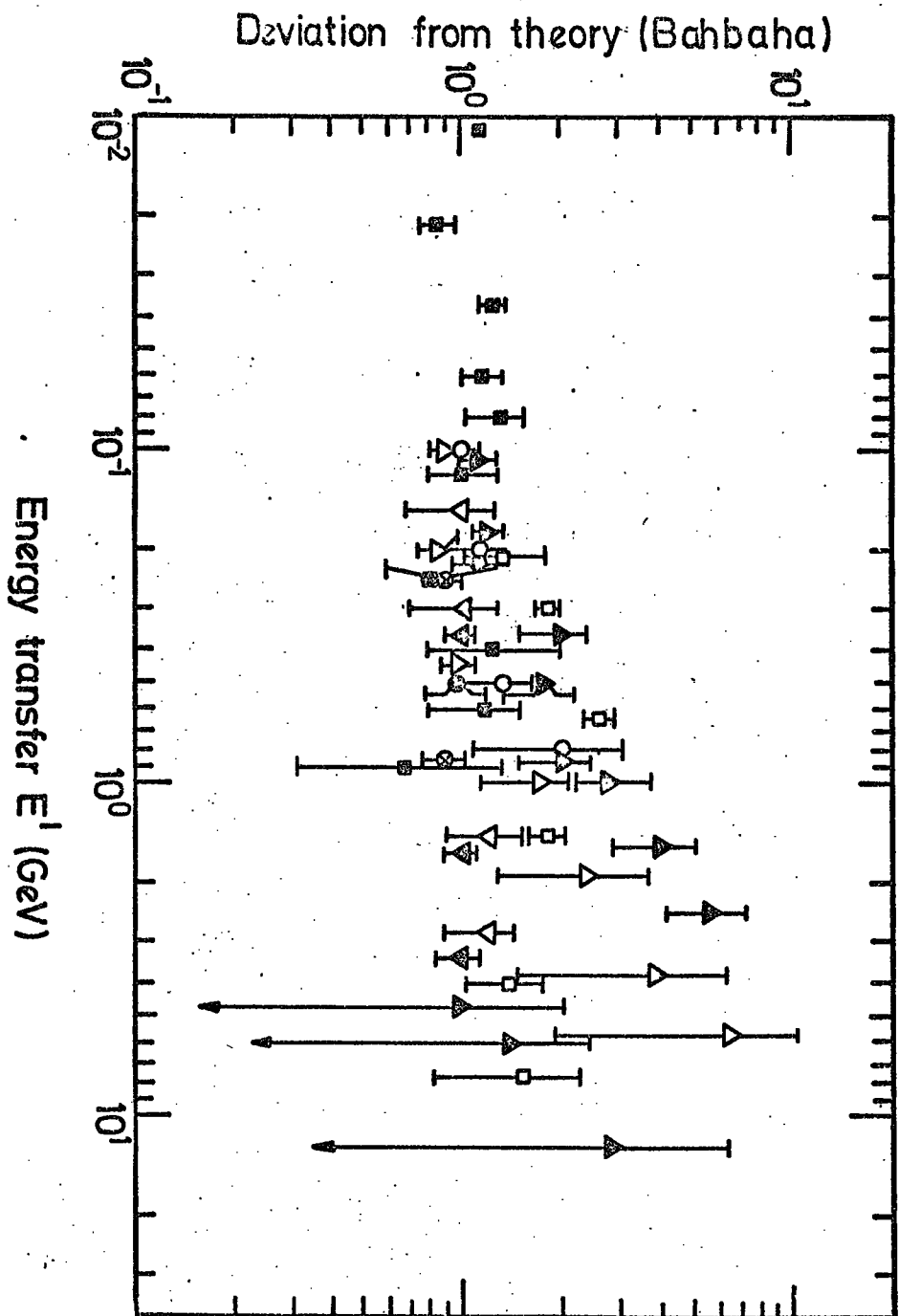
Figure 9.8 Survey of experimental results on K.O.'s as given by
Allkofer et al. (1971). The results of the present
experiment shown in this graph (see table 7.1).

given by Bhabha (1938).

The data of figure 9.8 have been obtained using cosmic ray muons or accelerators as a source of muons. Table 9.1 serves as a key to the data of figure 9.8.

It can be seen that there are deviations in the region of median energy transfers ($\gtrsim$ 1 GeV), in cosmic rays experiments.

Deery et al. (1961) were able to fit their experimental data by multiplying the expected cross section of K.O.'s by a factor, the so-called form factor F. This defines as $F = 1 + | q^2 |/\lambda_\mu^2$ where q is the invariant of the 4 - momentum transfer in units of $\hbar$ and λ_μ is the compton wave length of muons. (The energy transfer to electrons, initially at rest in the laboratory system, is $W = | q |^2/2m$, where m is the electron mass, thus $W = 10$ GeV for $| q | = 0.1$ GeV, and the incident muon required for this is 17 GeV).

The difference between theory and experiment could be either as a result of the invalidity of the theory of Q.E.D. at high energy transfer or could be due to the structure effect of muons.

Deery et al., however could not differentiate between the above mentioned effects in describing their results.

Kirk and Neddermeyer (1968) have interpreted their results, which is inconsistent with Bahbaha theory, at high energy transfer, as a confirmation of the validity of the applied correction (due to the systematic and random errors in estimating K.O. energy) rather than a direct verification of the theory.

9.10   Backward moving secondaries

9.10.1   Introduction

It was shown, in section 9.4, that due to the effect
of multiple scattering, the measured angular distribution
of the recoiled electrons are larger compared with theoretical
expectation.   The discrepency however is larger for low energy
K.O.'s.

As it can be seen from figure 9.3, the maximum observed
angular distribution of electrons is about 70°.   During the
course of scanning it was noticed that some of the produced
particles were emitted with angle of > 90°.   Since these
events could be due to the low energy electrons, scattered
backward, thus to reduce this effect only the events showing
a backward moving secondary with range ≥ 5 flashed tubes
considered.

9.10.2   Results

Table 9.3 shows the measured properties of the 22 back-
ward moving secondaries observed in 4,237 triggers.   The
events shown in table 9.3 have been grouped to 4 types as
follows:

Type (a):   This type of event showing the produced secondary
track being parallel to the aluminium electrodes.   These are
believed to be as a result of backward scattered K.O.'s.

Type (b):.   A total of 15 events of this type were observed.
This type of event could be produced in the same way as ment-
ioned for type (a).   The other possible way of production
could be due to low energy nuclear interaction.   Plate 9.2

Type of Event	Film-Event number	Range	Angle (degree)	Energy (MeV)	
				electron	pion
	C5 - 107	7, 1	102	12	-
(a)	C6 - 137	5, 0	96	8	-
	C20 - 175	5, 0	111	8	-
	C3 - 119	9, 3	-	17	43
	C4 - 66	6, 2	146	11	34
	C4 - 179	7, 3	166	12	37
	C5 - 124	11, 7	165	22	48
	C6 - 55	11, 4	136	22	48
	C7 - 111	11, 5	159	22	48
	C7 - 181	5, 2	146	8	30
(b)	C8 - 8	8, 3	135	15	40
	C8 - 103	12, 5	120	25	51
	C9 - 27	12, 5	162	25	51
	C9 - 105	5, 2	127	8	30
	C15 - 20	9, 3	142	17	43
	C15 - 186	5, 2	164	8	30
	C16 - 164	7, 2	120	13	37
	C19 - 16	28, 10	115	.78	88
(c)	C3 - 117	25, 15	97	-	78
	C9 - 111	39, 21	141	-	>130
(d)	C14 - 95	12, 8	164	-	> 51
	C20 - 118	35, 14	91	-	>100

Table 9.3   The measured properties of the backward moving secondaries.   In the third column (Range) the first number indicates the number of flashed tubes and the second number shows the number of electrodes in which the particle has passed through them.

PLATE 9.2   Event C16 - 164

An example of a backward
moving secondary particle
observed in the chamber.

shows an example of this type of event.

Type (c): One event of this type has been observed. The event is similar to a $\pi \rightarrow \mu + e$ decay.

Type (d): This type of event is the most interesting one. These events indicate the production of a backward moving secondary having traversed at least 15 cm of iron. These type of events, if they are genuine, are probably produced by muon electro production of a nucleon resonance followed by decay to the ground state in which a backward pion is emitted, the overall reaction being $\mu p \rightarrow \mu n \pi^+$. Two events of this type are listed in table 9.3 (events C9-111 and C14-95) but a third event of similar type has also been observed (event C20-118) in which a penetrating particle produces a secondary at 90° to its line of flight. After traversing 9 flash tube the secondary either scatters throuth 90° or decays to a charged and neutral particle, the charged particle penetrates 15 cm iron.

To obtain better statistics the 1,046 triggers obtained in single particle run (see chapter 3), i.e., films C1a - C1k, were analysed looking for this type of event. None was observed. Thus the three events of type (d) have been observed in 5,238 triggers. An example of this type of event is shown in plate 9.3.

The energy of the observed backward moving secondaries, listed in table 9.3, have been calculated assuming they are electrons (using figure 9.1) or pions (using Serre table, 1967).
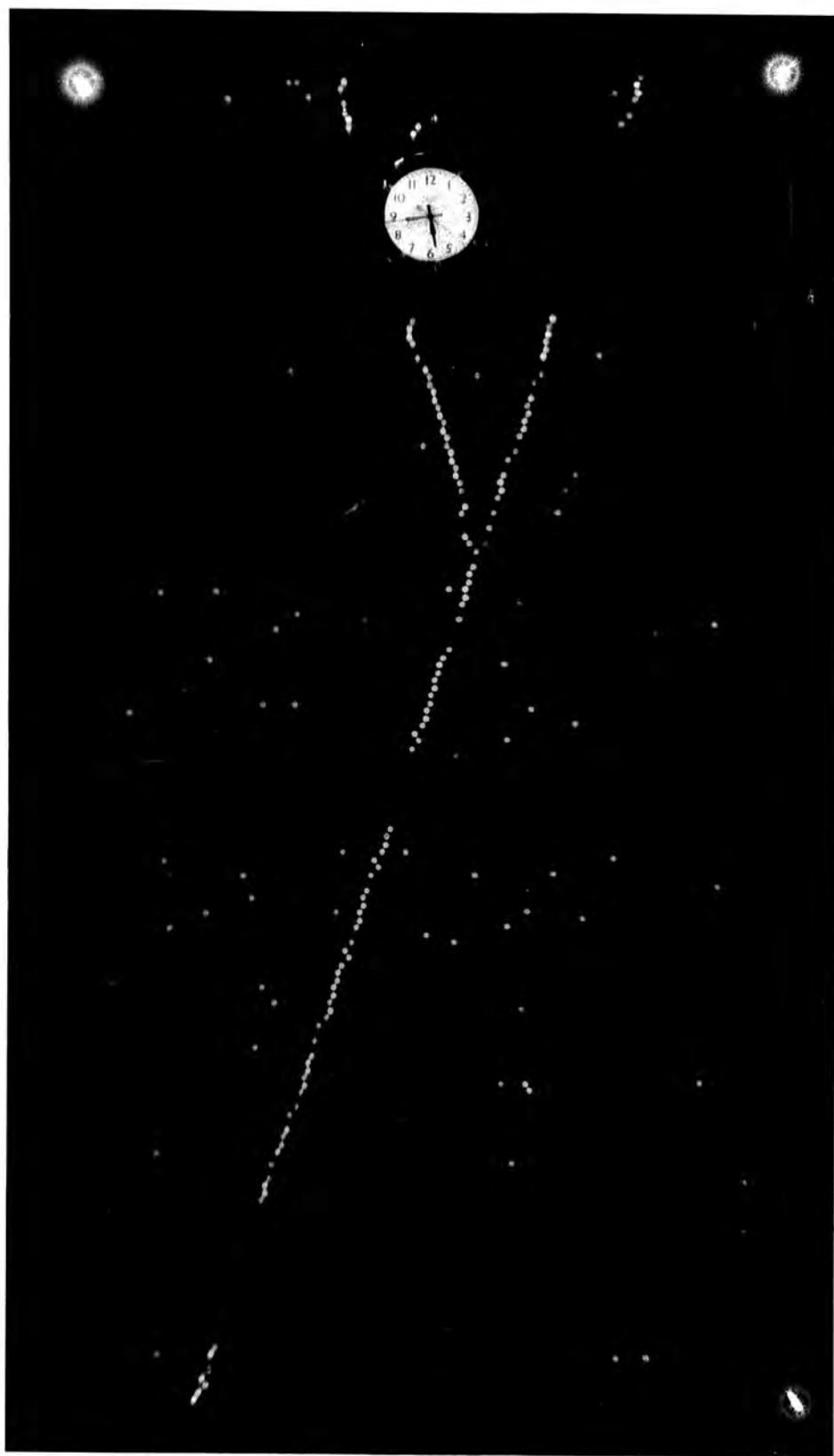
9.10.3   The number of backward moving particles simulated
         by background particles

A test was carried out to see whether the observed events

PLATE 9.3   Event C9 - 111
An example of a backward moving
secondary particle, having
traversed 15 cm of iron.

of type (d) are genuine or not. For this purpose the events of films C2-C22 were investigated and the number of triggers showing the presence of a second track in the chamber were counted. It was found that 75 events, from the total of 4,237 triggers, show a second particle having traversed 15 cm of iron and being not parallel to the single muon produced the trigger. Hence the expected number of the tracks simulating type (d) event is

$$\frac{75}{84.5} \times \frac{5,283}{4,237} \simeq 1$$

where 84.5 is the mean number of flash tubes in each layer of the chamber.

This is to be compared with the two observed events of type (d). It can be seen that the statistics of the observed events of type (d) is not good to get firm conclusion about the presence of such type of events.

9.11   Conclusion

The energy spectrum of K.O.'s produced by cosmic ray muons were measured in energy range of $E \simeq 10 - 1,000$ MeV. It was found that the measured differential energy spectrum of K.O.'s follows a law in the form of $1/E'^2$ dE'. The spectrum is parallel within experimental errors to the theory given by Bhabha (1938) assuming muons have a spin of 1/2. The results, however, are found to be lower than theory by a factor of about 2. This could be explained as a result of experimental limitation of the chamber in resolving tracks of distances of the order of one flash tube diameter.

It was found that 0.5% (= 22 events out of 4,237 triggers)

of the events produced backward moving secondaries with
range of ≥ 5 flashed tubes.   This rate is lower than the
rate of the observed K.O.'s of range ≥ 5 flash tubes by a
factor of about 32.   In a total of 5,238 trigger only 2 events
(0.04%) were observed which shows a backward moving secondary
having traversed 15 cm of iron.   Although these probably
produced by $\mu p \longrightarrow \mu n \pi^{+}$ they could conceivably be produced
by the decay of a heavy mass particle (for example the decay of
a non relativistic, $\beta < 1/3$, λ quark into a proton quark
plus π^{-}).   As the events of this type are rare a selection
system would be required.   A possible detector could be a
flash tube chamber with built-in alternative layers of
Cerenkov counters sensitive to downward moving and upward
moving particles respectively.

ACKNOWLEDGMENTS

The author wishes to thank Professors G.D. Rochester, F.R.S. and A.W. Wolfendale for the provision of the facilities for this work and for their interest and support.

He is extremely grateful to his supervisor, Dr.F. Ashton, for his willing guidance and invaluable help throughout the work.

Many members of Cosmic Ray Research Group are thanked for helpful discussions, in particular Dr. D.A. Cooper and Mr. A.J. Saleh and in later stage of work to Mr. I.A. Ward for their friendly assistance.

The technical staff of the Physics Department, in particular Mr. W. Leslie, Mr. M. Lee, Mr. E. Lincoln, Mr. K. Tindale and Mr.J. Storey are thanked for their help, and Mrs. A. Gregory for her invaluable help in drawing many of the diagrams for this thesis.

The Computing Unit is thanked for the provision of computing facilities.

The author is grateful to Mrs. J. Lincoln for her patient work in typing this thesis.

Finally, the University of Isfahan is thanked for the financial support.

APPENDIX A

IONISATION LOSS OF FAST CHARGED PARTICLES

A.1   Introduction

The saturation of the ionisation loss of fast charged particles in matter has been established experimentally (see Crispin and Fowler, 1970).   The exact magnitude of the effect in various detectors have not yet been measured precisely. Ramana Murthy (1968) has measured the ionisation loss of fast charged particles in proportional counter.   He finds that the ratio of minimum to plateau ionisation loss is 0.45 compared with 0.60 as predicted by Sternheimer (1953), at $P/mc = 2,000$.

The decrease in the ratio of plateau to minimum ionisation (observed by Murthy, 1968) has been investigated by Garibyan and Ispiryan (1972).   These authors suggest that when a fast charged particle traverses from solid to gas (as in a proportional counter) the energy loss at distances larger than t_{eff} is equal to the theoretical energy loss with allowance for the density effect in the gas, while on emerging from the solid matter the loss is equal to that in the gas without density effect, but decreased by the same factor as the energy loss in the solid matter of the window is decreased by the density effect.   (The value of t_{eff} is a function of Loretz factor of the primary particle, for instance is $\simeq 5 - 15$ cm at $\gamma = 10^3$ in the experiment of Murthy 1968).

A.2   Results of the present experiment

The negatives of the films obtained in measuring burst

size - burst width relationship were considered and the internal efficiency η_I of Fla due to the charged hadrons induced burst in iron were measured. The measurement of η_I were carried out for different energy range of hadrons. The results of the measurement as a function of Lorentz factor of the primary particle (assumed to be pions) are shown in figure A.1. The experimental data at $\gamma = 130$ is obtained measuring η_I of Fla due to the passage of muon component of EAS runs (averaged for the E,F and G series). The experimental data shown in figure A.1 at $\gamma = 20$ is derived from the single particle run. (The median energy of muons in EAS and single particle run is 14 GeV and 2.1 GeV respectively). All data shown in figure A.1 have been corrected for unresolved K.O.'s.

A.3. Comparison with theory and conclusion

The solid curve shows the theoretical prediction using Sternheimer theory (Hayakawa, 1969) for neon gas, which is 98% of the flash tube gas. The curve has been normalised at $\gamma = 20$, assuming a f Q = 9 for 20 μs time delay (see figure 4.1).

It can be seen that there is reasonable agreement between experimental data and Sternheimer theory. The dashed curve of figure A.1 is calculated including the transition effect due to Garibyan and Ispiryan (1972). It is seen that the experimental data do not follow this curve.

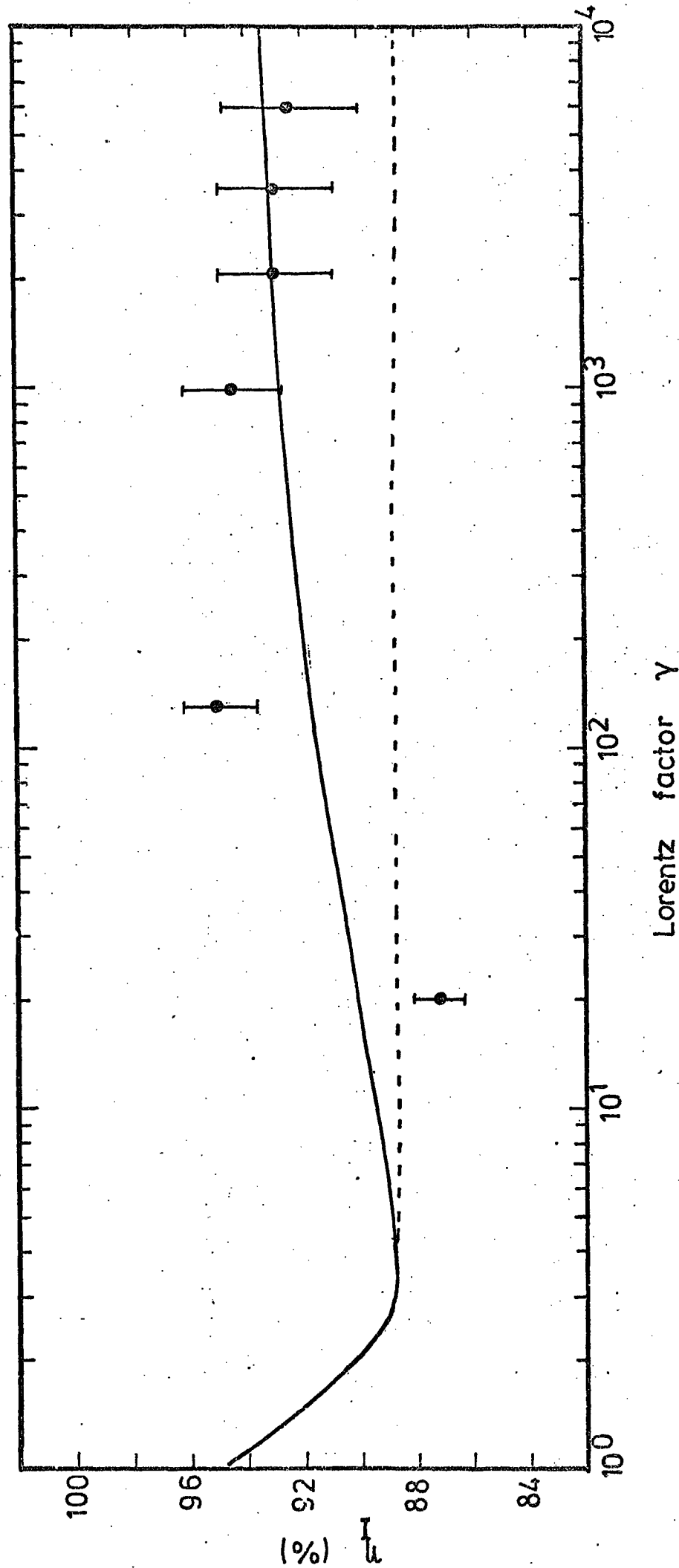Figure A.1 η_I as a function of γ. The solid curve indicates the theoretical prediction as given by Sternheimer (Hayakawa, 1969) with density effect. The curve has been normalised at a $\gamma Q = 9$ for $20\mu S$ time delay. The experimental data have been corrected for unresolved K.O.'s. The dashed curve is the expected variation using the transition effect of Garibyan and Ispirkyan (1972).

APPENDIX B

Deduction of the spatial angular distribution of Cosmic rays about the zenith angle from a measured projected angular distribution.

B.1 Introduction

Lovati et al. (1954) have introduced a method to convert the projected angular distribution of particles, measured in perpendicular plane, into the distribution function of particles foreseen by the $\cos^n \varphi$ law, in real space. Thus if one measures the projected angular distribution, one is enable to derive the best value of n using a chi-square method. The procedure of the calculation are as follows:

Let A and B (figure B.1) be two rectangular detectors placed above each other. Detector A has dimensions 2 Y cm. by 2 X cm. and detector B has dimensions 2 V cm. by 2 W cm. The vertical distance between A and B is Z cm. The direction of motion of one particle crossing the two detectors A and B is individulated by the angle ϑ and ψ, which are bound to zenith angle φ by

$$\cos \varphi = \cos \vartheta \, \cos \psi$$

As mentioned earlier, it is assumed that the angular distribution of particles follows as $I = I_0 \cos^n \varphi$ where I_0 is the vertical intensity ($cm^{-2} s^{-1} st^{-1}$) and I is the intensity at zenith angle φ. Then the total flux F_n of the particles through the sensitive volume of detector is

$$F_n = \iiint dx \, dy \, \cos \varphi \, I(\varphi) \, dw$$

$$= \iiint dx \, dy \, \cos \varphi \, I_0 \cos^n \varphi \, dw$$

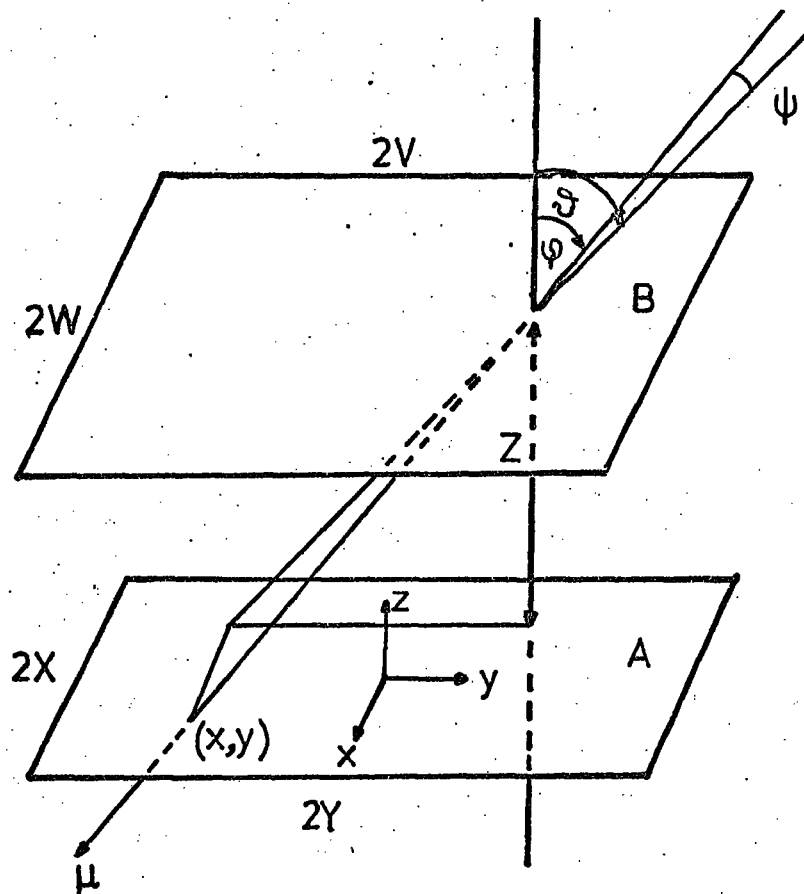where d w is the elementary solid angle and is given by

Figure B.1. The path of a muon through parallel detectors.

$$d \ w = Cos \ \psi \ d \ \psi \ d \vartheta$$

thus $F_n = \iiint dx \ dy \ Cos^{n+1}\vartheta \quad d\vartheta \ Cos^{n+2} \psi \ d\psi$

$$= 2 \ I_o \int_{\vartheta_1}^{\vartheta_2} \int_{Y_1}^{Y_2} \int_{X_1}^{X_2} \int_{\psi_1}^{\psi_2} Cos^{n+1}\vartheta \ d\vartheta \ dy \ dx \ Cos^{n+2}\psi \ d\psi$$

Re-write the above expression inverting the order of integration with the limits

$$\vartheta_1 = 0 \quad , \quad \vartheta_2 = arc \ tg \ ((Y + V)/Z)$$

$$Y_1 = -Y \quad , \quad Y_2 = Y - Z \ tg \vartheta$$

$$X_1 = -X \quad , \quad X_2 = X$$

and $\psi_1 = arc \ tg \ (\dfrac{W + X}{Z} \ Cos \vartheta)$, $\quad \psi_2 = arc \ tg \ (\dfrac{W - X}{Z} \ Cos \vartheta)$

Let the orthogonal projection of the angular distribution on the vertical plane Y Z be $N_n(\vartheta)$ then

$$F_n = \int N_n (\vartheta) \ d\vartheta$$

Hence

$$N_n(\vartheta) = 2 \ I_o \ Cos^{n+1}\vartheta \ (Y + -Z \ tg \vartheta) \int_{-x}^{x} dx \int_{\psi_1}^{\psi_2} cos^{n+2}\psi \ d\psi$$

with the limitation

$$Y + V - Z \ tg \vartheta \geq 0, \ i.e., \ tg \vartheta \leq (Y + V)/Z.$$

This equation can be integrated for integer values of n. The solutions for n = 0, n = 1 and n = 2 are as

follows:

(1) $N_0(\vartheta) = \frac{1}{2} K \cos\vartheta \left[(x-W)\text{arc tg}\left[\frac{(W-x)\cos\vartheta}{Z}\right] + (W+x)\text{arc tg}\left[\frac{(W+x)\cos\vartheta}{Z}\right] \right]$

(2) $N_1(\vartheta) = \frac{1}{3} K \cos\vartheta \left[\frac{Z^2 - 2(Z^2 + (W-x)^2\cos^2\vartheta)}{A_-^{1/2}} - \frac{Z^2 - 2(Z^2 + (W+x)^2\cos^2\vartheta)}{A_+^{1/2}} \right]$

(3) $N_2(\vartheta) = \frac{1}{8} K Z^3 \cos^2\vartheta (A_-^{-1} + A_+^{-1}) + \frac{3}{4} \cos^2\vartheta\, N_0(\vartheta)$

where $K = 4 I_0(Y + W - Z \text{ tg})$ $A_\pm = Z^2 + (W + x)^2 \cos^2\vartheta$

Pattison (Ph.D. thesis, 1965) gives the following general expression for n > 1

(4) $N_n(\vartheta) = \frac{K Z^{n+1}\cos^n\vartheta}{n(n+2)} (A_-^{-n/2} - A_+^{-n/2}) + \frac{n+1}{n+2} \cos^2\vartheta\, N_{n-2}(\vartheta)$

Thus one can calculate the predicted projected angular distribution of particles crossing the sensitive volume of a detector (rectangular) for different values of n.

The present cases are (i) The angular distribution of the penetrating particles observed in the chamber, (ii) The angular distribution of hadrons and (iii) The aperture of the chamber for bursts produced in glass.

The results of calculations have been mentioned, for these cases, in sections 5.3,7.3 and 7.4 respectively. In what follows I_0 is normalised to 1 cm^{-2} s^{-1} st^{-1}.

B.2. The angular distribution of the penetrating particles observed in the chamber.

The accepted events defined as the tracks crossing the top layer of F2 and one-third of F2 (see figure 5.1).

Thus $2Y = 2V = 151$ cm., $2W = 2x = 196$ cm., $Z = 30.8$ cm.
and the limit of integral $\vartheta_{max} = 78.47°$.

The results of the calculations for a range of n is
shown in figure B.2. The differential aperture demonstrated
in figure B.2. is expressed in units of cm^{-2} st/rad.

The area under the curves of figure B.2. normalised to
the total observed events and a chi-square test between the
predicted and observed distributions carried out, to find the
best value of n.

B.3. The angular distribution of the charged hadrons
     induced burst in iron.

The acceptable events satisfying the following criteria.

(i)   The hadrons traverse Fla (see figure 3.11)

(ii) The energy of bursts being ≤ 500 GeV and the primary
tracks do not pass within one centimetre (in scanning sheet)
in either side of the chamber.

Then $2V = 151$ cm., $2Y = 111.8$ cm., $2W = 2x = 165$ and
$Z = 50$ cm.

The best value of n was found in the same procedure
as described in B.2.

B.4. The aperture of the chamber for bursts produced in
     glass.

The interaction length of the bursts produced in F2 or
F3 (see figure 3.11) were measured in F series. This was
done determining the slope of the measured frequency distri-
bution of the distance between the point of interaction and
top of Fla. The measured distribution should be corrected
for the total aperture of the chamber. This is a function of
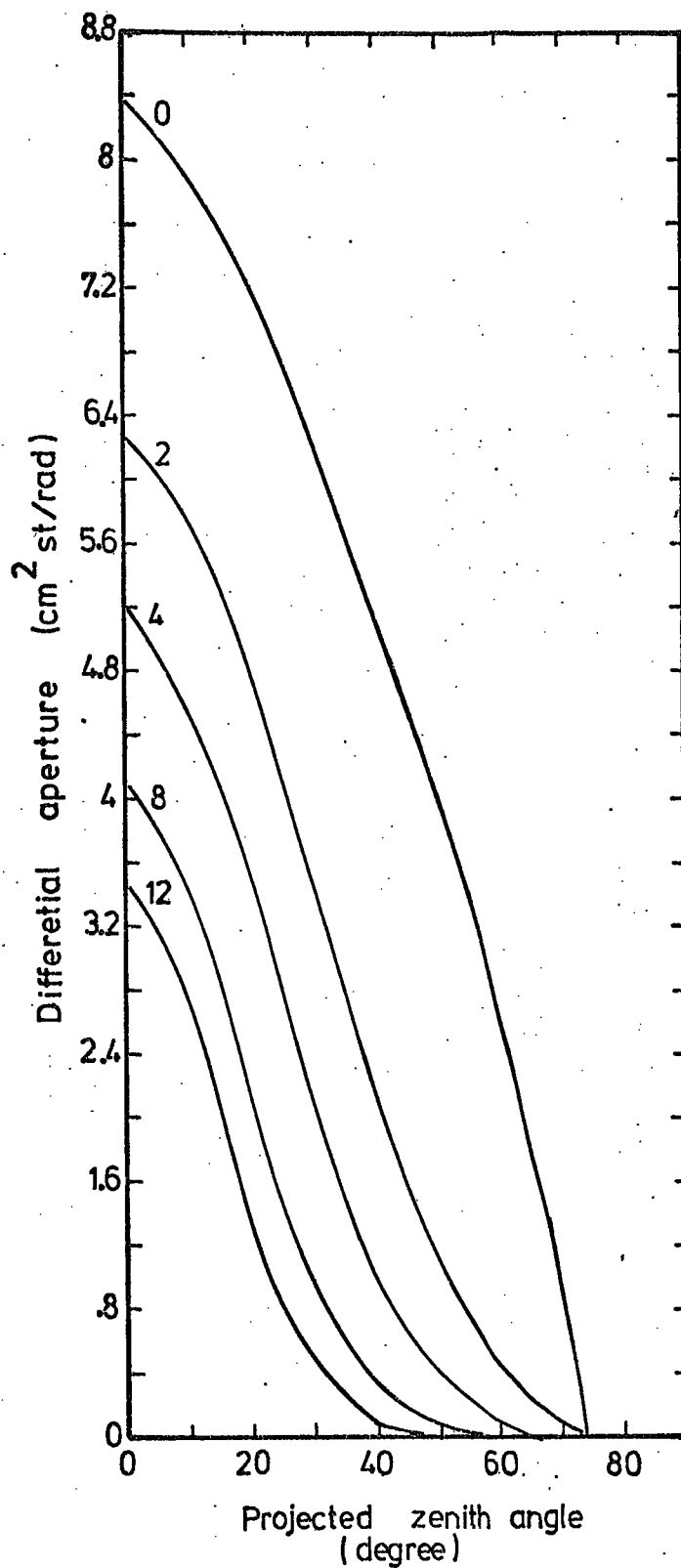
Figure B.2.   The acceptance function of the chamber in measuring the angular distribution of EAS particles with n as a parameter (in $I = I_0 \cos^n \vartheta$) as indicated for each curve.

the exponent n, of the angular distribution of particles induced bursts, and Z.

The total aperture of the chamber as a function of n, for different values of Z and $2V = 2Y = 151$ cm., $2W = 165$ cm. and $2 X = 196$ cm., is shown in figure B.3.

The measured frequency multiplied by N_{total} $(n=9, Z)$ to correct for the loss of the events due to the aperture of the chamber. (The value of $n = 9$ is taken from the measured angular distribution of hadrons in F series).

<u>Figure B.3.</u>   Integral aperture of the chamber
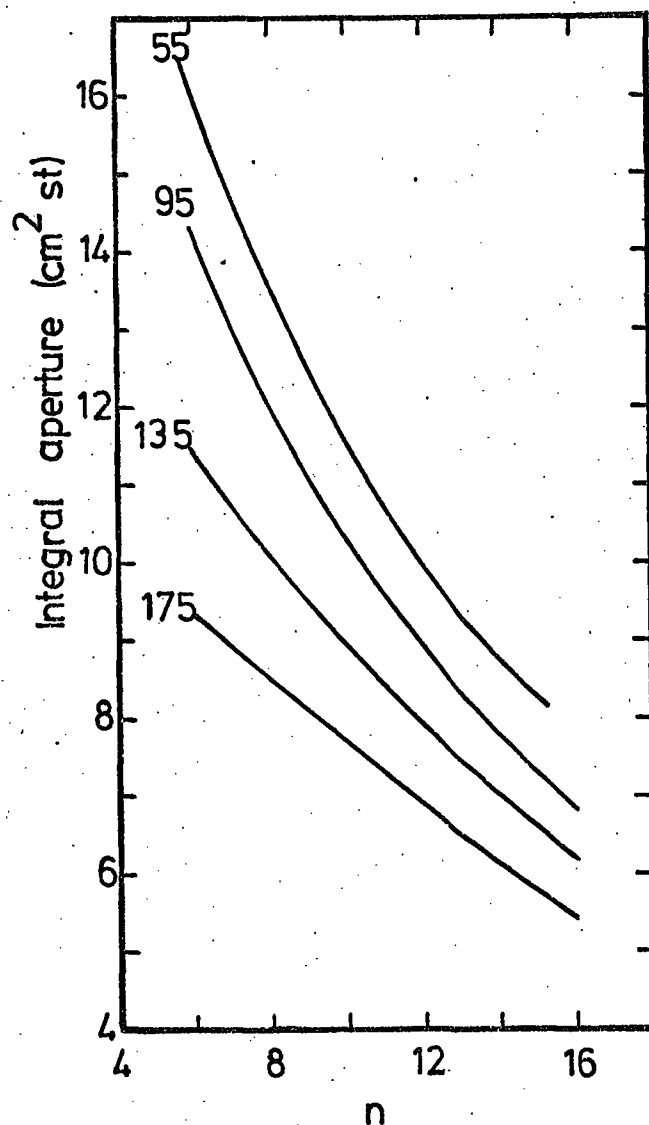for particles induced burst in
the glass as a function of n (in
$I = I_0 \cos^n \vartheta$) for different values
of Z in cm. as indicated for each
curve.

APPENDIX C

THE EFFECT OF DIFFERENT DETECTORS ON
THE MEASURED DENSITY OF EAS

It was mentioned that the density of EAS recorded by the liquid scintillators (on the roof of the chamber) are higher than the expected densities if one uses G-M counters or proportional counter (see table 4.2).

Brennan et al. (1958a) include a tray of forty G-M counters, of total area 0.382 m^2, with the array of liquid scintillation counters to compare the response of the G-M counter and scintillation counter. The scintillators were 10 cm. in depth and 0.23 m^2 in area each. For each shower detected by the array, they measure the density recorded by the tray of G-M counters. They came to the conclusion that the ratio of the density recorded by the G-M tray to the density recorded by the scintillator, at the location of G-M tray

$$\beta = \frac{\rho_G}{\rho_S} = 0.68 \pm 0.02 \quad \text{where } \rho_G \text{ and } \rho_S \text{ are}$$

the Geiger particle density and the predicted scintillator density respectively.

If one assumes that $\frac{\rho_S}{\rho_G}$ is proportional to the scintillator thickness, thus for a 15 cm depth (equal to the depth of scintillators used in EAS triggering system of the chamber, see figure 3.11).

$$\beta = 0.45$$

This is consistent with the ratio obtained in table 4.2.

The fact that β is not equal to one could be attributed to the multiplication of shower particles in the scintillator itself. The effect has been investigated by Katsumuta (1964), measuring the response of two plastic scintillators, positioned on top of each other, to the EAS particles. Katsumuta found that the ratio of pulse heights between first layer and second layer of detectors increase the number of charged particles passing 5 cm. plastic scintillator by about 30% in average and being almost independent of core distance for $r < 20$ m. The 30% increase found by Katsumuta is for 5 cm. scintillator. Thus for a 10 cm. scintillator the increase could be 60% which is almost the same as it is found by Brennan et al. (1958b).

One should note that it is quite possible that the ratio β may vary with core distance. Brennan et al. suggest that the dependence of β on core distance is such that it will not have a significant effect on the size spectrum measured by Brennan et al (1958b).

The inconsistency between the results of proportional counter and G-M counters (see table 4.2) could be explained as a result of contribution of photon interaction with the glass wall of the G-M counters.

APPENDIX D

MEASUREMENT OF THE BAROMETRIC COEFFICIENT
OF INCOHERENT SINGLE PARTICLES

The coincidence rate of the G-M telescope, used in the calibration of the proportional counter (see section 3.4.4), was measured as a function of the atmospheric pressure. The results are shown in figure D.1. The value obtained for the barometric coefficient is $\beta = 3.7 \pm 0.3$ % (cm Hg $)^{-1}$. Hence the absorption length of the incoherent single particle

$$\Lambda_I = 386\ ^{+32}_{-28}\ \text{g cm}^{-2}.$$

The proportion of muons in the recorded coincidence rate of the G-M telescope is 0.66 (the remainder 0.34 being due to electrons, see section 3.6), hence

$$\frac{1}{\Lambda_I} = \frac{0.66}{\Lambda_\mu} + \frac{0.34}{\Lambda_e}\ \text{where}\ \Lambda_\mu\ \text{and}\ \Lambda_e\ \text{are}$$

the absorption lengths of muons and electrons respectively.

Bercovitch (1967) has measured the barometric coefficient of muons at sea level as $\beta_\mu = 2.15$ % (cm Hg$)^{-1}$. Thus $\Lambda_\mu = 632$ g cm^{-2}. Substituting Λ_μ and Λ_I in the above formula one obtains $\Lambda_e = 203\ ^{+34}_{-23}\ \text{g cm}^{-2}.$
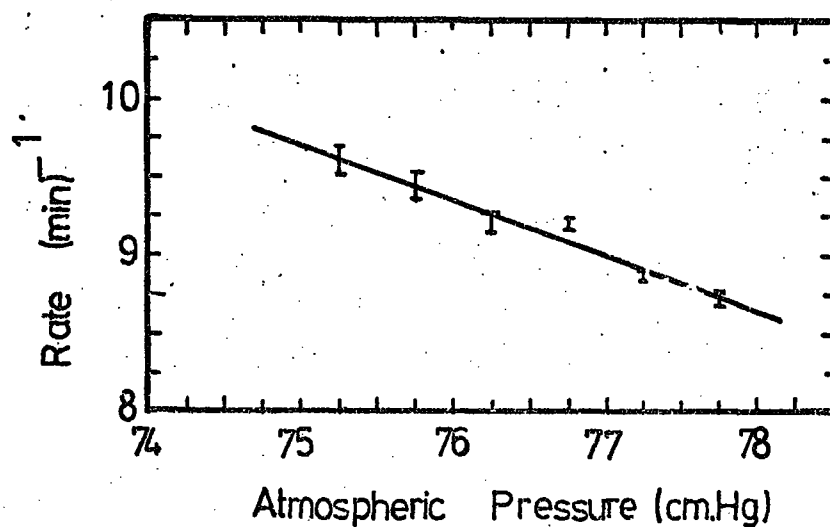
Figure D.1.   The coincidence rate of the G-M
               telescope as a function of atmospheric
               pressure.   The solid line is the best
               line through the experimental data.

APPENDIX E

SEPARATION DISTRIBUTION OF GROUPS OF MUONS

The separation distribution of the groups of muons with either two or three muons having traversed the flash tube area ($2.95 \ m^2$) have been measured. The results are shown in figure E.1. In measuring the distribution shown in figure E.1, the distance between muons in plane AB(see figure 4.3) have been determined. Table E.1 compares the measured mean separation of muons with the expected mean separation of muons, assuming they are randomly distributed. It can be seen that good agreement is found which indicates that the observed groups of muons, in the chamber, are randomly distributed.

Blake et al., (1971) have measured the separation distribution of groups of two and three muons, having traversed $4 \ m^2$ area of their detector, in showers with energy of $>10^{17}$ eV at distances $r > 100$ m. They come to the conclusion that the muons are randomly distributed. The group of parallel muons with $E \geq 10$ GeV have been studies by Ll'ina et al., (1974), using $4 \ m^2$ spark chamber. These authors show that the existence of parallel muon groups can be attributed to fluctuations of the muon lateral distribution function near the axis of the EAS.
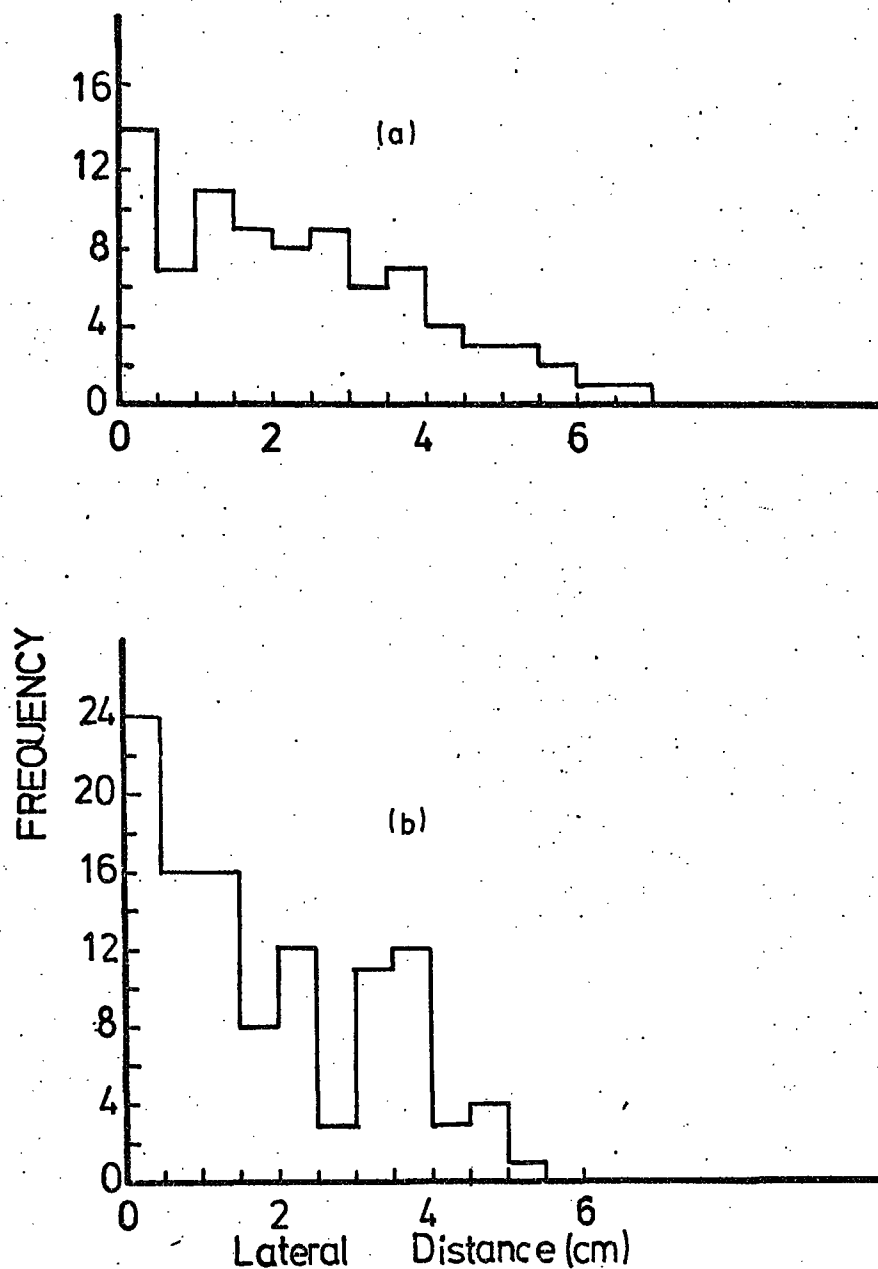
Figure. E.1   The lateral separation distribution
of groups of 2 muon (a) and 3 muon
(b).   1 cm. is equivalent to 20 cm. in
real space.

Muon multiplicity (muons/2.95 m^2)	Total number of observed events	Measured mean separation (cm of scanning sheet)	Expected mean separation (cm of scanning sheet).
2	85 (Films F1 -F20)	2.33 ± 0.18	2.57
3	110 (Films F1 -F20)	1.86 ± 0.13	1.92

Table E.1   The basic data of the separation distribution of groups of muons.   The expected mean separation are one-third and one-fourth of the total width of the chamber for muon multiplicities of 2 and 3 respectively. (1 cm. of scanning sheet is equivalent to 20 cm. in real space).

REFERENCES

PICCR=Proceeding Int. Conf. Cosmic Rays.

Abrosimov, A.T., et al. (1960), Sov. Phys. JETP, 38, 100.

Adair, R. and Kasha, H., (1969), Phys. Rev.Lett., 23, 1355.

Alexander, G., and Yekutieli, G., (1961), Nuvo Cim., 19, 103.

Allaby, J.V., et al., (1969), Nuvo Cim., 64A, 75.

Allkofer, O.C., Grupen, C., and Stamm, W., (1971), Phys. Rev.D., 4, 638.

Andrew, D.A. et al., (1970), Acta Phys. Hung. 29, Supp. 3, 343

Antipov, Y.U. M., et al., (1969), Phys. Lett., 29, B, 245.

Ashton, F., Coats, R.B., and Simpson, D.A., (1965) PICCR, London, 2, 1078.

Ashton, F., Coats, R.B., Kelly, G.N., Simpson, D.A., Smith, N.I., and Takahashi, T., (1968), J. Phys. A., 1, 569.

Ashton, F., Coats, R.B., King, J., T.Tsuji, K., and Wolfendale, A.W., (1971), J. Phys. A. 4, 895.

Ashton, F., (1973) Cosmic Rays at Ground Level, Ed. Wolfendale, A.W., (Inst. Phys.).

Ashton, F., (1973) unpublished.

Ashton, F., Cooper, D.A., Parvaresh, A., and Saleh, J., (1973a), J. Phys. A., 6, 577.

Ashton, F., et al. (1973b), PICCR, Denver, 4, 2489.

Ashton, F., et al., (1973c), PICCR, Denver, 4, 2610.

Ashton, F., et al., (1973d), PICCR, Denver, 4, 2997.

Ashton, F., et al., (1973e), PICCR, Denver, 3, 2096.

Auger, P., (1938), Compt. Rend., 207, 907.

Backenstoss, G., Hyams, B.D., Marin, P.C., and Stlerlin, U., (1963), Phys. Rev., 129, 2759.

Barrett, P.H., et al., (1952), Rev. Mod. Phys. 24, 133.

de Beer, J.F., Holyoak, B., Wdowczyk, J. and Wolfendale, A.W., (1966), Proc. Phys. Soc., 89, 567.

Bell, C.J., et al., (1974), J. Phys.A., 7, 990.

Bennett, S., Delvaille, J., Greisen, K., and Kendziorski, F., (1962), J. Phys. Soc. Japan, Suppl. A-III; 17, 196.

Bercovitch, M., (1967), PICCR, Calgary, 269.

Berger, M.J., and Seltzer, S.M., (1964), NASA, SP - 3012, unpublished.

Betev, B., Bogdanova, N., Stanev, T., and Valas, G., (1970), Acta Phys. Hung, 29, Suppl., 3, 595.

Bhabha, H.J., (1937), Proc. Roy. Soc., A159, 432.

Bhabha, H.J., (1938), Proc. Roy. Soc., A164, 257.

Bjorboe, J., et al., (1968), Nuvo Cim., 538, Supp. 3, 31.

Bjorken, J.D., and Glashaw, S.L., (1964), Phys. Lett., 11, 255.

Blake, P.R., Ferguson, H., and Nash, W.F., (1971), PICCR, 3, 1062.

Blunk, O., and Leisggang, S., (1950), Z. Physik, 128, 500.

Blunck, O., and Westphal, K., (1951), Z. Physik, 130, 641.
Bohm , E., et al., (1967), PICCR, Calgary, 2, 50
Bonczak, B., et al., (1968), Cana, J. Phys., 46, S102.

Bradt, H., et al., (1965), PICCR, London, 2, 715.

Bradt, H.V., and Rappaport, S.A., (1967), Phys. Rev., 164, 1567.

Braginskii, V.B., Zel'dovich, Ya. B., Martynov, Y.K., and Migulin, V.V., (1968), Sov. Phys. JETP, 27, 51.

Brennan, M.H., Millar D.D., Rathgeber, M.H., an d Wallace,C.S., (1958), Nature, 182, 1053. & Pg. 905

Brooke, G., Haymann, P.J., Kamiya, Y., and Wolfendale, A.W., (1964), Proc. Phys. Soc., 83, 853.

Bray, A.D., et al., (1964), Nuvo.Cim., 32, 827.

Burbidge, G., and Burbidge, M., (1967), Quasi - Stellar Objects, (San Fransisco : W.H. Freeman Co.), 206.

Cairns, J., McCuskev, C.B.A., Peak, L.A., and Woolcott, R.L.S., (1969), Phys. Rev., 186, 1394.

Carlson, J.F., and Schein, M., (1941), Phys. Rev., 59, 840.

Catz, PH., et al., (1969), PICCR, Budapest, 399, (1970), Acta Physia. Hung., 29, Suppl., 399.

Catz, PH., Gawin, J., Hochart, J.P., Maze, R., and Wdowczyk, J., (1971),PICCR, Hobart, 3, 1030.

Chatterjee, B.K., et al., (1965), PICCR, London, 2, 627.

Chatterjee, B.K., et al., (1968), Cana, J. Phys., 46, S137.

Chaudhuri, N., and Sinha, M.S., (1964), Nuvo Cim., 32, 853.

Chaudhuri, N., and Sinha, M.S., (1965), Nuvo Cim., 35, 13.

Citron, A., (1958), Habilitation Schrift, (Freiburg: Albert Ludwigs Universitat).

Clark, A.F., et al., (1971), Phys. Rev. Lett., 27, 51.

Clark, G., Earl, J., Kraushaer, W., Linsley, J., Rossi, O., and Scherb, F., (1958), Nuvo Cim., 8, Supp., 2, 623.

Clark, G.W., et al., (1960), Phys. Rev., 122, 637.

Clark, G.W., et al., (1963), PICCR, Jaipur, 4, 65.

Coats, R.B., (1967), Ph.D thesis, Durham, unpublished.

Cocconi, G., Cocconi - Tongiorgi, V., (1949), Phys. Rev., 75, 1058.

Cocconi, G., (1961), Handbuck der Physik, Vol. XLVI/I, 215-271.

Cocconi, G., Koester, L.S., and Perkins, D.H., (1961), UCRL High Energy Physics Study Seminars, 28, (UCID - 1444).

Cocconi, G., (1965), PPICCR, London, 2, 616.

Crispin, A., and Fowler, C.N., (1970), Rev. Mod. Phys., 42, 290.

Darda, M., Navarra, G., Penengo, P., and Sitte, K., (1972), Nuvo Cim., 9A, 319.

Deery, R.F., and Neddermeyer, S.H., (1961), Phys. Rev. 121, 1803.

Delaville, J., Kendziorski, F., and Greisen, K., (1960), PICCR, Moscow, 2, 79.

Dixon, H.E., et al. (1974), Proc. R. Soc. Lond. A., 339, 133.

Earnshaw, J.C., et al., (1967), Proc. Phys. Soc., 90, 91.

Earnshaw, J.C., Orfor, K.J., Rochester, G.D., Turver, K.E., and Walton, A.B., (1968), Cana. J. Phys. 46, S122.

Ebert, P.J., Lauzon, A.F., and Lent, E.M., (1969), Phys. Rev., 183, 422.

Edge, D.M., et al., (1973), J. Phys. 6A, 1612.

Euler, H., (1940), Z. Physik, 116, 73.

Evans, G.R., Fancey, N.E., Muir, J., and Watson, A.A., (1971/72), Proc. R.S.E. (A), 70, 143.

Fermi, E., (1940), Phys. Rev., 57, 485.

Fermi, E., and Yang, C.N., (1949), Phys. Rev., 76, 1739.

Feyman, R.P., (1969), Phys. Rev. Lett., 23, 1415.

Firkowski, R., Grochalska, B., Olejniczak, W., and Wdowczyk, J., (1973), PICCR, 4, 2605.

Frauenfelder, H., Kruse, U.E., and Sard, R.D., (1970), Phys. Rev. Lett., 24, 33.

Fukui, S., et al., (1960), Prog. Theor. Phys. Supp.,16, 1.

Galbraith, W., (1958), Extensive Air Showers, Published by Butterworths.

Gallinaro, G., and Morpurgo, G., (1966), Phys. Lett., 23,609.

Garibyan, G.M., and Ispiryan, K.A., (1972), JETP Lett., 16, 585.

Garmire, G., Leong, C., and Sreekantan, B.V., (1968), Phys. Rev., 166, 1280.

Gawin, J., Hibner, J., and Zwadzki, A., (1963), PICCR, Jaipur, 4, 180.

Gell-Mann, M., (1964), Phys. Lett., 8, 214.

Gemesy, T., Somogyi, A., and Valas, G., (1964), Nukleonika, 2, 365.

Giller, M., et. al., (1970), Acta Phys. Hung. 29, Supp. 3,545.
Goorevich, L., and Peak, L.S., (1973), PICCR, Denver, 4, 2617.
Greider, P.K.F., (1970), Inst. Nucl. Study, Tokyo, Pub. INS.J. 125.

Greider, P.K.F., (1972), Nuvo, Cim., 7A, 867.

Greider, P.K.E., (1973a), PICCR, Denver, 4, 2639.

Greider, P.K.F., (1937b), PICCR, Denver, 4, 2467.

Greisen, K., (1956), Progress in Cosmic Ray Physics, Vol.3, Chap.1. (Amsterdam, North Holland).

Greisen, K., (1960), Ann. Rev. Nucl. Sci., 10, 63.
Greisen, K., (1965), PICCR, London, 2, 609.
Grigorov, N.L., et. al., (1971), PICCR, Hobart, 5, 1752.

Hasegawa, H., Noma, M., Suga, K., and Toyoda, Y., (1965), PICCR, London, 2, 642.

Hayakawa, S., and Tomonaga, S., Prog. Theor. Phys., 4, 287, 496.

Hayakawa, S., (1969), Cosmic Rays (Wiley Interscience).

Hayman, P.J., and Wolfendale, A.W., (1962), Proc. Phys. Soc. 80, 710.

Hebbard, A.F., and Fairbank, W.M. (1971), Priprint.

Herford, F.L., (1950), Phys. Rev., 78, 727.

Higashi, S., et al., (1962), J. Phys. Soc. Japan, AIII, Suppl., 17, 209.

Hillas, A.M., (1970a), Acta Phys. Hung. 29, Suppl., 3, 539.

Hillas, A.M., (1970b), Acta, Pnys. Hung. 29, Suppl., 3, 355.

Hodson, L., (1953), Proc. Phys. Soc. 66A, 49, 65.

Hollows, J.D., Hunter, H.W., and Suri, A.N., (1968), J. Phys. A., 2, 591.

Ivanenko, I.P., and Samosudov, B.E., (1959), JETP, 8, 884, (Eng.Trans.).

Ivanenkov, J.P. and Samusodov, B.E., (1967a), Bull. Acad. Sci., U.S.S.R. (Phys. Ser.), 30., 1722.

Ivanenkov, I.P., and Samusodov, B.E., (1967b), Sov. J. Nucl. Phys., 5, 442.

Jones, L.W. et al., (1967), Phys. Rev., 164, 1584.

Jones, L.W., (1971), PICCR, Hobart, Rapporteur paper.

Jones, W.V., (1969), Phys. Rev., 187, 1868.

Jones, W.V., Pinkan, K., Polluogt, U., Schmidt, W.K.H., and Huggett, R.W., (1970), Acta Phys. Hung., 29, Suppl., 4, 521.

Kalmykov, N.M., Khristiansen, G.B., and Fomin, YU.A., (1971), PICCR, Hobart, 2074.

Kamata, K., and Nishimura, J., (1958), Prog. Theor. Phys. Suppl., 6, 93.

Kamata, K., et al.,(1968), Cana. J. Phys., 46, S72.

Kameda, T. Maeda, T., Oda, H., and Sugihara, T., (1965), PICCR, London, 2, 681.

Kanmangara, M.L.T., and Zlukovic, M., (1953), Phil. Mag., 44, 797.

Kaneko, T., et al., (1971), PICCR, Hobart, 3, 945.

Kasha, H. et. al., (1967), Phys. Rev. Lett., 20, 217.

Katsumuta, I., (1964), J. Phys. Soc. Japan, 19, 800.

Kearney, P.D. and Hazen, W.E., (1965), Phys. Rev., 138,173.

Kempa, J., Wdowczyk, K., and Wolfendale, A.W., (1974), J. Phys. A., 7, 1213.

Khristiansen, G.B., Kulikov, G.V. and Solov'eva, V.I., (1974), S.J. Nucl. Phys. 19, 162.

Kiarly, P., and Wolfendale, A.W., (1970), Phys. Lett., 31, B, 410.

Kirk, T.B., and Neddermeyer, S.H., (1968), Phys. Rev., 171, 1412.

Kolhorster, Matthes, and Webber, (1938), Naturwiss, 26, 576.

Kozlov, V.I. et al., (1973), PICCR, Denver, 4, 2588.

Krasilnikov, D.D., (1973), PICCR, Denver, 4, 2393.

Kraybill, H., (1949), Phys. Rev., 76, 1092.

Landsberg, L.G., (1974), Sov. Phys. USP., 16, 251.

La Pointe, M., et al., (1968), Cana, J. Phys., 46, 68.

Lattes, C.M., Occhialini, G.P.S., and Powell, C.F., (1947), Nature, 160, 453.

Linsley, J., and Scarsi, L., (1962), Phys. Rev. Lett., 9, 123.

Linsley, J., (1964), Proc. 8th. Int. Conf. on Cosmic Rays (Bombay: TIFR), 4, 77.

Linsley, J., (1973), PICCR, Denver, 5, 3212.

Lloyd, J.L., (1960), Proc., Phys. Soc., 75, 387.

Ll'ina, N.P. et al., (1974), Sov. J. Nucl. Phys., 18, 62.

Malos, J., (1960), PICCR, Moscow, 2, 84.

McCaughan, J.B.T., et al., (1965a), Nuvo Cim., 38, 697.

McCaughan, J.B.T., et al., (1965b), PICCR, London, 2, 720.

Messel, H., and Crawford, D., (1970), Tables, (Oxford, Pergamon).

Millikan, R.A., (1910), Phil. Mag., 19, 209.

Mishnev, S.I. and Nikolski, S.I., (1960), Zh. EXP. Teor. FIZ., 38, 257.

Miyake, S. et al., (1970), Acta Phys. Hung. 3, 471.

Miyake, S., Ito, N., Kawakami, S., Hayashida, N., and Hayashi, Y., (1973), PICCR, Denver, 5, 3220.

Morpurgo, G., (1967), Acta Phys. Hung., 22, 105.

Morpurgo, G., Gallinaro, G., and Palmieri, G., (1970), Nucl. Inst. Meth, 79, 95.

Murthy, G.T. (1967), Ph.D. Thesis, Bombay, Unpublished.

Murthy, G.T. et al., (1968a), Cana. J. Phys. 46, S147.

Murthy, G.T. et al., (1968b), Cana. J. Phys., 46, S153.

Murthy, G.T., et al., (1968c), Cana. J. Phys., 46, S159.

Murzin, V.S., and Rappoport, I.D., (1963), JETP, 20, 1-3.

Nambu, Y., (1966), Preludes in Theoretical Physics, Eds., de-Shalit, Feshbach, H., Van Hove, L., (North Holland, Amsterdam), 133.

Nikolski, S.I., (1963), Soviet USP., 5, 849.

Nishimura, J., and Kamata, K., (1952), Prog. Theor. Phys., 1, 185.

Norman, R.J., (1955), Aus. J. Phys., 8, 419; (1956), Phys. Rev., 72, 131.

Norman, R.J., (1956), Proc. Phys. Soc., 69, A, 804.

Orford, K.J., and Turver, K.E., (1969), PICCR, Budapest, 3, 585, (1970), Acta Phys. Hung., 29, Suppl., 3, 585.

Pattison, J.B.M., (1965), Ph.D. Thesis, Durham, unpublished.

Peters, B., (1952), Progress in Cosmic Ray Physics, Vol.1, (Amsterdam - North Holland), Chapt.4.

Pinkau, K., and Thompson, K.V., (1966), Rev. Sci. Inst., 37, 302.

Porter, N.A., et al., (1957), Phil. Mag., 2, 900.

Prescott, J.R., (1956), Proc.Phys. Soc., 69, A, 870.

Rahm, D.C., and Sternheimer, R.M., (1969), Brookhaven Priprint, BNL, 14072.

Rahm, D.C. and Loutitt, R.I., (1970), Phys.Rev.Lett., 24, 279.

Ramana Murthy, P.V., (1968), Nucl. Inst. Meth., 63, 77.

Rank, D.M., (1968), Phys. Rev., 176, 1635.

Reid, R.J. et al., (1961), Proc. Phys. Soc., 78, 103.

Reid, R.J. et al., (1962), J. Phys. Soc. Japan, A III, Suppl., 17, 234.

Rochester, G.D., and Butler, C.C., (1947), Nature, 160, 855.

Roe, B.P., and Ozaki, S., (1959), Phys. Rev., 116, 1022.

Rossi, B., (1952), High Energy Particles, (Prentice-Hall).

Rossi, B., (1960), PICCR, Moscow, 2, 18.

Ryan, M.J., et al., (1972), Phys. Rev. Lett., 28, 985.

Sakata, S., (1956), Prog. Theor. Phys., 16, 686(L).

Saleh, A.J., (1973), M.Sc. Thesis, Durham, unpublished.

Samurski, M., Stanbert, R., Trumper, J., and Bohm, E., (1971), PICCR, Hobart, 3, 959.

Saxena, V.C., (1973), Nuvo Cim., 17B, 53.

Schein, M., Jesse, W.P., and Wollan, E.O., (1941), Phys. Rev.,
59, 615.

Serre, C., (1967), CERN report, 67-5.

Simpson, D.A., (1964), M.Sc. Thesis, Durham, unpublished.

Sinanoglu, O., Skutnik, B., and Tousey, R., (1966),
Phys. Rev. Lett., 17, 785.

Sitte, K., (1970), Suppl. Nuvo. Cim., 6, 866.

Skobel'tsyn, D.V. (1929) Z. Physik,,54, 686.

Skutnik, B.J., (1970), Phys. Rev., 2, D, 635.

Staubert, R., et al., (1970), Acta Physica Hung., 29, Suppl.
3, 661.

Sternheimer, R.M., (1952), Phys. Rev., 88, 851.

Sternheimer, R.M., (1956), Phys. Rev., 103, 511.

Suga, K., et al., (1963), PICCR. Jaipur, 4, 9.

Swinson, D.B., and Prescott, J.R. (1965), PICCR, London, 2,721.

Swinson, D.B. and Prescott, J.R., (1968), Cana. J. Phys.,
46, S292.

Symon, K.R., (1948), Ph.D. Thesis, Harward University.

Tabata, T., Ito, R., Oskabe, S, and Fujita, Y., (1971), J.
Appl. Phys., 42, 3361.

Takbaev, Zh. S., Lukin Yu.T., and Emelyanov, Yu.A., (1965), PICCR
London, 2, 967.

Tanahashi,G.,(1965), J. Phys. Soc. Japan , 20 , 883.

Tanaka, Y., (1961), J. Phys. Soc. Japan, 16, 866.

Tarjanne, P., and Teplitz, V.L., (1963), Phys. Rev. Lett., 11,
447.

Thielheim, K.O., and Beirsdorf, R., (1969), J. Phys. A., 2, 341.

Tonwar, S.C., Naraman, S., and Sreekantan, B.V., (1971), PICCR,
Hobart, 3, 1171.

Ueda, A., (1960), Prog. Theor. Phys. 24, 1231.

Van Staa, R., Aschenbach, B., and Bohm, E., (1973), PICCR,
Denver, 4, 2676.

Vatcha, R.H., and Sreekantan, B.V., (1973), J. Phys. A., 6,
1067.

Vavilov, Y.N., Erstigneer, Y.F., and Nikolski, S.I., (1957), J. EXP. Theor. Phys., 32, 1319.

Vernov, S.N. (1961), Sov. Phys. JETP, 41, 340.

Vernov, S.N., et al., (1968), Cana, J. Phys. 46, S197.

Vernov, S.N., et al., (1970), Acta Phys.Hung. 29, Suppl., 3, 429.

Wdowczyk, J., (1973), Cosmic Rays at Ground Level, Ed. Wolfendale, A.W., (Inst. Phys).

Webber, W.R., (1973), PICCR, Denver, 5, 3568.

White, G.M., and Prescott, J.R., (1970), Acta Phys. Hung., 29, Suppl., 3, 31.

Wilson, J.G., (1970), Nature, 225, 1238.

Wilson, R.R., (1951), Phys. Rev., 84, 100.

Wolfendale, A.W., (1973), Cosmic Rays at Ground Level, Ed. Wolfendale, A.W., (Inst. Phys.).

Zatsepin, G.T., (1949), DOKI. Akad. Nauk. USSR, 67, 993.

Zweig, G., (1964), CERN, priprints, TH401, TH412.

Zweig, G., (1965), Symmetries in Elementary Particle Physics, (Acad. Press, New York), 192.